

7-6-2012

Dynamics and distribution of immunoglobulin E receptors : a dialog between experiment and theory

Kathrin Spendier

Follow this and additional works at: https://digitalrepository.unm.edu/phyc_etds

Recommended Citation

Spendier, Kathrin. "Dynamics and distribution of immunoglobulin E receptors : a dialog between experiment and theory." (2012).
https://digitalrepository.unm.edu/phyc_etds/65

This Dissertation is brought to you for free and open access by the Electronic Theses and Dissertations at UNM Digital Repository. It has been accepted for inclusion in Physics & Astronomy ETDs by an authorized administrator of UNM Digital Repository. For more information, please contact disc@unm.edu.

Kathrin Spendier

Candidate

Physics and Astronomy

Department

This dissertation is approved, and it is acceptable in quality and form for publication:

Approved by the Dissertation Committee:

James L. Thomas , Chairperson

V.M. Kenkre , Co-Chairperson

Sudhakar Prasad

Diane S. Lidke

Dynamics and Distribution of Immunoglobulin E Receptors: a Dialog between Experiment and Theory

by

Kathrin Spendier

B.Sc., Physics and Mathematics, University of New Mexico, 2006

M.S., Physics, University of New Mexico, 2008

DISSERTATION

Submitted in Partial Fulfillment of the
Requirements for the Degree of

Doctor of Philosophy,
Physics

The University of New Mexico

Albuquerque, New Mexico

May, 2012

©2012, Kathrin Spendier

Dedication

This dissertation is dedicated to my parents, Brigitte and Günther, and my husband Nathan. Thank you for your continuous support and encouragement.

Diese Dissertation ist meinen Eltern, Brigitte und Günther, und meinem Ehemann Nathan gewidmet. Ich danke Euch für Eure stetige Unterstützung und Ermutigung.

Acknowledgments

As only my name appears on the cover of this dissertation, I would like to take a moment and express my gratitude and appreciation to my mentors and collaborators, who have contributed to its production.

My deepest gratitude, which I cannot express in words, is to my two mentors, my experimental advisor Prof. James L. Thomas and my theoretical advisor Prof. V.M. Kenkre. I have been very fortunate to have two advisors who complemented each other in a very special way. Both taught me a tremendous amount and gave me the freedom to explore on my own. I also cherish the times we did not look at data or solved equations, when my mentors shared their personal life and their philosophical views. It was during these times, when I was introduced to Janus by Nitant and guided Jim safely around cliffs and down steep slopes.

I also must thank my collaborators. Specifically, Drs. Jerilyn Timlin and Amanda Carroll-Portillo, who gave me the opportunity to join their investigations on mast cells. I also am thankful to Profs. Diane Lidke and Keith Lidke, who took time for me when I had a question and allowed me to use their instruments. At this point, I also thank Prof. Bridget Wilson and the technicians of the Wilson lab for their support.

During my journey, I also was supported by the faculty of the Physics Department, which taught me a great deal during my undergraduate and graduate years and were very supportive during my years on the UNM skiteam.

I am thankful to the members of the Consortium of the Americas for Interdisciplinary Science for our stimulating weekly meetings, which were especially fun when Prof. Dave Dunlap participated.

Another group of people, who joined me on my journey, are the members of the Spatio Temporal Modeling Center. I am certain that we will meet again at future Biophysical Society meetings.

During my last three years as a graduate student, I was a fellow of the Program in Interdisciplinary Biology and Biomedical Science, short PiBBs. During this time, PiBBs did not only support me financially but also gave me a unique opportunity to learn from and work with fellow graduate students from other departments.

Most importantly, none of this would have been possible without the love and support of my family, who let me live my dreams far away from home. I know that it has not been easy for them.

Lastly, I thank my husband Nathan for his encouragement, understanding and optimism. You have been my pillar of support throughout my graduate career as well as in a foreign country, I now call home.

Dynamics and Distribution of Immunoglobulin E Receptors: a Dialog between Experiment and Theory

by

Kathrin Spendier

B.Sc., Physics and Mathematics, University of New Mexico, 2006

M.S., Physics, University of New Mexico, 2008

Ph.D., Physics, University of New Mexico, 2012

Abstract

This dissertation explores the dynamics and distribution of immunoglobulin E receptors (Fc ϵ RI) on mast cells by drawing on the techniques of experimental and theoretical physics. The motivation for these investigations is provided by a considerable interest in the transmembrane signaling mechanisms of immunoreceptors, especially when triggered with membrane-bound ligands.

Experimental investigations quantify the spatiotemporal dynamics of the redistribution of Fc ϵ RI due to membrane-bound monovalent ligands, using total internal reflection fluorescence microscopy and single-particle tracking. When mast cells contact such substrates, receptor clusters form at cell-substrate contact points. The initial rate of accumulation of receptors into these contact points or cell protrusions is consistent with diffusion-limited trapping. Over longer timescales (>10 s), individual clusters move with both diffusive and directed motion components and eventually coalesce to form a large central receptor patch surrounded by a receptor cluster depletion zone. Detailed analysis of single-particle

trajectories show that receptors maintain their diffusivity when confined within receptor clusters, and increase their diffusivity (above that of monomeric unliganded Fc ϵ RI) in central patches.

To study the kinetics of central patch formation, a new coalescence theory described by a melding process, which is not instantaneous, was developed. In these theoretical investigations, the difficult problem of moving boundaries is encountered. To handle the complexity, which stems from boundary growth due to particle melding, the study is divided into three parts. The first is about stationary trapping problems investigated by the standard defect technique, and the second is about a validity study of an adiabatic approximation for moving boundaries. In the last part of this dissertation, a new coalescence theory is developed, which is based on a completely self-consistent approach. Here, the time dependence of the moving boundary is not prescribed but obtained through feedback. Comparison of experiment and theory shows that observed biological cluster coalescence is delayed at early times and occurs at a faster rate at later times than predicted by a simple theory. The incompatibility at early times is addressed by a generalization of the theory to incorporate a time-dependent melding process by a memory concept, which quantitatively explains the observed delay.

Contents

Glossary	xvii
1 Introduction	1
1.1 Opening remarks	1
1.2 Introduction to the biological system under investigation	2
1.3 Overview of the dissertation	4
2 Experimental methods and materials	10
2.1 Introduction	10
2.2 Experimental model system	11
2.3 Cells	12
2.4 Chemically crosslinked surface preparation	13
2.5 Supported lipid bilayers	13
2.5.1 Bilayer mobility	14
2.5.2 Bilayer defects	15

Contents

2.6	Fluorescence microscopy	16
2.7	EMCCD camera calibration	18
2.8	Cell micromanipulation	19
2.9	Single-particle tracking	21
2.10	Image thresholding	22
2.11	Degranulation assay	26
3	Distribution and Dynamics of IgE Receptors on Ligand Presenting Surfaces	27
3.1	Introduction	27
3.2	Receptor trapping at cell protrusions	29
3.2.1	Image correlation spectroscopy with explicit noise removal	31
3.2.2	Spatial scale of initial heterogeneities	33
3.2.3	Finite-element diffusion model	34
3.3	Receptor cluster distribution	35
3.3.1	Radial distribution	36
3.3.2	Receptor cluster nearest-neighbor distribution	37
3.4	Receptor cluster dynamics	38
3.4.1	Receptor cluster transport	39
3.4.2	Temporal Image Correlation Spectroscopy	43
3.5	Mast cell signaling	45
3.5.1	Mast cell signaling due to different ligand-presenting surfaces	45

Contents

3.5.2	Time-dependent mast cell signaling due to ligand-bearing fluid bi-layer	47
3.6	Concluding Remarks	48
4	Single-particle Tracking of IgE Receptors in Clusters and Patches	51
4.1	Introduction	51
4.2	Details of experiment	52
4.3	Analysis of mean-squared displacement plot	53
4.4	Monte Carlo calculations	56
4.5	IgE-FcεRI receptors diffuse within clusters and patches	57
4.6	IgE-FcεRI receptors diffuse faster in patches	59
4.7	IgE-FcεRI receptors can hop between clusters	62
4.8	Slowly diffusing receptors are not influenced by receptor cluster motion	64
4.9	Closing Remarks	64
5	The Formation of a Receptor Cluster Depletion Zone	68
5.1	Introduction	68
5.2	Receptor cluster depletion zone	70
5.2.1	Proposed depletion zone model	72
5.3	Rotational correlation function of randomly distributed disks	73

Contents

5.3.1	Scaled hard disk correlation function	76
5.3.2	Comparison to cluster test image	78
5.4	Rotational correlation function of a depletion zone	79
5.5	Image correlation of a receptor cluster depletion zone	81
5.6	Validation of the model by experimental data	82
5.7	Concluding Remarks	84
6	Structure of our Coalescence Theory	86
6.1	Introduction	86
6.2	The need to develop a new coalescence theory	87
6.2.1	Modeling the immunological synapse	87
6.2.2	Kinetic theory of nucleation	88
6.3	Modeling particle coalescence	92
7	Repository of Exact Solutions for Stationary Trapping Problems	94
7.1	Introduction	94
7.2	Brief review of standard defect technique	96
7.3	A single stationary trap on a lattice	99
7.3.1	Perfect absorption	100
7.3.2	Imperfect absorption	102
7.4	Obtaining a continuous prescription	104

Contents

7.5	Repository of solutions in one-dimension	106
7.5.1	Localized initial condition	106
7.5.2	The principle of superposition	107
7.5.3	General prescription for any initial distributions	108
7.5.4	Trapping in a harmonic potential	111
7.6	Repository of solutions in two-dimensions	116
7.6.1	Two-dimensional free-space propagator	117
7.6.2	Circular trap	118
7.6.3	Infinite line trap	120
7.6.4	Finite line trap: open trapping surface	122
7.7	Repository of solutions in three-dimensions	123
7.7.1	Three-dimensional free-space propagator	124
7.7.2	Spherical trap: passive diffusion in biology	124
7.7.3	Infinite sheet of traps	127
7.7.4	Trapping ring in three-dimensions	128
7.8	Equivalence to theory of conduction of heat in solids	130
7.8.1	Equivalence to constant-density initial condition in one-dimension	130
7.8.2	Requirement on diffusion propagator for equivalence	131
7.8.3	Relationship between reaction and capture rate	134

Contents

7.9	Permeable versus impermeable trapping boundaries	135
7.9.1	Permeable membrane in two-dimensions	136
7.9.2	Permeable membrane in three-dimensions	138
7.9.3	Importance of transient effect	139
7.10	Concluding Remarks	141
8	Validity of an Adiabatic Approximation in a Reaction-Diffusion System	143
8.1	Introduction	143
8.2	A single diffusing trap	145
8.3	A linearly moving trap	148
8.4	Two stationary traps	151
8.5	Two moving boundaries: boundary fixing transformation	153
8.6	Two linearly shifting boundaries	155
8.6.1	Survival probability in the time domain for particle starting at mid-point	158
8.6.2	Comparison to stationary and single moving boundary	158
8.6.3	Comparison to numerical solution	159
8.6.4	Adiabatic Approximation	161
8.7	Two linearly receding boundaries	162
8.8	Two oscillating boundaries	164
8.8.1	In-phase oscillation	164

Contents

8.8.2	Out-of-phase oscillation	167
8.9	Concluding remarks	168
9	A Mathematical Model for Receptor Cluster Coalescence	171
9.1	Introduction	171
9.2	Coalescence feedback approach	173
9.3	Development of an analytic approximation	174
9.3.1	Approximation applied to perfect absorption in one-dimension . .	177
9.4	Feedback idea in Laplace domain	179
9.4.1	Perfect absorption in one-dimension	180
9.4.2	Model of a model in Laplace Domain	182
9.5	Coalescence theory compared to Monte Carlo	
	Calculations in one-dimension	183
9.5.1	Perfect absorption and random particle transport	184
9.5.2	Perfect absorption and biased particle transport	186
9.5.3	Imperfect absorption and random particle transport	189
9.5.4	Imperfect absorption and biased particle transport	191
9.5.5	Validation of theory for finite sized particles	195
9.6	Coalescence theory compared to Monte Carlo Calculations in two-dim... .	196
9.6.1	Perfect absorption and localized initial condition	197
9.6.2	Perfect absorption and random initial condition	199

Contents

9.7	Comparison of theory to experiments	202
9.7.1	Radiative trap boundary	203
9.7.2	Experimental growth of central patch	204
9.8	Incorporation of a time-dependent capture rate	206
9.8.1	Time-dependent capture rate in form of a memory function	207
9.8.2	Possible functional form of the capture memory	208
9.9	Concluding Remarks	210
10	Conclusions	214
11	Appendices	218
A	Image Correlation Spectroscopy of Randomly Distributed Disks	219
A.1	Conventional image correlation spectroscopy	220
A.2	Hard disk image correlation spectroscopy	222
A.3	Simulations of typical microscope images	224
A.4	Accuracy of conventional image correlation spectroscopy	224
A.4.1	Sensitivity to detect disk size	225
A.4.2	Sensitivity to estimate disk number	227
A.5	Image correlation spectroscopy of large fluorescent proteins	228
A.5.1	Single fluorophore at center	228

Contents

A.5.2	Fluorophores forming a radially symmetric ring	229
A.5.3	Single fluorophore placed off-center	232
A.5.4	General formalism	234
A.6	Concluding Remarks	235
B	Common Laplace transforms in reaction-diffusion systems	236
C	Numerical Laplace transform	240
C.1	Introduction	240
C.2	Fourier Series Expansion	241
C.3	Gaver-Stehfest Method	243
C.3.1	MATLAB code	245
D	Validation of general prescription for any initial distribution	247
D.1	Initial point particle	248
D.1.1	Details of calculation	248
D.2	Comparison to the rate of disappearance	250
E	The Crank-Nicolson method	252
	References	257

Glossary

RBL	Rat basophilic leukemia 2H3 cell line
IgE	Immunoglobulin E
FcεRI	High affinity immunoglobulin E receptor
IgE-FcεRI	IgE-FcεRI receptor complex
IS	Immunological synapse
TCR	T cell receptor
TIRF	Total internal reflection fluorescence
DNP	Dinitrophenyl
SPT	Single particle tracking
COM	Center of mass
ICS	Image correlation spectroscopy
EMCCD	Electron multiplied charged coupled device
TICS	Temporal image correlation spectroscopy
MEM	Minimal Essential Medium

Glossary

DNP-BSA	Dinitrophenyl-conjugated bovine serum albumin
EGS	Ethylene glycol bis(succinimidylsuccinate)
Glut	Glutaraldehyde
PBS	Phosphate buffer saline
POPC	1-palmitoyl-2-oleoyl-sn-glycero-3-phosphocholine
DNP-Cap PE	N-dinitrophenyl-aminocaproyl phosphatidylethanolamine
DPPC	1,2-dipalmitoyl-sn-glycero-3-phosphocholine
D	Diffusion coefficient
MSD	Mean-squared displacement
SD	Standard deviation
SEM	Standard error of the mean
c.f.	Correlation function
OZ	Ornstein-Zernike

Chapter 1

Introduction

1.1 Opening remarks

This dissertation illustrates the interplay between experimental and theoretical physics in the investigation of dynamics and distribution of immunoglobulin E receptors in mast cells. The presented research project utilizes an intense dialog between experiment and theory to learn more about the system under investigation. The dissertation is divided conceptually into two parts. The first consists of experimental investigations to observe the phenomenon, presented in chapters 2, 3, 4, and 5. The second part explores our experimental observations of receptor cluster coalescence at the most fundamental level. Chapter 6 makes the clear crossover from experimental to the theoretical part of the dissertation, which consists of chapters 7, 8, and 9. It is in this part, specifically chapter 9, where we compare our mathematical coalescence model directly to experimental data. Based on this comparison, experimental observations suggest a generalization of our theory, as well as further experiments, which will continue the symbiotic relationship of these two disciplines in the field of mast cell signaling.

There are ten chapters including an appendix in this dissertation, whose contents are

Chapter 1. Introduction

briefly summarized in section 1.3. The necessary biological background for the dissertation is given in section 1.2. In chapters devoted to our theoretical investigations, each individual chapter will open with its own introduction, discussing essential background in the presented subject.

1.2 Introduction to the biological system under investigation

Cells in a multicellular organism must be ready to respond to a variety of extracellular signals [1]. They need to interpret and translate these signals correctly and if they fail to do so diseases such as cancer can occur. Extracellular signals include ligands on the surface of cells, parasites, or allergens that can bind to cell surface receptors in the target cell membrane. Such transmembrane signaling through receptor-ligand interaction plays important roles in cancer and in immune responses, including allergic responses. Our interest is immune signaling by mast cells.

Mast cell are part of the immune system. They originate from the bone marrow and circulate in an immature form until they settle in tissue throughout the body, including the skin and mucosal surfaces, where they mature. In tissue they can cause allergic responses as well as protect our body from parasitic infection. Mast cells have high affinity Fc receptors (Fc ϵ RI) specific for immunoglobulin E (IgE) and granules which store chemical mediators of inflammation. Typically, a mast cell secretes its mediators after Fc ϵ RI receptors loaded with IgE are crosslinked. Crosslinking occurs when multivalent ligand binds to two or more IgE-receptor complexes [2]. Figure 1.1 depicts a cartoon of mast cell stimulation by multivalent antigen. After one antigen binds to two or more IgE-receptor complexes, receptors are aggregated and their cytoplasmic tails, which extend into the cell's cytoplasm, initiate a signaling cascade thorough phosphorylation [3, 4]. The signal-

Chapter 1. Introduction

ing cascade results in a degranulation event i.e. release of histamine, serotonin, and other mediators of inflammation [4].

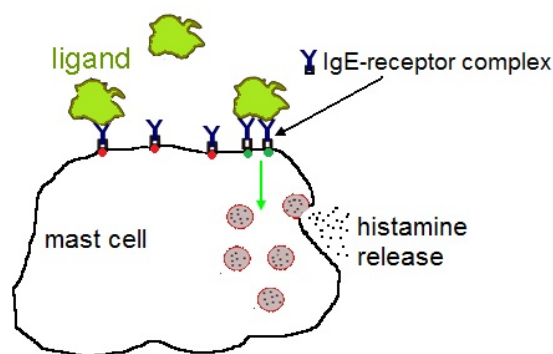


Figure 1.1: Multivalent ligand (green) crosslinks IgE-receptor complexes which initiates a downstream signaling cascade that result in degranulation, the extracellular release of the mediators.

Remarkably, not only multivalent ligand but also monovalent ligand, when incorporated into a supported fluid bilayer, can cause degranulation events. This ability of monovalent fluid membrane-bound ligands to stimulate mast cells was first recognized by Weis et al. [5]. Using a monovalent (dinitrophenyl, DNP) lipid, they showed that modest concentrations of this lipid in supported lipid monolayers led to IgE receptor aggregation in microclusters and subsequent (though weak) mast cell degranulation. Weis and collaborators suggested that laterally mobile haptens aggregated IgE receptors by trapping receptors at points of close contact between the rough cell surface and the lipid monolayer. In spite of a lack of quantitative confirmation, this hypothesis has become the accepted paradigm [3, 6, 7, 8]. Similar large-scale receptor clustering due to monovalent ligands in fluid membranes was observed a decade later in other immune cells, namely in T cells and B cells [9, 10]. In these experimental systems when liganded bilayers specific for IgE also contain adhesion molecules, a concentric pattern of clustered immunoreceptors surrounded by a ring of adhesion complexes was formed. The receptor pattern is called the immunological synapse (IS); it also forms at the interface between an ligand-presenting

Chapter 1. Introduction

(antigen-presenting) cell and a lymphocyte [11]. A ligand presenting cell is, for example, a dendritic cell or B cell, and lymphocytes are T cells, B cells, and natural killer cells [2]. This synapse is thought to play a critical role in immune cell signaling between contacting cells [12].

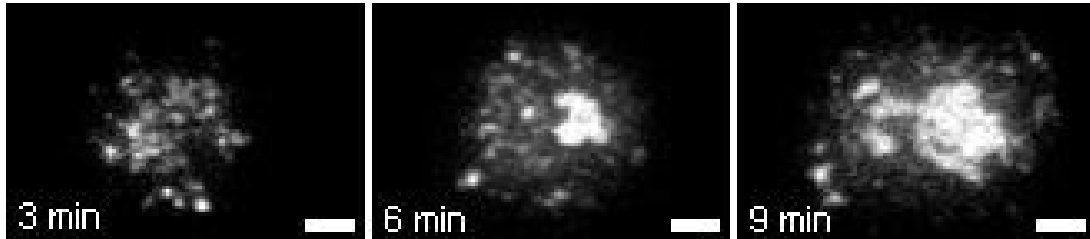


Figure 1.2: Total internal reflection fluorescence microscope image of mast cell loaded with fluorescent IgE-receptor complexes settling onto a fluid lipid POPC bilayer with 5 mol% DNP lipid under gravity. Large scale reorganization of fluorescent receptors into a synaptic like structure occurs within 6 min. Scale bar represents 5 μm .

It is interesting that a similar structure in the absence of adhesion molecules was recently observed in mast cells by us [13, 14]. Figure 1.2 depicts how a mast cell loaded with fluorescent IgE-receptor complexes settling under gravity onto a liganded fluid lipid bilayer forms a structure reminiscent of an immunological synapse, called the *mast cell synapse* [13]. The possible biological role of a mast cell synapse is as yet unclear, but the ability of the mast cell to respond to mobile, monovalent haptens may be important in interactions with parasites or with other immune cells [15]. It is noteworthy that mast cells may also act as antigen presenting cells [16] and form a classical immunological synapse with T helper cells [17].

1.3 Overview of the dissertation

The first chapter of this dissertation outlines applied experimental methods and materials. Most of the applied experimental techniques are well established in the field of experimental biophysics, such as total internal reflection fluorescence microscopy to selectively

Chapter 1. Introduction

image the cell-substrate interface [18], and single-particle tracking, which is used to obtain motion trajectories of biological molecules [19]. Besides these experimental techniques, we also implement a micropipette manipulation technique [20] to precisely control the contact of a cell with the substrate, which we believe to be a novel application. At the end of chapter 2, a thresholding algorithm is presented, which was specifically developed to determine the position and size of individual receptor clusters and patches.

In section 1.2, we mentioned that receptor clusters form on ligand presenting surfaces. A possible mechanism for the formation of receptor clusters was put forward by Weis et al. [5]. They suggested that free IgE-receptor complexes diffuse to cell-substrate contact points, where receptors eventually aggregate to form clusters. The main objective of chapter 3 is to test this hypothesis quantitatively for the first time. With our experimental tools in place and the utilization of image correlation spectroscopy [21] as well as a finite element diffusion model in MATLAB, we show that the mechanism of receptor clustering due to ligand presenting surfaces is trapping at cell protrusions. The remainder of chapter 3 analyzes the distribution and dynamics of receptor clusters, showing that at late times receptor clusters eventually coalesce to form a large central receptor patch. Understanding the underlying kinetics of this coalescence process is the main focus of our theoretical investigations.

According to previous experiments performed by our collaborators, individual receptors in the large central patch are mobile [13]. However, nothing is known about the mobility of receptors in initial receptor clusters. Therefore, the principal aim of the work presented in chapter 4 is to quantify the mobility of IgE-Fc ϵ RI within initial cell-substrate contact points (receptor clusters), and in the larger central patches, in order to address the role of IgE-Fc ϵ RI mobility in RBL cell activation and more fully characterize the diffusional behavior of this receptor. During these investigations, Monte Carlo simulations have proven to be very useful to estimate bias and statistical error in estimated diffusivities.

In chapter 5, we are interested in analyzing the formation of a receptor cluster deple-

Chapter 1. Introduction

tion zone, which appears around the large central receptor patch. A quantitative signature of this depletion zone is a dip in the rotationally averaged intensity autocorrelation function of a RBL cell TIRF image. Therefore, we developed a mathematical model for the correlation function of such images, which also shed some new light onto the exact intensity correlation function of a random distribution of large proteins labeled with a known distribution of fluorophore, which we further discussed in appendix A. It is important to note that the mathematical model presented in chapter 5 was based purely on geometric considerations. Hence, such a model only gives limited insight into the dynamics of receptor cluster coalescence. This limitation is one motivation pushing us to develop a more fundamental coalescence theory.

At this point of the thesis, we will have finished reporting our experimental investigations and make the transition to our theoretical work. This transition is bridged by chapter 6, which discusses the importance of developing a new theory of coalescence. This theory is developed in three parts and fundamentally based on the standard defect technique developed by Kenkre and collaborators [22, 23, 24, 25, 26, 27, 28, 29] for exciton transport and sensitized luminescence.

The first part is presented in chapter 7 and focuses on reaction-diffusion problems in d -dimensions; specifically, stationary trapping problems with a non-infinite *constant* capture rate. Our investigations of this subject naturally start with the formalism of the defect technique [23]. We utilize a continuous prescription of this formalism in our studies to solve many different problems, ranging from particle trapping in a harmonic potential in one-dimension to problems involving permeable, partially absorbing trapping boundaries in higher dimensions. This extensive investigation lead to a library of exact solutions; some can be found in literature, but others are completely new.

Stationary trapping problems are very useful in modeling various phenomena such as photosynthesis [30], molecular crystals [24] and other related systems [31]. However, the difficult yet important problem of moving traps or boundaries in this area remains

Chapter 1. Introduction

unsolved. We are faced with this problem in our investigations of a theory of receptor cluster coalescence in mast cells. Therefore, the second part in developing our coalescence theory is based on a validity study of an adiabatic approximation for moving boundaries with assigned time dependence. This analysis is presented in chapter 8 and consists of inserting the time dependence of the moving boundary into the static problem, which we know how to solve exactly.

In chapter 9, we present the final part of our theory of receptor cluster coalescence. This theory is based on a self-consistent approach in which the moving boundary time dependence is *not* prescribed but obtained through feedback. This problem cannot be solved exactly necessitating an approximation. After performing a detailed validity study, which includes extensive Monte Carlo simulations, of this approximation in one- and two-dimensions, we finally compared our theory to experiments. The results of this comparison to the simple form of the theory with *constant* melting probability does not explain experimentally observed cluster coalescence kinetics. At early times, the model does not describe the observed coalescence delay and at later times, it predicts slower kinetics as observed in the biological system. The former compatible problem is resolved by employing a generalization of our theory for time-dependent coalescence. The latter will be addressed in further work. Finally, to understand the underlying origin of these phenomena in more detail, future experiments are proposed, emphasizing the importance of a continued dialog between experimental and theoretical physics.

A brief conclusion of our results is given in chapter 10, which ends with a personal note of the author.

Finally, a dissertation appendix can be found in chapter 11. The first section of this appendix outlines an image correlation spectroscopy algorithm for large fluorescence proteins. In this analysis, we study excluded area effects for tightly packed particle distributions. In such distributions, the covered area fraction is high enough that particle positions cannot obey Poisson statistic. Since traditional image correlation spec-

Chapter 1. Introduction

troscopy [21], which is typically used to estimate protein densities from microscope images [32, 33, 34, 35, 36, 37] assumes underlying Poisson statistics, there is a need to compute the correct form of the intensity correlation. Even though, we chose to discuss this subject in the appendix, it is important to note that the presented contribution is an important generalization of this subject. The remaining sections of the appendix include a useful list of common Laplace transforms in reaction-diffusion systems, the Gaver-Stehfest Laplace inversion algorithm with implemented MATLAB code, the Crank-Nicolson method to numerically solve a parabolic partial differential equation, as well as a detailed calculation to validate a general prescription for the single stationary imperfect trap problem in one-dimension.

For completeness, we note that several parts of this dissertation have previously been published, as listed in table 1.1.

Chapter 1. Introduction

Chapter	Publication
Chapters 2 and 3	Amanda Carroll-Portillo, Kathrin Spendier , Janet Pfeiffer, Gary Griffiths, Haitao Li, Keith A. Lidke, Janet M. Oliver, Diane S. Lidke, James L. Thomas, Bridget S. Wilson and Jerilyn A. Timlin, <i>Formation of a Mast Cell Synapse: FcεRI membrane dynamics upon binding mobile or immobilized ligands on surfaces</i> , J. Immunol. 184 , 1328–1338 (2010) [13]
Chapters 2 and 3	Kathrin Spendier , Amanda Carroll-Portillo, Keith A. Lidke, Bridget S. Wilson, Jerilyn A. Timlin and James L. Thomas <i>Distribution and dynamics of Rat Basophilic Leukemia Immunoglobulin E receptors (FcεRI) on planar ligand-presenting surfaces</i> , Biophys. J. 99 , 388–397 (2010) [14]
Chapters 2 and 4	Kathrin Spendier , Keith A. Lidke, Diane S. Lidke and James L. Thomas, <i>Single particle tracking of immunoglobulin E receptors (FcεRI) in micron-sized clusters and receptor patches</i> , FEBS Lett. 586 , 416421 (2012) [38]
Chapter 5 and Appendix A	Kathrin Spendier and James L. Thomas, <i>Image correlation spectroscopy of randomly distributed disks</i> , J. Biol. Phys. 37 , 477–492 (2011) [39]

Table 1.1: List of publications and the corresponding parts of this dissertation.

Chapter 2

Experimental methods and materials

2.1 Introduction

This chapter outlines experimental materials and methods used in this dissertation. In section 2.2, the experimental model system of a mast cell in contact with different ligand-presenting surfaces is introduced. These surfaces presented chemically crosslinked immobile multivalent ligand (section 2.4), immobile monovalent ligand or mobile monovalent ligand in a supported lipid bilayer (see section 2.5). In order to observe the dynamics and distribution of FcεRI receptors, the cells were loaded with fluorescently-labeled IgE as outlined in section 2.3. The fluorescent marker was illuminated with laser light and its fluorescence collected with appropriate filters. Since the goal was to investigate receptor dynamics due to a ligand presenting surface, background fluorescence from regions above the cell-substrate contact zone was eliminated by using a total internal reflection microscope (TIRF), see section 2.6. In this contact zone RBL cells spread out while new receptor clusters form over time. This makes a quantitative analysis of the kinetics of receptor redistribution very complex. Therefore, to precisely define the initial contact time, a micropipette cell manipulation technique was used to bring individual cells into contact

Chapter 2. Experimental methods and materials

with substrates, see section 2.8. This technique proved to be very useful despite the low success rate due to the difficulty of manipulating single RBL cells with a micropipette. With the ability to control the contact time within 50 ms, individual receptors and receptor clusters were tracked as a function of time using a single-particle tracking (SPT) algorithm outlined in section 2.9. Due to the complexity of receptor cluster motion including cluster redistribution, and cluster-cluster melding as well as image time series of more than 200 individual images, it was useful to develop an imaging thresholding algorithm, which extracts the sizes and positions of individual receptor clusters and patches. Such a thresholding method is outlined in section 2.10. In section 2.11, we briefly outlined a RBL cell degranulation protocol to quantitatively measure mast cell activation.

Parts of this chapter have been published previously in the materials and method sections of Refs. [13, 14, 38]

2.2 Experimental model system

To investigate immune signaling by mast cells, the rat basophilic leukemia 2H3 (RBL) cell line is typically used as a model [40, 41, 42]. In the experimental model system RBL cells were primed with fluorescent anti-DNP IgE and then allowed to settle under gravity, or pipette-pressed (see section 2.8) onto different ligand-presenting and control surfaces in a TIRF microscope (see section 2.6). Figure 2.1 depicts a RBL cell pipetted-pressed onto two different ligand-containing surfaces. Immobilized multivalent ligand (DNP-BSA) was presented on a chemically crosslinked surface (Fig. 2.1A) and monovalent ligand was incorporated into a fluid (mobile ligand) or gel phase (immobile ligand) lipid bilayer (Fig. 2.1B).

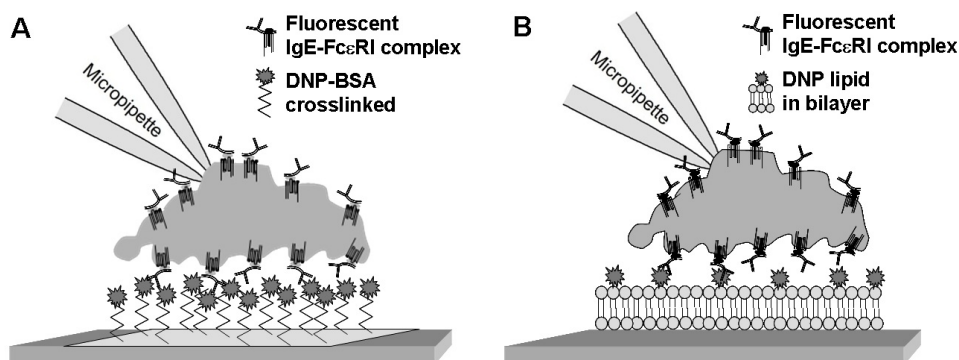


Figure 2.1: Illustration of the experimental model system in which a RBL cell primed with fluorescent anti-DNP IgE is pipette-manipulated onto different ligand-presenting surfaces. (A) Multivalent DNP-BSA chemically crosslinked to glass surface. (B) Monovalent ligand incorporated in solid or fluid supported lipid bilayer.

2.3 Cells

RBL cells were maintained in Minimal Essential Medium (MEM) (Invitrogen) with 10% Fetal Calf Serum. Anti-DNP IgE was obtained from collaborators [43] and purified as described in [44]. Fluorescent IgE conjugates were created using Alexa488 (Invitrogen), Dy-520XL (Dyomics GmbH), or Atto647 (ATTO-TEC GmbH).

For experiments presented in chapter 3, cells were IgE primed by incubation with 0.5 $\mu\text{g/mL}$ of fluorescent IgE (Alexa488 or Dy-520XL) overnight. At the day of the experiment cells were removed to suspension and the cell culture media was exchanged with MEM supplemented with 10% Fetal Bovine Serum, 1% Penicillin-Streptomycin, and 1% L-glutamine, which will be referred to as media in the remainder of this dissertation. Then 0.5 mL aliquots ($\sim 50\,000$ cells per aliquot) of primed cells were stored in 1 mL tubes at 37°C in a humidified chamber with 5% CO₂ until later use.

For experiments presented in chapter 4, cells were fluorescent IgE primed by first incubating with 35 or 50 pM Atto647-IgE anti-DNP in media for 10 min at 37°C and then washed 5 times with 2 mL media obtaining a final aliquot of 2 mL. Next 5 μL of Alexa488-

IgE anti-DNP at a concentration of 0.7 g/mL was added and incubated for 10 min at 37°C. The primed cells with both fluorescent markers were then washed 4 times with 2 mL media and divided into 0.5 mL aliquots (~50 000 cells per aliquot) stored in 1 mL tubes at 37°C in a humidified chamber with 5% CO₂ until later use.

2.4 Chemically crosslinked surface preparation

Chemically crosslinked surfaces were prepared on glass slides, which were cleaned prior to use from organic residues with a mixture of sulfuric acid and hydrogen peroxide, also known as *piranha* solution. To prepare crosslinked surfaces, Dinitrophenyl-conjugated bovine serum albumin (DNP-BSA at 1 µg/mL; Invitrogen) was crosslinked to poly-L-lysine coated coverslips with two homobifunctional crosslinkers; Ethylene glycol bis (succinimidylsuccinate) (EGS; Fisher) or glutaraldehyde (Glut; Sigma). Reactions were quenched with 100 mM glycine in phosphate buffer saline and prepared coverslips were stored in buffer until use for up to one day.

2.5 Supported lipid bilayers

Supported lipid bilayers [13] were made by spontaneous liposome fusion [45]. Lipids (Avanti) were dissolved in chloroform, dried under N₂ then placed under vacuum for 1 hr. The lipid film was then suspended in PBS + 2 mM Mg²⁺ to 1.3 mM and sonicated for 5 min using a probe sonicator. Laterally mobile bilayers were formed from 1-palmitoyl-2-oleoyl-sn-glycero-3-phosphocholine (POPC) and N-dinitrophenyl-aminocaproyl phosphatidylethanolamine (DNP-Cap PE), and immobile bilayers were formed using 1,2 - dipalmitoyl- sn-lycero-3-phosphocholine (DPPC). Bilayers were formed on piranha cleaned cover glass in 15 min on a slide warmer at 37°C (POPC) or in 8 min in an oven at 55°C (DPPC). Each bilayer coated coverslip was kept immersed during transfer to the

imaging chamber. Prior to adding cells to the bilayer, the chamber was flushed with 500 μl of media.

2.5.1 Bilayer mobility

Diffusion of lipids in the supported lipid bilayer was confirmed by SPT, see section 2.9. Trajectories over 15 s or 25 s of individual fluorescent IgE molecules bound to DNP-lipid (DNP-Cap PE) incorporated into the bilayer were analyzed in MATLAB. The calculated two-dimensional mean-squared displacement (MSD) from extracted particle positions was linear and fitted to a line to extract the diffusion coefficient (see section 2.9). The diffusion coefficient for IgE bound to DNP-Cap PE was $1.0 \pm 0.2 \mu\text{m}^2/\text{s}$ and $0.5 \pm 0.3 \mu\text{m}^2/\text{s}$ for bilayers incorporating the lipid at 5 mol% and 25 mol%, respectively. Here the error is the standard error of the mean. Figure 2.2 depicts typical fluorescent IgE trajectories for a fluid lipid bilayer with 5 mol% (Fig. 2.2A) and 25 mol% (Fig. 2.2B) DNP-Cap PE.

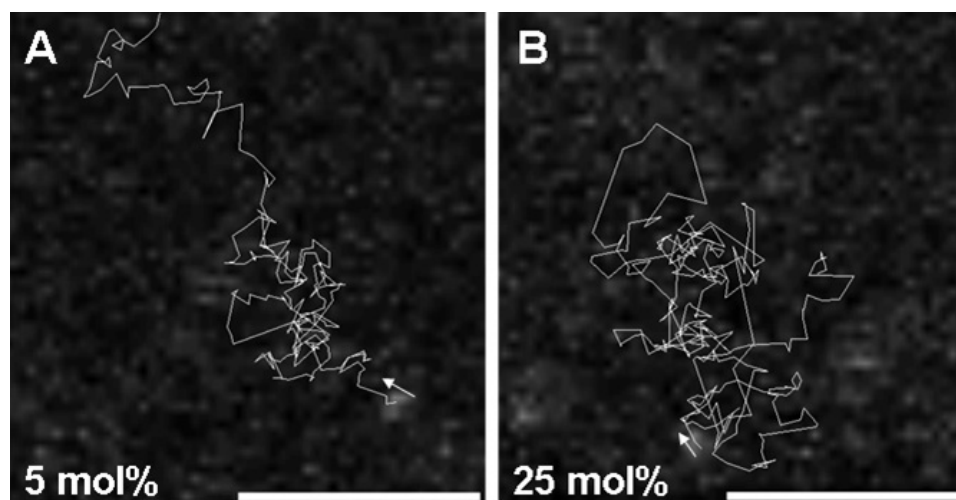


Figure 2.2: Characterization of lipid mobility in bilayer. (A) and (B) show trajectories of fluorescent IgE bound to a fluid lipid bilayer with 5 mol% and 25 mol% DNP-Cap PE, respectively. Arrows indicate starting point and initial direction of each track. Taken from Ref. [13]. Scale bar represents 5 μm .

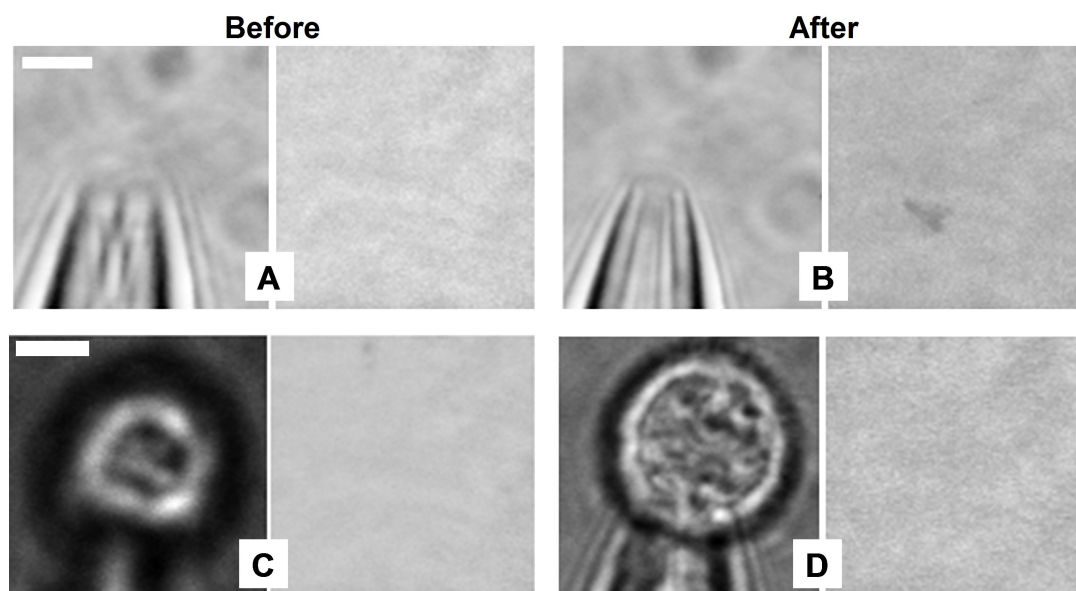


Figure 2.3: Membrane integrity before (left column) and after (right column) micromanipulation. Taken from Ref. [14]. Scale bars represents $5\ \mu\text{m}$.

2.5.2 Bilayer defects

To show that no apparent bilayer defects were caused by micro-manipulation, a fluorescent lipid N-(4,4-difluoro-5,7-dimethyl-4-bora-3a,4a-diaza-s-indacene-3-propionyl)-1, 2-dihexadecanoyl-sn-glycero-3-phospho-ethanolamine, triethylammonium salt (BODIPY - DHPE; Invitrogen, Carlsbad, CA) at 1 mol% was incorporated in addition to 25 mol% DNP-Cap PE. The bilayer integrity was observed before and after one cell was pipette-pressed onto the substrate. Figure 2.3 shows illumination profile corrected TIRF images which were focused on the substrate surface. A micrograph of an out-of-focus micropipette is depicted in the left panel of Fig. 2.3A and the corresponding TIRF image of a uniform fluorescent bilayer is shown in the right panel. There are no apparent defects in the bilayer before micromanipulation. The left panel of Fig. 2.3B shows a micrograph of an in-focus micropipette in contact with a bilayer and in the right panel the corresponding TIRF image of the fluorescent bilayer after a hole was purposely scratched into the bi-

layer to produce a bilayer defect. We note that the field of view was not changed between Fig. 2.3A and Fig. 2.3B and both TIRF images used the same brightness scaling. Figure 2.3C depicts a micrograph of an out-of-focus micropipette with anti-DNP-IgE loaded RBL cell caught out of suspension (left panel) and TIRF image of uniform fluorescent bilayer (right panel) before micromanipulation. Figure 2.3D depicts the same cell as in Fig. 2.3C pipette-pressed onto the fluorescent bilayer. We note that after initial contact with the fluorescent bilayer no apparent bilayer defects were observed (left panel). TIRF images in Fig. 2.3C and Fig. 2.3D use the same brightness scaling. The field of view was not changed between the two images. It is noteworthy that the slight overall decrease in fluorescence from Fig. 2.3C to Fig. 2.3D is due to photobleaching.

2.6 Fluorescence microscopy

To image receptor dynamics on a ligand presenting surface, the background fluorescence from fluorescent receptors away from the contact region has to be eliminated. This background fluorescence is typically eliminated by employing TIRF microscopy [18]. A crude cartoon of a TIRF microscope is shown in Fig. 2.4A. In TIRF microscopy, the excitation laser beam is totally internally reflected at the glass-water interface and only an evanescent wave traveling parallel to the interface will penetrate into the sample. The intensity of the wave, a perpendicular distance z from the interface, is given as [18, 46]

$$I(z) = I(0) \exp[-z/d], \quad (2.1)$$

where $I(0)$ is the intensity at the interface and d is the characteristic exponential penetration depth defined as

$$d = \frac{\lambda}{4\pi\sqrt{n_1^2 \sin^2(\theta) - n_2^2}}. \quad (2.2)$$

Here the penetration depth depends on the incident illumination wavelength λ , the angle of incidence θ , and the refractive indices of the media at the interface: $n_1 = 1.515$ is the

Chapter 2. Experimental methods and materials

index for glass and $n_2 = 1.333$ the index for the aqueous media solution. The penetration depth is independent of the incident light polarization direction and decreases as the reflection angle grows larger. The evanescent wave decays rapidly as shown in Fig. 2.4B and selectively excites the sample within a distance of about 200 nm from the surface. Since the mast cell is about 5 microns in radius and the lipid bilayer is tens of nanometers thick, background fluorescence can be successfully eliminated with this technique.

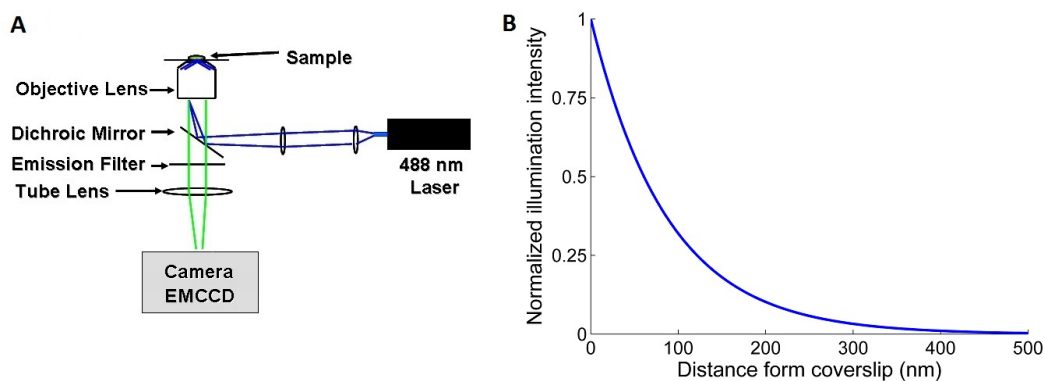


Figure 2.4: (A) Cartoon of TIRF microscope provided courtesy of Keith A. Lidke. The excitation laser beam is shown in blue and the fluorescence emission is shown in green. Dichroic mirrors and interference filters are used to separate the two wavelengths. (B) Exponential decay of a 488 nm evanescent field at a glass water interface for $\theta = 68^\circ$. The computed penetration depth from Eq.(2.2) was $d = 88$ nm

Objective-based TIRF microscopy was performed on an Olympus IX 71 (Olympus America Inc.) inverted microscope with a $60\times$ or $150\times$ 1.45 N.A. oil immersed objective using a 472 nm (CrystaLaser), 488 nm (Coherent Inc.) or 635 nm (Coherent Inc.) laser. A $1.6\times$ microscope tube lens was also used for the $60\times$ objective. Interference filters were used to block excitation. Images were collected with an EMCCD (iXon 887 or iXon + 897; Andor Technologies Inc.). The camera was cooled to -70°C (iXon + 897) or -100°C (iXon 887) and its gain was set to 100 (iXon 887) or 200 (iXon + 897). Sample temperatures were maintained at 37°C for POPC and the chemically crosslinked surface, and at 32°C for DPPC surfaces, with an objective heater. Images were collected and processed with in-house software implemented in MATLAB (The MathWorks) in conjunction with

DIPImage [47] an image processing library. In some experiments two spectrally distinguishable fluorescent dyes were used. In this case two-color TIRF images were collected on the EMCCD and spectrally separated by an image splitter.

2.7 EMCCD camera calibration

To correct the rotationally averaged correlation function (see section 3.2.1) for noise contributions, the EMCCD must be calibrated. To calculate the read noise and gain of a EMCCD camera, a image time series of at least 10 images must be made of a sample, which is constant in time but spatially varying. An appropriate calibration image, which samples all possible intensities, is obtained from out-of-focus fluorescent beads.

The signal S collected in an image pixel is given as

$$S = g I + N_{read}, \quad (2.3)$$

where g is the camera gain in analog-digital-units (ADU) per photon, I is the number of photons detected, and N_{read} is the read noise. Accordingly, the signal or noise variance in each pixel is written as

$$\delta S^2 = \langle S^2 \rangle - \langle S \rangle^2, \quad (2.4)$$

where $\langle \rangle$ represents the pixel intensity average over the collected image time series. Since the average of the read noise is zero, $\langle N_{read} \rangle = 0$, Eq.(2.4) reduces to

$$\delta S^2 = g^2 \delta I^2 + N_{read}^2. \quad (2.5)$$

Next, we make use of the fact that the detected number of photons in each pixel follows Poisson statistics, $\delta I^2 = \langle I \rangle$ and that the average signal obtained from Eq.(2.3) is

$$\langle S \rangle = g \langle I \rangle, \quad (2.6)$$

to obtain the final expression for the signal variance

$$\delta S^2 = g\langle S \rangle + N_{read}^2. \quad (2.7)$$

According to this simple expression, the functional form of pixel variance versus average pixel intensity (corrected for dark counts) is linear, where the slope represents the gain (ADU per photons) and the offset the read noise contribution (ADU^2), which is equivalent to the read noise variance.

It is worth noting that a EMCCD has other noise contributions besides read noise and Poisson noise. These noise contributions are due to the dark current and spurious noise, which are at least one order of magnitude smaller than typical read noise contributions [48]. Therefore, only Poisson and read noise contributions were accounted for in this dissertation.

2.8 Cell micromanipulation

To make quantitatively useful measurements of receptor dynamics and aggregation, the time of contact must be precisely determined. Previous observations of RBL-surface ligand interactions were done by allowing RBL cells to settle under gravity onto ligand-presenting surfaces [49, 13]. As a consequence, the contact area between the cell and the surface is gradually increasing (as the cell spreads out), while simultaneously IgE receptors are redistributing into clusters. This makes a quantitative analysis of the receptor aggregation behavior at early times exceedingly complex, as both new membrane area and new receptors are continually being added to the interface, see top row in Fig. 2.5. To precisely fix the time of first cell contact with a substrate, as shown in Fig. 2.5 (d and e), we implemented a micropipette manipulation technique. Micropipette manipulation has been extensively used to measure the physical properties of biomembranes [20, 50], and their interactions with cells [51, 52, 53]. Other techniques have been employed to control

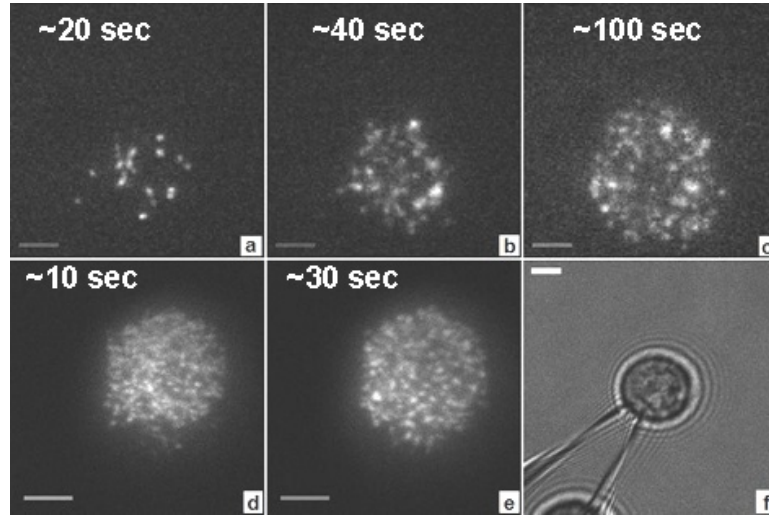


Figure 2.5: Top row: fluorescent images of under gravity settling cells onto a fluid bilayer with 25 mol% DNP-Cap PE. Bottom (d,e): fluorescent images of pipette-pressed cells onto a fluid bilayer with 25 mol% DNP-Cap PE. (f) depicts a RBL cell held with a glass pipette in suspension. Scale bar corresponds to $5\mu\text{m}$.

cell-surface contact. For example, a film-thinning technique [54] allows control of the initial contact time and area, but offers no control of the position of the cell in the field of view, which is problematic for our TIRF microscopy. Optical tweezers [55] apply small forces and thus give an uncertainty in the time at which full cell contact is achieved of ~ 2 seconds, which is 40-fold less precise than we obtain using pipette manipulation [14].

The single-cell micromanipulator used a glass micropipette. Micropipettes were pulled from soda lime glass tubes (No. 564 MicroHaematocrit-tubes, Carolina Biological Supply) on a DMZ-Universal Puller (Zeitz), using a four-step program to achieve approximately $2\mu\text{m}$ tip diameters. A pipette was then mounted onto Eppendorf's InjectMan NI2 (Eppendorf) and connected to a 30 mL plastic syringe. The micropipette was placed at the center of the camera's field of view, approximately one micron above the substrate. This position was stored in the micromanipulator. After a cell was captured in suspension, the position was recalled to automatically place the cell in contact with the substrate. EMCCD images were captured before cell contact and the final contact area was established within

50 ms, clearly defining an initial time point. In some instances, cells ruptured on contact; these were discarded.

2.9 Single-particle tracking

Single-particle tracking is a computer-enhanced video microscopy tool used to track the motion of biological molecules [19]. In SPT, the particle's trajectory is obtained from position coordinates (x, y) over a series of time steps. In this dissertation, particle trajectories of single fluorescent IgE-Fc ϵ RI receptor complexes, or an ensemble of them forming a micron-sized cluster, were obtained by using ImageJs (NIH) SpotTracker plug-in [56] (chapter 3) or a SPT algorithm implemented in MATLAB (chapter 4). The MATLAB algorithm was developed by Keith A. Lidke and collaborators and published in Ref. [57]. To identify the nature of motion of the tracked particle, the mean-squared displacement, $\langle r^2(\Delta t) \rangle$, was calculated, which is a measure of the average (denoted by brackets) distance a molecule travels and calculated for each time difference Δt in the track record. It is worth noting that the MSD is typically calculated in two different ways [58]: the average over independent overlapping segments or the average over all segments. Both ways to compute the MSD were used in this dissertation. After computing the MSD, a plot of square-displacements as a function of time has the ability to resolve different modes of particle motion [19]. The MSD signature for two-dimensional free, unconfined diffusion is linear

$$\langle r^2(\Delta t) \rangle = offset + 4D\Delta t \quad (2.8)$$

whereas for directed motion the MSD plot exhibits an upward curvature

$$\langle r^2(\Delta t) \rangle = offset + 4D\Delta t + v^2\Delta t^2, \quad (2.9)$$

where v is the drift velocity of the particle. Another two-dimensional mode of particle motion, which was observed in experiments presented in chapter 3, is confined diffusion.

In confined diffusion the MSD graph has a downward curvature and approaches a finite value, which corresponds to the square of the average size of the confinement zone, $\langle r_C^2 \rangle$

$$\langle r^2(\Delta t) \rangle = offset + \langle r_C^2 \rangle [1 - A \exp(-4BD\Delta t / \langle r_C^2 \rangle)]. \quad (2.10)$$

Here constants A and B are determined by the confinement zone geometry. In Eqs. (2.8), (2.9), and (2.10), *offset* represents the sum of the static and dynamic localization or measurement error variance [59]. Specifically, static errors arise from the uncertainty in determining the position of the particle due to experimental noise, and dynamic errors are due to particle diffusion within the integration time of each frame, leading to spot blurring.

2.10 Image thresholding

To estimate the size of receptor clusters and patches from RBL cell TIRF images, a global and adaptive thresholding methods were combined. The first method, known as Ridler and Calvard's method [60], uses a single global threshold to partition the intensity histogram into two regions. The second method, known as Niblack's algorithm [61], calculates a threshold surface by shifting a rectangular window across the image. This is a local thresholding method based on the calculation of the local mean and standard variation.

Ridler and Calvard's method defines an image intensity histogram as the sum of two distributions, namely the background $b(z)$ and foreground $f(z)$ distribution, where z is the grey value. After defining B and F as the prior probabilities for the foreground and background, respectively, where $B + F = 1$, the histogram (or more precisely the probability density function) can be modeled as a two-component distribution

$$p(z) = Ff(z) + Bb(z). \quad (2.11)$$

For this histogram, assuming that both distributions have the same variance, an optimal threshold T_{opt} that is equidistant from the average intensity of pixels below and above it is

Chapter 2. Experimental methods and materials

given by

$$Ff(z) = Bb(z) \quad (2.12)$$

at $z = T$. To compute T_{opt} , the two distributions are assumed to be Gaussian and the above expression becomes

$$\frac{F}{\sqrt{2\pi\sigma_F^2}} e^{-\frac{(T-\mu_F)^2}{2\sigma_F^2}} = \frac{B}{\sqrt{2\pi\sigma_B^2}} e^{-\frac{(T-\mu_B)^2}{2\sigma_B^2}}, \quad (2.13)$$

where μ is the mean of the distribution. After assuming that the two standard deviations are equal $\sigma_B = \sigma_F = \sigma$, the above expression can be solved for T

$$T = \frac{\mu_F + \mu_B}{2} + \frac{\sigma^2}{\mu_B - \mu_F} \ln \frac{F}{B}. \quad (2.14)$$

Finally, we assume that $B = F$, yielding to the Ridler-Calvard's expression for bimodal images

$$T = \frac{\mu_F + \mu_B}{2}, \quad (2.15)$$

where μ_F and μ_B are unknowns and must be determined by an iterative method based on an initial threshold T_{init} . To obtain the optimal threshold T_{opt} , the initial value for T_{init} is set to the mean of the image. Then, the image is segmented into two classes of pixels; one, whose grey values are smaller than T_{init} , representing the background and the other, whose grey values are larger, representing the foreground. For each of these regions average pixel intensities μ_B, μ_F are calculated and a new threshold is computed according to Eq.(2.15). This iteration is repeated until $\Delta T < 0.001$, resulting in the optimal global threshold. For typical cell images T_{opt} is reached within 10 iterations. Figure 2.6B shows a thresholded RBL cell TIRF image after applying the Ridler-Calvard's method. When the thresholded image is compared to the actual raw image depicted in Figure 2.6A, it is evident that the global thresholding method successfully separates the background fluorescent receptors. However, it fails to resolve individual receptor clusters. This result is expected, since pixel

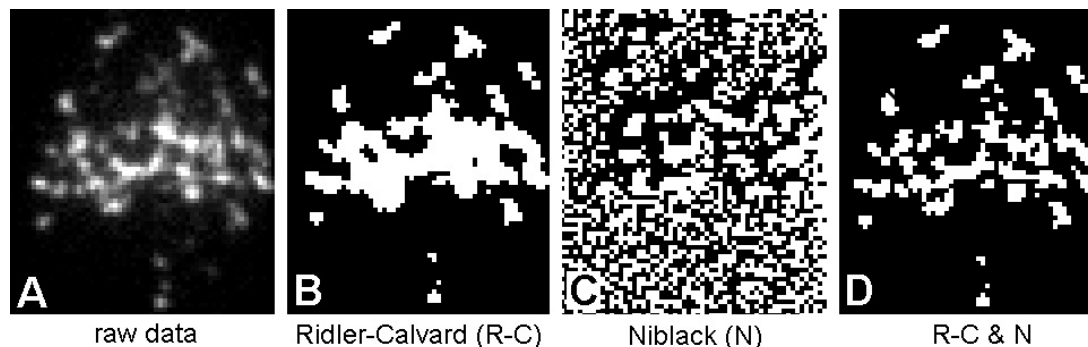


Figure 2.6: Thresholded RBL cell TIRF images obtained after applying different algorithms. (A): RBL cell TIRF image in contact for ~ 10 s with a 25 mol% fluid bilayer, (B): thresholded image (A) after applying the Ridler-Calvard's (R-C) method, (C): thresholded image (A) after applying the Niblack's (N) method, and (D): final thresholded image after combining (B) and (C) with a *logical and* command.

intensities of RBL cell TIRF images do not follow a bimodal distribution, which is an underlying assumption in the Ridler-Calvard's algorithm.

To increase the sensitivity for individual receptor clusters, it is apparent that more than a single threshold is needed. A simple adaptive thresholding method is the Niblack's algorithm, which is a local thresholding method. It calculates a threshold surface by shifting a rectangular window of n pixels in width across the image. The threshold for each window is computed by the following formula

$$T = \mu + k\sigma, \quad (2.16)$$

where k is an adjustable weight, μ is the mean and σ the variance of the pixel intensities in the window. The size n of the window should be small enough to preserve the signature of the receptor clusters, but at the same time large enough to detect larger patches and reduce noise. To select an appropriate window size, local maxima inside a mask obtained from the Ridler-Calvard's method were determined. The minimum distance between these maxima multiplied by a constant was used to estimate the window width. Figure 2.6C shows the corresponding thresholded RBL cell TIRF image in Figure 2.6A after applying the Niblack's method with a window width of $n = 4$ and weight $k = -0.05$. It is apparent

Chapter 2. Experimental methods and materials

that the implemented local thresholding algorithm introduces a noisy image especially in regions outside the contact area. The noise is due to the fact that a threshold is created in these areas. Therefore, using the Niblack's method alone to threshold receptor clusters will not be useful.

To overcome the limitations of both techniques, the two thresholded images shown in Figs. 2.6B and 2.6C are combined by a *logical and* command, resulting in Fig. 2.6D. From a direct comparison to the actual TIRF image shown in Fig. 2.6A, it is apparent that this combination of a global and adaptive thresholding method is able to resolve individual receptor clusters as well as eliminate background noise. It is important to note that the combination of these two methods works very well at early times of cell-substrate contact, when individual receptor clusters have not formed larger patches. However, at later times, when bigger receptor patches have formed and co-exist with smaller receptor patches, this method encounters its limitations. This shortcoming is based on the difference in ideal window size to resolve smaller receptor clusters and bigger patches. The window size to resolve clusters is smaller than the window size to resolve large patches. If the window size is too large, clusters which are blurred together cannot be resolved. On the other hand, if the window size is too small, bigger receptor patches might get holes or break up into smaller patches. Therefore, an intermediate window size was selected.

Finally, to estimate the size and position of receptor clusters and patches, thresholded images were analyzed with the DIPImage *measure* function [47]. Outlines of the cell-substrate contact zone to compute the cell center of mass were determined via a DIPImage thresholding function that uses Isodata algorithm [60].

2.11 Degranulation assay

Secretory response of a RBL cell in contact with a ligand-presenting surface was quantified by a degranulation assay [62]. This assay was performed on different surfaces as well as at different time points. To determine the strength of mast cell degranulation, the amount of β -hexosaminidase, a secreted mast cell enzyme was measured. In these experiments, 2×10^5 suspension cells were primed for 24 h with 1 mg/mL non-fluorescent anti-DNP IgE, then washed and resuspended in a Hank's buffer (see Ref. [63] for buffer composition). Primed cells were permitted to settle onto triplicate wells of 24-well plates pre-coated with mobile ligands, immobile ligands, or a chemically crosslinked surface and incubated for 30 min or less at 37°C for mobile bilayers as well as chemically crosslinked surfaces and at 32°C for immobile bilayers. Supernatants were then collected for degranulation assays. Degranulation data in this dissertation are presented as percent of total β -hexosaminidase content released into the medium over the incubation time period.

Chapter 3

Distribution and Dynamics of IgE Receptors on Ligand Presenting Surfaces

3.1 Introduction

In this chapter, we investigate IgE receptor dynamics and distribution after pipette-pressing mast cells on different ligand presenting surfaces. As discussed in detail in the introductory section 1.2, monovalent ligand, when incorporated into a fluid bilayer, leads to IgE-receptor aggregation in micron-sized clusters. Weis et al. [5] hypothesized that laterally mobile haptens aggregate IgE receptors by trapping receptors at points of close contact between the rough cell surface and the lipid monolayer. Although diffusion-mediated trapping is perhaps the simplest explanation of IgE receptor aggregation on fluid membranes, other hypotheses are tenable. For example, it has been proposed that some immunoreceptor signaling occurs through force transduction [64, 65]. If such signaling occurs with the IgE receptor, then aggregation could be a consequence. Given the recent interest in

Chapter 3. Distribution and Dynamics of IgE Receptors on Ligand Presenting Surfaces

such novel signaling mechanisms, it is appropriate to revisit the behavior of RBL cells on fluid membranes, with the goal of determining quantitatively whether that behavior can be explained by simple trapping, or whether the spatiotemporal dynamics of aggregate formation require as yet unidentified additional signals or processes.

Using pipette manipulation to precisely fix the time of first contact with the surface, the early time evolution of the fluorescence heterogeneities can be studied. On bare glass surfaces, the heterogeneities did not change significantly in brightness or size after initial contact for the first few seconds. On all ligand-coated surfaces, however, the heterogeneities brighten substantially in the first few seconds. In section 3.2.1, we discuss image correlation spectroscopy (ICS), which was used to measure the characteristic sizes of fluorescence heterogeneities. Since the observed heterogeneities were larger than the microscope point spread function, the rotationally averaged correlation peak was explicitly corrected for shot noise and camera read noise. It is worth noting that direct noise removal has been previously applied to *number and brightness analysis* by Gratton and collaborators [66] but not to ICS. Heterogeneities were seen on all cells, even on cells contacted with ligand-free surfaces. Moreover, the sizes of such heterogeneities were quite similar on ligand-bearing and ligand-free surfaces, suggesting the heterogeneities (initially) are simply points of close contact between the cell and the substrate, where the TIRF illumination is brightest, see section 3.2.2. In section 3.3 we show that these points of close contact are randomly distributed in the cell-substrate contact area. On ligand-bearing surfaces, the heterogeneities brighten over time, which we interpret as accumulation of receptors by binding to ligands at the points of close contact. It is worth noting that we use the term *aggregation* when the ligands are multivalent, and the more generic term *clustering* when ligands are monovalent. A finite element diffusion model outlined in section 3.2.3 fit the dynamics of cluster brightening well, and gave a diffusion coefficient consistent with reported IgE receptor mobility. These results quantitatively support a diffusion trapping model for the initial clustering of receptors. In section 3.4, we use single-particle tracking to investigate receptor cluster dynamics in detail. If the ligand is immobile, the spatial

scale and positions of the clusters do not change over time. With mobile ligands clusters do move and at longer times (~ 2 minutes) they coalesce into a large central patch reminiscent of the IS formed by T cells [11]. This large scale reorganization and localization of signaling molecules has been more fully characterized elsewhere [13]. At the end of the present chapter, section 3.5, we present degranulation data, which shows that monovalent ligands are capable of stimulating mast cell. It is worth noting that this level is significantly lower than mast cell activation due to multivalent ligand.

Parts of this chapter have been published previously in Refs. [13, 14].

3.2 Receptor trapping at cell protrusions

When RBL cells loaded with fluorescent IgE were either pipette-pressed or allowed to settle onto surfaces [13], an initial heterogeneous fluorescence distribution was always observed, even on bare glass as shown in Fig. 3.1A. The exponential decay of the evanescent field can result in heterogeneous fluorescence intensity even on membranes with uniform receptor distributions, if the membrane itself has regions that are more closely apposed to the substrate. On the length scale of optical microscopy, IgE-loaded Fc ϵ RI are uni-

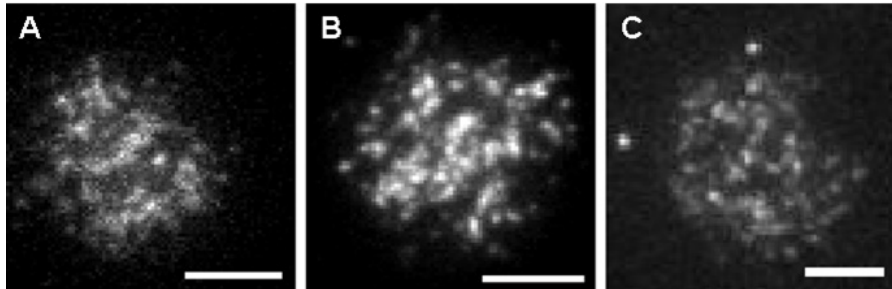


Figure 3.1: TIRF microscope images of mast cells loaded with fluorescent IgE-receptor complexes in initial contact (less than 1 min) with (A) bare glass, (B) a fluid lipid bilayer with 10 mol% DNP-Cap PE, and (C) crosslinked (EGS) DNP-BSA treated cover glass. Scale bar represents 5 μm .

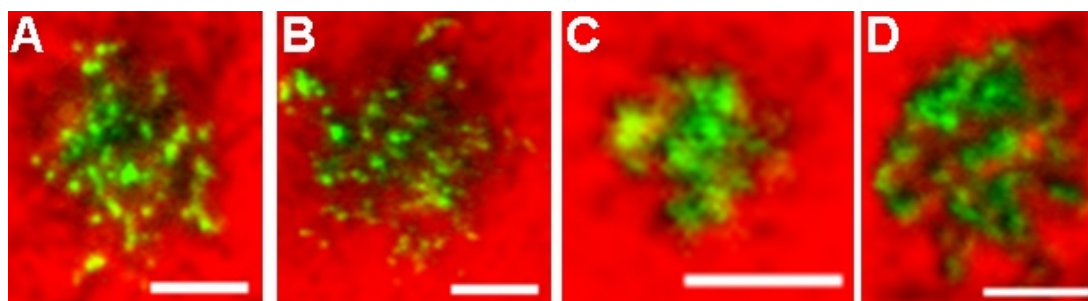


Figure 3.2: Two-color TIRF images of Fc ϵ RI receptors (green) and a soluble buffer marker (red). TIRF images were taken about 5 s after initial contact of a pipette-pressed cells with (A) crosslinked (EGS) DNP-BSA, (B) crosslinked (Glut) DNP-BSA, (C) POPC with 0 mol% DNP-Cap PE, and (D) bare glass. Taken from Ref. [14]. Scale bar represent 5 μ m.

formly distributed on the RBL surface, when not bound to antigens. Thus, we interpret the heterogeneities on bare glass surfaces as points of close contact between the cell and the surface. This interpretation is supported by previous studies using scanning electron microscopy [67] and transmission electron microscopy in cross section [68].

Additional support for the hypothesis that receptor clustering initially occurs at close contacts was obtained by adding a water soluble fluorescent dye (20 nM Alexa Fluor 647-R-phycoerythrin streptavidin, Invitrogen) to the buffer [57] resulting in a two color TIRF image. Figure 3.2 shows that at early time points, the receptor clusters (green) are found only where the soluble dye (red) is excluded. Furthermore, every contact zone (as indicated by dark regions in the red channel) contains clustered receptors. As a consequence, there are no dark regions in the composite image: all close contacts appear green, owing to the presence of fluorescent IgE. Qualitatively, there are no apparent differences in the size or distribution of the heterogeneities formed immediately after contact, regardless of the nature of the contacted surface, Fig. 3.1 and Fig. 3.2.

3.2.1 Image correlation spectroscopy with explicit noise removal

To characterize the heterogeneous distribution, the rotationally averaged image correlation function was computed; the width of this distribution is a measure of the spatial scale of heterogeneities (convolved with the point spread function of the optical system). The two dimensional spatial autocorrelation function, $g(\epsilon, \kappa)$ of an image $i(x, y)$ is:

$$g(\epsilon, \kappa) = \frac{\langle i(x, y) i(x + \epsilon, y + \kappa) \rangle}{\langle i(x, y) \rangle^2} - 1, \quad (3.1)$$

where the angular brackets denote spatial averaging over the image, and ϵ and κ are spatial lag variables [21, 32, 69]. In systems without orientational order, all the information in the correlation function is contained in its rotational average, $g(r)$ with $r = \sqrt{\epsilon^2 + \kappa^2}$, which we employ here. The peak of the autocorrelation at $g(0)$ (the intensity variance) includes a significant contribution from spatially uncorrelated camera read noise and shot noise; the contribution from these noise sources can be directly measured and then subtracted from the autocorrelation [70, 66]. Since signal i_s and noise i_n are uncorrelated [69],

$$\langle \delta i^2 \rangle = \langle \delta i_s^2 \rangle + \langle \delta i_n^2 \rangle \quad (3.2)$$

where $\delta i = i - \langle i \rangle$. Then

$$g(0) = \frac{\langle \delta i^2 \rangle}{\langle i \rangle^2} \quad (3.3)$$

and

$$g_s(0) = \frac{\langle \delta i_s^2 \rangle}{\langle i_s \rangle^2} = \frac{\langle \delta i^2 \rangle}{\langle i \rangle^2} - \frac{\langle \delta i_n^2 \rangle}{\langle i \rangle^2} \quad (3.4)$$

using the fact that mean of the noise is zero so that $\langle i \rangle = \langle i_s \rangle + \langle i_n \rangle = \langle i_s \rangle$. This also leads immediately to

$$\delta i_n^2 = (i_n - \langle i_n \rangle)^2 = i_n^2 \quad (3.5)$$

so that

$$g_s(0) = g(0) - \frac{\langle i_n^2 \rangle}{\langle i \rangle^2}. \quad (3.6)$$

Noise variance for the EMCCD camera was measured by repeated imaging of a stationary test sample containing the full range of intensities. The single-pixel noise variance was then computed over the time series of images and plotted as a function of single-pixel mean intensity. This calibration line was then used to estimate i_n^2 for each pixel in the cell images; pixel averaging gave $\langle i_n^2 \rangle$. Further information on camera noise calibration can be found in section 2.7 and in Ref. [71].

ICS was performed to determine the sizes of fluorescence heterogeneities on single cells pipette-pressed against ligand-bearing or ligand-free surfaces. The rotationally averaged correlation function depicted in Fig. 3.3 shows explicit noise removal from the variance $g(0)$ and the resultant halfwidth at half-maximum. Inset Fig. 3.3A is a TIRF image of a pipette-pressed RBL cell on a mobile bilayer with 1 mol% DNP-Cap PE and Fig. 3.3B depicts the same image masked with mean of cell interior, as was done in the analyses to eliminate the cell-size artifact from the autocorrelation.

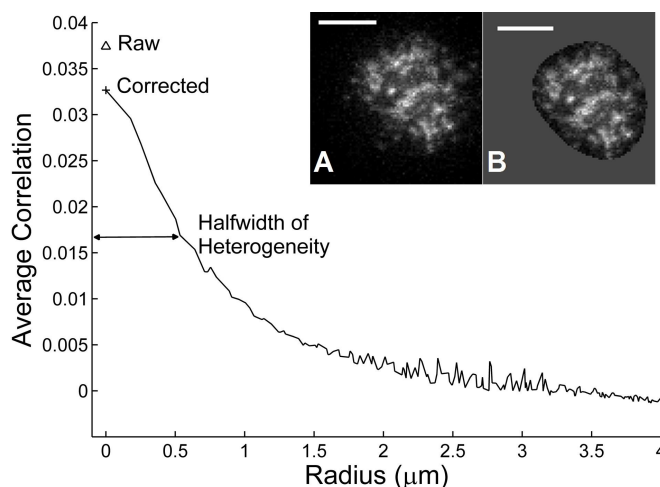


Figure 3.3: Rotationally averaged correlation function of a typical RBL cell (shown in A) loaded with fluorescent IgE pipette-pressed on a mobile bilayer with 1 mol% DNP-Cap PE. The correlation function shows explicit noise removal from the variance $g(0)$ and the resultant halfwidth at half-maximum. Taken from Ref. [14]. Scale bar represent $5 \mu\text{m}$.

3.2.2 Spatial scale of initial heterogeneities

Qualitatively, there are no apparent differences in the size or distribution of the heterogeneities formed immediately after contact, regardless of the nature of the contacted surface, Fig. 3.1 and Fig. 3.2. Quantitatively, the spatial scale of the heterogeneities, as assessed by the fullwidth at half-maximum (FWHM) of the correlation function, showed no statistically significant differences between surfaces, Fig. 3.4. The average size of heterogeneities on all surfaces (30 cells, 3 on each surface) is 1.2 ± 0.2 (SD) μm . Measured fluorescent heterogeneities are significantly larger than the FWHM of $0.34 \mu\text{m}$ computed for the theoretical microscope point spread function (Fig. 3.4, vertical black line) and $0.63 \mu\text{m}$ for measured 100 nm fluorescent beads (Fig. 3.4, vertical grey line). All analyzed data was obtained within 5 s of initial contact, during which time no coalescence of clusters was observed. The qualitative and quantitative similarities between hetero-

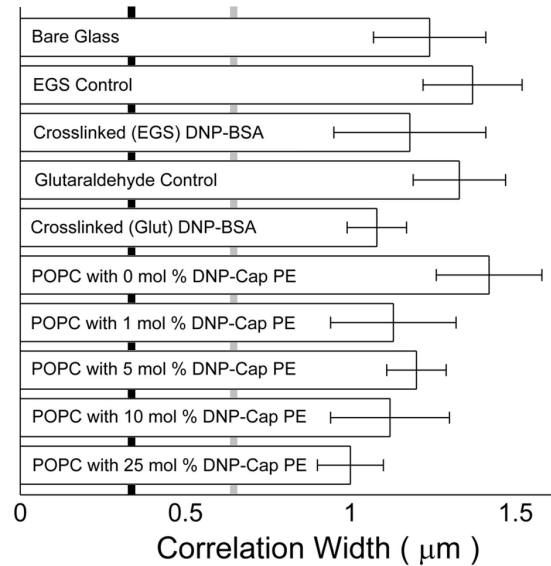


Figure 3.4: Average size of FcεRI receptor fluorescence heterogeneities on different surfaces, measured by the fullwidth at half-maximum (FWHM) of the rotationally averaged intensity autocorrelation. The vertical solid grey line shows the measured size of 100 nm fluorescent beads and the vertical black line is the size of the theoretical point spread function with effective NA = 1.33 and a wavelength of 550 nm. Taken from Ref. [14].

geneities observed on different surfaces, including surfaces that display no ligands for IgE, strongly support the contention that clusters of IgE receptors observed on contacting ligand-presenting surfaces are formed by diffusion-mediated trapping at points of close contact between the cell and the surface.

3.2.3 Finite-element diffusion model

On bare glass surfaces, the heterogeneities did not change significantly in brightness or size after initial contact for the first few seconds (data not shown). On all ligand-coated surfaces, however, the heterogeneities brightened substantially in the first few seconds. Hence, to further test the hypothesis that receptor clustering occurs at cell protrusions, we fit the rapidly increasing fluorescence in clusters to a simple finite-element diffusion model in MATLAB. The initial, brighter heterogeneities were treated as diffusion traps. The initial receptor distribution was taken to be uniform at $t=0$, then evolved in time via diffusion, with receptors in traps removed from the diffusing pool at each time step. Traps were taken as the actual cluster locations, determined by low-pass spatial filtering of cell images (removing the 10 lowest frequency components) and thresholding at 5% of the maximum intensity. As receptor clusters are dim at the very earliest time points, the trap mask generated at 0.5 s was used for earlier times as well. This method produced stationary receptor cluster traps for immobile bilayers and slowly moving cluster traps on mobile bilayers. In modeling diffusional trapping, periodic boundary conditions were used on a square lattice with an area equal to the total cell surface area. For the times modeled (0-3 s), the boundary conditions are irrelevant, as the total pool of receptors is not significantly depleted. Accumulation in the traps was then fit to the measured fluorescence increase with two adjustable parameters: the diffusion coefficient and the total fluorescence (Fig. 3.5). Insets in Fig. 3.5 depict analyzed cell on DPPC bilayer (Fig. 3.5A) and evolved free receptor concentration after 0.16 s (Fig. 3.5B) and 1 s (Fig. 3.5C). Only data from the first three seconds of accumulation (brightening) was analyzed, since photobleaching

causes significant dimming at long times. Very good fits were found for both immobile and mobile ligands. From measurements on three cells, the mean receptor diffusion coefficient was 0.30 ± 0.08 (SD) $\mu\text{m}^2/\text{s}$ (immobile ligands) and 0.24 ± 0.07 (SD) $\mu\text{m}^2/\text{s}$ (mobile ligands), consistent with reported IgE receptor diffusivity [72, 73]. To test the sensitivity of the fit diffusion coefficient to the trap sizes, the intensity threshold was increased from 5 % to 10 % and the data was re-fit; this gave the same diffusion coefficients, within experimental uncertainty.

3.3 Receptor cluster distribution

In the previous section of this chapter, we have shown that clusters form due to IgE-receptor trapping at cell protrusions. On mobile bilayers these clusters will eventually

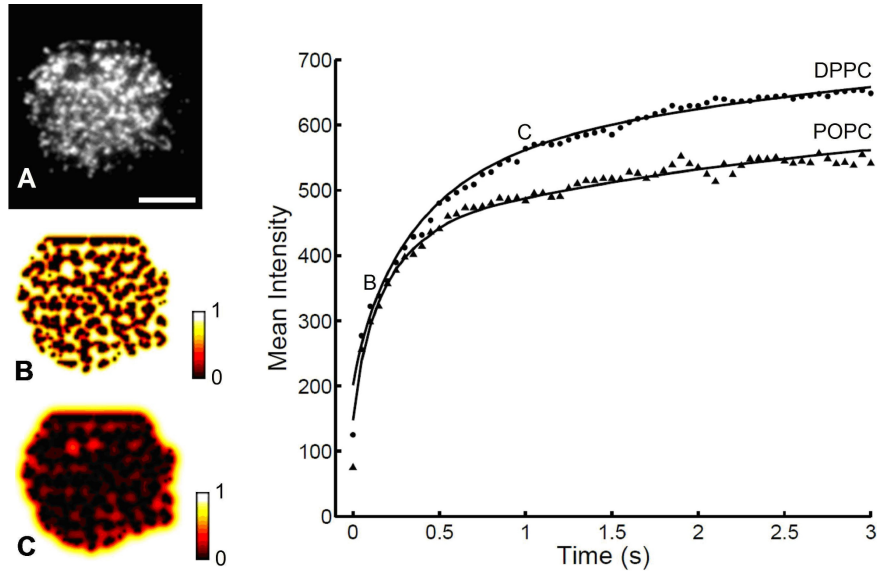


Figure 3.5: Mean receptor cluster intensity is used as a measure of number of receptors trapped in cell protrusions by immobile (DPPC) or mobile (POPC) ligands. The data (points and triangles) was fit to a numerical two-dimensional diffusion trapping model (solid line). (A) analyzed cell on DPPC bilayer and evolved free receptor concentration after (B) 0.16 s and (C) 1 s. Taken from Ref. [14]. Scale bar represents 5 μm .

move to form a large central receptor patch [13]. Before we analyze cluster motion, cluster distribution was studied in this section. At early times, the distribution of heterogeneities (clusters) on immobile substrates appeared random. To quantify this observation, two tests were performed. First, the radial distribution of clusters was examined and second, nearest-neighbor distance distributions for receptor clusters were measured.

3.3.1 Radial distribution

The radial distribution of clusters was examined by histogram analysis of cluster distances from the center of the contact area (Fig. 3.6). The number of clusters at a radial distance (r) was proportional to r , as expected for a uniform density of randomly positioned clusters. This radially uniform distribution was found on all immobile two-dimensional substrates, and on mobile substrates at early time points after cell contact. Thus, at early times, clusters are no more likely to be found in the center of the contact zone than in the periphery. Therefore, it is likely that points of close contact are formed by cell protrusions (such

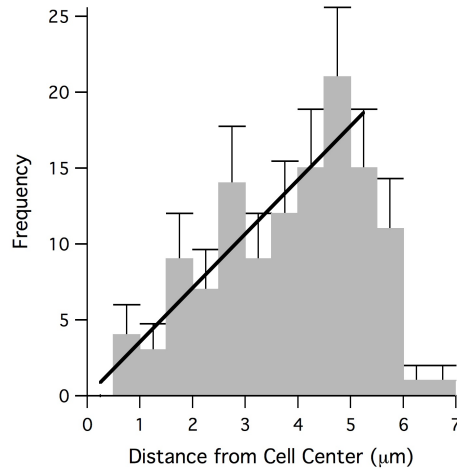


Figure 3.6: The number of clusters at a radial distance r is proportional to the distance from the center of a cell as expected for a uniform density of randomly positioned clusters. Taken from Ref. [14].

as microvilli) that are randomly distributed on the cell surface before the cell is brought into contact with the planar substrate. Similar, apparently random distributions of receptor clusters have been observed in RBL cells [13] and in T cells [7] that are allowed to settle by gravity onto ligand-bearing membrane substrates.

3.3.2 Receptor cluster nearest-neighbor distribution

A further test of cluster randomness was performed by studying the nearest-neighbor distances of receptor clusters. For randomly placed disks of diameter h , the nearest-neighbor distance distribution is given by Torquato et al. [74]:

$$P(r) = 2\pi r \rho e^{-\pi \rho r^2}, r > h, \quad (3.7)$$

where $P(r)$ is the probability of a disk having a nearest neighbor at a distance between r and $r + dr$, and ρ is the number density of disks. As not all clusters had the same diameter, Eq. 3.7 was weighted by the fraction of disks with each diameter h :

$$P(r) = \int P'(h) 2\pi r \rho e^{-\pi \rho (r^2 - h^2)} H(r - h) dh, \quad (3.8)$$

where H is the Heaviside step function. Hence, identical randomly positioned disks give a Gaussian distribution (Eq.(3.7)), but with a sharp cutoff for distances less than the disk diameter. The width of the Gaussian is determined solely by the density of clusters, ρ . As the actual clusters have a range of sizes, we plotted the random disk model, weighted with the measured distribution of cluster diameters $P'(h)$ given in Eq.(3.8)). Using the measured cluster density ρ and the total number of receptor clusters, the theoretical nearest-neighbor distribution (solid lines in Fig. 3.7) then has zero *free* parameters. As depicted in Fig. 3.7A, this theoretical distribution fits the measured distribution on immobile bilayers extremely well, supporting the contention that clusters are randomly distributed. On mobile bilayers (Fig. 3.7B), clusters are slightly closer together than predicted for a perfect random distribution at the measured density. This result may indicate that, even at early times, there is

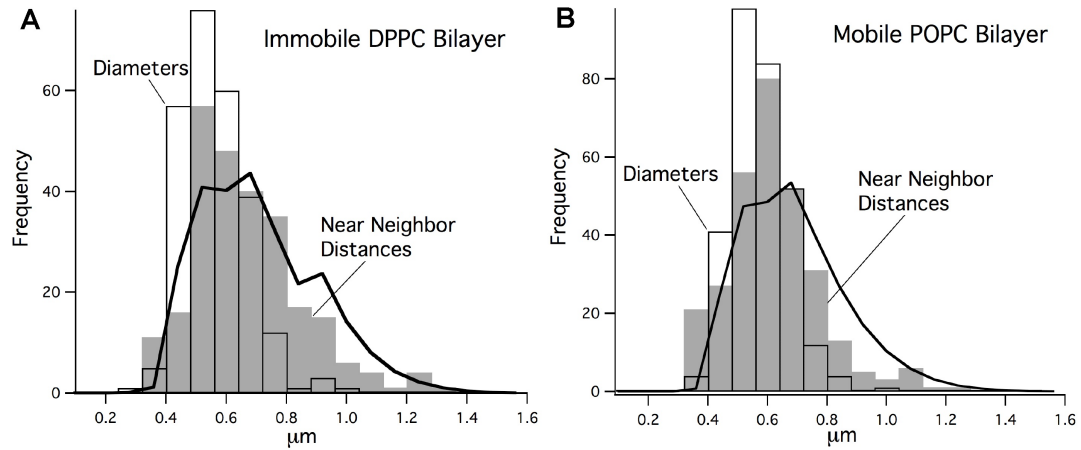


Figure 3.7: Distributions of cluster diameters and nearest-neighbor distances on immobile (A) and mobile (B) ligand substrates. The area of each bar is the fraction of clusters with nearest-neighbor distances (grey bars) or diameters (white bars) in the x -range of the bar. The solid lines are the nearest-neighbor distances expected from a random spot model. Taken from Ref. [14].

some change in the cluster distribution on mobile ligands that may be a precursor to later coalescence. In Fig. 3.7 cluster density $\rho = 1.139$ clusters per square micron on DPPC (255 clusters on 3 cells), and $\rho = 1.145$ clusters per square micron on POPC (296 clusters on 3 cells).

3.4 Receptor cluster dynamics

As mentioned previously, receptor dynamics differed depending on the mobility of the ligand. On immobile ligand substrates, the clusters brightened but did not move appreciably over the observation time of > 1 min. On mobile ligand substrates, clusters of receptors on pipette-pressed cells (and on gravity-settled cells) moved and coalesced to form a large central patch of receptors within two minutes, while small isolated clusters remained at the periphery of the contact zone. Similar receptor patching has been observed in T cells and has been termed a *synapse*. The similarity in receptor organization has led to the des-

ignation of this large patch as a mast cell synapse [13]. In the current section, we studied this receptor cluster motion in more detail.

3.4.1 Receptor cluster transport

Prior to the onset of big patch formation approximately 2 minutes after contact, the receptor clusters do not grow measurably in size, nor do they coalesce. Thus, individual receptor clusters may be tracked to phenomenologically characterize their motion, in order to compare the dynamics with other immunoreceptor clusters. MSD plots for 20 individual clusters were obtained from extracted coordinates. All plots had upward curvature; such MSD curves can be best fit with a combination of diffusion and drift velocity. A typical MSD plot is shown in Fig. 3.8B. The TIRF image in Fig. 3.8A shows the root mean-squared diffusional spread (parabolas) and drift velocity (arrows) of six receptor trajectories dur-

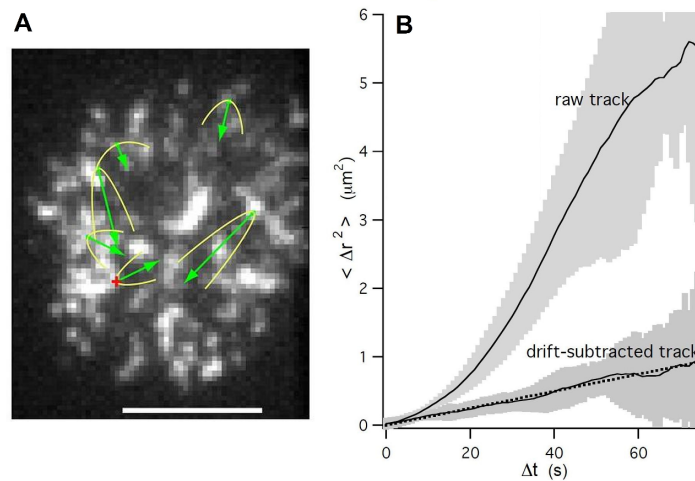


Figure 3.8: (B) Raw and drift-subtracted mean-squared displacement for cluster track indicated with + in (A). Shaded area represents the standard error of the mean from multiple measurements. (A) Tracked receptor clusters after ~ 55 s of initial contact of POPC bilayer with 25 mol% DNP-Cap PE lipid. Parabolas (yellow) show the root mean-squared diffusional spread of the cluster. Arrows (green) are proportional to the drift velocity and show how far each cluster would drift in 66 s. Scale bar represents $5 \mu\text{m}$. Taken from Ref. [14].

ing 55 s of initial contact. The cluster drift velocity was 37 ± 5 (mean \pm SE.) nm/s. In contrast, TCR clusters have slightly slower velocities when initially formed, but faster velocities during synapse formation [75]. We also investigated whether IgE-Fc ϵ RI receptor clusters undergo centripetal motion. A histogram of receptor cluster hop directions over a 10 s interval, relative to the direction of the geometric cell center, is shown in Fig. 3.9 in a polar plot. The same number of correlated (251) and anticorrelated (248) hops was observed, within statistical variation. Thus, there was no statistical significant centripetal motion of the clusters. In contrast, TCR clusters have strong centripetal velocities during synapse formation [75]. The computed mean diffusion coefficient of clusters was $5.1 \pm 0.7 \times 10^{-3}$ (mean \pm SE.) $\mu\text{m}^2/\text{s}$, which is comparable to that of TCR clusters when their centripetal motion is inhibited by pharmacological or physical mechanisms [7]. In our previous studies [13], we observed that at late times of cell-substrate contact the actin cytoskeleton depolymerizes (decomposes into smaller compounds) at the central region

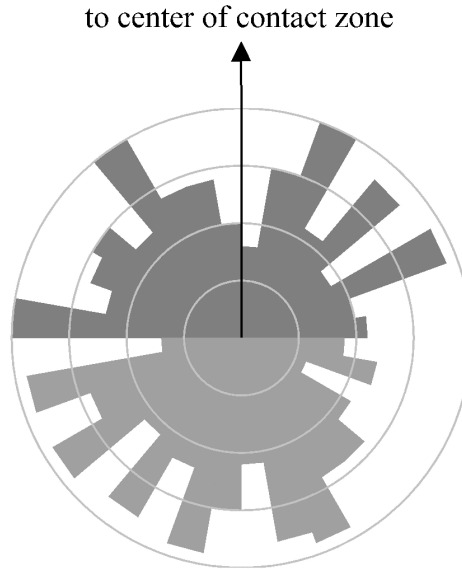


Figure 3.9: Histogram in polar coordinates of IgE-Fc ϵ RI receptor cluster hop direction over a 10 s interval, relative to the direction of the geometric cell center, which is represented by the arrow. The data suggests that there are the same number of correlated (251) and anticorrelated (248) hops, within statistical variation.

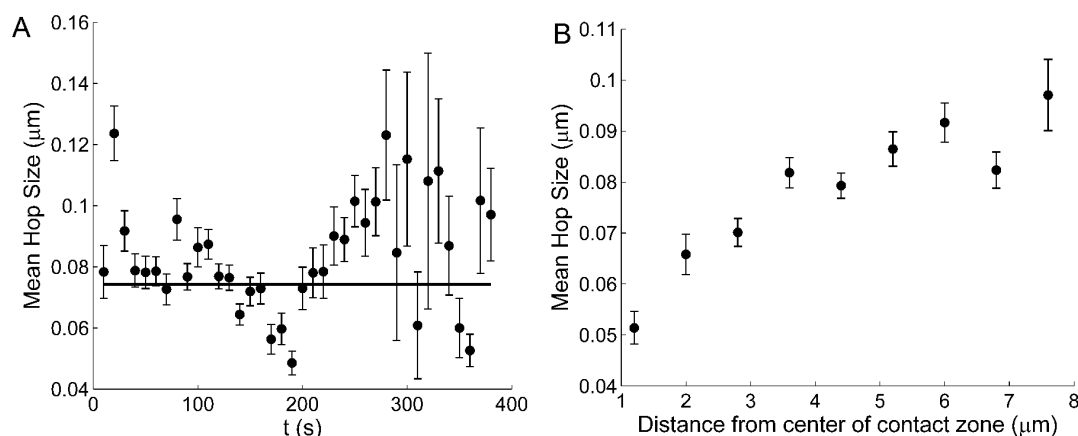


Figure 3.10: Mean cluster hop for one second time intervals as a function of (A) time and (B) distance from the center of the cell-substrate contact area. Line in (A) represents the best fit to a constant. Error bars represent standard error of the mean.

of the contact area. This change in the actin cytoskeleton might affect the motion of the receptor clusters. Therefore, we investigated whether cluster motion depends on time of contact or the radial distance from the center of the cell-substrate contact zone. For this investigation, the mean cluster hop size over a 1 s interval was analyzed for more than 60 individual trajectories obtained from 3 RBL cells in contact with a POPC bilayer with 25 mol% DNP-lipid. Figure 3.10A depicts the functional form of the mean cluster hop size over time. The data suggests that cluster motion does not vary over time. The mean cluster hop length obtained from a best fit to a constant was approximately 74 nm. However, the data showed a correlation between hop size and distance from the cell center. Figure 3.10B suggests that, on average, clusters that are farther from the center move more rapidly. It is worth noting that a similar trend has been observed previously in T cells [75].

Lastly, we investigated the size dependence of cluster motion. According to the Saffman-Delbrück formula [76] the diffusion constant decreases with increasing radius of the diffusing entity. Figure 3.11 compares the mean cluster hop length of 136 individual trajectories to cluster size (open circles). Here, cluster size was determined as follows. For each trajectory, a cluster image of $\sim 9 \times 9 \text{ pixel}^2$ was obtained. Pixel values were

summed along the x and y coordinate and fit to a one-dimensional Gaussian in each direction. The cluster diameter σ was obtained from the square root of the sum of the squares of σ_x and σ_y , where σ_x and σ_y represent the Gaussian variance times $\sqrt{2}$ obtained from the fit. From Fig 3.11 it is apparent that there is no significant dependence of hop length on cluster size (open circles). To compare this finding to theoretical predictions, we used the following equation given by Petrov and Schwille [77] to estimate the diffusion coefficient for a cylindrical object of radius similar to our experimentally determined cluster size

$$D(\xi) = \frac{k_B T}{4\pi\eta} \times \left[\ln(1/\xi) - \gamma + 4\xi/\pi - (\xi^2/2)\ln(2/\xi) \right] \times \left[1 - (\xi^3/\pi)\ln(2/\xi) + c_1\xi^{b_1}/(1 + c_2\xi^{b_2}) \right]. \quad (3.9)$$

In Eq.(3.9), the reduced radius is $\xi = \frac{\sigma(\mu_1 + \mu_2)}{2\eta}$, where $\eta = 7 \times 10^{-5}$ Pa s m is the effective membrane surface viscosity, $\mu_1 = \mu_2 = 2 \times 10^{-3}$ Pa s are viscosities of the media surrounding the membrane, $\gamma = 0.577215$ is the Euler constant, $k_B = 1.3806504 \times 10^{-23}$ Pa m³ is the Boltzmann constant, and $T = 310$ K. c_1 , b_1 , c_2 , and b_2 are constants given as 0.73761,

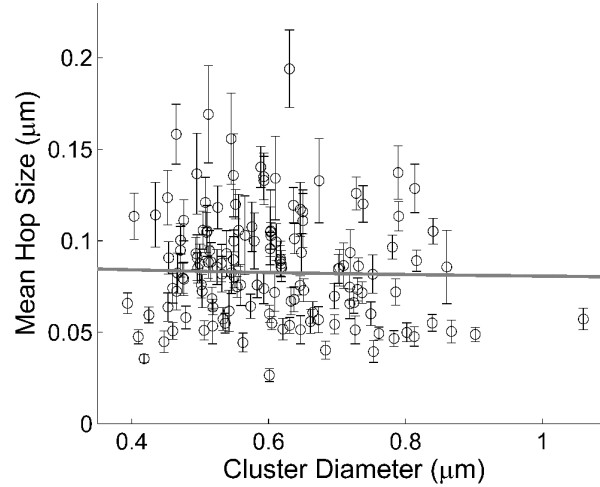


Figure 3.11: Experimental mean cluster hop size as a function of cluster diameter (open circles) compared to a theoretical hop size predicted from Eq.(3.10) (grey line). The cluster diameter was obtained from a Gaussian fit in the x and y coordinate of individual cluster image. Error bars represent standard error of them mean.

2.74819, 0.52119, and 0.61465, respectively. After computing the theoretical predicted hop size from

$$\Delta r = \sqrt{4D(\xi)\Delta t}, \quad (3.10)$$

where $\Delta t = 1$ s, the functional form of Eq.(3.10) (grey line) was compared to our experimental data (open circles) in Fig 3.11. We see that the theoretical predicted decrease in hop length due to increasing cluster size is very small. Therefore, experimental data as well as theoretical predictions, suggest that the hop length does not significantly depend on cluster size for our experimental parameters. It is worth noting that the effective surface viscosity in Eq.(3.9) was two orders of magnitude larger than the surface viscosity measured in red blood cells [78]. However, the chosen smaller value of η produces a line with a comparable slope as expected from a surface viscosity appropriate for red blood cells.

3.4.2 Temporal Image Correlation Spectroscopy

Receptor clusters on ligand-bearing membranes undergo active (directed) transport. Interestingly, cells on ligand-free surfaces also exhibit fluorescence fluctuations in TIRF imaging. These fluctuations are much too large in intensity and in spatial extent to be caused by stochastic receptor density fluctuations. They most likely reflect fluctuations in the proximity of various regions of the cell surface to the substrate. To further explore the possible relationship between cell fluctuations on unliganded surfaces and cluster motion on ligand-containing membranes, the temporal autocorrelation was computed. Temporal image correlation spectroscopy (TICS) was adapted from Kolin et al. [36] to extract IgE receptor cluster dynamics. The normalized intensity fluctuation temporal autocorrelation function of an image series as a function of time lag τ is:

$$g'(\tau) = \frac{\langle i(x,y,t)i(x,y,t+\tau) \rangle}{\langle i \rangle^2} - 1, \quad (3.11)$$

where the angular brackets denote spatial and temporal averaging. To characterize the mode of transport of IgE receptors, the normalized temporal correlation function was fit to

a flow + diffusion model for a single population of particles [36] (fit parameters in bold):

$$g'(\tau) = \frac{\tau_d}{\tau_d + \tau} e^{-(\tau/\tau_f)^2} + \text{offset}. \quad (3.12)$$

The fit diffusion time τ_d was used to compute the diffusion constant $D = h^2/4\tau_d$ and the flow time τ_f was used to calculate the flow speed $v = h/\tau_f$ [36] where h is the typical cluster diameter (measured from the spatial correlation function). The decay of the temporal autocorrelation function depends on the persistence of the intensity variations between images in a time-series [36]. Figure 3.12 depicts the temporal autocorrelation of fluorescence images from six different cells (three on 0 mol% DNP-Cap PE and three on 25 mol% DNP-Cap PE bilayer). For intervals of a few seconds or less, the kinetics of both cluster motion and cell membrane fluctuations are similar (although one cell on ligand-free membranes was somewhat slower, as shown). For longer time intervals, the autocorrelation on ligand-free membranes showed greater persistence; this may be caused by the fact that bright patches on cells on ligand-free membranes are somewhat larger than receptor clusters, and they grow in time as the cells spread. (Fig. 3.12, images). The similarities in the kinetics of cell membrane fluctuations and cluster motions suggest that similar biological mechanisms may be responsible for both. It is possible that as the clusters initially formed at contact zones move, the contact zones themselves move, via (for example) cytoskeletal dynamics. In this context, it is interesting that motion of microvilli over the cell surface has been reported in A6 toad kidney epithelium cells, using scanning ion conductance microscopy [79].

The temporal autocorrelation on ligand-bearing membranes was also checked for consistency with the results from individually tracked clusters. A diffusion + flow model was fit to the autocorrelation, Eq.(3.12). A very good fit was obtained (Fig. 3.12, solid lines) and the extracted mean diffusion coefficient and flow speed were $7.4 \pm 1.2 \cdot 10^{-3}$ (SD) $\mu\text{m}^2/\text{s}$ and 30 ± 7 (SD) nm/s respectively, consistent with numbers obtained from IgE receptor tracks in section 3.4.1.

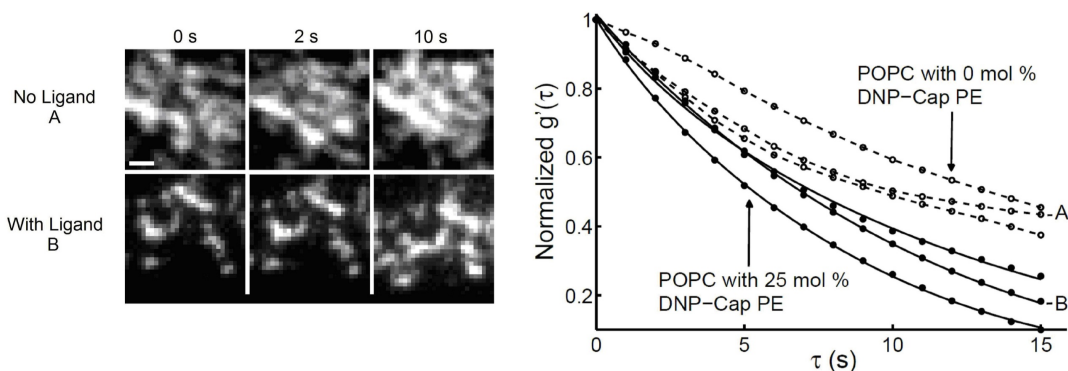


Figure 3.12: Temporal autocorrelation functions of three cell images on mobile bilayers with 25 mol% DNP-Cap PE (filled circles, cell in Fig. 3.8) and 0 mol% DNP-Cap PE (open circles). Data obtained from 25 mol% bilayers was fit to the flow + diffusion model (solid lines), Eq.(3.12). Images depict cell regions analyzed here for POPC bilayer with 0 mol% DNP-Cap PE (top row, A in plot) and with 25 mol% DNP-Cap PE (bottom row, B in plot) at 0 s, 2 s, and 10 s. Taken from Ref. [14]. Scale bar represents 1 μm .

3.5 Mast cell signaling

As previously mentioned in section 1.2, Weis et al. [5] showed three decades ago that monovalent ligand in fluid membranes can cause weak mast cell degranulation. In this section, we study the mast cell secretory response due to mobile monovalent ligand, immobile monovalent as well as immobile multivalent ligand in more detail.

3.5.1 Mast cell signaling due to different ligand-presenting surfaces

In the first experiment, degranulation assays (see section 2.11) were performed to characterize β -hexosaminidase release from cells engaged for 30 min at 37°C by mobile monovalent and immobilized multivalent ligand. Results depicted in table 3.1 are expressed as a percent of total β -hexosaminidase content in mast cell granules. Interaction of IgE-receptor complex with immobile multivalent ligand (DNP-BSA) resulted in degranulation levels equivalent to that attained by stimulating cells in solution with DNP-BSA [13].

Chapter 3. Distribution and Dynamics of IgE Receptors on Ligand Presenting Surfaces

Degranulation was also significant after settling of IgE primed mast cells onto mobile monovalent 5, 10, or 25 mol% DNP-lipid bilayers. This result confirmed, as previously observed by Weis et al. [5], that the mobile monovalent ligand, which is not capable of receptor crosslinking, leads to mast cell activation. To confirm that observed IgE receptor clustering on immobile liganded bilayers with 25 mol% DNP-Cap PE can cause also signaling, a similar degranulation assay was conducted. To ensure immobility of the bilayer, the assay was conducted at 32°C. Consistent with results presented in table 3.1 for mobile bilayers with 25 mol% DNP-lipid, the mean percentage of β -hexosaminidase release from two independent experiments with immobile bilayers was 7.3 ± 2.5 (SD) %; small but still significantly higher than the spontaneous release of 0.5 ± 0.4 (SD) %. This result suggests that most of the signaling occurs in the small receptor clusters.

Surface	% Release
Bare Glass	1.5 ± 0.5
0 mol% mobile DNP bilayer	1.4 ± 0.2
1 mol% mobile DNP bilayer	2.2 ± 0.4
5 mol% mobile DNP bilayer	$2.8 \pm 0.3^*$
10 mol% mobile DNP bilayer	$6.4 \pm 0.4^*$
25 mol% mobile DNP bilayer	$10 \pm 1^*$
Glutaraldehyde treated glass	0.4 ± 1.5
Glutaraldehyde + DNP-BSA	30 ± 1
EGS treated glass	1.4 ± 2.2
EGS + DNP-BSA	38 ± 8

Table 3.1: Percent β -hexosaminidase release from cells settled onto glass, mobile ligand, or immobile chemically crosslinked ligand. Asterisks indicate results that are significantly higher than spontaneous release (bare glass). Errors represent standard deviation from multiple measurements.

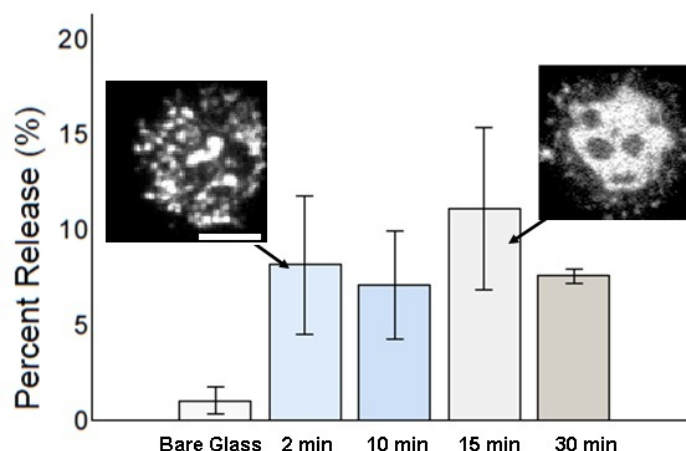


Figure 3.13: Time-dependent measurement of percent β -hexosaminidase released from gravity settling RBL cells on mobile bilayers with 25 mol% DNP-Cap PE. Insets depict TIRF images of typical gravity settling cells after ~ 2 min and ~ 15 min of initial contact. Error bars depict the standard deviation from multiple measurements.

3.5.2 Time-dependent mast cell signaling due to ligand-bearing fluid bilayer

At the beginning of this chapter we have shown that receptors aggregate through diffusion-limited trapping at cellular protrusions. On mobile bilayers these aggregates, called clusters, move to form a big central patch. An interesting question which remains to be answered, is when mast cell signaling occurs. Does signaling occur in the initially formed clusters or later in the large patch? To answer this question, we measured dose and time-dependent release of β -hexosaminidase of gravity settling mast cells on fluid bilayers. Figure 3.13 depicts a histogram of the β -hexosaminidase release after 2 min, 10 min, 15 min, and 30 min mast cell incubation on mobile bilayers with 25 mol% DNP-Cap PE. The release from gravity settling RBL cells after 2 min settling time is significantly higher than spontaneous release (bare glass) and does not significantly increase up to 30 min. Hence, the results suggests that low level signaling on fluid membranes occurs within ~ 1 minute before receptor clusters coalesce to form larger central patches.

It is worth noting that Aaron et al. [80] have previously conducted a single cell degranulation assay. In this experiment RBL cells were transfected with fluorescent Fas ligand, a secretory component in the lysosomes, to visualize RBL cell degranulation. Their results indicated that the majority of mast cell signaling occurs within 40 s of initial contact, which is consistent with our results presented in Fig. 3.13.

3.6 Concluding Remarks

In this chapter, we present the first quantitative evidence that anti-DNP IgE-Fc ϵ RI complexes form microclusters at RBL cell protrusions through diffusion mediated trapping at initial contact with monovalent ligands in supported lipid bilayers [14]. To quantitatively measure early IgE receptor dynamics, the time of cell-surface contact was fixed by micropipette cell manipulation, with an onset precision of ± 50 ms. At early time points, the typical size of the fluorescence heterogeneities was the same for all surfaces, regardless of the presence or absence of ligand, or the ligand mobility, see section 3.2.2. On ligand-free surfaces, these heterogeneities most likely reflect the variation in the separation between the cell and the substrate, as the exponential decay in the TIRF field will cause close contacts to appear brighter. The hypothesis that receptor clusters develop at close contacts was supported by simultaneous TIRF imaging of a water-soluble fluorescent marker dye in section 3.2.

We have shown that the cluster brightness increases substantially in the first few seconds of initial contact with monovalent ligands incorporated in either mobile or immobile supported lipid bilayers, and this increase is well modeled by diffusional trapping, see section 3.2.3. The initial cluster locations appeared to be random, as quantified by both a radial density analysis and a near-neighbor distance analysis. At later times (> 10 s), liganded IgE receptor clusters on mobile surfaces, which mimics a parasitic membrane or the membrane of another immune cell contacting the mast cell [15], undergo a combina-

Chapter 3. Distribution and Dynamics of IgE Receptors on Ligand Presenting Surfaces

tion of directed and diffusive motion, indicating involvement of active cellular processes. The data further suggested that cluster motion does not change significantly over time. However, receptor clusters farther from the cell center were observed to move faster than clusters closer to the cell center. Moreover, cluster motion was not dependent on cluster size, as expected from theoretical predications for experimental parameters, see section 3.4.

A question, which remains to be investigated in the near future, is whether receptor clusters remain associated with or restricted to cellular protrusions. During mast cell activation with multivalent ligand, RBL cells are known to change their cell morphology. During activation, the cell membrane undergoes a microvillous (unstimulated) to lamellar or ruffled (stimulated) membrane transition as depicted in Fig. 3.14. As we have discussed in the present chapter, mast cells are also activated (albeit weakly) when in contact with

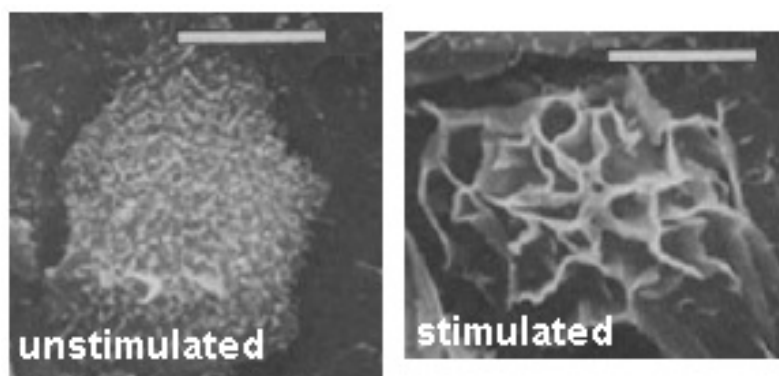


Figure 3.14: Scanning electron microscope micrograph of RBL-2H3 mast cell in resting, unstimulated state (left panel) and 10 min after stimulation with multivalent antigen (right panel). Taken from Ref. [81]. Bar represents 10 μm .

fluid lipid bilayers containing monovalent ligands. Therefore, activation with monovalent ligands may result in a similar change of cell morphology as observed during multivalent activation. It remains to be investigated how cell membrane shape transformation affects the coalesce of receptors in this model system. Although the clusters form at protrusions (Fig. 3.15A), they may persist even after the cell becomes smooth (Fig. 3.15B); if so, the

mechanism which holds them together would have to be identified. Another unanswered question is where the ruffles depicted in Fig. 3.14 (right panel) are with respect to the central patch.

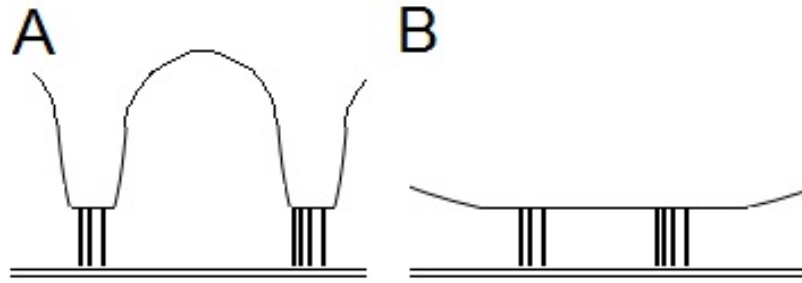


Figure 3.15: Illustration of membrane shape and receptor aggregation: (A) receptors aggregate at close contact points, (B) receptor clusters are maintained in a smooth surface.

Chapter 4

Single-particle Tracking of IgE Receptors in Clusters and Patches

4.1 Introduction

In chapter 3, we showed that receptor clusters on ligand-presenting fluid bilayers originate from cell surface protrusions that form the initial contact points with the substrate. Receptor accumulation at these contact points was shown to be kinetically consistent with diffusion limited trapping. Moreover, the cell membrane was far from the substrate except at receptor clusters, as shown by a dye exclusion study. After initial IgE-Fc ϵ RI cluster formation, small clusters diffused slowly and coalesced to form a big central patch, in which IgE-Fc ϵ RI were qualitatively observed to be laterally mobile [13]. The ability of monovalent ligands presented on fluid membranes to stimulate RBL cells speaks to a longstanding debate on the relationship between IgE-Fc ϵ RI mobility and signaling. Recently, it has been demonstrated that small multivalent antigen induced IgE-Fc ϵ RI clusters can induce signaling while retaining mobility [82]. The aim of this chapter is to quantify the mobility of of IgE-Fc ϵ RI within initial cell-substrate contact points (receptor clusters) and receptor

Chapter 4. Single-particle Tracking of IgE Receptors in Clusters and Patches

patches in detail, in order to address the role of IgE-Fc ϵ RI mobility in RBL cell activation.

Because receptor clusters are typically smaller than a micron, methods such as photobleaching recovery [83] or far-field fluorescence correlation spectroscopy [84] are ill-suited for measuring receptor diffusion. Instead, we have turned to single-particle tracking, using the fluorescent dye Atto647, which yielded receptor trajectories with ca. 50 nm localization precision, see section 4.3. To ensure that tracked receptors were in clusters, the majority of the receptor complexes were labeled with Alexa488; both dyes were imaged using a two-color TIRF microscope. Analysis of single-particle trajectories in sections 4.5 and 4.6 showed that receptors maintain their diffusivity even when confined within receptor clusters, and increase their diffusivity (above that of monomeric unliganded IgE-Fc ϵ RI) in synaptic patches. In order to ensure absence of significant bias in fit parameters, and to determine the extent of statistical variation in diffusivity, Monte Carlo simulations of diffusion tracks were made as outlined in section 4.4. The simulations showed that biological variation in diffusivity exceeds the statistical variation. Therefore, results presented in the present chapter show the diversity in receptor mobility in mast cells, and provide further evidence that receptor immobilization is not a prerequisite for signaling since mast cell signaling occurs on these mobile monovalent ligand substrates [5, 13], also see section 3.5.

Parts of this chapter have been published previously in Ref. [38].

4.2 Details of experiment

To investigate whether individual IgE-Fc ϵ RI complexes are laterally mobile within receptor clusters and synaptic patches, a two-color fluorescence experiment was performed. In this experiment single IgE-Fc ϵ RI were distinguished from receptor clusters and synaptic patches by labeling IgE with two spectrally distinguishable fluorescent markers at two dif-

Chapter 4. Single-particle Tracking of IgE Receptors in Clusters and Patches

ferent concentrations; a higher concentration to determine the location and spatial extent of receptor clusters and patches (Alexa488, green fluorescent) and a lower concentration to identify single IgE-receptor complexes (Atto647, red fluorescent).

Fluorescent IgE loaded RBL cells were allowed to settle under gravity on fluid lipid bilayers with 12 mol% DNP-CAP PE and simultaneously excited with a blue and red laser beam. TIRF microscopy was used to image fluorescent structures within 200 nm of the cell-substrate interface as outlined in section 2.6. Microscope time series of 50 s (1000 frames) were collected after ~ 30 s and ~ 4 min of initial cell-substrate contact. Receptor motion in clusters and synaptic patches was investigated at early and late time points, respectively. In this two-color TIRF experiment, the images were collected in two channels. The red channel recorded the lower concentration Atto647-IgE in the single-particle regime. Images in the green channel (Alexa488) recorded the fluorescent label at higher concentration to outline the spatial extent of receptor clusters and synaptic patches. To overlay these two channels, a dilute sample of $0.1\ \mu\text{m}$ diameter fluorescent microspheres (yellow/green FluoSpheres, Molecular Probes Inc.) emitting spectral components detectable in both channels was imaged. The images of these microspheres were used to align the two channels. After spatially overlaying the two spectrally separated time series, the majority of IgE-Fc ϵ RI were observed to be mobile within clusters and synaptic patches. Figure 4.1 depicts a two-color overlay at early time, Fig. 4.1A, and at late time, Fig. 4.1B. Here the green label outlines receptor clusters and bigger patches whereas the red label depicts single IgE-Fc ϵ RI receptor complexes.

4.3 Analysis of mean-squared displacement plot

Single-particle trajectories of fluorescent receptor clusters and IgE-Fc ϵ RI receptor complexes were obtained by using a single-particle tracking algorithm implemented in MATLAB as previously described in section 2.9. IgE-Fc ϵ RI were tracked only if they were

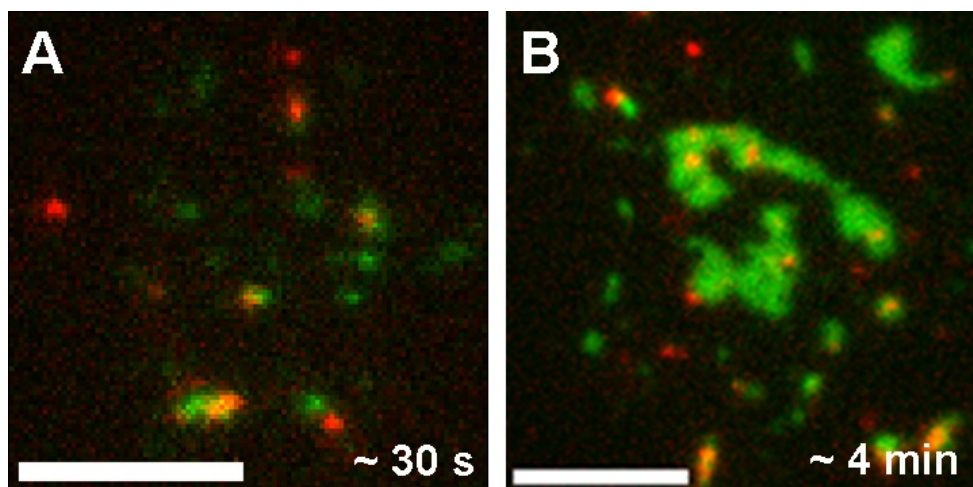


Figure 4.1: Two-color TIRF images with a labeling ration of 20:1 of green fluorescent dye (Alexa488) to red fluorescent dye (Atto467). Images depict gravity settling mast cell on a POPC fluid bilayer with 12 mol% DNP-lipid after (A) ~ 30 s and (B) ~ 4 min. Single particle tracking was performed on red fluorescent IgE-receptor complexes. Taken from Ref. [38]. Bar represents $5 \mu m$.

located within a receptor cluster or a synaptic patch as determined from the two-color image overlay. The particles were tracked for at least 65 time steps of 50 ms each. The average track length was ~ 100 time steps. The MSD was calculated from all n available displacements of a given duration $n\Delta t$ in the track record [85, 58, 86]. To characterize the motion, the MSD plot was computed up to $\Delta t < 1/4$ of the total number of acquired time frames [58, 87]. In MSD plots computed in this chapter, all points were equally weighted, which has been shown to give unbiased parameters if all available displacements are used [58, 86].

The MSD graph for IgE-Fc ϵ RI inside receptor clusters and in the central patch showed a downward curvature (see Fig. 4.3C (circles) and 4.3F) and asymptotically approached a finite value, which is a signature for confined diffusion. As the exact shape of the confinement (if it is not too eccentric) has a negligible effect on the form of the MSD [19] (see Eq.(2.9)), we fit to a circular confinement zone. The exact solution [88] contains an infinite sum of exponentials, but the second term is two orders of magnitude smaller than

Chapter 4. Single-particle Tracking of IgE Receptors in Clusters and Patches

the first and each subsequent term at least another order of magnitude smaller. Hence, a good approximation is obtained from the first exponential only

$$MSD(\Delta t) = 4\sigma + R^2[1 - 0.99\exp(-1.84^2 D\Delta t/R^2)]. \quad (4.1)$$

Fitting parameter D is the diffusion coefficient, R is the confinement zone radius, and σ represents the uncertainty (variance) in particle localization. It is worth noting that the Laplace transform of the exact solution, which includes an infinite sum of exponential terms, can be computed precisely and is given as [89]

$$\widetilde{MSD}(\epsilon) = \frac{4D}{\epsilon^2} \left[1 - \frac{1}{\sqrt{\epsilon\tau}} \frac{I_1(\sqrt{\epsilon\tau})}{I_1'(\sqrt{\epsilon\tau})} \right]. \quad (4.2)$$

Here ϵ is the Laplace variable, $\tau = R^2/D$ is a diffusion time, and $I_1(z)$ is the first modified Bessel function of the second kind, where the prime represents the first derivative with respect to $\sqrt{\epsilon\tau}$. To ensure that the approximation given in Eq.(4.1) is appropriate, we numerically Laplace inverted Eq.4.2 by applying the Gaver-Stehfest inversion algorithm outlined in appendix C and compared it to the approximation. As expected, the functional form of Eq.(4.1) was in excellent agreement with the exact numerically inverted solution. The sum of the static and dynamic localization (measurement) uncertainty is represented by σ in Eq.(4.1). This value was determined by fitting a straight line through time lags $2\Delta t$, $3\Delta t$, and $4\Delta t$. The offset determined by this method avoids using the part of the MSD plot between times 0 and $2\Delta t$ which is known to be complicated and times longer than $4\Delta t$ after which the confinement effects were apparent [90]. The average localization uncertainty for IgE-FcεRI diffusing inside clusters and synaptic patches was $\sigma = 47 \pm 18$ nm and $\sigma = 30 \pm 38$ nm, respectively, where the error represents one standard deviation.

Cluster diffusion was also estimated from MSD plots of the cluster center, as determined from a two-dimensional Gaussian fit to intensity. The MSD graph of receptor cluster trajectories was linear as depicted in Fig. 4.3C (squares) and fit to Eq.(2.8) with $offset = 4\sigma$ to estimate cluster diffusivity. The average localization uncertainty for clusters was $\sigma = 32 \pm 13$ nm.

4.4 Monte Carlo calculations

To determine statistical uncertainties and possible biases in fitting for diffusivity, model diffusion tracks were constructed using a random-step-length continuum algorithm, and the tracks were analyzed with same procedure employed for cell data as outlined in section 4.3. A point particle was initially placed at a random position within a circular domain of radius R . At each time step, the particle was moved a displacement $\gamma\sqrt{2Dt}$ in x and y , where t is the time step, D the diffusion coefficient, and γ is a normally distributed pseudorandom number with zero mean and unit standard deviation. When a particle attempted to cross the boundary, its trajectory was reflected by the boundary resulting in confined diffusion. To simulate simple diffusion we applied the same algorithm in the absence of a reflecting boundary. The final simulated real particle trajectory (without localization uncertainty) contained 100 position measurements. To obtain an experimentally observed particle trajectory a dynamic and static localization uncertainty must be added. As mentioned above, static errors arise from the uncertainty in determining the position of the particle due to experimental noise. Dynamic errors are due to particle diffusion within the integration time of each frame, leading to intensity blurring. Both sources of error have a Gaussian distribution and can be combined into one parameter $\gamma\sigma$ which was added to each x and y coordinate of the trajectory.

Monte Carlo simulations were performed in MATLAB and the simulation was repeated 50,000 times for each initial Monte Carlo diffusion coefficient D and corral radius R . D_{fit} and R_{fit} obtained from the fits to the MSD plots were nearly lognormally distributed, deviating only at the tails from the phenomenological distribution as depicted in Fig. 4.2. A lognormal distribution in diffusivity given as

$$f(D_{fit}) = \frac{1}{D_{fit}\eta\sqrt{2\pi}} \exp\left[\frac{-(\ln D_{fit} - \mu)^2}{2\eta^2}\right], \quad (4.3)$$

where μ and η are fitting parameters, has been reported for unconfined diffusion [58, 91]. Accordingly, we characterized the distribution by the (exponential of the) mean log dif-

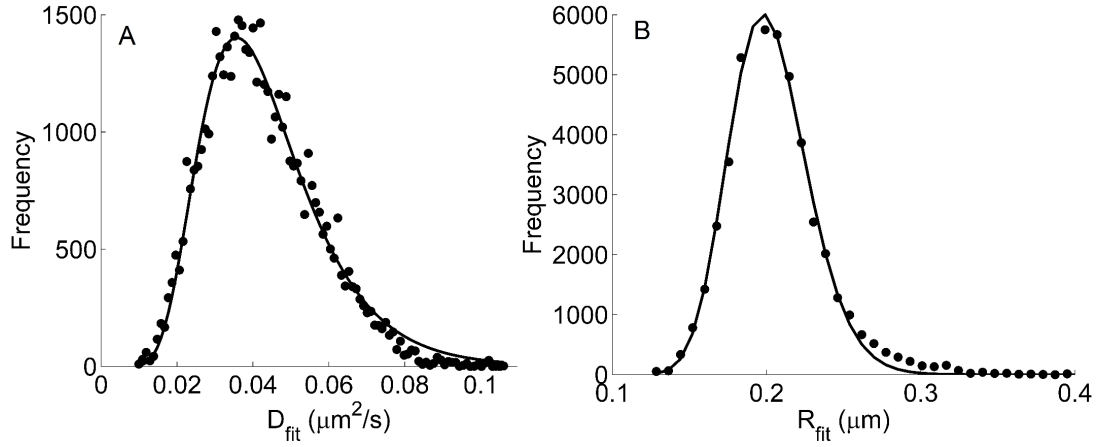


Figure 4.2: Distribution of D_{fit} (A) and R_{fit} (B) obtained from 50,000 Monte Carlo simulated trajectories. The MSD in (A), computed for each trajectory, was fit to a circular confinement zone given in Eq.(4.1). The initial Monte Carlo diffusion coefficient and corral radius were $D = 4.1 \times 10^{-2} \mu m^2/s$ and $R = 206$ nm, respectively. The simulation input parameter for static and dynamic localization uncertainty was $\sigma = 47$ nm. The solid line represents a fit to a lognormal distribution given in Eq.(4.3). Taken from Ref. [38].

fusivity $\langle D_0 \rangle_{ln}$ and corral radius $\langle R_0 \rangle_{ln}$, and the corresponding standard deviations, expressed as multiplicative factors. In the remainder of this chapter, we will drop the subscript and use the averaging brackets to denote the logarithmic mean, and $\times/$ to indicate the uncertainty factor. Note that many studies of diffusion on cells report uncertainties as the standard error or the mean (or log mean), which is much smaller than the spread in the distribution of measurements.

4.5 IgE-FcεRI receptors diffuse within clusters and patches

In a recent study [13] our group showed that individual IgE-FcεRI were mobile within a synaptic patch by a fluorescent bleaching and recovery experiment. However, the collected experimental data did not allow us to estimate a receptor diffusion coefficient. To make

Chapter 4. Single-particle Tracking of IgE Receptors in Clusters and Patches

quantitative useful measurements of receptor motion within clusters and synaptic patches the method of single-particle tracking [19, 57, 59] was applied.

Figure 4.3B and 4.3E depict a typical IgE-Fc ϵ RI trajectory (red) imaged at 20 frames/s within a cluster (green) and a synaptic patch (green), respectively. Corresponding MSD plots depicted in Fig. 4.3C (circles) and 4.3F showed downward curvature and asymptotically approached a finite value, which is a signature for confined diffusion. From the asymptotic MSD value the estimated cluster and patch radius was $\sqrt{0.03}\mu\text{m}$ (160 nm) and $\sqrt{0.21}\mu\text{m}$ (460 nm), respectively. This functional form was expected since it is evident from Fig. 4.3B and 4.3E that receptor trajectories were confined within the cluster and synaptic patch. The cluster image (Fig. 4.3B, green) was obtained from an intensity sum over a 4.6 s time series. The cluster moved approximately 140 nm in this time period. The tracked receptor remained within the patch at all times. The patch image (Fig. 4.3E, green) was obtained from an intensity sum over a 3.3 s time series.

Qualitatively, the much steeper initial slope of the MSD for the receptor in the patch (Fig. 4.3F) compared to that for the receptor in the small cluster (Fig. 4.3C, circles) shows that the former diffuses much faster. To show that receptors are indeed mobile within clusters and eliminate the possibility that the trajectory shown in Fig. 4.3B (red) describes the actual cluster motion, the cluster was separately tracked. The MSD plot obtained from the cluster trajectory is shown in Fig. 4.3C (squares). From the linear fit, we find that the diffusion of the cluster as a whole is an order of magnitude slower than that of the individually tracked receptor. In addition, for a fraction of IgE-Fc ϵ RI that had very slow diffusion, we found no directional correlation between receptor hops and cluster hops, *vide infra*.

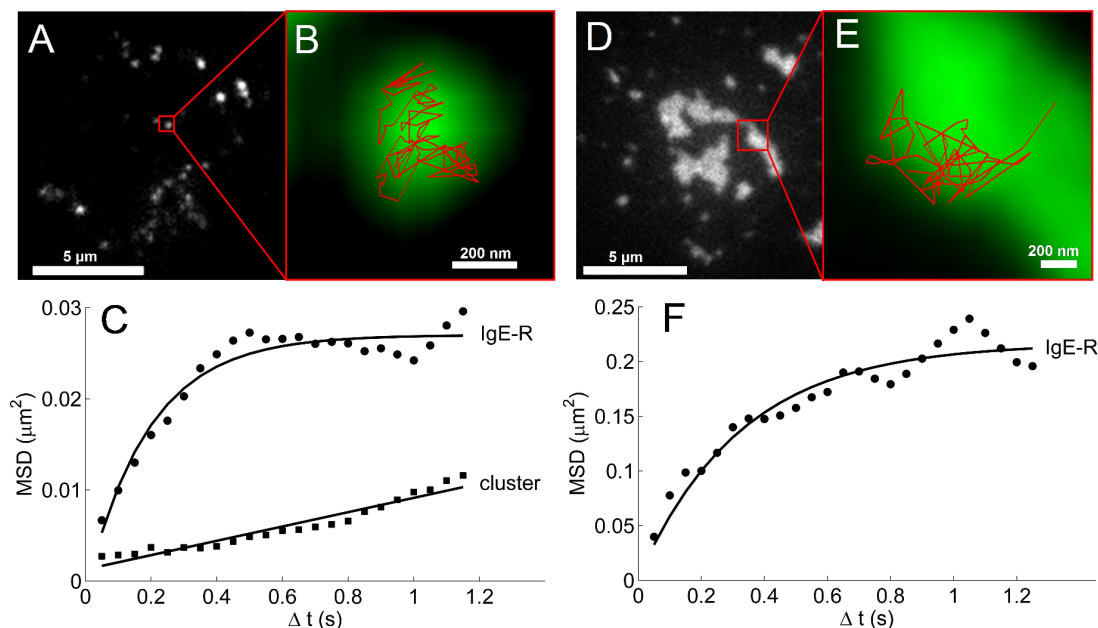


Figure 4.3: Fluorescent IgE-FcεRI receptor (IgE-FcεRI) complexes undergo confined diffusion in clusters and synaptic patches. (A,D) TIRF microscope image of gravity settling RBL cell on POPC fluid lipid bilayer with 12 mol% DNP-CAP PE after ~30 s (A) and ~4 min (D) of initial contact. Red box highlights cluster or synaptic patch in which a single fluorescent IgE-FcεRI complex was tracked at 20 frames/s. Bar represents 5 μm. (B) Demonstrates that IgE-FcεRI complex trajectory (red) is restricted to the area occupied by the cluster (green). (C) MSD plots of IgE-FcεRI complex trajectory shown in (B) (circles) and cluster trajectory (squares). (E) Demonstrates that IgE-FcεRI complex trajectory (red) is restricted to the area occupied by the synaptic patch (green). (F) MSD plot of IgE-FcεRI complex trajectory shown in (E). Taken from Ref. [38].

4.6 IgE-FcεRI receptors diffuse faster in patches

For a receptor confined within a cluster, the cluster trajectory was obtained separately. The MSD was calculated for each trajectory and fit to a simple diffusion (cluster tracks) or confined diffusion model (IgE-FcεRI tracks) to estimate diffusivity and domain size as outlined in section 4.3. For receptors diffusing inside clusters, two clearly distinguishable populations were observed: one diffusing significantly faster than the cluster (Fig. 4.3C) and the other (~ 30% of receptor tracks) with a diffusivity comparable to the clusters

Chapter 4. Single-particle Tracking of IgE Receptors in Clusters and Patches

themselves. The second population will be analyzed separately in a later section (section 4.8). The average (logarithmic mean) diffusion coefficient of IgE-FcεRI in clusters of the first population was $\langle D \rangle = 4.1 \times 10^{-2} \mu\text{m}^2/\text{s}$, with a spread of a factor of 2.03. The IgE-FcεRI diffusivity in clusters is similar to that of the monomeric, uncrosslinked IgE-FcεRI [57, 73]. The average cluster radius $\langle R \rangle$ was 206 nm ($\times/1.36$), which is consistent with the microscopically observable cluster size and measurements presented in section 3.2.2 [14]. IgE-receptor complexes confined within synaptic patches of apparent average radius $\langle R \rangle = 503$ nm ($\times/1.45$) diffused faster than expected, with an average diffusivity of $\langle D \rangle = 0.17 \mu\text{m}^2/\text{s}$ ($\times/1.7$). This diffusion coefficient is significantly faster than the measured diffusivity of monomeric IgE-FcεRI on resting cells [57] and consistent with the apparent absence of actin cytoskeleton in this region [13]. It is also consistent with diffusion measurement of FcεRI mobility using high speed (750 frames/s) single particle tracking [92] and FRAP on cells swollen by hypoosmotic stress [40], where the constraints of the cytoskeleton are removed. Figure 4.4 shows the average diffusion coefficient (solid black line) for IgE-receptor complexes diffusing within synaptic patches (circles) and clusters (squares). The average diffusivity of clusters (triangles) was $\langle D \rangle = 3.3 \times 10^{-3} \mu\text{m}^2/\text{s}$ ($\times/2.1$), significantly smaller than IgE-FcεRI diffusivity and within reported observations outlined in section 3.4.1 [14]. Clusters tracked in this experiment did not show evidence of directed motion as we found in section 3.4.1. However, the tracking time was shorter in the study presented in this chapter, making detection of directed motion more difficult. For each population, the dashed line above and below the mean represents one standard deviation in the lognormal distribution. To compare the data sets statistically, the two-sample Kolomogorov-Smirnov test [93] was implemented. This test determined that the three experimental data sets presented in Fig. 4.4 were drawn from three different distributions at the 5×10^{-4} significance level.

To determine if the variation and uncertainty in diffusivity is consistent with that expected from statistics, Monte Carlo simulations as outlined in section 4.4 were performed. The experimentally observed average diffusivity $\langle D \rangle$ and corral radius $\langle R \rangle$ (if applicable)

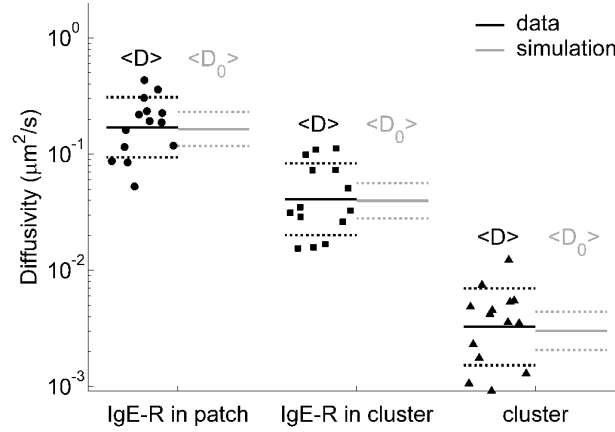


Figure 4.4: Experimental (solid black lines) and Monte Carlo simulated (solid grey lines) average (logarithmic mean) diffusivity of IgE-FcεRI receptor complexes confined to synaptic patches (circles) and clusters (squares) as well as average diffusivity of freely diffusing clusters (triangles). For each population, the dashed line above and below the average represents one standard deviation in the lognormal distribution. The average diffusion coefficient $\langle D \rangle$ and corral radius $\langle R \rangle$ obtained from experiments were used as input parameters for the simulation. Here, the averaging brackets denote the logarithmic mean. $\langle D_0 \rangle$ is the average diffusivity obtained from 50,000 simulations which incorporated dynamic and static localization uncertainty estimated from experimental data. Taken from Ref. [38].

for each population were used as simulation input parameters, as well as the localization uncertainty σ . After 50,000 Monte Carlo simulations, the population mean and standard deviation of $\langle D_0 \rangle$ and $\langle R_0 \rangle$ were calculated. The average diffusivity for receptors confined within synaptic patches and clusters was $\langle D_0 \rangle = 1.6 \times 10^{-1} \mu\text{m}^2/\text{s}$ ($\times/1.4$) and $\langle D_0 \rangle = 4.0 \times 10^{-2} \mu\text{m}^2/\text{s}$ ($\times/1.4$) with average confinement zone radius of $\langle R_0 \rangle = 513 \text{ nm}$ ($\times/1.3$) and $\langle R_0 \rangle = 204 \text{ nm}$ ($\times/1.17$), respectively, in good agreement with measured values. This demonstrates that the analysis procedure, with overlapping intervals and equal weighting, does not introduce any substantial bias in parameter estimation, even in confined diffusion. As shown in Fig. 4.2, there is evidence of a very small residual bias at the tails, which may be caused by the slight deviation of fit diffusivities from a lognormal distribution.

Chapter 4. Single-particle Tracking of IgE Receptors in Clusters and Patches

Monte Carlo simulation of cluster diffusion gave an average diffusivity of $\langle D_0 \rangle = 3.0 \times 10^{-3} \mu\text{m}^2/\text{s}$ ($\times/1.47$), in agreement with the measured value. As discussed above, it has been previously noted that MSD fitting for unconfined diffusion gives unbiased estimates when overlapping intervals and equal weighting are used [58, 86], so good agreement was expected. Uncertainty in σ resulted in a systematic error of less than 10% of the reported values. Figure 4.2 shows results obtained from the simulations, where the solid grey lines indicate the mean and dashed grey lines one standard deviation above and below the mean.

The simulations also show that the variation in D observed on cells cannot be explained on the basis of statistics, as the simulation includes localization uncertainty, finite track length, exposure time, and equal weight fitting. Thus, there is additional variation of biological origin.

As discussed in chapter 3, we believe that receptor clusters originate from cell surface protrusions that form the initial contact points with the substrate. The cluster is thus maintained (while it is maintained, i.e. before coalescence) by the cell morphology. This allows for the relatively free diffusion of receptors confined within it. Hence this study, and other recent studies [82] indicate clearly that receptor immobilization is not required for signaling, as signaling (albeit weak signaling) still occurs with fluid lipid membrane substrates [5, 13].

4.7 IgE-Fc ϵ RI receptors can hop between clusters

Although receptors are generally confined, on rare occasions, a receptor can be observed to leave one cluster and enter a different cluster. Figure 4.5 depicts a trajectory of such a cluster-hopping receptor. The color coding indicates the relative brightness of the receptor, with red being dimmest and blue brightest. During transit, the IgE-Fc ϵ RI appears to

Chapter 4. Single-particle Tracking of IgE Receptors in Clusters and Patches

be farther from the substrate, as it is dimmer in TIRF. Thus, during transit this receptor is no longer in close proximity to the supported lipid bilayer; either the IgE must dissociate from the lipid-bound ligand, or the lipid-bound ligand must be extracted from the membrane. Although cells can easily develop sufficient force to extract phospholipids from membranes [94], we believe that this event involved ligand dissociation from IgE. Firstly, spontaneous IgE-DNP dissociation is rather fast, binding time ≈ 100 s [95]. Secondly, the trajectory of the receptor appears to be diffusive, not directed, as might be expected if the cell were exerting force on the receptor.

It is noteworthy that the IgE-Fc ϵ RI appeared to diffuse more rapidly when in transit in between clusters, comparable to observed IgE-Fc ϵ RI motion in synaptic patches. This may indicate that the relaxation of diffusional constraints over much of the cell surface is a precursor to the formation of the larger central patches and patch coalescence.

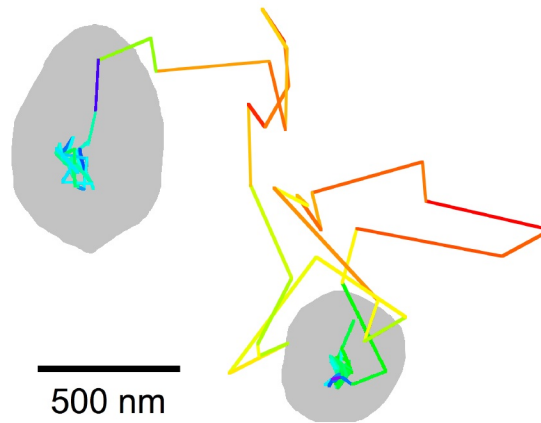


Figure 4.5: Fluorescent IgE-Fc ϵ RI receptor (IgE-Fc ϵ RI) trajectory obtained from single-particle tracking at 20 frames/s. TIRF microscope images were collected ~ 30 s after initial cell-substrate contact. The color coding indicates the relative brightness of the IgE-Fc ϵ RI, with red being dimmest and blue brightest. The IgE-Fc ϵ RI is initially confined in the bottom left cluster (grey) and then transits to the top cluster. During transit the receptor appears to be no longer in close proximity (dimmer in TIRF) to the supported lipid bilayer and appears to move more rapidly (larger hops). Taken from Ref. [38]. Scale bar represents 500 nm.

4.8 Slowly diffusing receptors are not influenced by receptor cluster motion

As previously mentioned $\sim 30\%$ of receptors in clusters are no more mobile than the clusters themselves. This raises the possibility that they are, in fact, immobile within the cluster, and their motion is simply the collective motion of the cluster. To address this hypothesis, we looked for correlation between the cluster and the single receptor hop directions. A total of 508 cluster-receptor vector pairs obtained from individual hops (every 50 ms) were analyzed (7 IgE-Fc ϵ RI and cluster trajectories). A histogram of receptor hop directions, relative to the cluster hop direction, is shown in Fig. 4.6 in a polar plot. The same number of correlated (251) and anticorrelated (258) hops was observed, within statistical variation. Thus, slowly diffusing receptors are not simply moving with the cluster as a whole. In fact, they do not even appear to be influenced by the cluster motion. This may indicate that the cytoskeletal elements responsible for maintaining cluster (contact) points do not move as initially suggested in section 3.4.2, but rather assemble and disassemble so as to produce contact zone movement.

4.9 Closing Remarks

This chapter presented a study what we believe to be the first quantitative evidence that anti-DNP IgE-Fc ϵ RI receptor complexes undergo relatively free diffusion within micron-sized receptor clusters [38]. As outlined in chapter 3, these clusters originate from cell surface protrusions that form initial contact points with a monovalent ligand-bearing fluid lipid bilayer, which is known to trigger mast cells [5, 13], see section 3.5. To directly observe IgE-Fc ϵ RI receptor motion within these contact points, we applied two-color TIRF microscopy together with single-particle tracking and MSD analysis as outlined in section 4.2 and 4.3, respectively. To ensure the absence of bias in the fitting of

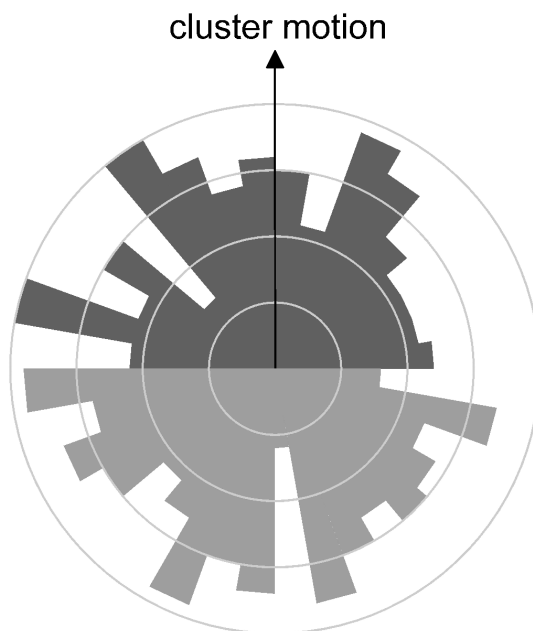


Figure 4.6: Histogram in polar coordinates of IgE-Fc ϵ RI hop direction, relative to receptor cluster hop direction, which is represented by the arrow. Here, receptors were no more mobile than the clusters themselves. The data suggests that there are the same number of correlated (251) and anticorrelated (258) hops, within statistical variation. Taken from Ref. [38].

MSD plots, Monte Carlo simulations of diffusion tracks (with localization uncertainty), as described in section 4.4, were fit by the same procedure.

The typical diffusion coefficient of liganded receptor in clusters in section 4.6 was comparable to that of the monomeric, uncrosslinked IgE-Fc ϵ RI receptor on free cell surfaces [57]. Although about 30% of the receptors did diffuse slowly, their motion was uncorrelated with that of the micron-sized clusters in which they were located as outlined in section 4.8. In the synaptic patches that result from coalescence of clusters, receptors diffused much faster (sections 4.5 and 4.6), consistent with the apparent absence of actin cytoskeleton in the synaptic region [13]. Hence RBL cell synaptic patches may prove to be a useful model system to study protein diffusion in the absence of cytoskeletal interactions. On rare occasions, as shown in section 4.7, a receptor was observed to leave one

Chapter 4. Single-particle Tracking of IgE Receptors in Clusters and Patches

cluster and enter a different cluster; the loss of confinement appears to be caused by IgE dissociation from its ligand. In between clusters, receptors showed very rapid diffusion (even before the central synaptic patches have formed), suggesting that the loss of diffusional constraints is actually a precursor to the formation of the large synaptic patch. In conclusion, our results suggest at least three diverse states of receptor mobility in mast cells, and provide further evidence that receptor immobilization is not a prerequisite for signaling.

Lastly, we want to note that through our investigations, we have made a direct connection to a relatively new field in cell membrane biology, namely the subject of membrane curvature generation and sensing [96]. In cell membranes, surface energy was considered historically a passive, geometric feature of biological membranes due to the small curvature of the cell as a whole [96]. However, when the membrane curvature radius is close to the membrane thickness, the membrane curvature is quite large. Curvature of a normally flat bilayer expands the lipid heads on the outer leaflet and compresses them on the inner; since molecular compression is more limited, the overall effect is an area increase, giving a higher surface energy. This increase in surface energy may affect protein motion. One mechanism which may cause this motion is based on the principles of hydrostatics. Figure 4.7 shows how a curved interface, e.g. oil-water interface, can cause particle migration based on the principle of capillarity [97]. A particle embedded in an interface creates a local deformation which can interact with the host surface energy gradient. To minimize surface area, an anisotropic particle must orient itself properly and move along its host interface to minimize the difference between the curvature of its deformation field and that of the host. If there are multiple particles embedded in a host interface, their individual deformation fields will interact as well. Since we have studied diffusion limited trapping of receptors at cellular protrusions in chapter 3 and we have observed individual receptors to leave on cell-substrate contact point and enter a different one in the present chapter, see section 4.7, an investigation of the effect of membrane curvature gradients on Fc ϵ RI transport would be a natural and important extension of our studies.

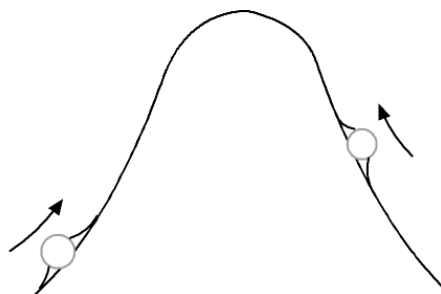


Figure 4.7: Illustration of anisotropic particles, e.g. cylinders, moving on a curved interface. The particles rotate and move on the host interface to minimize the overall curvature.

Chapter 5

The Formation of a Receptor Cluster Depletion Zone

5.1 Introduction

In chapter 3, experimental investigations showed that receptor clusters are initially randomly distributed over the cell-substrate contact area. These clusters move over the cell surface with a combination of diffusive and directed transport. At late time, clusters coalesce to form a large central receptor patch. This formation of a large central patch seemed to be accompanied by the formation of a receptor cluster depletion zone. In the present chapter, we developed a simple mathematical model for the rotationally averaged correlation function of such a depletion zone.

In section 5.2, we present experimental data which qualitatively shows that a receptor cluster depletion zone forms around the central receptor patch. The corresponding rotationally averaged image correlation function (c.f.) shows the development of a dip, which we believe to be a quantitative signature of the formation of a receptor cluster depletion zone. The goal of the present chapter is to develop a mathematical model for such a c.f.

Chapter 5. The Formation of a Receptor Cluster Depletion Zone

and fit this model to individual c.f.s of RBL cell TIRF images in a time series to extract essential parameters such as depletion zone and central patch radius. Plotting these parameters over time should give us some new insight into the dynamics of depletion zone formation as well as central patch growth.

To develop a mathematical depletion zone model, which is based on the contribution of two c.f., seven important model parameters are selected in section 5.2.1. The first contribution is the intensity c.f. of non-overlapping disks with a top-hat intensity profile. Section 5.3 outlines an approximate but highly accurate semianalytical algorithm to compute this correlation function. It is worth noting that the algorithm for non-overlapping disks can be extended to estimating particle number and size from the intensity autocorrelation of a typical microscope image of fluorescent disk-like particles as outlined in appendix A. In section 5.4, the c.f. of a depletion zone, which is the second contribution, is derived from geometrical considerations. In section 5.5, we show that a simple superposition of these two contributions fit the c.f. of a computer generated receptor cluster depletion zone very well.

Finally, the model was applied to radial averaged c.f.s obtained from the image autocorrelation of thresholded RBL cell TIRF images in section 5.6. This direct comparison showed that the presented mathematical model cannot describe our experimental data. The main short coming of our model is accounted to the asymmetric shape of receptor clusters and patches, which can lead to the disappearance of the dip in the rotationally averaged correlation function.

Parts of this chapter have been published previously in Ref. [39].

5.2 Receptor cluster depletion zone

The formation of the big central receptor patch due to a fluid ligand presenting bilayer is shown in Fig. 5.1. At early time points, clusters are small and nearly homogeneously distributed. Over time, clusters become larger due to cluster coalescence, eventually resulting in the emergence of a central patch. The appearance of a receptor cluster depletion zone becomes apparent after ~ 1 min after initial cell-substrate contact. Quantitatively, the formation of the depletion zone and the large central patch, can be characterized by the rotationally averaged c.f., which has been previously used to determine receptor cluster size in section 3.2.2. Figure 5.1 depicts the spatial c.f. for a RBL cell TIRF image shown in the inset. The depicted rotationally averaged c.f. was corrected for noise contributions and obtained from TIRF images masked with mean of cell interior, as was done previously to estimate receptor cluster size, see section 3.2.1. Figure 5.1 depicts an apparent dip in the c.f., which we believe to be a signature of a receptor cluster depletion zone, even though

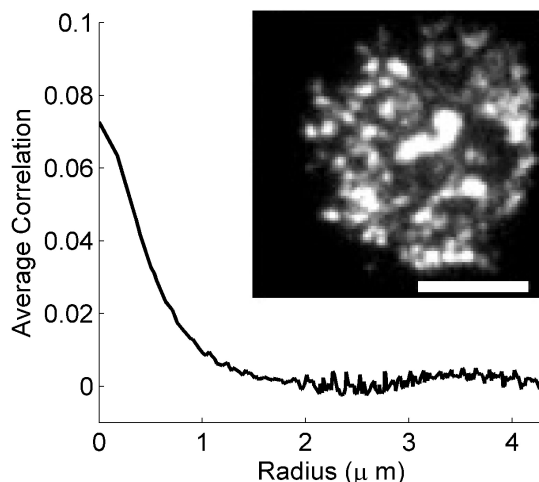


Figure 5.1: Rotationally averaged correlation function of RBL cell pipette-pressed onto a POPC bilayer with 25 mole % DNP-Cap PE after 80 s of initial cell-substrate contact. Inset shows corresponding TIRF image. It is apparent from the correlation function that there is a receptor depletion zone around the big receptor patches, which manifests itself in a dip in the correlation function. Bar represents 5 μm .

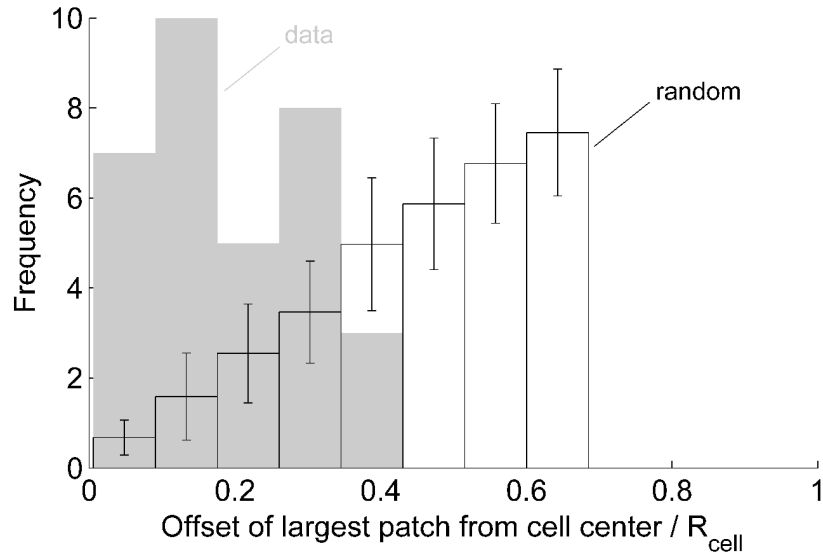


Figure 5.2: Frequency distribution of the radial distance of the center of the biggest patch from the center of the contact zone (grey bars) compared to the distribution expected for a random patch distribution within the contact zone (white bars).

the dip is not very pronounced.

As mentioned above, the position of the big receptor patch seems to be in the center of the cell-substrate contact zone. This observation was confirmed by computing the radial distance of the geometric center of the largest receptor patch to the center of the cell-substrate contact area. Figure 5.2 depicts a frequency plot of the radial distance of the largest patch from the cell center, normalized by the cell radius, for 33 individual cells (grey bars). Each cell was in contact with a monovalent ligand bearing fluid lipid bilayer for at least 2 min. The data suggests that the largest receptor patch forms closer to the center of the contact zone than predicted from a random patch distribution in the contact zone, Fig. 5.2 (white bars).

It is worth noting the appearance of the largest receptor patch in the center of the cell-substrate contact area, raises an interesting question "how does the cell know where its middle is?" This question remains to be investigated in the near future.

5.2.1 Proposed depletion zone model

In order to develop a mathematical model for the rotationally averaged correlation function of RBL cell TIRF images as depicted in Fig. 5.1, we first select essential model parameters. Our experimental observations suggested that important model parameters are the size, intensity, and number density of clusters as well as the central patch and depletion zone radius. To reduce this list of parameters, we decided to threshold RBL cell TIRF images before the computation of the c.f., see section 2.10. Figure 5.3 depicts an illustration of a typical RBL cell TIRF image, which depicts a receptor cluster depletion zone. There are a total of seven essential parameters, which include the cluster radius R_c , patch radius R_p , and depletion zone radius R_d . Due to image thresholding the intensity values of receptors I_s and the central patch I_p can be set to one, whereas the intensity value of the depletion zone I_d is set to zero. Finally, the intensity of the background I_b can be determined exactly, since it is the average intensity of the cell interior. Including the background intensity in the model is essential to correct the radial c.f. for cell size artifacts, see section 3.2.1.

A simple mathematical model of the radial c.f. for an intensity distribution depicted in

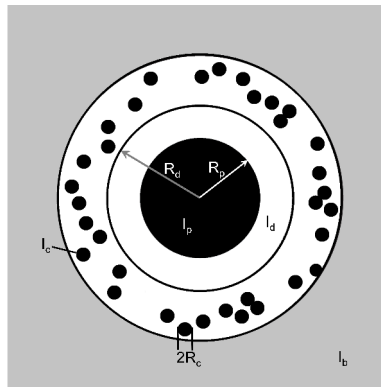


Figure 5.3: Illustration of receptor cluster depletion zone and selected model parameters. Here, R_d , R_c , and R_p represent the depletion zone, cluster, and patch radius, respectively and I_d , I_c , and I_p are their corresponding intensity values. I_b is the background intensity defined as the mean intensity of the cell interior.

Fig. 5.3 can be constructed from three contributions as follows. The first contribution, is a radial correlation of a random distribution of clusters with a top-hat intensity profile, which we will call autocorrelation of randomly distributed non-overlapping disks of identical radius $g_c(r)$. The second contribution is the autocorrelation of a ring $g_d(r)$ of outer radius R_d and inner radius R_p . The ring has uniform intensity, where the intensity inside the ring for a radius less than R_p is set to zero and the intensity outside the ring, i.e. $r > R_d$, is a constant less than one. The third contribution, which is small compared to the other two, is the crosscorrelation of a cluster with the central patch. For simplicity, we will neglect this contribution. Therefore, our model will consist of a simple superposition of the first two contributions.

5.3 Rotational correlation function of randomly distributed disks

In the present section, we derive an approximate but highly accurate algorithm for the computation of the intensity c.f. for hard disks in two dimensions. Kruglov [98] (and elaborated by Li et al. in Ref. [99]) has shown how the density c.f. for a system of homogeneous spheres can be derived from the pair correlation function, using geometrical considerations. (The pair correlation function gives the probability of finding an object with its center at a distance r , given an object at the origin.) For image correlation, the density corresponds to the image intensity. Following Kruglov, the two-dimensional density or intensity correlation for a population of disks of identical radius may be written as

$$g_c(\vec{r}) = \int_A g_{auto}(\vec{r} - \vec{r}') [\delta(\vec{r}') + \rho\gamma(\vec{r}') - \rho] d^2\vec{r}', \quad (5.1)$$

where g_{auto} is the normalized density or intensity autocorrelation for a single disk, $\delta(r)$ is the two-dimensional Dirac delta function, $\gamma(r)$ is the pair c.f., and ρ is the number density

Chapter 5. The Formation of a Receptor Cluster Depletion Zone

of the disks. The integration is performed over the image area A . For an isotropic system, Eq.(5.1) may be rewritten in a symmetric form by averaging $g_{auto}(r)$ over all possible relative orientations of the vectors r and r' :

$$g_c(r) = g_{auto}(r) + \rho \int_0^\infty \int_0^\pi g_{auto} \left(\sqrt{r^2 + r'^2 - 2rr' \cos(\theta)} \right) [\gamma(r') - 1] 2r' d\theta dr'. \quad (5.2)$$

Note that g_{auto} plays a different role outside the integral (where it represents the correlation of each disk with itself) and inside the integral (where it represents the crosscorrelation between disks). For uniform (*top hat*) disk fluorescence, the autocorrelation $g_{auto}(r)$ can be computed from geometry and is

$$g_{auto}(r) = \begin{cases} 1 - \frac{r\sqrt{R_c^2 - r^2/4}}{\pi R_0^2} - \frac{2}{\pi} \sin^{-1} \left(\frac{r}{2R_0} \right), & 0 \leq r \leq 2R_c \\ 0, & 2R_c < r \end{cases} \quad (5.3)$$

normalized to $g_{auto}(0) = 1$, where R_c is the disk radius [100]. Equation (5.2) is the normalized per particle rotationally averaged equivalent of Eq.(3.1) and can be applied to systems without rotational order. The calculation of the intensity correlation function now requires the substitution of the pair c.f. into Eq.(5.2) and an evaluation of the integral therein.

Guo and Riebel [101] developed an analytic approximation for the pair c.f. for a monolayer of monodispersed hard disks using the Ornstein-Zernike (OZ) equation [102, 103]:

$$h(\vec{r}) = c(\vec{r}) + \rho \int_0^\infty h(\vec{r}') c(|\vec{r} - \vec{r}'|) d\vec{r}', \quad (5.4)$$

where $h(r) = \gamma(r) + 1$ is termed the total c.f. for two particles, and $c(r)$ is termed the direct correlation function. The OZ equation reflects the *indirect* contributions of three particle correlations to the total or pair correlation function. The OZ equation is a recursive equation and can be solved using a closure relation. Guo and Riebel [101] applied the Percus-Yevick closure relation for a hard-core pair potential to approximate the direct c.f.

Chapter 5. The Formation of a Receptor Cluster Depletion Zone

as

$$c(r; \eta) = \Theta \left(1 - \frac{r}{2R_c} \right) \left(-\frac{1 - q\eta^2}{(1 - 2\eta + q\eta^2)^2} \right) \times \left\{ 1 - a(\eta)^2\eta + \frac{2a(\eta)^2\eta}{\pi} \left[\sin^{-1} \left(\frac{r}{2R_c a(\eta)} \right) - \frac{r}{2R_c a(\eta)} \sqrt{1 - \frac{r^2}{4R_c^2 a(\eta)^2}} \right] \right\}, \quad (5.5)$$

where $\Theta(r)$ is the Heaviside step function, $q = (4\pi\sqrt{3} - 12)/\pi^2$, $\eta = \rho\pi R_c^2$ is the area fraction occupied by the disks and

$$a(\eta) = 0.399\eta^4 - 1.251\eta^3 + 2.019\eta^2 - 0.399\eta + 2.1.$$

In Fourier space the Ornstein-Zernike equation given in Eq.(5.4) can be written as

$$H(k; \eta) = \frac{C(k; \eta)}{1 - \rho C(k; \eta)}, \quad (5.6)$$

where $H(k; \eta)$ and $C(k; \eta)$ are the Bessel transforms of the total c.f. and the direct c.f., respectively, i.e.,

$$C(k; \eta) = 2\pi \int_0^\infty c(k; \eta) J_0(kr) r dk. \quad (5.7)$$

Here $J_0()$ is the zeroth order Bessel function. Combining $h(r) = \gamma(r) + 1$, Eqns. (5.5) and (5.6), the pair c.f. is obtained by computing the following inverse Bessel transform

$$\gamma(r) = 1 + \frac{1}{2\pi} \int_0^\infty \frac{C(k; \eta)}{1 - \rho C(k; \eta)} J_0(kr) k dk. \quad (5.8)$$

We numerically apply the Guo and Riebel direct c.f., Eq.(5.5) to Eqns. (5.7) and (5.8) to find the pair c.f.; the pair c.f. is directly substituted into Eq.(5.2) to obtain the normalized per particle intensity correlation function. The essential features of the pair correlation function given in Eq.(5.8) are shown in Fig. 5.4, which depicts $\gamma(r)$ for $R_c = 8$ pixel and $\eta = 0.31$. As mentioned above, $\gamma(r)$ is related to the probability of finding the center of

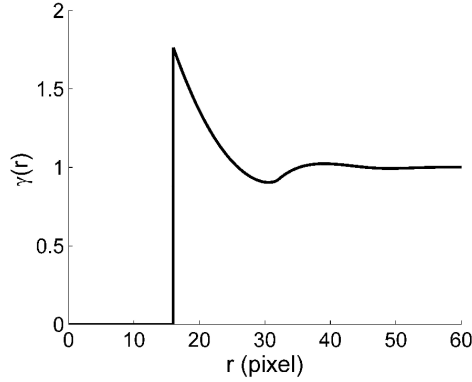


Figure 5.4: Pair correlation function $\gamma(r)$ obtained from Eq.(5.8) for $R_c = 8$ pixel and $\eta = 0.31$.

a disk a given distance from the center of another disk. For $r < 2R_c$, hard disks cannot overlap and $\gamma(r) = 0$, corresponding to the excluded volume. For large values of r , disks are uniformly distributed and $\gamma(r) \rightarrow 1$. In between, the region of decaying oscillations, the pair correlation function shows short-range structure as disks try to fit in the two-dimensional space without overlapping.

5.3.1 Scaled hard disk correlation function

The number of particles in a given observation volume can be determined if Eq.(5.2) is scaled appropriately. The scaling constant C can be obtained by computing the peak of the c.f. $g_N(0)$, where the subscript N refers to the properly normalized c.f. of N particles. Following Eq.(3.1) the peak of the rotationally averaged c.f. $g_N(0)$, is given as

$$g_N(0) = \frac{i^2 N \pi R_c^2 \setminus w^2}{[i N \pi R_c^2 \setminus w^2]^2} - 1 = \frac{w^2}{N \pi R_c^2} - 1 = \frac{1}{\eta} - 1, \quad (5.9)$$

where i describes the intensity of a homogeneous disk, w^2 is the observation area, and η is the area fraction occupied by the disks defined above. Using Eq.(5.9) one can compute the scaling constant C

$$C = \frac{g_N(0)}{g_c(0)} = \left(\frac{1}{\eta} - 1 \right) \frac{1}{g_c(0)}, \quad (5.10)$$

Chapter 5. The Formation of a Receptor Cluster Depletion Zone

where $g(0)$, is the peak of the normalized c.f. given in Eq.(3.1). Finally the un-normalized rotationally averaged c.f. is obtained by multiplying the normalized c.f. $g(r)$, given in Eq.(3.1) by the scaling constant C

$$g_N(r) = \left(\frac{1}{\eta} - 1 \right) \frac{g_c(r)}{g_c(0)}. \quad (5.11)$$

To verify Eq.(5.11), test images of randomly distributed hard disks with uniform intensity were created in MATLAB using the DIPimage toolbox. The intensity c.f. of each test image was calculated by Fourier transform methods and rotationally averaged. Figure 5.5 depicts the simulated rotationally averaged c.f. $g_N(r)$, (open circles) for two test images with $R_c = 8$ pixel, $w = 300$ pixel, $\eta = 0.05$ (Fig. 5.5A), and $\eta = 0.30$ (Fig. 5.5B). Using these parameters, the theoretical intensity c.f. obtained from Eq.(5.11) (solid line) was compared to the directly computed c.f. for both test images. The theoretical c.f. fits the simulated data quite well, validating the developed theory. Small deviations between simulation and theory may be attributed to the finite size and pixelation of the image, the analytic approximation of the pair correlation function, and the numerical implementation of the Bessel transforms.

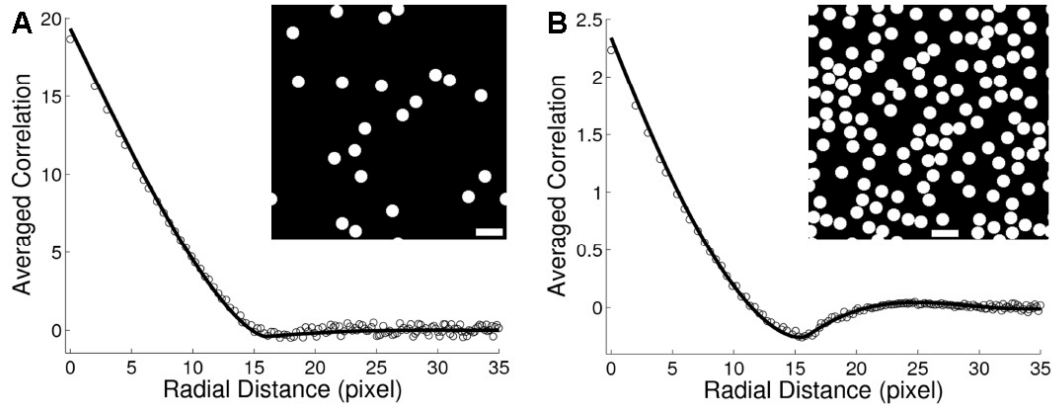


Figure 5.5: Rotationally averaged spatial correlation function of two simulated distributions of hard disks with uniform intensity (open circles) compared to the theoretical intensity correlation function given by Eq.(5.11) (solid line) for $R_c = 8$ pixel, $w = 300$ pixel, $\eta = 0.05$ ($N = 22$) in (A) and $\eta = 0.30$ ($N = 134$) in (B). Small insets depict the two spatially autocorrelated images. Taken from Ref. [39]. Bar represents 32 pixels.

5.3.2 Comparison to cluster test image

Figure 5.5 showed that the developed algorithm fits a simulated image of randomly distributed hard disks quite well. Next, we want to apply the algorithm to a test c.f. of randomly distributed disks of uniform intensity $I_c = 1$ inside a circle, which outlines the cell-substrate contact area. The area outside the circle is filled with the mean of the cell interior, see inset of Fig. 5.6. The radially averaged correlation function of the test image obtained from Fourier transform methods was fit to

$$g(r) = A g_c(r; R_c, \rho), \quad (5.12)$$

where the amplitude A , the disk radius R_c , and the number density of disk ρ are free parameters. Figure 5.6 compares the test correlation function (line) to the best fit of Eq.(5.12) (open circles). Equation (5.12) fits the test c.f. very well. Both, the best fit disk radius R_c and cluster density ρ were within 4% of the test image parameters.

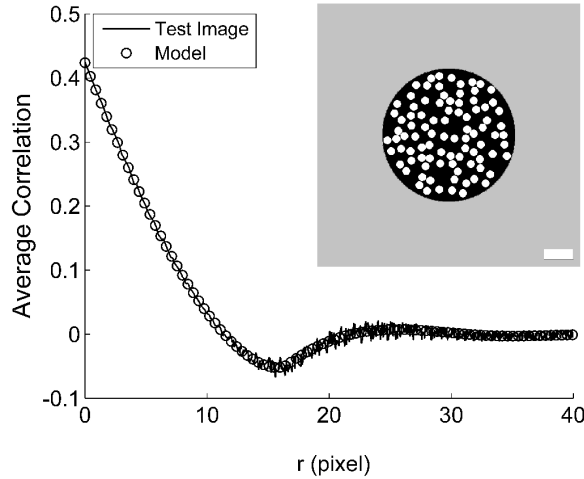


Figure 5.6: Rotationally averaged correlation function of test image shown in inset compared to a three parameter fit of Eq.(5.12). Bar represents 60 pixel and the cluster has uniform intensity $I_c = 1$.

5.4 Rotational correlation function of a depletion zone

A model for the radial c.f. of a depletion zone, i.e. a ring of uniform intensity, where the intensity bounded by the inner radius is set to zero and the intensity outside the outer radius is a constant (see inset Fig. 5.7), was obtained also from geometrical considerations. From the investigation of overlapping disks of different intensities, $I_p = 1$ and $I_d = 0$, we define the following list of parameters:

$$\begin{aligned}
 g'_{d1}(r) &= g_{auto}(r, R_p), \\
 g'_{d2}(r) &= \pi R_p^2, \\
 g'_{d3}(r) &= 2I_b \pi R_p^2, \\
 g'_{d4}(r) &= 2I_b [\pi R_p^2 - g_{cross}(r, R_d, R_p)], \\
 g'_{d5}(r) &= I_b^2 [w^2 + g_{auto}(r, R_d) - 2\pi R_d^2], \\
 g'_{d6}(r) &= I_b^2 (r_{\max}^2 - 2\pi R_d^2), \\
 g'_{d7}(r) &= I_b^2 (r_{\max}^2 - \pi R_d^2).
 \end{aligned} \tag{5.13}$$

Here, the autocorrelation g_{auto} is given in Eq.(5.3), the crosscorrelation of two disks of different radius g_{cross} is given in Eq.(A.12), and w^2 is the area of the correlated image. Depending on the difference of the radius of the depletion zone R_d and the radius of the large central patch R_p compared to twice the radius of the large patch, the above expressions can be combined to give the radial c.f. of a depletion zone for two different cases. For $2R_p \leq R_d - R_p$, the geometrical consideration gives

$$g'_d(r) = \begin{cases} g'_{d3}(r) + g'_{d6}(r), & r \geq 2R_d, \\ g'_{d3}(r) + g'_{d5}(r), & (R_d + R_p) \leq r < 2R_d, \\ g'_{d4}(r) + g'_{d5}(r), & (R_d - R_p) < r < (R_d + R_p), \\ g'_{d5}(r), & 2R_p \leq r \leq (R_d - R_p), \\ g'_{d1}(r) + g'_{d5}(r), & 0 < r < 2R_p, \\ g'_{d2}(r) + g'_{d7}(r), & r = 0, \end{cases} \tag{5.14}$$

Chapter 5. The Formation of a Receptor Cluster Depletion Zone

and for $R_d - R_p < 2R_d$, we obtain

$$g'_d(r) = \begin{cases} g'_{d3}(r) + g'_{d6}(r), & r \geq 2R_d, \\ g'_{d3}(r) + g'_{d5}(r), & (R_d + R_p) \leq r < 2R_d, \\ g'_{d4}(r) + g'_{d5}(r), & 2R_p < r < (R_d + R_p), \\ g'_{d1}(r) + g'_{d4}(r) + g'_{d5}(r), & (R_d - R_p) < r < 2R_p, \\ g'_{d1}(r) + g'_{d5}(r), & 0 < r \leq (R_d - R_p), \\ g'_{d2}(r) + g'_{d7}(r), & r = 0. \end{cases} \quad (5.15)$$

Using the expressions given in Eqs.(5.14) and (5.15), the normalized c.f. of a depletion zone is written as

$$g_d(r; R_p, R_d) = \frac{g'_d(r)}{w^2 \langle I \rangle^2} - 1 \quad (5.16)$$

Here, $\langle I \rangle$ is the mean image intensity

$$\langle I \rangle = \frac{1}{w^2} [I_b (w^2 - \pi R_d^2) + \pi R_p^2], \quad (5.17)$$

as it appears in Eq.(3.1).

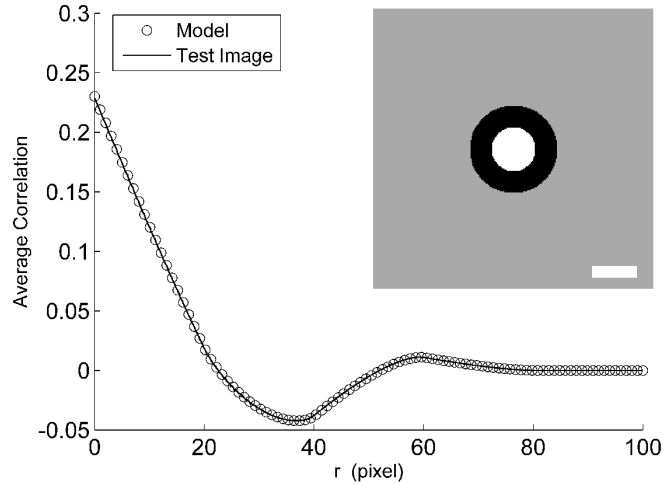


Figure 5.7: Rotationally averaged correlation function of test image shown in inset compared to the functional form of Eq.(5.16). Here, $R_p = 20$, $R_d = 40$, $I_p = 1$, $I_d = 0$, and $I_b = R_p^2/R_d^2$ were used to generate the test image as well as constants in Eq.(5.16). Bar represents 40 pixel.

Figure 5.7 compares the radial c.f. obtained from a test image of a depletion zone to the functional form obtained from Eq.(5.16). The zero parameter fit (open circles) is in excellent agreement with the c.f. computed from the image (line). Here, R_p , R_d , $I_p = 1$, $I_d = 0$, and $I_b = R_p^2/R_d^2$ used to generate the image, where the same parameters used to evaluate Eq.(5.16).

5.5 Image correlation of a receptor cluster depletion zone

As outlined above, our goal is to construct a model that consists of a simple superposition of the radial c.f. of randomly distributed hard disks given, Eq.(5.12), and the c.f. of a depletion zone, Eq.(5.16). This superposition is written as

$$g(r) = A g_c(r) + B g_d(r). \quad (5.18)$$

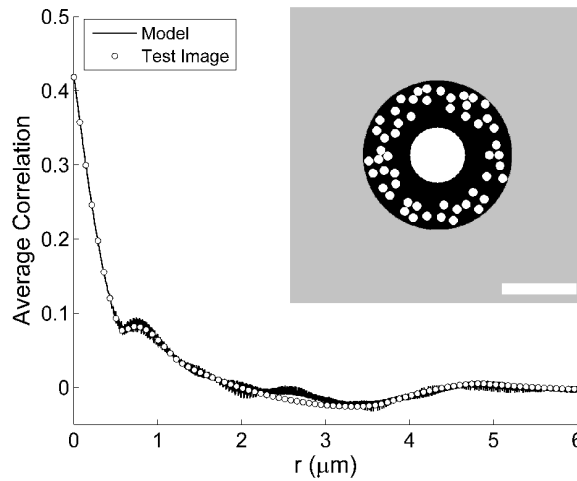


Figure 5.8: Rotationally averaged correlation function of test image of a receptor cluster depletion zone shown in inset compared to a four parameter fit obtained from Eq.(5.18). Here, $R_p = 1.9 \mu m$, $R_c = 0.4 \mu m$, $I_p = 1$, $I_d = 0$, $I_c = 0$, and I_b is the mean intensity inside the cell interior, which can be computed exactly. Parameter estimated obtained from the fit for ρ and R_d were within 10% of the expected value. Bar represents $5 \mu m$.

Here, A and B are free parameters, characterizing the strength of each contribution. As shown in Fig. 5.8, this simple superposition, describes the radial c.f. of a test image of disks and a depletion zone very well. The test image, depicted as inset in Fig. 5.8, was generated from parameters obtained from experiment, such as particle density and cluster radius. Here, the c.f. was fit to Eq.(5.18) with four free parameters: A , B , R_d , and ρ . As shown in the figure, the model fits test data very well. Moreover, the parameter estimates for the depletion radius R_d and the density of disk ρ were within 10% of the expected values.

5.6 Validation of the model by experimental data

We have shown above that our mathematical model fits a test c.f. of a receptor cluster depletion zone quite well. Next, the model was fit to actual experimental data. Figure 5.9 depicts a rotationally averaged c.f. of a thresholded RBL cell TIRF image collected ~ 2 min after cell-substrate contact. The thresholded image was obtained by combining a global and adaptive thresholding algorithm as outlined in section 2.10 with a window size

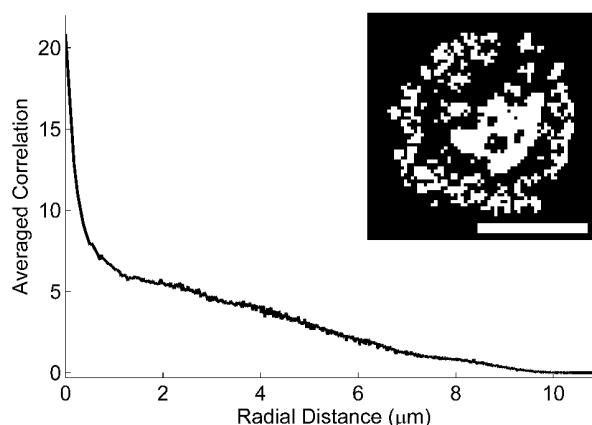


Figure 5.9: Rotationally averaged correlation function of thresholded RBL cell pipette-pressed onto a POPC bilayer with 25 mole % DNP-lipid after 140 s of initial cell-substrate contact. Inset shows corresponding thresholded TIRF image. Bar represents 5 μm .

Chapter 5. The Formation of a Receptor Cluster Depletion Zone

of $n = 5$ and weight $k = 0.05$. Looking at the figure's inset, it is apparent that there is a depletion of receptor clusters around the big central patch. However, the averaged c.f. does not depict a dip and our simple model of a receptor cluster depletion zone cannot explain the experimental data. It is important to note that the absence of a dip is observed also in the c.f. of the corresponding un-thresholded image. Therefore, we believe that the disappearance of the dip is due to the rotational average of asymmetric receptor clusters and patches. Since our simple depletion zone model was constructed from a single size population of circular clusters and a single circular patch, it cannot reproduce the experimental correlation function.

We sought a different analysis method to confirm and quantify the depletion zone. Cluster density was computed as a function of distance $\Delta x = 2 \text{ pixel}$ or $\Delta x = 350 \text{ nm}$ from the central patch as depicted in Fig. 5.10. This quantitative measure was obtained by utilizing the DIPImage pixel *dilation* function, where the boundary of the central patch

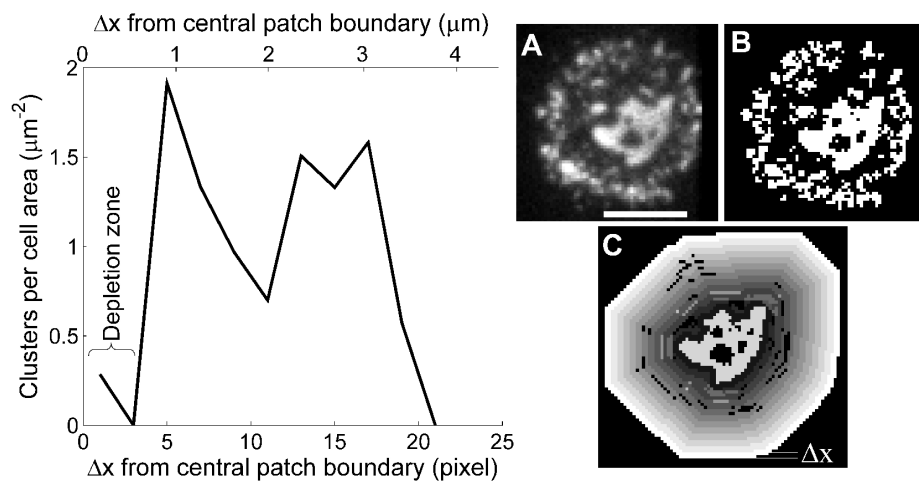


Figure 5.10: Receptor clusters per cell area as a function of dilated distance Δx in pixel (bottom scale) and μm (top scale) from the large central cluster boundary. Inset (A) depicts a TIRF image of a pipette-pressed RBL cell onto a POPC bilayer with 25 mole % DNP-Cap PE after 140 s of initial cell-substrate contact. Bar represents $5 \mu\text{m}$. (B) depicts the TIRF image after a combined threshold algorithm based on a global and adaptive thresholding algorithm. (C) shows individual layers of width $\Delta x = 2 \text{ pixel}$ or 350 nm .

Chapter 5. The Formation of a Receptor Cluster Depletion Zone

was dilated in steps of size Δx as shown in inset C of Fig. 5.10. In each layer of width Δx , the number of clusters per cell-substrate contact area was computed, clearly indicating a receptor cluster depletion zone for $\Delta x < 5$ pixel or $\Delta x < 900$ nm. As expected, outside the contact area, $\Delta x > 20$ pixel or $\Delta x > 3.6 \mu\text{m}$, cluster density goes to zero.

5.7 Concluding Remarks

In this chapter, we develop a mathematical model of a receptor cluster depletion zone, which is observed during the central Fc ϵ RI receptor patch formation, when mast cells are in contact with a fluid, monovalent ligand-presenting bilayer. The intensity autocorrelation of a RBL cell TIRF image depicting an apparent cluster depletion zone as a dip in the c.f. as shown in section 5.2. Based on this observation, a simple model of this c.f. function was developed.

The model introduced in section 5.2.1, which we believe to be the simplest possible one, is initially described by seven parameters, namely the cluster radius, large patch radius, depletion zone radius, cluster intensity, patch intensity, depletion zone intensity, and background intensity. In this model the large patch always forms in the cell center as suggested by experimental observations. After applying a thresholding algorithm to RBL cell TIRF images, this set of free parameters was reduced to four. Moreover, the background intensity can be computed exactly, which results in only three free parameters in the model. The theoretical intensity c.f. was derived from geometric considerations and based on a superposition of two individual correlation functions. The first c.f. for randomly distributed hard disks with a top-hat intensity profile of one was derived in section 5.3 and the second describing a depletion zone in section 5.4. Both c.f.s were validated by test images. In section 5.5, these two correlation functions were combined in a superposition, adding two additional parameters to quantify the amplitude of each contribution, increasing the total number of free parameters in the final model to five. This superposition was validated with

Chapter 5. The Formation of a Receptor Cluster Depletion Zone

a test image, showing that the theoretical c.f. followed the c.f. of a cluster depletion zone test image quite well. Finally, in section 5.6, a rotationally averaged c.f. of a thresholded RBL cell TIRF image was computed. From a cluster density analysis it was verified that a receptor cluster depletion zone was present. However, the corresponding rotationally averaged c.f. did not exhibit a dip and therefore our mathematical model did not explain the data. We believe that the disappearance of the dip is due to the rotational average of asymmetric receptor cluster and patches, which were not included in our model. Therefore, a possible generalized model of a cluster depletion zone may incorporate a distribution of cluster sizes.

Finally, it is worth noting that a geometric model of the intensity correlation function, which can be fit to individual intensity autocorrelated RBL cell TIRF images at different time points, can give only some insight into the dynamics of receptor cluster coalescence. Moreover, this approach is computationally expensive due to the long list of free parameters. Since our goal is to obtain fundamental understanding of receptor cluster coalescence kinetics, it is essential to develop a full coalescence model. In the remainder of this dissertation, we will develop such a theory.

Chapter 6

Structure of our Coalescence Theory

6.1 Introduction

The role of this chapter is to make the crossover from the experimental to the theoretical part of this thesis. Here starts the dialog between experimental results obtained so far and the construction of a theory of receptor cluster coalescence. In the first section of the present chapter, we discuss existing theoretical models on the formation of the immunological synapse and the kinetics of nucleation. We point out that existing models cannot be directly applied to experimental observations presented in this dissertation. This pushes us to develop a new theory of coalescence, which will, naturally, also shed some new light on the subject of nucleation. The second section of this chapter gives a prescription on how to construct a coalescence theory. The prescription will be elaborated on in subsequent chapters discussing individual elements in more detail.

6.2 The need to develop a new coalescence theory

Before we present the structure of our coalescence theory we review existing literature of two different subjects sharing the problem of particle aggregation and discuss how they motivate us to develop the presented theory of coalescence.

6.2.1 Modeling the immunological synapse

As mentioned earlier in section 1.2, two other immune cells, namely T cells and B cells, form a big central patch called immunological synapse [12, 9], when in contact with a ligand presenting bilayer. Since the immunological synapse is thought to play a critical role in immune cell signaling between contacting cells [12], the kinetics of synapse formation in T cells [104, 105, 106] and B cells [107, 108, 109] has been modeled extensively. However, nothing is known about the kinetics of synapse formation in mast cells. Therefore, investigating the kinetics of mast cell receptor cluster coalescence in detail may be important in understanding mast cell signaling.

Even though there has been an extensive effort in modeling the synapse formation in other immune cells, our experimental observations presented in this thesis motivate us to develop a new coalescence theory. Synapse formation models for B cells and T cells are based on two different receptor-ligand pairs which have different length scales in the bound configuration [104, 105, 106, 107, 108, 109]. In our experiments however, we only have one receptor-ligand pair. Moreover, T cell [75] and B cell receptor [109] clusters undergo biased diffusion towards the cell center. This directed transport of receptor molecules has been shown recently to be a possible formation mechanism for the B cell synapse [109]. Since in our experiments the biased motion component of receptor cluster transport had no preferred radial direction, centripetal motion cannot be an underlying mechanism of the central receptor patch formation in mast cells. Moreover, we have shown that IgE-receptor

Chapter 6. Structure of our Coalescence Theory

clusters, which form at cell protrusions, seem to move as an entity to form the big central patch. Hence, in our coalescence theory we will start with preformed randomly distributed receptor clusters (see section 3.3) rather than individual receptor-ligand pairs as done for T cells and B cells. These major differences require that we develop a new coalescence theory to address mast cell synapse formation kinetics. It is also worth noting that most of T cell and B cell synapse formation models are based on Monte Carlo simulations [105, 107, 108, 106, 109] or numerical solutions of coupled reaction-diffusion equations [104] on the basis of a finite difference scheme. This makes the model of receptor coalescence very complex and hard to implement readily. Hence our goal is to develop a theory of coalescence simple enough to be understood physically, and implemented explicitly, yet powerful enough to be applied readily to any dimension and nature of particle motion.

6.2.2 Kinetic theory of nucleation

A field of research which is different from the field explored in this thesis but is concerned with the problem of particle aggregation is the field of nucleation and growth of thin films [110, 111, 112, 113, 114]. The general concept of nucleation is the creation of a new phase from a metastable state made out of germs, or embryos, of the new phase. Germs may be viewed as small, transient clusters of the new phase. Continuous fluctuations in the sizes of these clusters, via the incorporation of additional molecules and the detachment of others, may result in a germ growing large enough to become stable and form a nucleus of critical size. Nucleation of a new phase starts when its growth becomes overwhelmingly more probable than decay. When germs are viewed as isolated clusters dispersed in the parent phase (requires a greater degree of metastability) one refers to homogeneous nucleation. Germs that are attached to some pre-existing structure, most likely a solid surface, increase their likelihood to reach stability and undergo heterogeneous nucleation.

Chapter 6. Structure of our Coalescence Theory

The kinetic description of nucleation and growth can be divided into three stages [114]. The first stage is called nucleation stage during which a population of clusters of various sizes, typically nanoscopically small, is created. In this stage, the cluster concentration is relatively low and the clusters grow and decay by gaining and losing monomers only. The second stage, in which our own interested lies, is the coalescence stage in which two or more smaller clusters merge into a bigger cluster. The last stage is called aging stage in which the newly formed disperse phase occurs either by continuing coalescence between already formed clusters or by decay of the smaller clusters by loss of monomers which feed the growth of the larger clusters (Ostwald-ripening).

A kinetic theory of nucleation is presented in a book on nucleation by Kashchiev [114]. He introduces a Master equation of one-component nucleation

$$\frac{dZ_n(t)}{dt} = \sum_{m=1}^{M(t)} [f_{mn}(t)Z_m(t) - f_{nm}(t)Z_n(t)] + K_n(t) - L_n(t), \quad (6.1)$$

where $Z_n(t)$ is the concentration of cluster size n at time t , f_{nm} is the transition frequency from n - to m -sized clusters, and f_{mn} is the transition frequency from m - to n -sized clusters. The total number of molecules on the substrate at time t is $M(t)$ and can be set as a constant if the total number of molecules does not change in time. Moreover, as a result of mass conservation, $Z_n(t)$ and $M_n(t)$ are connected by the relation

$$\sum_{n=1}^{M(t)} nZ_n(t) = M(t)/V,$$

where V is the volume of the system. It should be replaced by area of the substrate in the case of heterogeneous nucleation. In Eq.(6.1), K_n is the rate of cluster appearance and L_n is the rate of cluster disappearance. Hence Eq.(6.1) is nearly tautological. The concentration of n -sized clusters is fed by K_n and goes away by L_n and can increase or decrease by transitioning at certain rates from and to clusters of different size. To solve this equation set of ordinary differential equations, one needs to know the initial cluster size distribution and the transition rates. The initial cluster size distribution and size distribution over time

Chapter 6. Structure of our Coalescence Theory

can be obtained in principle from experiments. The transition rates however, have to be calculated. The computational difficulty can be severe if these rates are not constant (the simplest situation) or do not at least have a linear dependence.

Depending on the specifics of the problem, finding the attachment rates f_{nm} and detachment rates f_{mn} of multimers can be very difficult. To simplify the problem, one might consider ignoring the detachment rate and assuming that only monomers attach at a rate f_n , provided that such a simplification is physically warranted. For the simplest problem of monomers attaching to a stationary absorber one can solve for f_n by following Smoluchowski as realized by Ruckenstein and Pulvermacher [110]. For volume-diffusion controlled attachment, Smoluchowski [115, 116] considered that a stationary particle acting as a perfect absorber with radius R at the origin of a medium of infinite extent in which a number of noninteracting Brownian point particles are uniformly distributed at time $t = 0$. He sought a solution of the three-dimensional diffusion equation for the monomer concentration $Z(r, t)$ with absorbing boundary condition at $r = R$ to determine the rate f at which diffusing particles coalesce with a stationary particle

$$f(R, t) = 4\pi R^2 D \frac{\partial Z(r, t)}{\partial r} \Big|_{r=R}. \quad (6.2)$$

Here Eq.(6.2) defines the rate as product of the surface area of the spherical absorbing particle $4\pi R^2$ and the flux of its surrounding particles $D \frac{\partial Z(r, t)}{\partial r}$. It is clear that Smoluchowski's aim was to describe diffusion-limited coalescence. He did not include the time it takes for the particles to merge when they are in contact (reaction rate). Ruckenstein and Pulvermacher [110] included this reaction rate in the transition rate by replacing the perfectly absorbing boundary condition at $r = R$ with a radiative for time $t > 0$

$$\alpha Z(r, t) = D \frac{\partial Z(r, t)}{\partial r}, \quad (6.3)$$

where α is the reaction rate constant for merging. It turns out the expression for the flux which includes the diffusion as well as merging process is rather involved and that Ruckenstein and Pulvermacher as well as Kashchiev simplify the expression by looking at

Chapter 6. Structure of our Coalescence Theory

two limiting cases. The process under consideration is purely reaction controlled ($\alpha < D$) or the process is diffusion controlled ($\alpha \rightarrow \infty$). In both cases the transition frequency simplifies and is given by a constant dependent only on α or D , respectively. Hence, Kashchiev [114] simply multiples Smoluchowski's reaction rate, Eq.(6.2) by a merging probability γ

$$f(R, t) = \gamma 4\pi R^2 D \frac{\partial Z(r, t)}{\partial r} \Big|_{r=R}. \quad (6.4)$$

to account for a non-instantaneous reaction.

This prescription used by Kashchiev involving a mere product of probabilities cannot be correct in general. Indeed in a series of papers by Kenkre and collaborators [23] the related general problem of reaction-diffusion which is not merely motion-limited has been analyzed in the context of exciton transport and sensitized luminescence. For instance, Ref. [26] shows that the exciton absorption time is the sum of the time it takes to move to the trap and the time it takes to get captured. Hence the transition rate for this problem is a sum of probabilities. And Ref. [28] relates the full situation in the context of sensitized luminescence. While those considerations do not disprove Kashchiev's prescription, they certainly motivate the need to re-examine this problem.

Kashchiev's reaction rate is further unsatisfactory in the nature of ignoring the effect produced on the diffusion field by the moving boundary of the stationary absorber. This mechanism makes these kind of problems extremely difficult and hence obtaining exact results almost impossible. A small collection of moving-boundary problems, which can be solved exactly, can be found in Refs. [117, 118, 119]. It is noteworthy that it has been long recognized that the motion of the moving boundary must perturb the diffusion field and hence several attempts have been made to model this effect [120, 121, 118]. Our coalescence theory to be described in this dissertation also focuses on this problem.

6.3 Modeling particle coalescence

In the previous section, we motivated the need to build a new theory of coalescence. Our theory is constructed as follows.

We first address a simplified problem. We start with a certain amount of material that is divided into two parts. The first part is made into a disk of uniform density and radius $R(0)$ placed with its center at the origin. This disk represents the nucleation site of the central receptor patch observed in our experiments. The initial disk radius is given by experimental observations outlined in section 3.2.2. The rest of the material of which the amount is $Q(0)$ is considered to be powdered and sprinkled as point particles throughout the two-dimensional space outside the disk with a given known distribution. At a later stage the finite size of these particles will be incorporated. As time proceeds, the point particles move with any type of motion, e.g. diffusive or biased, until they touch the edge of the disk. With non-infinite probability (finite capture rate) the particles are absorbed into the disk. The process of the absorption makes the disk attain a larger radius. In other words, we make the simplifying assumption that the shape of the disk does not change as a result of an assumed process which instantaneously distributes the absorbed material over the entire disk. This is an important ingredient, which sets our coalescence theory apart from the subject of diffusion-limited aggregation [122, 123], where finger-like structures develop. The purpose of the rest of the study is then to calculate the evolution of $R(t)$. For simplicity at this stage of the calculation, the point particles do not absorb one another, although in the experiments described in the earlier chapters the contrary is certainly observed.

Clearly our simplified study may be formulated as a trapping problem with a trap whose location (boundary) changes dynamically. The analysis proceeds by solving the appropriate trapping problem and obtaining an expression for $Q(t)$ (total survival probability at time t) the amount of the sprinkled material not yet absorbed into the central disk.

Chapter 6. Structure of our Coalescence Theory

The standard defect technique [22, 23, 24, 25, 26, 27, 28, 29] is therefore employed without modification. The $Q(t)$ thus computed is actually dependent on both t and the radius R so it is best expressed as $Q(t; R)$. In a self-consistent way, from $Q(t; R)$ one obtains the rate $dQ(t; R)/dt$ of particle absorption which is also the rate at which the trap increases resulting in a new disk radius. It becomes clear that this approach is of feedback type, iterating until self-consistency is achieved.

Finally, from the above paragraphs the following three steps emerge as basis for our coalescence theory. Each of these steps is discussed in detail in the next three chapters:

Chapter 7 develops the basis of the theory. It applies the standard defect technique to solve stationary trapping problems with a non-infinite capture rate in d-dimensions, and collects some exact solutions.

Chapter 8 presents a validity of an adiabatic approximation for moving boundary problems. In this approximation, the time-dependence of a moving boundary is explicitly assigning into the static problem, which we know how to solve exactly by applying tools from chapter 7.

Chapter 9 discusses the final step in constructing our coalescence theory, in which the time dependence of the moving boundary is not prescribed but obtained through a feedback idea. The proposed calculation relates the growing trap radius to the time-dependent particle survival probability, obtained from the static result, in a self-consistent way.

Chapter 7

Repository of Exact Solutions for Stationary Trapping Problems

7.1 Introduction

In this chapter, we outline the first step in modeling our coalescence theory. It focuses on the subject of trapping or absorption processes occurring with non-infinite capture rates in random walks or diffusion processes and is based on the defect technique developed by Kenkre and collaborators [22, 23, 24, 25, 26, 27, 28, 29] to study exciton motion in molecular crystals. In these systems, particles annihilate at a finite rate on contact and one is interested in the time-dependent particle survival probability. Obtaining analytic expressions for such a survival probability forms the basis of our coalescence theory.

Due to the wide applicability of reaction-diffusion scenarios, this subject has produced many hundreds of published articles in various fields of research. While attempting to review this enormous body of literature, it became evident that there exist many exact results for the kinetics of *instantaneous* absorption [124, 125, 126], whereas a generalization to

Chapter 7. Repository of Exact Solutions for Stationary Trapping Problems

include finite reaction [127, 128, 129] has not received as much attention. This fact might be responsible for a relatively recent claim by Leyvraz [130] that an exact solution can only be obtained when assuming instantaneous reaction. A similar statement that a generalization to include finite reaction makes the problem perhaps impossible to solve, was made earlier by Zhong and ben-Avraham [128].

Finding these statements in literature was surprising to us, since the Montroll defect technique [131] for non-infinite trapping problems was developed three decades before Leyvraz's statement. Therefore, due to this misconception and our experimentally motivated interest in higher dimensional non-infinite trapping, we decided to reinvestigate stationary trapping problems, following the formalism of the defect technique [23]. A brief review of this method, outlining the derivation of a discrete trapping prescription, is given in section 7.2. Using this prescription, we were able to derive some new results on the one-dimensional lattice in section 7.3. After applying the continuum limit to the discrete prescription in section 7.4, the discrete formalism gives a continuous space trapping prescription also derived independently by Szabo et al. [132]. We use the continuous space trapping prescription to solve numerous problems in one-, two-, and three-dimensions in sections 7.5, 7.6, and 7.7, respectively. Some of our results can be found in literature, but others we believe to be new. Therefore, this chapter serves as a repository of exact solutions of stationary trapping problems.

After collecting solutions to trapping problems, we address, in the last part of this chapter, the connection of sink problems to boundary value problems. In section 7.8 we show that expressions obtained by these two methods are equivalent only if the appropriate diffusion propagator in the absence of the trapping process is translationally invariant.

7.2 Brief review of standard defect technique

In this section, we review the standard defect technique. The notation and development follow the discussion given by Kenkre and collaborators [22, 23, 24, 25, 26, 27, 28, 29] and used in a number of applications to molecular crystals. In such systems a particle may occupy a site m in a discrete space of arbitrary dimensions with probability $P_m(t)$ at time t and move in some way, e.g., with or without translational invariance. A standard Master equation for $P_m(t)$ is

$$\frac{dP_m(t)}{dt} = \text{motion terms} - C_d \sum_r' \delta_{m,r} P_m(t), \quad (7.1)$$

where the motion terms are linear in probabilities, C_d is the d-dimensional reaction rate, and sites r denote the reaction locations at which the particle disappears. Here $\delta_{m,r}$ represents the Kronecker delta function and the prime denotes a sum over all reaction locations at which one produces trapping or coalescence or similar effects. If the particles hops via nearest neighbor rates F in one-dimension the motion terms could be of the form $F(P_{m+1} + P_{m-1} - 2P_m)$.

The Master equation given in Eq.(7.1) can be transformed into Laplace domain

$$\tilde{P}_m(\epsilon) = \tilde{\eta}_m(\epsilon) - C_d \sum_r' \tilde{\Psi}_{m,r}(\epsilon) \tilde{P}_r(\epsilon), \quad (7.2)$$

where tilde denote Laplace transforms and ϵ the Laplace variable. Ψ is the probability propagator of the homogeneous part of Eq.(7.1) and η is the homogeneous solution in the absence of the trap i.e. $C_d = 0$. The interest in the standard defect technique is to calculate the total survival probability $Q(t) = \sum_m P_m(t)$. To obtain this quantity one notes that the sum over all m over both $\tilde{\eta}_m$ and $\tilde{\Psi}_{m,r}$ gives $1/\epsilon$ since the probability sum over all sites of the homogeneous solution is always one in the domain. Therefore, in Laplace domain the survival probability is given as

$$\tilde{Q}(\epsilon) = \frac{1}{\epsilon} \left[1 - C_d \sum_r' \tilde{P}_r(\epsilon) \right]. \quad (7.3)$$

Chapter 7. Repository of Exact Solutions for Stationary Trapping Problems

Instead of the total survival probability one can also compute the rate of disappearance, which is in time domain minus the total probability at the trapping sites

$$\frac{dQ(t)}{dt} = -C_d \sum_r P_r(t). \quad (7.4)$$

This expression can be also obtained from Eq.(7.1) by summing over m . The total probability at the starting site given in Eq.(7.3) has to be calculated in the *presence* of the trapping sites. Let us define its counterpart in the absence of the trapping sites i.e. $C_d = 0$ and the same initial conditions

$$\left(\sum_r P_r(t) \right)_0$$

and rewrite Eq.(7.4) as

$$\frac{dQ(t)}{dt} = - \int_0^t dt' \mathcal{M}(t-t') \left(\sum_r P_r(t) \right)_0. \quad (7.5)$$

The important quantity in Eq.(7.5) is the memory $\mathcal{M}(t)$. In the limit of small C_d it is simply $C_d \delta(t)$ so that we have a simplified form of Eq.(7.4) with $\left(\sum_r P_r(t) \right)_0$ in place of $\sum_r P_r(t)$. This is the capture-limited case. In the opposite limit of small motion (large C_d) the memory turns out to be more complicated and determined by motion parameters. That is the motion-limited case.

In order to understand these last statements accurately, we substitute $m = s$ where s is the trap site into Eq.(7.2) and sum over trap locations s

$$\sum_s \tilde{P}_s(\epsilon) = \sum_s \tilde{\eta}_s(\epsilon) - C_d \sum_s \sum_r \tilde{\Psi}_{s,r} \tilde{P}_r(\epsilon). \quad (7.6)$$

The quantity

$$\mathbf{v}_r = \sum_s \Psi_{s,r} \quad (7.7)$$

is the sum of the probability propagators from one trap site r to all trap sites s . While this expression actually does depend on the site r , that dependence will disappear in highly

Chapter 7. Repository of Exact Solutions for Stationary Trapping Problems

symmetrical situations or in an averaging sense. We are now going to assume that the r -dependence has been removed either exactly or in an averaging sense. One can for instance calculate an average over all trap sites r of v_r and call it v (independent of r). After such an assumption/approximation we can write the actual $\sum_r' \tilde{P}_r$ in terms of the homogeneous counterpart $\left(\sum_r' \tilde{P}_r\right)_0$, which is precisely $\sum_r' \tilde{\eta}_r$

$$\sum_r' \tilde{P}_r(\epsilon) = \frac{\sum_r' \tilde{\eta}_r}{1 + C_d \tilde{v}(\epsilon)}. \quad (7.8)$$

At once we get the above mentioned Eq.(7.5) where the memory is precisely given by

$$\tilde{\mathcal{M}}(\epsilon) = \frac{1}{1/C_d + \tilde{v}(\epsilon)}. \quad (7.9)$$

We see here that generally the memory is of a form compatible with the concept of a sum of the capture time and a motion time. This result is in contradiction to Kashchiev's form of the reaction rate, which involves a mere product of probabilities, see section 6.2.2 for details. Much discussion has occurred in the exciton field in molecular crystals about the consequence of the form of Eq.(7.9) [23, 29]. In the motion limit, C_d is large enough relative to the motion term and $1/C_d$ can be neglected to give $\tilde{\mathcal{M}}(\epsilon) = 1/\tilde{v}(\epsilon)$ whereas in the capture limit $\tilde{\mathcal{M}}(\epsilon) = C_d$.

Finally, a general prescription for the total survival probability in Laplace domain and discrete space is therefore

$$\tilde{Q}(\epsilon) = \frac{1}{\epsilon} \left[1 - \frac{\sum_r' \tilde{\eta}_r}{1/C_d + \tilde{v}(\epsilon)} \right]. \quad (7.10)$$

The key quantity to calculate is the v -function, which is the (ensemble average of) the sum of propagators of the homogeneous system (in absence of traps) from one trap location to all others. The idea of the v -function was first put forward by Kenkre [27] where it was also calculated for periodic one-dimensional array of trapping sites with nearest-neighbor

motion rates F . It was used in luminescence calculations for molecular crystals [28] for arbitrary kind of motion and different placements of trap sites and in other contexts such as of cellular membranes [31].

7.3 A single stationary trap on a lattice

In this section we solve for $Q(t)$ of a particle initially placed at site a on a one-dimensional lattice and a single trap at the origin by applying the prescription given in Eq.(7.10). In this case, there is only a single trap and the prescription becomes

$$\tilde{Q}(\epsilon) = \frac{1}{\epsilon} \left[1 - \frac{\tilde{\eta}_a}{1/C + \tilde{v}(\epsilon)} \right], \quad (7.11)$$

where $\eta_a = \Psi_{a,0}$ and $v = \Psi_{0,0}$, the homogeneous solution starting at site a in the absence of the trap and the self-propagator, respectively. The discrete space self-propagator for this problem is well known [27] and given as

$$\Psi_m(t) = I_m(2Ft) \exp(-2Ft), \quad (7.12)$$

where I_m is the modified Bessel function of the first kind. Next, the Laplace transform of both propagators can be obtained from a table of Laplace transforms [133]

$$\begin{aligned} \tilde{v}(\epsilon) &= \frac{1}{\sqrt{(\epsilon+2F)^2 - 4F^2}}, \\ \tilde{\eta}_a(\epsilon) &= \frac{(2F)^a}{\sqrt{(\epsilon^2+2F)^2 (2F)^2} \left[\epsilon+2F + \sqrt{(\epsilon^2+2F)^2 - (2F)^2} \right]^a}. \end{aligned}$$

After using the following substitution $\cosh \zeta = 1 + \epsilon/(2F)$ [27], Eq.(7.11) becomes

$$\tilde{Q}(\epsilon) = \frac{1}{\epsilon} \left[1 - \frac{\exp(-\zeta a)}{2F \sinh \zeta / C + 1} \right], \quad (7.13)$$

where $\sinh \zeta = \sqrt{4F\epsilon + \epsilon^2}/(2F)$. Equation (7.13) is the exact solution in Laplace domain and can be inverted for the case of perfect absorption ($C = \infty$), see section 7.3.1. For imperfect absorption however, an analytic solution in time domain cannot be obtained (see section 7.3.2). However, a numerical Laplace inversion, as outlined in Appendix C, can be applied to obtain the functional form in time domain.

7.3.1 Perfect absorption

For instantaneous reaction $C \rightarrow \infty$ and Eq.(7.13) becomes

$$\tilde{Q}(\epsilon) = \frac{1}{\epsilon} \left[1 - e^{-\zeta a} \right]. \quad (7.14)$$

To invert this expression the exponential term is rewritten using $\cosh \zeta = 1 + \frac{\epsilon}{2F}$ and $\sinh \zeta = \frac{\sqrt{4F\epsilon + \epsilon^2}}{2F}$ as

$$e^{-\zeta a} = \frac{(2F)^a}{\left(2F + \epsilon + \sqrt{4F\epsilon + \epsilon^2} \right)^a} = \frac{p^a}{\left[s + \sqrt{s^2 - p^2} \right]^a},$$

where $s = \epsilon + 2F$, $p = 2F$ to obtain

$$\tilde{Q}(s) = \frac{1}{s-p} - \frac{\sqrt{s+p}}{\sqrt{s-p}} \frac{p^a}{\sqrt{s^2 - p^2} \left[s + \sqrt{s^2 - p^2} \right]^a}. \quad (7.15)$$

This expression can be Laplace inverted, represented by L_ϵ^{-1} , by applying the convolution theorem

$$L_\epsilon^{-1} \{ g(\epsilon) f(\epsilon) \} = \int_0^t g(t-\tau) f(\tau) d\tau,$$

to the second term on the right-hand side of Eq.(7.15) to give

$$Q(t) = 1 - e^{-pt} I_a(pt) - p e^{-pt} \int_0^t [I_0(pt - p\tau) + I_1(pt - p\tau)] I_a(p\tau) d\tau \quad (7.16)$$

Equation (7.16) was obtained by Laplace transforming $\sqrt{s+p}/\sqrt{s-p}$ and

$$\frac{p^a}{\sqrt{s^2 - p^2} \left[s + \sqrt{s^2 - p^2} \right]^a}$$

(see Appendix B), noting that $s = \epsilon + 2F$ introduces a shift, which corresponds to a multiplication of an exponential decay. The integral in Eq.(7.16) can be expressed in terms of an infinite sum of Bessel functions of the first kind, J_m , by using the identity [134] $I_\nu(x) = i^{-\nu} J_\nu(ix)$ with [135]

$$\int_0^Z J_\mu(\eta) J_\nu(Z-\eta) d\eta = 2 \sum_{k=0}^{\infty} (-1)^k J_{\mu+\nu+2k+1}(Z),$$

Chapter 7. Repository of Exact Solutions for Stationary Trapping Problems

to obtain

$$Q(t) = 1 - i^{-a} \exp(-pt) J_a(ipt) - \exp(-pt) \left[\frac{2}{i^{a+1}} \sum_{k=0}^{\infty} (-1)^k J_{1+a+2k}(ipt) + \frac{2}{i^{a+2}} \sum_{k=0}^{\infty} (-1)^k J_{2+a+2k}(ipt) \right]. \quad (7.17)$$

or

$$Q(t) = 1 - e^{-pt} \left[I_a(pt) - 2 \sum_{k=0}^{\infty} (-1)^k [I_{1+a+2k}(pt) + I_{2+a+2k}(pt)] \right] \quad (7.18)$$

by using [134] $J_\nu(x) = i^\nu I_\nu(-ix)$, where $p = 2F$. A similar expression of $1 - Q(t)$ was derived by Spouge [136].

However, as we will show below, Eq.(7.17) can be rewritten in terms of a finite sum of Bessel functions resulting in a new expression for the perfect absorber case. To obtain this expression, one has to use the following properties [134]

$$\begin{aligned} \cos x &= J_0(x) + 2 \sum_{n=1}^{\infty} (-1)^n J_{2n}(x), \\ \sin x &= 2 \sum_{n=0}^{\infty} (-1)^n J_{2n+1}(x), \end{aligned}$$

with $\cos(i2Ft) - i \sin(i2Ft) = \exp(2Ft)$. After some algebra one obtains for a random walker initially placed at site $a = 1, 2, 3$ and $a = 4$

$$Q(t) = e^{-2Ft} I_0(2Ft) + e^{-2Ft} \begin{cases} I_1(2Ft), a = 1 \\ 2I_1(2Ft) + I_2(2Ft), a = 2 \\ 2I_1(2Ft) + 2I_2(2Ft) + I_3(2Ft), a = 3 \\ 2I_1(2Ft) + 2I_2(2Ft) + 2I_3(2Ft) + I_4(2Ft), a = 4 \end{cases} \quad (7.19)$$

Looking at the expressions given in Eq.(7.19) shows that a pattern emerges and that Eq.(7.19) can be recast in the form of a finite sum of modified Bessel functions of the

first kind

$$Q(t) = e^{-2Ft} \left(I_0(2Ft) - I_a(2Ft) + 2 \sum_{n=1}^a I_n(2Ft) \right). \quad (7.20)$$

Equation (7.20) is a new expression and was validated by comparing its functional form to the numerical Laplace transform of Eq.(7.14). The numerical inversion algorithm is outlined in Appendix C. For the special case of a particle initially starting at lattice site $a = 1$, our expression reduces to

$$Q(t) = e^{-2Ft} [I_0(2Ft) + I_1(2Ft)], \quad (7.21)$$

and agrees with [136].

7.3.2 Imperfect absorption

Above we obtained an expression for the total survival probability in the case of perfect absorption. A more interesting and general case describes finite reaction. However, it will become clear from the next few paragraphs that this simple extension makes this problem difficult to solve.

At the beginning of this section we have derived an exact solution for finite trapping in Laplace domain, see Eq.(7.11). The rate of disappearance dQ/dt is given by the inverse Laplace transform of

$$-\frac{dQ(t)}{dt} = L_{\epsilon}^{-1} \left\{ \frac{\exp(-\zeta a)}{1 + \frac{2F}{C} \sinh(\zeta)} \right\}, \quad (7.22)$$

where $\sinh \zeta = \sqrt{4F\epsilon + \epsilon^2}/(2F)$. Here and in the remainder of the dissertation $L_{\epsilon}^{-1} \{ \}$ denotes the inverse Laplace transform. This expression can be rewritten in the following product form

$$-\frac{dQ(t)}{dt} = L_{\epsilon}^{-1} \left\{ \left(\frac{C}{C + \sqrt{u^2 - p^2}} \right) \left[\frac{u - \sqrt{u^2 - p^2}}{p} \right]^a \right\}, \quad (7.23)$$

Chapter 7. Repository of Exact Solutions for Stationary Trapping Problems

where $u = \varepsilon + 2F$ and $p = 2F$. After using the convolution theorem together with the appropriate inverse Laplace transforms (see Appendix B) and applying the shifting theorem one obtains an analytic expression involving definite integrals in time domain

$$\begin{aligned} -\frac{dQ(t)}{dt} = & Cae^{-2Ft} \int_0^t \left(\frac{1}{t-\tau} \right) I_a[2F(t-\tau)] e^{-C\tau} d\tau \\ & + 2FCae^{-2Ft} \int_0^t \left[\left(\frac{1}{t-\tau} \right) I_a[2F(t-\tau)] \int_0^\tau e^{-C\sqrt{\tau^2-w^2}} I_1(w) dw \right] d\tau. \end{aligned} \quad (7.24)$$

From the above result it is evident that the seemingly simple inclusion of a finite reaction rate makes the problem more difficult and an exact analytic solution seems not possible. Even though Eq.(7.24) can be evaluated numerically, it would be useful to obtain an analytic expression. However, an analytic expression can be obtained only in the limiting case of a high probability of reaction. In this case ζ as well as the reaction rate C are large and following exponential approximation [137]

$$\frac{1}{1 + \frac{2F}{C} \sinh(\zeta)} \rightarrow e^{-2F\zeta/C}$$

can be applied to Eq.(7.22) yielding

$$-\frac{dQ(t)}{dt} = L_\varepsilon^{-1} \left\{ e^{-\zeta(\varepsilon+2F/C)} \right\}. \quad (7.25)$$

This expression can be rewritten as

$$-\frac{dQ(t)}{dt} = L_\varepsilon^{-1} \left\{ \frac{p^{(a+2F/C)}}{\left[u + \sqrt{u^2 - p^2} \right]^{(a+2F/C)}} \right\} \quad (7.26)$$

and Laplace inverted exactly (see Appendix B) resulting in

$$-\frac{dQ(t)}{dt} = \frac{(a+2F/C)}{t} e^{-2Ft} I_{(a+2F/C)}(2Ft). \quad (7.27)$$

7.4 Obtaining a continuous prescription

In this section, we display the continuum limit of the above discrete formalism. If we start on a one-dimensional discrete lattice with a single stationary trap at site r and a particle hopping via nearest neighbor rates F between lattice sites, the starting equation, given in Eq.(7.1), would have the explicit form

$$\frac{dP_m}{dt} = F(P_{m+1} + P_{m-1} - 2P_m) - \delta_{m,r}CP_m, \quad (7.28)$$

where $\delta_{m,r}$ the Kronecker delta function and C is the capture rate. The continuum prescription is obtained by dividing Eq.(7.28) by the lattice constant a

$$\frac{d}{dt} \left(\frac{P_m}{a} \right) = Fa^2 \frac{\left(\frac{P_{m+1}-P_m}{a} + \frac{P_{m-1}-P_m}{a} \right)}{a^2} - aC \frac{\delta_{m,r}}{a} \frac{P_m}{a}, \quad (7.29)$$

and applying the limit [25, 31]

$$\begin{aligned} \lim_{a \rightarrow 0} (ma) &= x, \\ \lim_{a \rightarrow 0} (a) &= dx, \\ \lim_{a \rightarrow 0} (Fa^2) &= D, \\ \lim_{a \rightarrow 0} \left(\frac{P_m}{a} \right) &= P(x, t), \\ \lim_{a \rightarrow 0} (aC) &= C, \\ \lim_{a \rightarrow 0} \left(\frac{\delta_{m,r}}{a} \right) &= \delta(x - x_r), \end{aligned}$$

to obtain

$$\frac{\partial P(x, t)}{\partial t} = D \frac{\partial^2 P(x, t)}{\partial x^2} - C \delta(x - x_r) P(x, t). \quad (7.30)$$

Here x represents the one-dimensional space coordinate, D the particle diffusion constant, C the capture rate in units m/s , and $\delta(x - x_r)$ a Dirac delta function. Equation (7.30) is the one-dimensional diffusion equation with the addition of a trapping term. This result is expected when one applies the continuum limit directly to the discrete space Master

Chapter 7. Repository of Exact Solutions for Stationary Trapping Problems

equation [138, 139, 140]. It should be noticed that the simultaneous limit $F \rightarrow \infty$, $C \rightarrow \infty$, where F tends as $1/a^2$ and C as $1/a$, is essential to make the continuum prescription viable. This has been discussed by Kenkre and collaborators elsewhere [25, 31]. Following this procedure, we can divide also

$$\tilde{P}_m = \tilde{\eta}_m - \tilde{\Psi}_{mr} \frac{\tilde{\eta}_r}{1/C + \tilde{\Psi}_{rr}} \quad (7.31)$$

by the lattice constant a and take $a \rightarrow 0$ to obtain

$$\tilde{P}(x, \epsilon) = \tilde{\eta}(x, \epsilon) - \tilde{\Psi}(x, \epsilon) \frac{\tilde{\eta}(x_r, \epsilon)}{1/C + \tilde{\Psi}(0, \epsilon)}. \quad (7.32)$$

Similarly, we have

$$\tilde{P}(x_r, \epsilon) = C \frac{\tilde{\eta}(x_r, \epsilon)}{1 + C\tilde{\Psi}(0, \epsilon)}. \quad (7.33)$$

Next we calculate the rate of disappearance of $dQ(t)/dt$ from Eq.(7.30) by integrating over half-space

$$\frac{dQ}{dt} = \int_{x_r}^{\infty} \frac{\partial P}{\partial t} dx = \int_{x_r}^{\infty} \left[D^2 \frac{\partial^2 P}{\partial x^2} - C \delta(x - x_r) P(x, t) \right] dx \quad (7.34)$$

and since

$$\int \delta(x - x_r) P(x, t) dx = P(x_r, t)$$

we obtain in the Laplace domain

$$\frac{d\tilde{Q}(\epsilon)}{dt} = C\tilde{P}(x_r, \epsilon) = \frac{\tilde{\eta}(x_r, \epsilon)}{1/C + \tilde{\Psi}(0, \epsilon)},$$

which leads to a continuous prescription

$$\tilde{Q}(\epsilon) = \frac{1}{\epsilon} \left[1 - \frac{\sum_r' \tilde{\eta}(x_r, x)}{1/C_d + \sum_r' \tilde{\Pi}(x_r, x_r)} \right]. \quad (7.35)$$

Here $\tilde{\Pi}(x_r, x_r)$ is the self-propagator and its sum \sum_r' thus corresponds to the v -function. $\tilde{\eta}(x_r, x)$ is the homogeneous solution at the trap site in the absence of the trap, \sum_r' represents

Chapter 7. Repository of Exact Solutions for Stationary Trapping Problems

the sum over all trap sites, and C_d is the d-dimensional capture rate. Both of these propagators are obtained from the homogeneous solution to the diffusion equation. Therefore, as expected from the discrete formalism, the continuum prescription in Laplace domain given in Eq.(7.35), independently derived by Szabo et al. [132] by a different method, expresses the Green's function describing the reaction in terms of the Green's function for diffusion in the absence of the reaction. Note that the diffusion propagator, which is used to obtain the self-propagator as well as the homogeneous solution, need not be the free-space Green's function. For example, for diffusion in a potential the propagator must be appropriate for diffusion in the presence of a potential.

7.5 Repository of solutions in one-dimension

In this section the continuous prescription given in Eq.(7.35) is applied to one-dimensional trapping problems with a single stationary trap of non-infinite capture rate.

7.5.1 Localized initial condition

Thus far we have solved simple trapping problems on a discrete lattice. In the remainder of this chapter we will solve several problems related to continuous diffusion. The simplest is the problem of a diffusing particle in one-dimension, where the particle is initially a distance x_0 away from a trap located at the origin. This problem can be solved by applying the prescription given in Eq.(7.35). To evaluate the prescription, we first use the one-dimensional free-space diffusion propagator

$$P(x, x_0; t) = \frac{1}{\sqrt{4\pi Dt}} \exp \left[-\frac{(x - x_0)^2}{4Dt} \right] \quad (7.36)$$

to obtain the self-propagator

$$\Pi(0, 0) = \frac{1}{\sqrt{4\pi Dt}} \quad (7.37)$$

and the homogeneous solution at the trap site

$$\eta(0, x_0) = \frac{1}{\sqrt{4\pi Dt}} \exp\left[-\frac{x_0^2}{4Dt}\right] \quad (7.38)$$

in time domain. Then we insert the Laplace transform of these propagators (see Appendix B) into the prescription to obtain

$$\tilde{Q}(\varepsilon) = \frac{1}{\varepsilon} \left[1 - \frac{\exp(-\sqrt{\varepsilon\tau})}{1 + \xi\sqrt{\varepsilon\tau}} \right], \quad (7.39)$$

where $\tau = x_0^2/D$ is the diffusion time and $\xi = 2D/(Cx_0)$ describes the reaction process. This expression for finite reaction can be inverted exactly (see Appendix B) with the property $f(t/\tau) \rightarrow \tau\tilde{g}(\varepsilon\tau)$

$$Q(t) = \operatorname{erf}\left(\frac{1}{2}\sqrt{\frac{\tau}{t}}\right) + e^{\frac{1}{\xi} + \frac{1}{\xi^2}\left(\frac{t}{\tau}\right)} \operatorname{erfc}\left(\frac{1}{2}\sqrt{\frac{\tau}{t}} + \frac{1}{\xi}\sqrt{\frac{t}{\tau}}\right) \quad (7.40)$$

and reduces for an instantaneous absorber ($C \rightarrow \infty$) to

$$Q(t) = \operatorname{erf}\left(\frac{1}{2}\sqrt{\frac{\tau}{t}}\right). \quad (7.41)$$

Both, the perfect absorption result given in Eq.(7.41) [141, 136, 142, 143, 144] as well as the finite reaction, Eq.(7.41) [141, 138, 145, 143] are well known. Moreover, it is trivial to compute the perfect absorber result from the method of images (calculation is omitted here) without employing the Laplace transform. The purpose of this calculation was to show that the prescription can be applied successfully to obtain new results. In the remainder it will become evident that this prescription is very powerful.

7.5.2 The principle of superposition

In the previous subsection we obtained an exact solution for a point initial condition. Since the problem is linear, the superposition principle can be applied to obtain a solution for any

initial distribution of point particles. In the special case of perfect absorption the principle of superposition states that

$$Q(t) = \int_0^{\infty} \rho(x_0) \operatorname{erf}\left(\frac{x_0}{\sqrt{4Dt}}\right) dx_0, \quad (7.42)$$

where $\rho(x_0)$ is the initial distribution of point particles.

To demonstrate the application of the above equation we first compute the survival probability for an initial random distribution. In this case $\rho(x_0)$ is of Poisson form $\rho(x_0) = c \exp(-cx_0)$, where c is an arbitrary constant. Substituting $\rho(x_0)$ into Eq.(7.42) one obtains

$$Q(t) = \exp(c^2 Dt) \operatorname{erfc}(c\sqrt{Dt}), \quad (7.43)$$

which has been calculated by Torney and McConnel [146] and later by Sancho et al. [126] by different methods. Another initial distribution is the Rayleigh distribution, also known as a biased Gaussian, $\rho(x_0) = x_0 \exp(-x_0^2/(2\sigma^2)) / \sigma^2$, where σ describes the width of the distribution. Substituting this distribution into Eq.(7.42) and after evaluating the integral, the following simple expression is obtained

$$Q(t) = \frac{\sigma}{\sqrt{2Dt + \sigma^2}}. \quad (7.44)$$

This result was reported by Doering and ben-Avraham [124].

7.5.3 General prescription for any initial distributions

The principle of superposition is obviously not restricted to perfect absorption and also applies to imperfect finite reaction. However, multiplying the expression given in Eq.(7.40) by an initial distribution and integrating the product over the position x_0 becomes algebraically tedious. To simplify this calculation, we apply here the superposition principle

Chapter 7. Repository of Exact Solutions for Stationary Trapping Problems

in Laplace domain

$$\tilde{Q}(\epsilon) = \int_0^{\infty} \rho(x_0) \tilde{Q}(\epsilon, x_0) dx_0, \quad (7.45)$$

where $\tilde{Q}(\epsilon, x_0)$ is given in Eq.(7.39). For example, one can obtain an exact expression for an initial random distribution, $\rho(x_0) = c \exp(-cx_0)$, in Laplace domain

$$\tilde{Q}(\epsilon) = \frac{1}{\epsilon} - \frac{\gamma}{\gamma\epsilon(\sqrt{\gamma\epsilon} + 1)^2}, \quad (7.46)$$

where $\gamma = 4D/C^2$. This expression can be inverted exactly (see Appendix B) with $f(t/\tau) \rightarrow \tau f(\epsilon\tau)$ to give

$$Q(t) = \left(1 - \frac{2t}{\gamma}\right) \exp(t/\gamma) \operatorname{erfc}\left(\sqrt{\frac{t}{\gamma}}\right) - \frac{2}{\sqrt{\pi}} \sqrt{\frac{t}{\gamma}}, \quad (7.47)$$

which is, to our knowledge, a new expression. Even though this method is useful, we are always left to Laplace invert an expression and might not obtain an exact analytic solution in time domain. It is true that one always can apply a numerical inversion algorithm (see Appendix C) to obtain the exact solution. However, it would be useful to have a prescription, which does not require the computation of any Laplace transforms. As we will show in the remainder of this subsection, it is indeed possible to derive such a formula.

To derive a general prescription as outlined in unpublished work by Kenkre [22], we start with $\tilde{Q}(\epsilon, x_0)$ given in Eq.(7.39)

$$\tilde{Q}(\epsilon, x_0) = \frac{1}{\epsilon} \left[1 - \frac{e^{-\sqrt{\frac{\epsilon}{D}}x_0}}{\frac{\sqrt{4\epsilon D}}{C} + 1} \right].$$

As mentioned previously, the problem is linear and \tilde{Q} can be integrate over any initial distribution, $\rho(x_0)$, obtaining

$$\tilde{Q}(\epsilon) = \frac{1}{\epsilon} - \frac{1}{\epsilon} \left(\frac{1}{1 + \sqrt{4D\epsilon}/C} \right) \int_0^{\infty} \rho(x_0) e^{-x_0\sqrt{\frac{\epsilon}{D}}} dx_0. \quad (7.48)$$

Chapter 7. Repository of Exact Solutions for Stationary Trapping Problems

Looking at the above equation we notice that the integral expression is the Laplace transform of $\rho(x_0)$ with $\varepsilon \rightarrow \sqrt{\varepsilon/D}$. Hence if $\rho(x_0)$ Laplace transforms to $\tilde{\rho}(\varepsilon)$, Eq.(7.48) becomes

$$\tilde{Q}(\varepsilon) = \frac{1}{\varepsilon} - \frac{1}{\varepsilon} \left(\frac{1}{1 + \sqrt{4D\varepsilon}/C} \right) \tilde{\rho}(\varepsilon), \quad (7.49)$$

or equivalently since $Q(t=0) = 1$ and $\tilde{Q}(\varepsilon)\varepsilon - 1 = d\tilde{Q}(\varepsilon)/(d\varepsilon)$ we may write

$$\frac{d\tilde{Q}(\varepsilon)}{d\varepsilon} = - \left(\frac{1}{1 + \sqrt{4D\varepsilon}/C} \right) \tilde{\rho}(\varepsilon). \quad (7.50)$$

Now we are left with inverting Eq.(7.50).

First we consider that $\tilde{\rho}(\varepsilon)[1/\varepsilon + p]$ is the Laplace transform of

$$h(x) = \int_0^x \rho(x - x_0) \exp(-px_0) dx_0, \quad (7.51)$$

where $p = C/(2D)$. The Laplace transform of $h(t)$ is then

$$\tilde{h}(\varepsilon) = \tilde{\rho}(\varepsilon) \left(\frac{1}{\varepsilon + p} \right),$$

and since we are interested in a transform involving $\sqrt{\varepsilon/D}$ we can make use of the following identity [133]

$$\tilde{h}(\sqrt{\varepsilon}) \rightarrow \frac{1}{2\sqrt{\pi}} t^{-3/2} \int_0^\infty u e^{-\frac{u^2}{4t}} h(u) du$$

with $f(t/\tau) \rightarrow \tau \tilde{f}(\varepsilon\tau)$ to invert

$$\tilde{h} \left(\sqrt{\frac{\varepsilon}{D}} \right) \rightarrow \frac{D}{2\sqrt{\pi}} (Dt)^{-3/2} \int_0^\infty x e^{-\frac{x^2}{4Dt}} h(x) dx.$$

Next, Eq.(7.50) is written as

$$\frac{d\tilde{Q}(\varepsilon)}{d\varepsilon} = -p \left(\frac{1}{\varepsilon + p} \right) \tilde{\rho}(\varepsilon), \quad (7.52)$$

Chapter 7. Repository of Exact Solutions for Stationary Trapping Problems

with $\varepsilon \rightarrow \sqrt{\varepsilon/D}$ and a wonderfully simple general prescription for any distribution $\rho(x_0)$ is obtained

$$\frac{dQ(t)}{dt} = -\frac{C}{4\sqrt{\pi}} (Dt)^{-3/2} \int_0^\infty x e^{-\frac{x^2}{4Dt}} h(x) dx, \quad (7.53)$$

where

$$h(x) = \int_0^x \rho(x - x_0) e^{-px_0} dx_0 \quad (7.54)$$

and $p = C/(2D)$.

Equation (7.53) [22] is a useful formula since one does not need to compute any Laplace transforms. Moreover, we notice that there is a physical meaning for the function $h(x)$, which can be written also as

$$h(x) = \exp(-px) \int_0^x \rho(y) e^{py} dy.$$

From this expression we see that $h(x)$ describes all the material, which is initially present weighted by an exponential. If we put $h(x)$ into Eq.(7.53) and ignore the one-dimensional free-space diffusion propagator, the integral simply describes the mean distance from the trap. By multiplying the integrand by the one-dimensional propagator we indicate that the particles move diffusively. It remains to be investigated how this prescription changes if the nature of motion is directed or ballistic. Maybe the only parameter, which changes in the prescription is the propagator. Finally, the prescription presented above was evaluated by computing $Q(t)$ for a localized initial condition as outlined in the Appendix D.

7.5.4 Trapping in a harmonic potential

In this section we study the problem of a particle diffusing in a harmonic potential centered at the origin in one-dimension. A single sink is located at the bottom of the potential. We

Chapter 7. Repository of Exact Solutions for Stationary Trapping Problems

are interested in the total particle survival probability when the reaction rate at the origin occurs at a finite rate. Similar situations arise in a number of diverse biological systems. Examples are when animal feel a driving force pointing towards their *nest* [147] and generally in the context of home ranges [148]. To solve the problem of a particle moving in a harmonic potential, we make use of the general prescription given in Eq.(7.35).

To apply the prescription we first need to obtain the diffusion propagator in the presence of a potential, which is given by the Fokker-Planck equation

$$\frac{\partial P(x,t)}{\partial t} = \frac{\partial}{\partial x} \left[\frac{dU(x)}{dx} P(x,t) + D \frac{\partial P(x,t)}{\partial x} \right] \quad (7.55)$$

with a quadratic potential of the form $U(x) = \gamma x^2/2$ and a localized initial condition, $P(x,0) = \delta(x - x_0)$. One way to solve this equation is by substituting $P(x,t) = \exp[-\gamma x^2/(4D)]\Psi(x,t)$ into Eq.(7.55) resulting in an expression involving sums of Hermite polynomials, which can be simplified to obtain [149]

$$P(x, x_0, t) = \frac{1}{\sqrt{4\pi D\omega}} e^{-\frac{[x-x_0 \exp(-\gamma t)]^2}{4D\omega}}, \quad (7.56)$$

where $\omega = (1 - \exp[-2\gamma t])/(2\gamma)$. This propagator is very useful and another derivation of this result can be found in Ref. [150].

After obtaining the diffusion propagator for this problem we are left computing two Laplace transforms. First, we compute the Laplace transform of the self-propagator by setting $x = x_0 = 0$ in Eq. (7.56)

$$\eta(t) = \sqrt{\frac{\gamma}{2\pi D}} \frac{1}{\sqrt{\exp(2\gamma t) - 1}} \quad (7.57)$$

and Laplace transforming this expression using Ref. [133], where

$$\frac{(1 - e^{-t})^\nu}{(1 - ce^{-t})^\mu} \rightarrow B(\epsilon, \nu + 1) {}_2F_1(\mu, \epsilon; \epsilon + \nu + 1; c).$$

Here $B(a, b) = \frac{\Gamma(a)\Gamma(b)}{\Gamma(a+b)}$ is the Beta function and ${}_2F_1(a, b; c, 1) = \frac{\Gamma(c)\Gamma(c-a-b)}{\Gamma(c-a)\Gamma(c-b)}$ is a special value of the hypergeometric function also known as Gauss's hypergeometric function.

Chapter 7. Repository of Exact Solutions for Stationary Trapping Problems

Both expressions are given in terms of the Gamma function $\Gamma(x)$. After evaluating the above expressions with $\nu = 0$, $\mu = 1/2$, and using $f(2\gamma t) \rightarrow 1/(2\gamma)\tilde{g}(\epsilon/a)$ with $\Gamma(z+1) = z\Gamma(z)$, we obtain in Laplace domain

$$\tilde{\eta}(\epsilon) = \frac{\sqrt{\gamma}}{\epsilon\sqrt{2D}} \frac{\Gamma\left(\frac{\epsilon}{2\gamma} + 1\right)}{\Gamma\left(\frac{\epsilon}{2\gamma} + \frac{1}{2}\right)}. \quad (7.58)$$

Next the Laplace transform of the homogeneous solution at the trap site $x = 0$ in the absence of the trap is computed. This propagator is given in time domain by setting $x = 0$ in Eq. (7.56)

$$\Pi(t) = \sqrt{\frac{\gamma}{2\pi D}} \frac{\exp(\gamma t)}{\sqrt{\exp(2\gamma t) - 1}} \exp\left[-\frac{\gamma x_0^2/(2D)}{\exp(2\gamma t) - 1}\right]. \quad (7.59)$$

To obtain the Laplace transform of this expression, Ref. [133] is used to transform

$$(e^t - 1)^{\nu-1} e^{-\frac{a}{\exp(t)-1}} \rightarrow a^{\frac{\nu-1}{2}} e^{\frac{a}{2}} \Gamma(\epsilon - \nu + 1) W_{\frac{\nu-1}{2}-\epsilon, \frac{\nu}{2}}(a).$$

Here $W_{a,b}(z) = e^{-z/2} z^{b+1/2} U(-a+b+1/2, 2b+1, z)$ is known as Whittaker W-function defined by the confluent hypergeometric function of the second kind $U(a, b, z) = z^{-a} {}_2F_0(a, 1+a-b; -z^{-1})$ together with

$$\exp(\gamma t) f(2\gamma t) \rightarrow 1/(2\gamma) \tilde{g}[\epsilon/(2\gamma) - 0.5]$$

to obtain

$$\tilde{\Pi}(\epsilon) = \sqrt{\frac{1}{8\pi\gamma D}} \left(\frac{x_0^2\gamma}{2D}\right)^{-1/4} e^{\frac{x_0^2\gamma}{4D}} \Gamma\left(\frac{\epsilon}{2\gamma}\right) W_{\frac{1}{4}-\frac{\epsilon}{2\gamma}, \frac{1}{4}}\left(\frac{x_0^2\gamma}{2D}\right). \quad (7.60)$$

After computing $\tilde{\eta}(\epsilon)$ and $\tilde{\Pi}(\epsilon)$ and substituting Eqs.(7.58) and (7.60) into the prescription given in Eq.(7.35) one obtains an exact expression for the total survival probability in Laplace domain

$$\tilde{Q}(\epsilon) = \frac{1}{\epsilon} - \frac{\frac{1}{2\gamma\sqrt{\pi}} \left(\frac{\gamma}{2}\right)^{-1/4} e^{\frac{\gamma}{4}} W_{-\frac{1}{4}, \frac{1}{4}}\left(\frac{\gamma}{2}\right) \Gamma\left(\frac{\epsilon}{2\gamma}\right)}{\frac{\epsilon\sqrt{\gamma}}{\xi\sqrt{2\gamma}} + \frac{\Gamma\left(\frac{\epsilon}{2\gamma}+1\right)}{\Gamma\left(\frac{\epsilon}{2\gamma}+\frac{1}{2}\right)}}, \quad (7.61)$$

Chapter 7. Repository of Exact Solutions for Stationary Trapping Problems

where $\tau = x_0^2/D$ is the motion time and $\xi = \frac{2D}{Cx_0}$ describes the capture process. As far as we know this expression is a new expression and cannot be inverted directly. However, for instantaneous reaction Eq.(7.61) one can obtain an exact expression.

Perfect absorption

For perfect absorption $C \rightarrow \infty$ and Eq. (7.61) may be written as

$$\tilde{Q}(\varepsilon) = \frac{1}{\varepsilon} - \frac{A^{-1/4} e^{\frac{A}{2}}}{2\gamma\sqrt{\pi}} \frac{\Gamma(\varepsilon' + 1/4) \Gamma(\varepsilon' + 3/4)}{\Gamma(\varepsilon' + 5/4)} W_{-\varepsilon', \frac{1}{4}}(A), \quad (7.62)$$

where $\varepsilon' = 1/4 - \varepsilon/(2\gamma)$ and $A = x_0^2\gamma/(2D)$. This expression can be inverted exactly after using a table of Laplace transforms [133]

$$\frac{\Gamma(\varepsilon + 1/2 + \nu) \Gamma(\varepsilon + 1/2 - \nu)}{\Gamma(\varepsilon' + 1 - \mu)} W(-\varepsilon, \nu, a) \rightarrow \left(e^{a\mu/2} - e^{t\mu} \right) e^{\left[\frac{-a/2}{\exp(t)-1} \right]} W_{\mu, \nu} \left(\frac{a}{\exp(t)-1} \right),$$

where $\nu = 1/4$, $\mu = -1/4$ and $a = A$ together with $\tilde{g}[\varepsilon/(2\gamma) - 1/4] \rightarrow 2\gamma \exp(\gamma t/2) f(2\gamma t)$. After some rearranging one obtains in time domain the following expression

$$Q(t) = 1 - \frac{A^{-1/4}}{\sqrt{\pi}} (e^{2\gamma t} - 1)^{1/4} e^{\frac{-A}{2[\exp(2\gamma t)-1]}} W_{-\frac{1}{4}, \frac{1}{4}} \left(\frac{A}{\exp(2\gamma t)-1} \right). \quad (7.63)$$

At first Eq.(7.63) looks very complicated. However, the complementary error function can be defined in terms of the Whittaker W-function as follows. Abramowitz and Stegun [151] define the Whittaker W-function in terms of the Whittaker M-function $M_{\kappa, \mu}(z)$

$$W_{\kappa, \mu}(z) = \frac{\Gamma(-2\mu)}{\Gamma(1/2 - \mu - \kappa)} M_{\kappa, \mu}(z) + \frac{\Gamma(2\mu)}{\Gamma(1/2 + \mu - \kappa)} M_{\kappa, -\mu}(z) \quad (7.64)$$

and with $\kappa = -1/4$ and $\mu = 1/4$

$$W_{-\frac{1}{4}, \frac{1}{4}}(z) = -2M_{-\frac{1}{4}, \frac{1}{4}}(z) + \sqrt{\pi} M_{-\frac{1}{4}, -\frac{1}{4}}(z). \quad (7.65)$$

Now using the definition of the Whittaker M-function given in Ref. [151] in terms of the Kummer confluent hypergeometric function $M(a, b, z)$,

$$M_{\kappa, \mu}(z) = e^{-z/2} z^{1/2+\mu} M(1/2 + \mu - \kappa, 1 + 2\mu, z) \quad (7.66)$$

Chapter 7. Repository of Exact Solutions for Stationary Trapping Problems

one can write

$$W_{-\frac{1}{4}, \frac{1}{4}}(z) = z^{1/4} e^{-z/2} [\sqrt{\pi} M(1/2, 1/2, z) - 2\sqrt{z} M(1, 3/2, z)]. \quad (7.67)$$

Since $M(1/2, 1/2, z) = \exp(z)$ and $M(1, 3/2, z)$ is related to $\operatorname{erf}(z)$ as given in [151]

$$\operatorname{erf}(z) = \frac{2\sqrt{z}}{\sqrt{\pi}} e^{-z} M(1, 3/2, z), \quad (7.68)$$

and the Whittaker W-function used here can be defined in terms of the complementary error function

$$W_{-\frac{1}{4}, \frac{1}{4}}(z) = \sqrt{\pi} z^{1/4} e^{z/2} \operatorname{erfc}(z). \quad (7.69)$$

Now we can substitute Eq.(7.69) into Eq.(7.63) with $z = A/[\exp(2\gamma t) - 1]$ where $A = x_0^2 \gamma / (2D)$ and write

$$Q(t/\tau) = \operatorname{erf} \left(\frac{\sqrt{\gamma \tau}}{\sqrt{2}[\exp(2\gamma t) - 1]} \right). \quad (7.70)$$

Equation (7.70) is an exact expression for the total survival probability of a particle, which is instantaneously absorbed at the origin while diffusing in a harmonic potential centered at the origin. It turns out that this expression can be also obtained from the method of images as outlined by Bagchi, Fleming and Oxtoby [152] and Kenkre [22].

Imperfect absorption: long time limit

As mentioned above the expression for finite absorption in Laplace domain, Eq.(7.61), cannot be inverted exactly. However in the long time limit as $t \rightarrow \infty$ or $\varepsilon \rightarrow 0$, Eq.(7.61) can be written as

$$\tilde{Q}(\varepsilon) = \frac{1}{\varepsilon} - \frac{\frac{1}{2\gamma} \left(\frac{x_0^2 \gamma}{2D} \right)^{-1/4} e^{\frac{x_0^2 \gamma}{4D}} W_{-\frac{1}{4}, \frac{1}{4}} \left(\frac{x_0^2 \gamma}{2D} \right) \left[\frac{2\gamma}{\varepsilon} - E_\gamma \right]}{\frac{\sqrt{2D\pi\varepsilon}}{C_{1d}\sqrt{\gamma}} + 1}, \quad (7.71)$$

Chapter 7. Repository of Exact Solutions for Stationary Trapping Problems

where $E_\gamma = 0.5772\dots$ is the Euler's constant. Since it is straight forward to invert $1/(a\varepsilon^2 + \varepsilon)$ and $1/(a\varepsilon + 1)$ we obtain in time domain for imperfect absorption in the long time limit

$$Q(t/\tau) = 1 - \left(\frac{\gamma\tau}{2}\right)^{-1/4} e^{\frac{\gamma\tau}{4}} W_{-\frac{1}{4}, \frac{1}{4}}\left(\frac{\gamma\tau}{2}\right) \left[1 - e^{\sqrt{\frac{2\gamma}{\pi\tau}} \frac{t}{\xi}} \left(1 + \frac{\xi}{\sqrt{2\pi\gamma\tau}}\right)\right]. \quad (7.72)$$

Here γ describes the strength of the potential. To our knowledge this expression is new.

Other initial distributions

Since the exact solution is known for a point initial condition, one can solve the problem for any initial condition by applying the principle of superposition. For example, in the perfect absorption case, the exact solution for a localized initial condition is given in Eq.(7.70) and for any other initial distribution $\rho(x_0)$ the principle of superposition says

$$Q(t) = \int_0^\infty \rho(x_0) \operatorname{erf}\left(\sqrt{\frac{\gamma}{2D}} \frac{x_0}{\sqrt{\exp(2\gamma t) - 1}}\right) dx_0. \quad (7.73)$$

For an initial random distribution $\rho(x_0) = c_0 \exp(-c_0 x_0)$ the above expression becomes

$$Q(t) = e^{\frac{c_0^2 D [\exp(2\gamma t) - 1]}{2\gamma}} \operatorname{erfc}\left(c_0 \sqrt{\frac{D [\exp(2\gamma t) - 1]}{2\gamma}}\right). \quad (7.74)$$

For an initial Rayleigh distribution $\rho(x_0) = x_0 \exp[-x_0^2/(2D\sigma^2)]/\sigma^2$, another exact expression can be obtained

$$Q(t) = \sqrt{\frac{\gamma\sigma^2}{\gamma\sigma^2 + D e^{2\gamma t} - D}}. \quad (7.75)$$

Both results are new expressions as far as we know.

7.6 Repository of solutions in two-dimensions

The stationary trapping prescription given in Eq.(7.35) can also be applied to higher dimensions where a trap in one-dimension becomes an absorbing surface in higher dimen-

Chapter 7. Repository of Exact Solutions for Stationary Trapping Problems

sions [132]. The second term in the denominator of Eq.(7.35) is the ensemble average of the sum of propagators of the homogeneous system (in absence of traps) from one trap location to all others. If the system is two-dimensional, the absorber (trap) sites are the points forming the circumference of a circle (disk) and the motion obeys a diffusion equation. The circle has radius R . Let us take the circle to have the origin as the center and therefore any two points on the circumference to be labeled by polar coordinates R and two values of θ . The two-dimensional propagators are simply products of Gaussian one-dimensional propagators (isotropy assumed) and therefore independent of θ . So we will take one of the angles to be 0 and the cartesian coordinates of the two points are therefore $R \cos \theta$, $R \sin \theta$ and R , 0 respectively. Thus $\Pi(t)$ is proportional to the integral [22]

$$\Pi(t) = \text{constant} \int_0^{2\pi} \frac{\exp\left[-\frac{R^2[(1-\cos\theta)^2 + \sin^2\theta]}{4Dt}\right]}{4\pi Dt} d\theta. \quad (7.76)$$

The integral is evaluated in terms of the I_0 Bessel function of argument $R^2/2Dt$. In one-dimension there would be no integral and the denominator would have a square root of t . We will show in one of the following subsections that the Laplace transform of $\Pi(t)$ given above is known precisely and one can obtain exact expressions for two-dimensional trapping problems. In the remainder of this section we will solve trapping problems for open and closed trapping surfaces in two-dimensions.

7.6.1 Two-dimensional free-space propagator

To apply the trapping prescription to problems describing simple diffusion in two-dimensions, we need to compute the two-dimensional free-space propagator. The Green's function in two-dimensions is simply the product of two one-dimensional Green's function in the x and y direction. In polar coordinates the expression is then

$$G(\vec{r}, \vec{r}'; t) = \frac{1}{4\pi Dt} e^{-\frac{|\vec{r}-\vec{r}'|^2}{4Dt}} \quad (7.77)$$

Chapter 7. Repository of Exact Solutions for Stationary Trapping Problems

where $|\vec{r} - \vec{r}'|^2 = (x - x')^2 + (y - y')^2$. For rotationally symmetric initial condition, $P(\vec{r}, 0) = \delta(r - R_0)/(2\pi r)$, the rotationally symmetric solution is

$$\begin{aligned} P(\vec{r}, t) &= \int_0^{2\pi} \int_0^\infty G(\vec{r}, \vec{r}'; t) P(\vec{r}, 0) r' dr' d\theta' \\ &= \frac{1}{8\pi^2 Dt} \int_0^{2\pi} \int_0^\infty e^{-\frac{r^2 + r'^2 - 2rr' \cos(\theta')}{4Dt}} \delta(r' - R_0) dr' d\theta'. \end{aligned} \quad (7.78)$$

Carrying out the integration over r' ,

$$P(r, t) = \frac{1}{8\pi^2 Dt} e^{-\frac{r^2 + R_0^2}{4Dt}} \int_0^{2\pi} e^{\frac{2rR_0 \cos(\theta')}{4Dt}} d\theta' \quad (7.79)$$

and realizing that the left integral is the I_0 Bessel function

$$2\pi I_0(z) = \int_0^{2\pi} e^{z \cos \theta} d\theta$$

we get the following two-dimensional free-space diffusion propagator

$$P(r, R_0; t) = \frac{1}{4\pi Dt} e^{-\frac{r^2 + R_0^2}{4Dt}} I_0\left(\frac{rR_0}{2Dt}\right). \quad (7.80)$$

This propagator is well known [141] and is the two-dimensional counterpart in polar coordinates of Eq.(7.36).

7.6.2 Circular trap

In this subsection we solve for the total survival probability of a stationary circular trap and an initial circular symmetric distribution of diffusing non-interacting point particles at R_0 . The circular trap is centered at the origin and has a radius R , where $R < R_0$. Using the two-dimensional free-space propagator in Eq.(7.80) the self-propagator in time domain is given as

$$\Pi(R, R) = \frac{1}{4\pi Dt} e^{-\frac{R^2}{2Dt}} I_0\left(\frac{R^2}{2Dt}\right)$$

Chapter 7. Repository of Exact Solutions for Stationary Trapping Problems

and the homogeneous solution at the trap site is

$$\Pi(R, R_0) = \frac{1}{4\pi Dt} e^{-\frac{R^2 + R_0^2}{4Dt}} I_0\left(\frac{RR_0}{2Dt}\right).$$

Both expressions can be Laplace transformed (see Appendix B) and substituted into the prescription, Eq.(7.35) to give

$$\tilde{Q}(\epsilon) = \frac{1}{\epsilon} \left[1 - \frac{\frac{1}{2\pi D} K_0\left(\sqrt{\frac{\epsilon}{\gamma_0}}\right) I_0\left(\sqrt{\frac{\epsilon}{\epsilon_0}}\right)}{\frac{1}{C} + \frac{1}{2\pi D} K_0\left(\sqrt{\frac{\epsilon}{\epsilon_0}}\right) I_0\left(\sqrt{\frac{\epsilon}{\epsilon_0}}\right)} \right], \quad (7.81)$$

where $\epsilon_0 = D/R^2$ and $\gamma_0 = D/(R_0^2)$. For perfect absorption $C \rightarrow \infty$ in Eq.(7.81) and one obtains

$$\tilde{Q}(\epsilon) = \frac{1}{\epsilon} \left[1 - \frac{K_0\left(\sqrt{\frac{\epsilon}{\gamma_0}}\right)}{K_0\left(\sqrt{\frac{\epsilon}{\epsilon_0}}\right)} \right]. \quad (7.82)$$

Here I_0 and K_0 are the zero order modified Bessel functions of the first and second kind, respectively. Both expression for imperfect and perfect absorption cannot be inverted exactly and hence one can only obtain exact expressions for long and short times. However, it is trivial to compute the numerical Laplace transform by implementing the algorithm outlined in Appendix C. The expression for finite reaction in Eq.(7.81) appears to be new. The perfect-absorption limit Eq.(7.82) of our general result can be found, however, in the book on heat conduction by Carslaw and Jaeger [141].

Let us now obtain limiting expressions for long and short times. For short time, $t \rightarrow 0$, $\epsilon \rightarrow \infty$ and the zero-order modified Bessel functions of the first and second kind can be approximated as follows [151]

$$\begin{aligned} K_0(z) &\sim \sqrt{\frac{\pi}{2z}} e^{-z} \\ I_0(z) &\sim \sqrt{\frac{1}{2\pi z}} e^z \\ K_0(z) I_0(z) &\sim \frac{1}{2z}. \end{aligned}$$

Then, for the case of finite reaction,

$$\tilde{Q}(\varepsilon) = \frac{1}{\varepsilon} \left[1 - \sqrt{\frac{R}{R_0}} \frac{e^{-\sqrt{\varepsilon\tau_{2d}}}}{\xi_{2d}\sqrt{\varepsilon\tau_{2d}} + 1} \right], \quad (7.83)$$

where $\tau_{2d} = (R_0 - R)^2/D$ is the two-dimensional motion parameter and $\xi_{2d} = 4\pi DR/[C(R_0 - R)]$ describes the two-dimensional capture process. Equation (7.83) can be inverted exactly (see Appendix B) giving

$$Q(t) = 1 - \sqrt{\frac{R}{R_0}} \left[\operatorname{erfc} \left(\frac{1}{2} \sqrt{\frac{\tau_{2d}}{t}} \right) - e^{\frac{1}{\xi_{2d}} + \frac{1}{\xi_{2d}^2} \frac{t}{\tau_{2d}}} \operatorname{erfc} \left(\frac{1}{2} \sqrt{\frac{\tau_{2d}}{t}} + \frac{1}{\xi_{2d}} \sqrt{\frac{t}{\tau_{2d}}} \right) \right]. \quad (7.84)$$

This result is very similar to the one-dimensional result for a point trap and initial delta function condition given in Eq.(7.40). As far as we know, the result for finite absorption and short time given in Eq. (7.84) is a new result. It is straightforward to obtain a short time approximation for perfect absorption:

$$Q(t) = 1 - \sqrt{\frac{R}{R_0}} \operatorname{erfc} \left(\frac{1}{2} \sqrt{\frac{\tau_{2d}}{t}} \right). \quad (7.85)$$

This result has been derived by Taitelbaim [153].

To obtain expressions for the long time limit one can follow Ritchie and Sakakura [154] and Taitelbaim [153] to obtain for imperfect absorption [153]

$$Q(t) = 2 \left[\ln \left(\frac{R_0}{R} \right) + \frac{2\pi D}{C} \right] \frac{1}{\ln \left(\frac{4Dt}{R^2} \right) + \frac{4\pi D}{C} - 2\gamma} \quad (7.86)$$

and for instantaneous reaction [154]

$$Q(t) = 2 \ln \left(\frac{R_0}{R} \right) \frac{1}{\ln \left(\frac{4Dt}{R^2} \right) - 2\gamma}. \quad (7.87)$$

7.6.3 Infinite line trap

In this section $Q(t)$ is obtained for an infinite line of traps along the y -axis from $-\infty$ to ∞ through $x = 0$ and initial point particles placed on an infinite line from $-\infty < y < \infty$

Chapter 7. Repository of Exact Solutions for Stationary Trapping Problems

through $x = x_0$. This problem can be solved by using the expression for a trapping ring of radius R and an initial radially symmetric distribution of point particles given in Eq.(7.81) by replacing R_0 with at $R_0 = R + x_0$

$$\tilde{Q}(\epsilon) = \frac{1}{\epsilon} \left[1 - \frac{\frac{1}{2\pi D} K_0 \left([R + x_0] \sqrt{\frac{\epsilon}{D}} \right) I_0 \left(R \sqrt{\frac{\epsilon}{D}} \right)}{\frac{1}{C_{2d}} + \frac{1}{2\pi D} K_0 \left(R \sqrt{\frac{\epsilon}{D}} \right) I_0 \left(R \sqrt{\frac{\epsilon}{D}} \right)} \right]. \quad (7.88)$$

As $R \rightarrow \infty$, the arguments of both $K_0(z)$ and $I_0(z)$ tend to infinity

$$\begin{aligned} I_0 \left(R \sqrt{\frac{\epsilon}{D}} \right) K_0 \left(R \sqrt{\frac{\epsilon}{D}} \right) &\simeq \frac{\sqrt{D}}{2R\sqrt{\epsilon}}, \\ I_0 \left(R \sqrt{\frac{\epsilon}{D}} \right) K_0 \left((R + x_0) \sqrt{\frac{\epsilon}{D}} \right) &\simeq \frac{\sqrt{D}}{2R(1 + \frac{x_0}{R})\sqrt{\epsilon}} e^{-x_0 \sqrt{\frac{\epsilon}{D}}}. \end{aligned}$$

Substituting these expressions into Eq.(7.88) with $C_{2d} = 2\pi R C_{1d}$, and taking the limit as $R \rightarrow \infty$, we obtain

$$Q(t/\tau) = \text{erf} \left(\frac{1}{2} \sqrt{\frac{\tau}{t}} \right) + e^{\frac{1}{\xi} + \frac{1}{\xi^2} \left(\frac{t}{\tau} \right)} \text{erfc} \left(\frac{1}{2} \sqrt{\frac{\tau}{t}} + \frac{1}{\xi} \sqrt{\frac{t}{\tau}} \right), \quad (7.89)$$

where $\tau = x_0^2/D$ and $\xi = 2D/(C_{1d}x_0)$. As one might expect, this result is identical to the expression obtained for a single trap at the origin and an initial particle placed at $x = x_0$, Eq.(7.40). Ben-Naim et al. [145] have previously pointed out that the infinite one-dimensional trapping system with an imperfect trap is equivalent to a semiinfinite one-dimensional diffusion system. This equivalence has been used by Park et al. [155] to explain results in a photobleaching experiment resulting from an infinite line trap.

A second way of solving this problem is by utilizing the trapping prescription. In this case we start with the two-dimensional cartesian Gaussian propagator

$$P(x, x_0, y, y_0; t) = \frac{1}{4\pi D t} e^{-\frac{(x-x_0)^2 + (y-y_0)^2}{4Dt}}. \quad (7.90)$$

Since the infinite trapping line is along the y -axis through $x = 0 = x_0$ the propagator becomes

$$P(y, y_0; t) = \frac{1}{4\pi D t} e^{-\frac{(y-y_0)^2}{4Dt}}. \quad (7.91)$$

Chapter 7. Repository of Exact Solutions for Stationary Trapping Problems

After obtaining the diffusion propagator for this system, the self-propagator, which is the sum over all propagators from one trap site at point $(0, y' = 0)$ to all other trap sites $(0, y)$ from $-\infty < y < \infty$, is given as

$$\Pi(t) = \frac{1}{4\pi Dt} \int_{-\infty}^{\infty} e^{-\frac{y^2}{4Dt}} dy = \frac{1}{\sqrt{4\pi Dt}}. \quad (7.92)$$

Similarly, the homogeneous solution is the sum of all propagators from point $(x_0, 0)$ to point $(0, y)$ from $-\infty < y < \infty$

$$\eta(t) = \frac{1}{4\pi Dt} e^{-\frac{x_0^2}{4Dt}} \int_{-\infty}^{\infty} e^{-\frac{y^2}{4Dt}} dy = \frac{1}{\sqrt{4\pi Dt}} e^{-\frac{x_0^2}{4Dt}}. \quad (7.93)$$

The Laplace transforms of these two expressions are known (see Appendix B) and can be substituted into the trapping prescription to arrive at Eq.(7.89).

7.6.4 Finite line trap: open trapping surface

Thus far we have restricted our discussion to closed trapping surfaces. In this section we investigated the possibility of applying the trapping prescription to open trapping surfaces like a finite trap segment. Here, a line segment of traps through $x = 0$ from $-l \leq y \leq l$ is considered. The self-propagator is computed from Eq.(7.90) by integrating y and y_0 from $-l$ to l and dividing by $2l$ for appropriate normalization

$$\Pi(t) = \frac{1}{4\pi Dt} \int_{-l}^l \int_{-l}^l e^{-\frac{(y-y')^2}{4Dt}} dy' dy = \frac{1}{\sqrt{4\pi Dt}} \operatorname{erf}\left(\frac{l}{\sqrt{Dt}}\right) - \frac{1}{\pi l} e^{-\frac{l^2}{2Dt}} \sinh\left(\frac{l^2}{2Dt}\right). \quad (7.94)$$

We see that if we take $l \rightarrow \infty$ we obtain the same self-propagator as for an infinite line of traps. The first term in the above expression cannot be transformed exactly. However, for the second term the exact Laplace transform can be found in Ref.[133] and one obtains

$$\tilde{\Pi}(\epsilon) = \frac{1}{\sqrt{4\pi D}} \int_0^\infty e^{-\epsilon t} \operatorname{erf}\left(\frac{l}{\sqrt{Dt}}\right) \frac{dt}{\sqrt{t}} - \frac{1}{2\pi l \epsilon} + \frac{1}{\pi \sqrt{\epsilon D}} K_1\left(2l \sqrt{\frac{\epsilon}{D}}\right), \quad (7.95)$$

where $K_1(z)$ is the first order modified Bessel function of the second kind. If the particles are initially placed on a line from $-l$ to l through $x = x_0$ to the right of the trapping line,

Chapter 7. Repository of Exact Solutions for Stationary Trapping Problems

we can use Eq. (7.90) to compute the homogeneous solution at the trap site

$$\begin{aligned}\eta(t) &= \frac{1}{2l} \frac{1}{4\pi Dt} e^{-\frac{x_0^2}{4Dt}} \int_{-l}^l \int_{-l}^l e^{-\frac{(y-y')^2}{4Dt}} dy dy' \\ &= \frac{1}{\sqrt{4\pi Dt}} e^{-\frac{x_0^2}{4Dt}} \operatorname{erf}\left(\frac{l}{\sqrt{Dt}}\right) - \frac{1}{\pi l} e^{-\frac{2l^2+x_0^2}{4Dt}} \sinh\left(\frac{l^2}{2Dt}\right).\end{aligned}$$

After Laplace transforming the above expression the propagator becomes

$$\begin{aligned}\tilde{\eta}(\varepsilon) &= \frac{1}{\sqrt{4\pi D}} \int_0^\infty e^{-\varepsilon t} e^{-\frac{x_0^2}{4Dt}} \operatorname{erf}\left(\frac{l}{\sqrt{Dt}}\right) \frac{dt}{\sqrt{t}} \\ &- \frac{1}{\pi l \sqrt{\varepsilon}} \left[\frac{x_0}{2\sqrt{D}} K_1\left(x_0 \sqrt{\frac{\varepsilon}{D}}\right) - \sqrt{\frac{4l^2+x_0^2}{4D}} K_1\left(\sqrt{\frac{(4l^2+x_0^2)\varepsilon}{D}}\right) \right].\end{aligned}\quad (7.96)$$

Substituting Eqs.(7.95) and (7.96) into Eq.(7.35) we obtain the following expression in Laplace domain

$$\tilde{Q}(\varepsilon) = \frac{1}{\varepsilon} \left[1 - \frac{\int_0^\infty e^{-\varepsilon t} e^{-\frac{\tau}{4t}} \operatorname{erf}\left(\frac{1}{2} \sqrt{\frac{\chi}{t}}\right) \frac{dt}{\sqrt{t}} - \frac{4}{\sqrt{\pi\chi\varepsilon}} \left[\frac{\sqrt{\tau}}{2} K_1(\sqrt{\tau\varepsilon}) - \frac{1}{2} \sqrt{\tau+\chi} K_1(\sqrt{(\tau+\chi)\varepsilon}) \right] \right]}{\sqrt{\pi\tau\xi} + \int_0^\infty e^{-\varepsilon t} \operatorname{erf}\left(\frac{1}{2} \sqrt{\frac{\chi}{t}}\right) \frac{dt}{\sqrt{t}} - \frac{2}{\varepsilon\sqrt{\pi\chi}} + \frac{2}{\sqrt{\varepsilon\pi}} K_1(\sqrt{\varepsilon\chi})} \right].\quad (7.97)$$

Here $\chi = 4l^2/D$ and $\tau = x_0^2/D$ are motion parameters and $\xi = 2D/(Cx_0)$ describes the capture process as usual. Looking at Eq.(7.97) it becomes obvious that solutions for open trapping surfaces become more complex due to missing symmetry in the problem. However, we reiterate that, as long as we obtain an expression in Laplace domain, it is possible to invert the solution numerically. Finally, we note that Eq.(7.97) is a new expression.

7.7 Repository of solutions in three-dimensions

In this section we will solve stationary trapping problems in three-dimensions.

7.7.1 Three-dimensional free-space propagator

To apply the trapping prescription to three-dimensional problems described by simple diffusion, we need to compute the three-dimensional free-space propagator. The Green's function in three dimensions is a product of three one-dimensional Gaussian propagators and written in spherical polar coordinates as

$$G(\vec{r}, \vec{r}_0; t) = \frac{1}{(4\pi Dt)^{3/2}} e^{-\frac{|\vec{r}-\vec{r}_0|^2}{4Dt}} \quad (7.98)$$

where $|\vec{r}-\vec{r}_0|^2 = (x-x_0)^2 + (y-y_0)^2 + (z-z_0)^2$. For a spherically symmetric initial condition, $P(\vec{r}, 0) = \delta(r-R_0)/(4\pi r^2)$, the spherically symmetric solution is

$$\begin{aligned} P(\vec{r}, t) &= \int_0^\pi \int_0^{2\pi} \int_0^\infty G(\vec{r}, \vec{r}'; t) P(\vec{r}, 0) r'^2 \sin\theta dr' d\theta d\phi \\ &= \frac{1}{2(4\pi Dt)^{3/2}} \int_0^\pi \int_0^\infty e^{-\frac{r^2+r'^2-2rr'\cos\theta}{4Dt}} \delta(r'-R_0) dr' \sin\theta d\theta. \end{aligned} \quad (7.99)$$

Carrying out the integration over r' and substituting $u = \cos\theta$, we obtain

$$P(r, R_0; t) = \frac{1}{8\pi r R_0 \sqrt{\pi Dt}} \left(e^{-\frac{(r-R_0)^2}{4Dt}} - e^{-\frac{(r+R_0)^2}{4Dt}} \right). \quad (7.100)$$

This useful expression can be found in Ref. [141].

7.7.2 Spherical trap: passive diffusion in biology

In this subsection the trapping problem of a spherical trapping shell and an initial spherical distribution of point particles is investigated. This problem seems to have important biological applications in the process of passive diffusion. In this process small molecules may diffuse across a phospholipid bilayer. For example, in the process of photosynthesis, oxygen molecules may be absorbed by oxygen-evolving complexes embedded in the

Chapter 7. Repository of Exact Solutions for Stationary Trapping Problems

thylakoid membrane [156] while undergoing passive diffusion through the membrane. In such a system one might be interested in the total amount of unbound oxygen, which is a measure of energy production in this process.

To solve this problem, we follow our previous methodology. First, the self-propagator for a trap of radius R located at the origin is obtained from the free-space propagator given in Eq.(7.100)

$$\Pi(R, R) = \frac{1}{8\pi R^2 \sqrt{\pi D t}} \left(1 - e^{-\frac{R^2}{Dt}} \right). \quad (7.101)$$

Second, the homogeneous solution at the spherical trap sites for an initial spherical distribution of point particles at $R_0 > R$ is given as

$$\eta(R, R_0) = \frac{1}{8\pi R R_0 \sqrt{\pi D t}} \left(e^{-\frac{(R_0 - R)^2}{4Dt}} - e^{-\frac{(R_0 + R)^2}{4Dt}} \right). \quad (7.102)$$

Both expressions can be Laplace transformed exactly (see Appendix B) and the particle survival probability in Laplace domain for finite reaction is

$$\tilde{Q}(\epsilon) = \frac{1}{\epsilon} \left[1 - \frac{\frac{1}{4\pi R R_0 \sqrt{D\epsilon}} e^{-\sqrt{\frac{\epsilon}{\gamma_0}}} \sinh \sqrt{\frac{\epsilon}{\epsilon_0}}}{\frac{1}{C} + \frac{1}{4\pi R^2 \sqrt{D\epsilon}} e^{-\sqrt{\frac{\epsilon}{\epsilon_0}}} \sinh \sqrt{\frac{\epsilon}{\epsilon_0}}} \right], \quad (7.103)$$

where $\epsilon_0 = D/R^2$ and $\gamma_0 = D/R_0^2$. This expression is a new expression and cannot be inverted directly as far as we know. For instantaneous reaction, $C \rightarrow \infty$, Eq.(7.103) becomes

$$\tilde{Q}(\epsilon) = \frac{1}{\epsilon} \left(1 - \frac{R}{R_0} e^{-\sqrt{\epsilon} \left(\sqrt{\frac{1}{\gamma_0}} - \sqrt{\frac{1}{\epsilon_0}} \right)} \right). \quad (7.104)$$

This expression can be inverted exactly (see Appendix B) giving in time domain

$$Q(t) = 1 - \frac{R}{R_0} \operatorname{erfc} \left(\frac{R_0 - R}{\sqrt{4Dt}} \right). \quad (7.105)$$

Equation (7.105) is given by Carslaw and Jaeger [141] and has been rederived by Rice [157].

Chapter 7. Repository of Exact Solutions for Stationary Trapping Problems

To obtain an asymptotic approximation for finite reaction, we use the property that any function $\tilde{f}(\epsilon)$ in Laplace domain can be expressed as a complex valued function where ϵ is replaced with $z = r \exp(i\theta)$ [158]. Here, we are interested in finding the following singularities, z_0 , of $\tilde{f}(z)$ when $\tilde{f}(z)$ goes to zero or infinity: poles of order m , essential singularities, branch points, and branch cuts. To obtain an asymptotic approximation $\tilde{f}(\epsilon)$ is expanded around z_0 in a Laurent series, where z_0 is the right most singularity [158]

$$\tilde{f}(z) = \sum_{v=0}^{\infty} c_v (z - z_0)^{\lambda_v}, \quad (7.106)$$

According to Doetsch [158], the asymptotic approximation of $f(t)$ is then given as

$$f(t) \approx \exp(z_0 t) \sum_{v=0}^{\infty} \frac{c_v}{\Gamma(-\lambda_v)} t^{-\lambda_v-1}. \quad (7.107)$$

This expression is zero if λ_v takes one of the values $0, 1, 2, \dots$. To obtain more terms in the expansion, this method can be applied to the next singularity, which is to the left of the first singularity, and add the two results. Following this methodology, Eq.(7.103) has a branch cut at $(-\infty, 0]$ and the Laurent expansion around $\epsilon = 0$ gives the following long time limit

$$Q(t) \sim 1 - \frac{RC}{R_0(4\pi DR + C)} + \frac{1}{\sqrt{t}} \left(\frac{RC}{\sqrt{D}(4\pi DR + C)} - \frac{C^2 R}{\sqrt{D}(4\pi D + C)^2} \right), \quad (7.108)$$

which is a new expression. In the limit of infinite time, $t \rightarrow \infty$, Eq.(7.108) reduces to a known expression given by Rice [157]

$$Q(t) = 1 - \frac{RC}{R_0(4\pi DR + C)}.$$

For perfect absorption the asymptotic expression given in Eq.(7.108) becomes

$$Q(t) = 1 - R/R_0,$$

which has been given by Rice [157]. Therefore, for finite and instantaneous reaction in three-dimensions, the survival probability will never reach zero. This result is expected since, in three-dimensions, the probability of a diffusing particle reaching any point (including the starting point) as time approaches infinity is less than one.

7.7.3 Infinite sheet of traps

Similarly, one can obtain also an expression for an infinite sheet in three-dimensions. The obtained expression should be equivalent to the result obtained for a single trap and point particle initial condition in one-dimension. We again start with the solution for a spherical trap given in Eq.(7.103) and replace $R_0 = R + R_0$ to obtain

$$\tilde{Q}(\epsilon) = \frac{1}{\epsilon} \left[1 - \frac{\frac{1}{4\pi R^2(1+\frac{R_0}{R})\sqrt{D\epsilon}} e^{-(R+R_0)\sqrt{\frac{\epsilon}{D}}} \sinh\left(R\sqrt{\frac{\epsilon}{D}}\right)}{\frac{1}{C_{3d}} + \frac{1}{4\pi R^2\sqrt{D\epsilon}} e^{-R\sqrt{\frac{\epsilon}{D}}} \sinh\left(R\sqrt{\frac{\epsilon}{D}}\right)} \right]. \quad (7.109)$$

Since $\sinh z = 1/2[\exp(z) - \exp(-z)]$ and $C_{3d} = 4\pi R^2 C_{1d}$ we can rewrite the above expression as

$$\tilde{Q}(\epsilon) = \frac{1}{\epsilon} \left[1 - \frac{\frac{1/2}{4\pi R^2(1+\frac{R_0}{R})\sqrt{D\epsilon}} e^{-R_0\sqrt{\frac{\epsilon}{D}}}}{\frac{1}{4\pi R^2 C_{1d}} + \frac{1/2}{4\pi R^2\sqrt{D\epsilon}}} \right]. \quad (7.110)$$

In the limit as $R \rightarrow \infty$ it is trivial to show that Eq.(7.110) becomes the one-dimensional result given in Eq.(7.39) after Laplace inversion.

Applying the trapping prescription

This problem can be solved also by applying the trapping prescription. Here we start with the three-dimensional cartesian Gaussian propagator from point (x_0, y_0, z_0) to point (x, y, z)

$$P(x, x_0, y, y_0, z, z_0, t) = \frac{1}{(4\pi Dt)^{3/2}} e^{-\frac{(x-x_0)^2 + (y-y_0)^2 + (z-z_0)^2}{4Dt}}. \quad (7.111)$$

Using this propagator for an infinite sheet of traps, which extends from minus infinity to infinity in the y and z direction through $x = 0$, the self-propagator is given as

$$\Pi(t) = \frac{1}{(4\pi Dt)^{3/2}} \int_{-\infty}^{\infty} e^{-\frac{z_0^2}{4Dt}} dz_0 \int_{-\infty}^{\infty} e^{-\frac{y_0^2}{4Dt}} dy_0 = \frac{1}{\sqrt{4\pi Dt}}. \quad (7.112)$$

Similarly, the homogeneous solution at the trap sites for an initial distribution of particles on a sheet extending from minus infinity to infinity in the y and z direction through $x = x_0$ can be computed

$$\Pi(t) = \frac{1}{(4\pi Dt)^{3/2}} e^{-\frac{x_0^2}{4Dt}} \int_{-\infty}^{\infty} e^{-\frac{z_0^2}{4Dt}} dz_0 \int_{-\infty}^{\infty} e^{-\frac{y_0^2}{4Dt}} dy_0 = \frac{1}{\sqrt{4\pi Dt}} e^{-\frac{x_0^2}{4Dt}}. \quad (7.113)$$

We have encountered both these propagators (Eq.(7.112) and Eq.(7.113)) earlier in section 7.5 when we solved a trapping problem for a stationary trap and a point initial condition in one-dimension. The survival probability of an infinite sheet of traps and an initial distribution of particles also along an infinite sheet in three-dimensions is thus given in Eq. (7.40).

7.7.4 Trapping ring in three-dimensions

The last problem, we investigate in three-dimensions, is diffusion-limited reaction in presence of a trapping ring of radius R centered at the origin in the x, y plane ($z = 0$ or $\phi = \pi/2$) and an initial point particle at $(0, 0, z)$ above the ring on the z -axis. We first compute the self-propagator from Eq.(7.111)

$$\Pi(t) = \frac{1}{2\pi(4\pi Dt)^{3/2}} e^{-\frac{R^2}{2Dt}} \int_0^{2\pi} e^{\frac{R^2}{2Dt} \cos(\theta)} d\theta = \frac{1}{2\pi(4\pi Dt)^{3/2}} e^{-\frac{R^2}{2Dt}} I_0\left(\frac{R^2}{2Dt}\right). \quad (7.114)$$

To Laplace transform the above expression, we use a table of Laplace transforms [133]. First we transform

$$\frac{1}{t\sqrt{t}} e^{-\frac{b}{t}} I_0\left(\frac{b}{t}\right) \rightarrow \int_{\epsilon}^{\infty} du \sqrt{\frac{\pi}{u}} \left[I_0(\sqrt{8bu}) - L_0(\sqrt{8bu}) \right],$$

where $L_\alpha(z)$ is the Struve function and $b = R^2/2D$. After evaluating the following two integrals

$$\begin{aligned} \int_{\epsilon}^{\infty} du \sqrt{\frac{\pi}{u}} I_0(\sqrt{8bu}) &= -2\sqrt{\pi\epsilon} {}_1F_2\left(\frac{1}{2}; 1, \frac{3}{2}; 2b\epsilon\right), \\ \int_{\epsilon}^{\infty} du \sqrt{\frac{\pi}{u}} L_0(\sqrt{8bu}) &= \frac{2\gamma + \ln(32b)}{\sqrt{b}} - \frac{8\epsilon\sqrt{b}}{\sqrt{2\pi}} {}_2F_3\left(1, 1; 1, \frac{3}{2}, \frac{3}{2}; 2b\epsilon\right), \end{aligned}$$

Chapter 7. Repository of Exact Solutions for Stationary Trapping Problems

where ${}_pF_q$ is the generalized hypergeometric function and γ is Euler's constant, we obtain in Laplace domain

$$\begin{aligned}\tilde{\Pi}(\epsilon) &= \frac{1}{(4\pi D)^{3/2}} \left[\frac{4R\epsilon}{\sqrt{\pi D}} {}_2F_3 \left(1, 1; 1, \frac{3}{2}, \frac{3}{2}, 2; \frac{R^2\epsilon}{D} \right) - \frac{\sqrt{2D} \left(2\gamma + \ln \left(\frac{16R^2}{D} \right) \right)}{R} \right] \\ &- \frac{1}{(4\pi D)^{3/2}} \left[2\sqrt{\pi\epsilon} {}_1F_2 \left(\frac{1}{2}; 1, \frac{3}{2}; \frac{R^2\epsilon}{D} \right) \right].\end{aligned}\quad (7.115)$$

Next we compute the homogeneous solution given an initial point particle at $(0, 0, z)$ above the ring on the z -axis. The homogeneous solution at the trap site is given as

$$\Pi(t) = \frac{1}{(4\pi Dt)^{3/2}} e^{-\frac{R^2+z^2}{4Dt}} \quad (7.116)$$

and the Laplace transform of this expression is [133]

$$\tilde{\eta}(\epsilon) = \frac{1}{4\pi D \sqrt{R^2+z^2}} e^{-\sqrt{\frac{(R^2+z^2)\epsilon}{D}}}. \quad (7.117)$$

Now substituting Eqs. (7.115) and (7.117) into the trapping prescription, Eq. (7.35), we obtain a new expression for the survival probability in Laplace domain

$$\begin{aligned}\tilde{Q}(\epsilon) &= \frac{1}{\epsilon} - \frac{e^{-\sqrt{(R^2+z^2)\epsilon/D}}}{\epsilon 4\pi D \sqrt{R^2+z^2}} \\ &\times \left\{ \frac{1}{C} + \frac{1}{(4\pi D)^{3/2}} \left[\frac{4R\epsilon}{\sqrt{\pi D}} {}_2F_3(A) - \frac{\sqrt{2D}}{R} \left[2\gamma + \ln \left(\frac{16R^2}{D} \right) \right] - 2\sqrt{\pi\epsilon} {}_1F_2(B) \right] \right\}^{-1},\end{aligned}\quad (7.118)$$

where ${}_pF_q$ is the generalized hypergeometric function, $A = 1, 1; 1, \frac{3}{2}, \frac{3}{2}, 2; \frac{R^2\epsilon}{D}$, $B = \frac{1}{2}; 1, \frac{3}{2}; \frac{R^2\epsilon}{D}$, and $\gamma = 0.57721\dots$ is Euler's constant. This expression cannot be inverted directly and must be evaluated through numerical methods.

7.8 Equivalence to theory of conduction of heat in solids

In the last section of this chapter, the equivalence of solutions obtained from sink terms and boundary conditions in reaction-diffusion equations is investigated. Many results, which were obtained by applying the trapping prescription, have been previously obtained by solving diffusion problems in the presence of boundary conditions. However, this equivalence only applies to translationally invariant systems.

7.8.1 Equivalence to constant-density initial condition in one-dimension

Most of the results derived from the trapping prescription presented in this chapter are equivalent to expressions obtained by solving the diffusion equation with a constant-density initial conditions and radiative or perfectly absorbing boundary condition. A collection of these results can be found in the book by Carslaw and Jaeger [141]. Due to the wide applicability of reaction-diffusion problems to the subject of trapping and absorption a large literature has developed [142, 143, 153, 157, 159, 160, 161], rederiving and using results collected in Ref. [141].

To outline this equivalence we investigate the problem of a particle diffusing in one-dimension in the presence of a stationary trap located at the origin. The absorption process at the trap site occurs at a finite rate. The equivalent problem solved in Ref. [141] is the one-dimensional diffusion equation

$$\frac{\partial c}{\partial t} = D \frac{\partial^2 c}{\partial x^2} \quad (7.119)$$

with constant-density initial condition $c(x,0) = c_0$ and radiative boundary condition at $x = 0$

$$\left. \frac{\partial c}{\partial x} \right|_{x=0} = hc(x,t)|_{x=0}. \quad (7.120)$$

Chapter 7. Repository of Exact Solutions for Stationary Trapping Problems

Here $c(x, t)$ is the one-dimensional concentration profile and h is the reaction rate at the boundary. The solution for $x \geq 0$ is

$$\frac{c(x, t)}{c_0} = \operatorname{erf}\left(\frac{x}{\sqrt{4Dt}}\right) + e^{hx+h^2Dt} \operatorname{erfc}\left(\frac{x}{\sqrt{4Dt}} + h\sqrt{Dt}\right). \quad (7.121)$$

When we compare this expression to the expression obtained for the survival probability due to a point initial condition given in Eq.(7.40)

$$Q(x_0, t) = \operatorname{erf}\left(\frac{x_0}{\sqrt{4Dt}}\right) + e^{\frac{C_{1d}x_0}{2D} + \frac{C_{1d}^2}{4D}t} \operatorname{erfc}\left(\frac{x_0}{\sqrt{4Dt}} + \frac{C_{1d}}{2}\sqrt{\frac{t}{D}}\right),$$

we notice that these two expressions are equivalent if $h = C_{1d}/(2D)$, where C_{1d} is the one-dimensional capture rate at the trap site in units of m/s . The equivalence of the two problems for simple diffusion and a single boundary has been pointed out by Rodriguez et al. [138].

7.8.2 Requirement on diffusion propagator for equivalence

To investigate why this equivalence occurs we look at the evolution of the probability density function. In general, the one-dimensional diffusion propagator in the presence of the trap is $\Pi(x, x'; t)$ and the probability to find a reactant at position x at time t is

$$c(x, t) = \int \Pi(x, x'; t) c(x', 0) dx', \quad (7.122)$$

where $c(x', 0)$ is the initial reactant distribution. To compare the result obtained from the trapping prescription to the expression obtained by Carslaw and Jaeger [141], we focus on two different initial conditions. For a point initial condition $c(x', 0) = \delta(x' - x_0)$ and for a uniform initial condition $c(x', 0) = c_0$. Substituting the point initial condition into Eq.(7.122) and integrating over x' we get

$$c(x, t) = \Pi(x, x_0; t). \quad (7.123)$$

Chapter 7. Repository of Exact Solutions for Stationary Trapping Problems

Since we are interested in the total reactant survival probability we integrate this expression over all space

$$Q(t) = \int c(x, t) dx \quad (7.124)$$

and obtain for a point initial condition

$$Q(t) = \int \Pi(x, x_0; t) dx. \quad (7.125)$$

Next, we substitute the uniform initial condition into Eq.(7.122) obtaining

$$\frac{c(x, t)}{c_0} = \int \Pi(x, x'; t) dx'. \quad (7.126)$$

Comparing Eqs.(7.124) and (7.126), we notice that these two expressions are only equivalent if $\Pi(x, x'; t) = \Pi(x', x; t)$. This condition is only true for translationally invariant systems, as pointed out by Redner [143].

To investigate this condition we compare the two quantities

$$\begin{aligned} Q(t, x_0) &= \int \Pi(x, x_0) dx \\ \frac{c(x, t)}{c_0} &= \int \Pi(x, x') dx' \end{aligned}$$

in more detail. Under which condition are they equivalent? To answer this, we start very generally by investigating these two quantities on a discrete lattice. On a lattice, the particle may occupy site m at a given probability $P_m = \sim -C\delta_{m,r}P_m$. If the particle jumps from site l to site m without translational invariance we may write in Laplace domain

$$\tilde{P}_{m,l} = \tilde{\eta}_{m,l} - C\tilde{\Pi}_{m,r}^0 \tilde{P}_{r,l}.$$

Here the trap is located at site r and $\Pi_{a,b}^0$ is the propagator in the absence of the trap. Since we can obtain $\tilde{P}_{r,l}$ from this expression, we obtain as a result an explicit expression of the propagator, which includes trapping

$$\tilde{\Pi}_{m,l} = \tilde{\Pi}_{m,l}^0 - \frac{\tilde{\Pi}_{r,l}^0 \tilde{\Pi}_{m,r}^0}{1/C + \tilde{\Pi}_{r,r}^0}. \quad (7.127)$$

Chapter 7. Repository of Exact Solutions for Stationary Trapping Problems

The expression in Eq.(7.127) is very useful. It tells us precisely how to calculate the propagator in the presence of traps if you know the propagator in the absence of the traps. At this point we calculate $\tilde{Q}(\epsilon)$, the number of surviving particles in Laplace domain for an initial point particle, which is obtained by summing Eq.(7.127) over lattice sites m

$$\tilde{Q}(\epsilon, l) = \sum_m \tilde{\Pi}_{m,l} = \frac{1}{\epsilon} \left[1 - \frac{\tilde{\Pi}_{r,l}^0}{1/C + \tilde{\Pi}_{r,r}^0} \right]. \quad (7.128)$$

Next we compute the equivalent quantity for a uniform initial distribution by summing Eq.(7.127) over lattice sites l

$$\frac{\tilde{c}(\epsilon, m)}{c_0} = \sum_l \tilde{\Pi}_{m,l} = \sum_l \tilde{\Pi}_{m,l}^0 - \frac{\left(\sum_l \tilde{\Pi}_{r,l}^0 \right) \tilde{\Pi}_{m,r}^0}{1/C + \tilde{\Pi}_{r,r}^0}. \quad (7.129)$$

If we define $\sum_l \tilde{\Pi}_{m,l}^0 = \tilde{\xi}_m$ and $\sum_l \tilde{\Pi}_{r,l}^0 = \tilde{\xi}_r$ we can write

$$\frac{\tilde{c}(\epsilon, m)}{c_0} = \tilde{\xi}_m - \frac{\tilde{\xi}_r \tilde{\Pi}_{m,r}^0}{1/C + \tilde{\Pi}_{r,r}^0}. \quad (7.130)$$

Since the probability sum over all sites of the homogeneous solution is always one we have $\tilde{\xi}_m = \tilde{\xi}_r = 1/\epsilon$ and hence obtain

$$\frac{\tilde{c}(\epsilon, m)}{c_0} = \frac{1}{\epsilon} \left[1 - \frac{\tilde{\Pi}_{m,r}^0}{1/C + \tilde{\Pi}_{r,r}^0} \right]. \quad (7.131)$$

Equations (7.128) and (7.131) are equivalent for $m = l$ if

$$\tilde{\Pi}_{l,r}^0 = \tilde{\Pi}_{r,l}^0.$$

Therefore, to have equivalence between these two approaches, translational invariance in the absence of a capture process is required. It is worth noting that a similar statement has been made by Szabo, Lamm, and Weis [132]. They showed that the trapping prescription can solve two problems. The first problem is described by sink terms and a point initial condition. As we have shown in this chapter, this problem can be solved by substituting the Laplace transform of the appropriate Green's function $\tilde{G}_f(x|x_0)$ in the absence of the

Chapter 7. Repository of Exact Solutions for Stationary Trapping Problems

reaction into the prescription. The second problem solved by the same prescription, is the boundary value problem. If the Green's function, which satisfies a purely reflecting boundary condition at the absorbing boundary $\tilde{G}_r(x|x_0) = \tilde{G}_f(x|x_0) + \tilde{G}_f(x|-x_0)$, is used, then the prescription gives the solution to the radiative boundary value problem. Hence, only when the Green's function is translationally invariant, $\tilde{G}_f(x|x_0) = \tilde{G}_f(x|-x_0)$ the two solutions become equivalent.

In the case of simple diffusion in one-dimension it is obvious that the free-space propagator or Green's function is translationally invariant. This is the reason for the equivalence of the solution for a point and uniform initial condition as outlined in section 7.8.1. To understand how such an equivalence may *not* be valid, consider a particle moving in a quadratic potential, $U(x) = \gamma x^2/2$ (see section 7.5.4). The diffusion propagator is now given by (see Eq.(7.56))

$$P(x, x_0, t) = \frac{1}{\sqrt{4\pi D\omega}} e^{-\frac{[x-x_0 \exp(-\gamma t)]^2}{4D\omega}},$$

where $\omega = (1 - \exp[-2\gamma t])/(2\gamma)$. This propagator is *not* translationally invariant

$$P(x, x_0, t) \neq P(x_0, x, t).$$

7.8.3 Relationship between reaction and capture rate

In this subsection the relationship between the reaction rate h due to radiative boundary conditions and the d-dimensional capture rate C_d for systems exhibiting invariant motion is investigated. From the diffusion equation one can compute the flux (number of particles per second crossing unit area), J , of the diffusing species $J = D\partial c/\partial r$. The total number of particles crossing the surface area per second is the particle current I given as

$$I(r) = \text{Area} * J = \text{Area} * D \left. \frac{\partial c}{\partial r} \right|_r. \quad (7.132)$$

Chapter 7. Repository of Exact Solutions for Stationary Trapping Problems

The current I can be related to the radiative boundary condition $\left. \frac{\partial c}{\partial r} \right|_r = h c(r)|_r$ via the reaction rate h as follows

$$I(r) = Area * D \left. \frac{\partial c}{\partial r} \right|_r = Area * Dh c(r)|_r. \quad (7.133)$$

Hence, $Area * Dh$ is the rate at which particles get trapped, which is equivalent to the trapping rate C_d giving the following relation

$$C_d = Area * Dh. \quad (7.134)$$

Here $Area$ corresponds to the surface area of the trap. Now in one-dimensions we have $C_{1d} = 2Dh$, in two-dimensions with a trap of radius R , $C_{2d} = 2\pi R Dh$, and in three-dimension with a spherical trap of radius R , $C_{3d} = 4\pi R^2 Dh$.

7.9 Permeable versus impermeable trapping boundaries

In a previous section 7.8.2 we have shown that a diffusion-reaction problem described by sink terms with a point initial condition give equivalent results as a similar problem described by radiation boundary condition with an initial continuous distribution if the motion is translationally invariant. However, even for translationally invariant motion there is a subtle difference between these two approaches. In principle, any boundary value problem may be solved by obtaining the appropriate Green's function of the diffusion equation and applying the Green's theorem. Here, the Green's function must satisfy either homogeneous Dirichlet or Neumann conditions.

However, there might be diffusion problems where it is not possible to provide the correct Green's function. Moreover, this method requires that reaction processes can be described adequately by boundary conditions. But there is no reason why the reaction process should be required to satisfy a boundary condition. As pointed out by Wilemski [163], the boundary condition may, and perhaps should, be considered only a consequence of a

particular choice of sink terms. Thus far, we have encountered multiple example where appropriate sink terms provide a better description of the reaction than do boundary conditions. In section 7.6.4, we discussed a problem of an open capturing region, which cannot be described by appropriate boundary conditions. In such systems, the boundary value approach cannot be used to solve the problem adequately. Another restriction is obvious from the following negative statement that surfaces when utilizing boundary conditions: "If the reactant is not absorbed it has to be reflected". This means that the requirement of satisfying boundary conditions does not allow one to describe permeable trapping boundaries. In section 7.7.2, we solved a reaction-diffusion model describing passive diffusion across biological membranes. To describe such systems, it is a requirement that the trapping boundary is permeable.

Finally, an alert reader might have noticed that some expressions obtained for $Q(t)$ and $\tilde{Q}(\epsilon)$ for permeable trapping boundaries are equivalent to expressions obtained from the boundary value counterpart describing impermeable walls. The goal of the present section is to investigate this point in more detail for translationally invariant systems in two- and three-dimensions.

7.9.1 Permeable membrane in two-dimensions

In section 7.6.2 we investigated the problem of a stationary circular trap and an initial circular symmetric distribution of diffusing non-interacting point particles at radius R_0 . The circular trap of radius R is centered at the origin, where $R < R_0$. This systems was properly described by a translationally invariant diffusion propagator given in Eq.(7.80). Hence according to our previous arguments, the solution to the differential equation obeying radiative boundary conditions at $r = R$ and an initial continuous distribution should be equivalent to the expression of $Q(t)$ obtained from the trapping prescription. This statement is true for an instantaneous absorption process at the boundary, since in both

Chapter 7. Repository of Exact Solutions for Stationary Trapping Problems

approaches instantaneous absorption describes an impermeable boundary. However, for finite absorption these two expressions are not equivalent. In this case $Q(t)$ is the solution obtained for a permeable trapping surface.

To investigate this observation, we directly compare the two expressions $\tilde{Q}(\epsilon)$ and $\tilde{c}(\epsilon)/c_0$. The exact expression for the particle survival probability in Laplace domain is given in Eq.(7.81)

$$\tilde{Q}(R_0\epsilon) = \frac{1}{\epsilon} \left(1 - \frac{\frac{1}{2\pi D} K_0 \left(R_0 \sqrt{\frac{\epsilon}{D}} \right) I_0 \left(R \sqrt{\frac{\epsilon}{D}} \right)}{\frac{1}{C_{2d}} + \frac{1}{2\pi D} K_0 \left(R \sqrt{\frac{\epsilon}{D}} \right) I_0 \left(R \sqrt{\frac{\epsilon}{D}} \right)} \right),$$

where $I_0(z)$ and $K_0(z)$ are the zero order modified Bessel function of the first and second kind, respectively. The equivalent problem of a spherical boundary satisfying radiative boundary conditions and an initial continuous distribution has been solved by Carslaw and Jaeger [141] as well as by Taitelbaum [153]. The expression in Laplace domain is

$$\frac{\tilde{c}(r, \epsilon)}{c_0} = \frac{1}{\epsilon} \left(1 - \frac{h K_0 \left(r \sqrt{\frac{\epsilon}{D}} \right)}{\sqrt{\frac{\epsilon}{D}} K_1 \left(R \sqrt{\frac{\epsilon}{D}} \right) + h K_0 \left(R \sqrt{\frac{\epsilon}{D}} \right)} \right), \quad (7.135)$$

where h is the reaction rate and $K_1(z)$ is the first order modified Bessel function of the second kind. We notice that in the limit of perfect absorption, $C_{2d} \rightarrow \infty$ and $h \rightarrow \infty$, both expressions are equivalent for $r = R_0$. To investigate whether these two expressions are equivalent imperfect absorber as well, Eq.(7.135) is rewritten as

$$\frac{\tilde{c}(r, \epsilon)}{c_0} = \frac{1}{\epsilon} \left[1 - \frac{\frac{1}{2\pi D} K_0 \left(r \sqrt{\frac{\epsilon}{D}} \right) I_0 \left(R \sqrt{\frac{\epsilon}{D}} \right)}{\frac{1}{2\pi D h} \sqrt{\frac{\epsilon}{D}} K_1 \left(R \sqrt{\frac{\epsilon}{D}} \right) I_0 \left(R \sqrt{\frac{\epsilon}{D}} \right) + \frac{1}{2\pi D} K_0 \left(R \sqrt{\frac{\epsilon}{D}} \right) I_0 \left(R \sqrt{\frac{\epsilon}{D}} \right)} \right]. \quad (7.136)$$

Comparing Eqs.(7.81) and (7.136), we notice that they are equivalent for $r = R_0$ if

$$\frac{1}{2\pi D h} \sqrt{\frac{\epsilon}{D}} K_1 \left(R \sqrt{\frac{\epsilon}{D}} \right) I_0 \left(R \sqrt{\frac{\epsilon}{D}} \right) \rightarrow \frac{1}{C_{2d}}.$$

Chapter 7. Repository of Exact Solutions for Stationary Trapping Problems

It turns out that this expression holds for $\varepsilon \rightarrow 0$ or equivalently in the long time limit. Using Ref. [151] it can be shown that for $z \rightarrow 0$

$$I_\nu(z)K_{(\nu+1)}(z) \rightarrow 1/z.$$

Hence in the limit of $\varepsilon \rightarrow 0$ the expression in the denominator of Eq.(7.136) becomes

$$\frac{1}{2\pi D h} \sqrt{\frac{\varepsilon}{D}} K_1 \left(R \sqrt{\frac{\varepsilon}{D}} \right) I_0 \left(R \sqrt{\frac{\varepsilon}{D}} \right) = \frac{1}{2\pi R D h}. \quad (7.137)$$

Now, we need to relate the reaction rate h to the two dimensional capture rate C_{2d} . A relation is derived in section 7.8.3, which gives $C_{2d} = 2\pi R D h$. This shows that the two expressions given in Eqs.(7.81) and (7.136) are equivalent in the long time limit for $R_0 = r$.

7.9.2 Permeable membrane in three-dimensions

It can also be shown that in the long time limit the two expressions for the three-dimensional case (see section 7.7.2) and a trapping spherical shell, are equivalent. For a spherical boundary of radius R centered at the origin and satisfying radiative boundary conditions, Carslaw and Jaeger [141] give the exact solution in time domain for an initial continuous particle distribution

$$\begin{aligned} \frac{c(r,t)}{c_0} = & 1 - \frac{hR^2}{r(Rh+1)} \operatorname{erfc} \left(\frac{r-R}{\sqrt{4Dt}} \right) \\ & + \frac{hR^2}{r(Rh+1)} e^{(h+\frac{1}{R})(r-R)+(h+\frac{1}{R})^2 Dt} \operatorname{erfc} \left[\frac{r-R}{\sqrt{4Dt}} + \left(h + \frac{1}{R} \right) \sqrt{Dt} \right]. \end{aligned} \quad (7.138)$$

To compare this expression to $\tilde{Q}(\varepsilon)$ given in Eq.(7.103)

$$\tilde{Q}(R_0, \varepsilon) = \frac{1}{\varepsilon} \left[1 - \frac{\frac{1}{4\pi R R_0 \sqrt{D\varepsilon}} e^{-R_0 \sqrt{\frac{\varepsilon}{D}}} \sinh \left(R \sqrt{\frac{\varepsilon}{D}} \right)}{\frac{1}{C_{3d}} + \frac{1}{4\pi R^2 \sqrt{D\varepsilon}} e^{-R \sqrt{\frac{\varepsilon}{D}}} \sinh \left(R \sqrt{\frac{\varepsilon}{D}} \right)} \right],$$

Eq.(7.138) is Laplace transformed (see Appendix B) to give after some re-arranging

$$\begin{aligned} \frac{\tilde{c}(r, \varepsilon)}{c_0} = & \frac{1}{\varepsilon} - \frac{1}{4\pi R \varepsilon^{3/2} \sqrt{D}} \\ & \times \left[\frac{\frac{1}{r} e^{-r\sqrt{\frac{\varepsilon}{D}}} \sinh\left(R\sqrt{\frac{\varepsilon}{D}}\right)}{\frac{1}{Rh} \left(\sqrt{\frac{\varepsilon}{D}} + \frac{1}{R}\right) e^{-R\sqrt{\frac{\varepsilon}{D}}} \sinh\left(R\sqrt{\frac{\varepsilon}{D}}\right) + \frac{1}{R} e^{-R\sqrt{\frac{\varepsilon}{D}}} \sinh\left(R\sqrt{\frac{\varepsilon}{D}}\right)} \right]. \end{aligned} \quad (7.139)$$

Comparing Eqs.(7.103) and (7.139) we see that they are equivalent for perfect absorption, $h \rightarrow \infty$ and $C_{3d} \rightarrow \infty$. This equivalence is expected since for instantaneous reaction at the boundary as well as trap sites, the spherical boundary is impermeable. The two results are also the same if the first term in the denominator of Eq.(7.139) goes to $1/C_{3d}$. To obtain this equivalence in the long time limit we look at the following expression as $z \rightarrow 0$

$$\lim_{z \rightarrow 0} \left[\left(1 + \frac{1}{z} \right) \exp(-z) \sinh z \right] = 1,$$

which results for $\varepsilon \rightarrow 0$ in

$$\frac{1}{4\pi R^2 D h} \left(1 + \frac{1}{R} \sqrt{\frac{D}{\varepsilon}} \right) e^{-R\sqrt{\frac{\varepsilon}{D}}} \sinh\left(R\sqrt{\frac{\varepsilon}{D}}\right) \rightarrow \frac{1}{4\pi R^2 D h}.$$

Since $C_{3d} = 4\pi R^2 D h$ (see section 7.8.3) Eqs.(7.103) and (7.139) are equivalent in the long time limit for $R_0 = r$.

7.9.3 Importance of transient effect

As outlined above in two-dimensions for a finite reaction, the solution for the particle survival probability for a radially distributed point particle initial condition at R_0 and a circular trapping ring at $R < R_0$ is equivalent to the expression obtained by imposing a radiative boundary condition at R and a continuous initial condition in the long time limit. We have pointed out that this result is due to the resulting permeable and impermeable

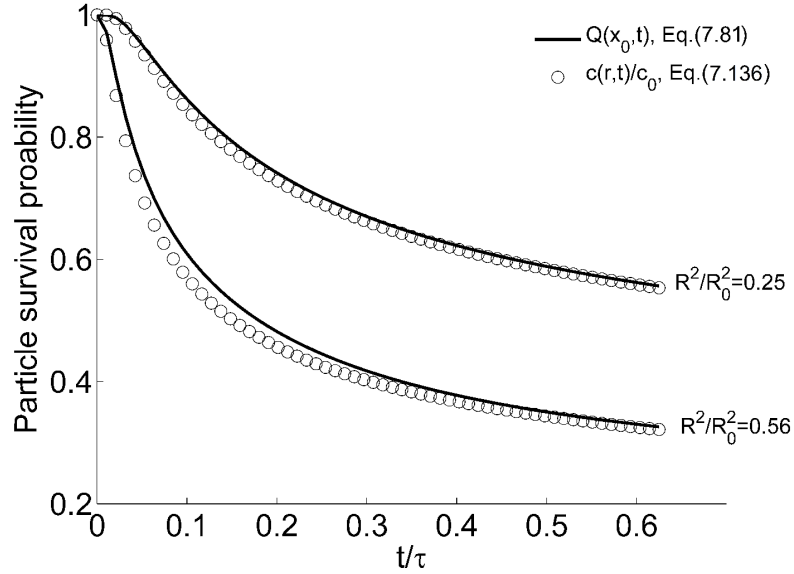


Figure 7.1: Survival probability obtained via a numerical Laplace inversion from Eq.(7.81) (line) describing a permeable circular trapping ring of radius R with an initial distribution of point particles at $R_0 > R$ and Eq.(7.136) (open circles) describing a radiative boundary condition at $r = R$ (impermeable boundary) and a continuous initial condition. Both solutions describe a two-dimensional reaction-diffusion system. In the long time limit, $t/\tau > R^2/R_0^2$, and $r = R_0$ the two functional forms become equivalent. This transient effect is related to the time, $t_{trans} = R^2/D$, it takes a particle to diffuse inside the circular trapping region of radius R . Here $\tau = R_0^2/D = r^2/D$, $D/C_{2d} = 1$ and $h = C_{2d}/(2\pi RD)$.

trapping boundaries, respectively. The same observation is applicable for an equivalent three-dimensional system with a spherical trapping boundary. Figure 7.1 compares the two expression, $Q(R_0, t)$ and $c(r, t)/c_0$ with $r = R_0$, for the two-dimensional system given in Eq.(7.81) (line) and Eq.(7.136) (open circles), respectively. It is apparent from the Fig 7.1 that $Q(R_0, t)$ decays slower than $c(r, t)/c_0$ until approximately $t/\tau = R^2/R_0^2$ with $\tau = R_0^2/D = r^2/D$, after which these two expressions become equivalent. This observation suggests that at short time, the transient time $t_{trans} = R^2/D$ it takes a particle to diffuse around inside the trap, the particle has less opportunities to get captured if the trapping boundary is permeable.

7.10 Concluding Remarks

This chapter serves as a repository [162] of some exact solutions for reaction-diffusion systems in d -dimensions. The discussion focuses on static traps with non-infinite capture rate centered at the origin and point initial conditions. We have applied existing formalisms [23, 132] to derive several results in this chapter. Some of them we have found in earlier literature, after we derived them. To the best of our knowledge, equations (7.20), (7.47), (7.61), (7.72), (7.74), (7.75), (7.81), (7.84), (7.97), (7.103), (7.108), and (7.118) are new.

By investigating reaction-diffusion problems described by sink terms and point initial conditions, a natural connection to boundary value problems is made. It is known that for translationally invariant particle motion in one-dimension, the expression obtained from the trapping prescription is equivalent to the solution obtained from a diffusion equation [138, 143]. To obtain equivalency, the diffusion equation must satisfy proper radiative boundary conditions subject to a continuous initial condition. In section 7.8, we show that the equivalence holds only if the motion propagator is translationally invariant in the absence of the reaction. However, as pointed out earlier [163], there are many reaction-diffusion systems which cannot be described by boundary value problems. It has been suggested in that work that the boundary condition used to solve boundary value problems may, and perhaps should, be considered only a consequence of a particular choice of sink terms. For example, as discussed at the beginning of section 7.9, the kinetics of particle motion in the presence of an open trapping surface cannot be described properly by a boundary value problem. Moreover, its application is limited to impermeable absorbing boundaries, since an unsuccessful reaction always results in particle reflection away from the boundary. Therefore, to model permeable absorbing membranes, the sink term approach must be used. The difference between these two approaches becomes evident for translationally invariant particle motion in higher dimensions, specifically in the presence of a static trapping ring or sphere. The resulting expressions are only equivalent when the

Chapter 7. Repository of Exact Solutions for Stationary Trapping Problems

reaction occurs instantaneously. This should not be surprising, since both models describe an impermeable perfectly absorbing boundary. For finite reaction, the two expressions are not identical, since the boundary described by partially absorbing sink terms is permeable. In this system the particle can move around inside the trapping ring or sphere. For long time, after the particle probed the entire trapping volume, the two approaches give equivalent results. This investigation is outlined in section 7.9 and our findings are believed to be new contributions in the field of reaction-diffusion systems.

Chapter 8

Validity of an Adiabatic Approximation in a Reaction-Diffusion System

8.1 Introduction

By constructing a theory of receptor cluster coalescence, which is formulated as a trapping problem with a trap whose location (boundary) changes dynamically, we have encountered naturally the problem of moving boundaries. In the present chapter, we focus on moving boundary problems in reaction-diffusion systems. We present a simple analysis of the validity of an adiabatic approximation for moving boundaries with assigned time dependence. A succinct description of this adiabatic approximation is that it consists of inserting the time dependence of the moving boundary into the static problem, which we know how to solve exactly, see chapter 7. Results obtained from the validity study of this approximation, presented in this chapter, are used in chapter 9, where we construct a simplified theory for the more general systems in which the traps or boundaries move/grow due to particle aggregation.

In the following sections, we will focus on systems of two or three particles. The mo-

Chapter 8. Validity of an Adiabatic Approximation in a Reaction-Diffusion System

tion of the particles can be probabilistic and/or deterministic. In these systems, a particle diffuses in the presence of a single or two traps/boundaries, which move with an explicitly assigned time dependence. Throughout the present chapter, *traps* and *boundaries*, as used in our terminology, are distinguished as follows. When a particle reaches a trap it is absorbed at a finite rate with the ability to pass through a trap without being absorbed. On the other hand, a particle in contact with a boundary is absorbed instantaneously and cannot penetrate the boundary. In sections 8.2 and 8.3, we analyze the validity of an adiabatic approximation in systems of one moving particle in the presence of a moving trap. For systems of two linearly moving boundaries with a single particle placed between them, the stationary boundary problem, which is used to construct an adiabatic approximation, is solved in section 8.4. In section 8.5, we outline how for certain systems one can exactly solve for the particle survival probability in the presence of two moving traps by introducing a boundary fixing transformation. For example, the problem of two boundaries moving with the same time dependence can be solved exactly and hence be used to validate our adiabatic approximation (see section 8.6). In sections 8.6 and 8.8, systems of receding and oscillating boundaries will be discussed.

It is worth noting that many problems arising in science and engineering such as heat flow, molecular diffusion, and flame propagation involve a domain whose boundary changes its shape and size in time. These problems are described by a differential equation, which has to satisfy certain conditions on the boundary and are typically called boundary-value problems, referred to in certain circles as Stefan problems, see Refs. [117, 119]. In boundary-value problems, the boundary of the domain is not known and has to be assigned as part of the solution. One differentiates between two types of problems: Free-boundary problems describing stationary boundaries for which a steady-state solution exists and time-dependent moving-boundary problems in which the position of the boundary has to be described as a function of time and space. Due to the general applicability of moving boundary problems, our analysis presented in this section will, naturally, also give some new insight on these subjects.

8.2 A single diffusing trap

First, we study the validity of an adiabatic approximation for the simplest system of a particle and a trap moving in one-dimension. The trap and the particle, initially a distance x_0 apart, diffuse with a diffusion constant D_θ and D_p , respectively, and annihilate each other on contact. This annihilation process may occur at a finite rate. For instantaneous annihilation, this problem was solved for the survival probability Q by Kenkre [24] on a discrete lattice in Laplace domain and in continuum by Spouge [136] giving the time-dependent survival probability Q as

$$Q\left(\frac{t}{\tau}\right) = \text{erf}\left(\frac{1}{2}\sqrt{\frac{\tau}{t(\alpha+1)}}\right), \quad (8.1)$$

where $\tau = x_0^2/D_p$ is the motion time of the particle and $\alpha = D_\theta/D_p$ is the ratio of the two diffusion constants. When $\alpha = 0$, we recover the well known result for a single stationary trap and a particle diffusing with D_p [141]

$$Q\left(\frac{t}{\tau}\right) = \text{erf}\left(\frac{1}{2}\sqrt{\frac{\tau}{t}}\right). \quad (8.2)$$

This result is expected since Eq.(8.1) is analogous to the survival probability for a fixed trap, Eq.(8.2), but replacing D_p by $D_p + D_\theta$. In a similar fashion, one can construct an adiabatic approximation for Eq.(8.1) by inserting the time dependence of the trap directly into x_0 in the stationary solution, Eq.(8.2). Hence, for a diffusing trap $x_0 \rightarrow x_0 \pm \sqrt{2D_\theta t}$ to account for a trap diffusion to the left and right. In this case an adiabatic approximation may be written as the arithmetic average of two expressions

$$Q_{adia}\left(\frac{t}{\tau}\right) = \frac{1}{2}\text{erf}\left(\frac{1}{2}\sqrt{\frac{\tau}{t}} + \sqrt{\frac{\alpha}{2}}\right) + \frac{1}{2}\text{erf}\left(\frac{1}{2}\sqrt{\frac{\tau}{t}} - \sqrt{\frac{\alpha}{2}}\right). \quad (8.3)$$

As expected for a stationary trap, $\alpha = 0$, Eq.(8.3) reduces to Eq.(8.2). Figure 8.1 compares the exact solution, Eq.(8.1), represented by the solid line to the adiabatic approximation, Eq.(8.3), depicted by open triangles for $\alpha = 0$, $\alpha = 1$, and $\alpha = 10$. When α increases the trap diffuses faster than the particle and the adiabatic approximation deviates significantly from the exact solution. In the long time limit, both expressions go to zero.

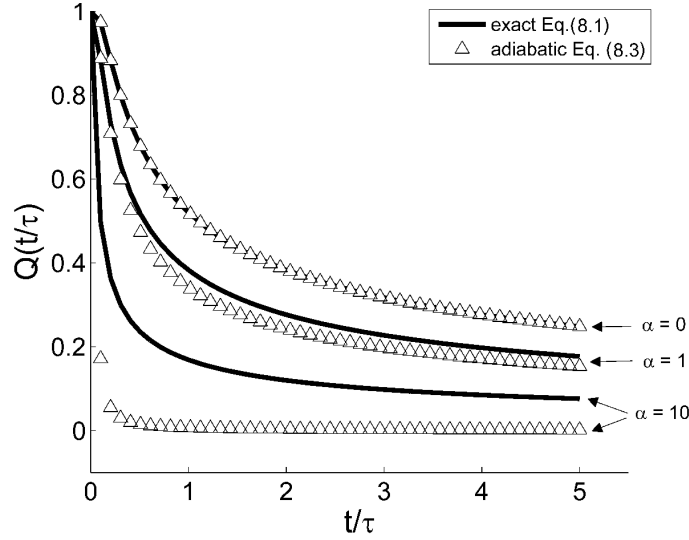


Figure 8.1: Trap and particle both move randomly and annihilate instantaneously on contact. Exact solution Eq.(8.1) (line) is compared to our adiabatic approximation Eq.(8.3) (open triangles) for $\alpha = 0$, $\alpha = 1$, and $\alpha = 10$.

Next, we investigate the validity of our approximation for the case of finite annihilation. For a stationary trap located at the origin and a diffusing particle initially at x_0 the solution is well known [141, 138, 143] and the survival probability is given as

$$Q\left(\frac{t}{\tau}\right) = \text{erf}\left(\frac{1}{2}\sqrt{\frac{\tau}{t}}\right) + e^{\frac{1}{\xi} + \frac{1}{\xi^2}\frac{t}{\tau}} \text{erfc}\left(\frac{1}{2}\sqrt{\frac{\tau}{t}} + \frac{1}{\xi}\sqrt{\frac{t}{\tau}}\right). \quad (8.4)$$

Here, $\xi = \frac{2D_p}{Cx_0}$ describes the capture process and C is the annihilation rate. In the limit of instantaneous annihilation $C \rightarrow \infty$ or $\xi \rightarrow 0$, Eq.(8.4) becomes the perfect absorption result, Eq.(8.2). To obtain the solution for a system in which both the trap and the particle move, we replace D_p with $D_p + D_\theta$, which is equivalent to a transformation into the particle's reference frame to obtain

$$Q\left(\frac{t}{\tau}\right) = \text{erf}\left(\frac{1}{2}\sqrt{\frac{\tau}{t(\alpha+1)}}\right) + e^{\frac{1}{\xi(\alpha+1)} + \frac{1}{\xi^2}\frac{t}{(\alpha+1)\tau}} \text{erfc}\left(\frac{1}{2}\sqrt{\frac{\tau}{t(\alpha+1)}} + \frac{1}{\xi}\sqrt{\frac{t}{(\alpha+1)\tau}}\right). \quad (8.5)$$

As expected for $\alpha = 0$, the above expression reduces to the stationary trap result(see

Chapter 8. Validity of an Adiabatic Approximation in a Reaction-Diffusion System

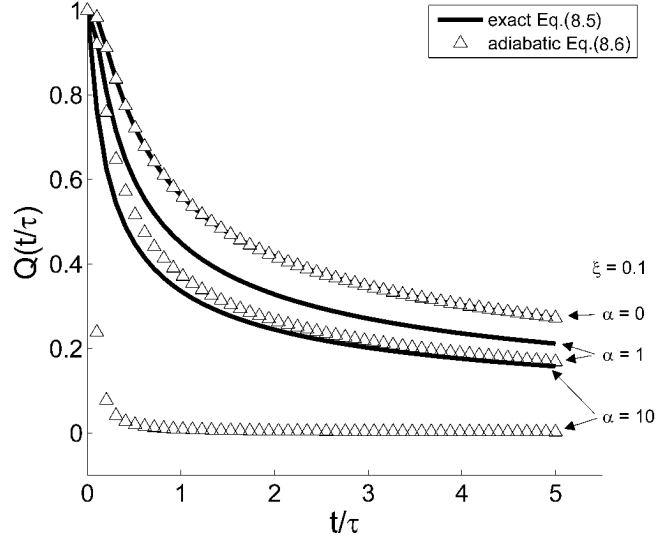


Figure 8.2: Trap and particle both move randomly and annihilate at a finite rate on contact. Exact solution Eq.(8.5) (solid line) is compared to our adiabatic approximation Eq.(8.6) (open triangles) for $\alpha = 0$, $\alpha = 1$, and $\alpha = 10$ with $\xi = 0.1$.

Eq.(8.2)). To construct an adiabatic approximation for Eq.(8.5), x_0 in τ is replaced by $x_0 \pm \sqrt{2D_0 t}$ in Eq.(8.4) and the arithmetic average of the two expressions is computed

$$\begin{aligned}
 Q_{adia}\left(\frac{t}{\tau}\right) &= \frac{1}{2} \left[\operatorname{erf}\left(\frac{1}{2}\sqrt{\frac{\tau}{t}} + \sqrt{\frac{\alpha}{2}}\right) + \operatorname{erf}\left(\frac{1}{2}\sqrt{\frac{\tau}{t}} - \sqrt{\frac{\alpha}{2}}\right) \right] \\
 &+ \frac{1}{2} e^{\frac{1}{\xi} + \frac{1}{\xi^2} \frac{t}{\tau} - \frac{1}{\xi} \sqrt{\frac{2\alpha}{\tau}}} \operatorname{erfc}\left(\frac{1}{2}\sqrt{\frac{\tau}{t}} - \sqrt{\frac{\alpha}{2}} + \frac{1}{\xi} \sqrt{\frac{t}{\tau}}\right) \\
 &+ \frac{1}{2} e^{\frac{1}{\xi} + \frac{1}{\xi^2} \frac{t}{\tau} + \frac{1}{\xi} \sqrt{\frac{2\alpha}{\tau}}} \operatorname{erfc}\left(\frac{1}{2}\sqrt{\frac{\tau}{t}} + \sqrt{\frac{\alpha}{2}} + \frac{1}{\xi} \sqrt{\frac{t}{\tau}}\right). \quad (8.6)
 \end{aligned}$$

For a stationary trap, $\alpha = 0$, Eq.(8.5) and the adiabatic approximation Eq.(8.6) are equivalent. Figure 8.2 compares the exact solution in Eq.(8.5) (line) to the adiabatic approximation in Eq.(8.6) (open triangles) for $\xi = 0.1$ and three different values of: $\alpha = 0$, $\alpha = 1$, and $\alpha = 10$. Similarly, to perfect absorption, the approximation deviates with increasing α and seems to get worse when annihilation occurs at a probability less than one i.e. increasing ξ (compare Fig. 8.1 to Fig. 8.2).

8.3 A linearly moving trap

Another, more complex system, for which the exact solution is known, is the system in which both the trap and particle undergo biased diffusion. In this section we will consider a specific case in which a trap moving at constant speed v_θ drifts towards a diffusing particle. The trap and the particle are initially a distance x_0 apart and the annihilation process is taken to occur instantaneously. The problem can be solved by transforming to the reference frame of the particle in which the trap is performing a biased diffusion towards the particle. The more general problem, in which both undergo biased diffusion, was solved independently by Szabo et al. [132] and Sanchez [164]. The survival probability Q for the case discussed here reduces from Sanchez's result

$$Q\left(\frac{t}{\tau}\right) = 1 - \frac{1}{2} \operatorname{erfc}\left(\frac{1}{2}\sqrt{\frac{\tau}{t}} - \frac{1}{\beta}\sqrt{\frac{t}{\tau}}\right) - \frac{1}{2} e^{2/\beta} \operatorname{erfc}\left(\frac{1}{2}\sqrt{\frac{\tau}{t}} + \frac{1}{\beta}\sqrt{\frac{t}{\tau}}\right). \quad (8.7)$$

It is worth mentioning that the same result is obtained by applying the general trapping prescription outlined in chapter 7. Here, it is convenient to define a new dimensionless parameter $\beta = \frac{2D_p}{v_\theta x_0}$ which describes the drift process. As expected for zero drift or $\beta \rightarrow \infty$, Eq.(8.7) reduces to the stationary trap result Eq.(8.2). Also, in the long time limit, this expression goes to zero as is expected for perfect absorption. Following the procedure outlined above we can construct an adiabatic approximation for a trap drifting towards a diffusing particle by replacing x_0 in τ with $x_0 - v_\theta t$ in the stationary trap result Eq.(8.2)

$$Q_{adia}\left(\frac{t}{\tau}\right) = \operatorname{erf}\left(\frac{1}{2}\sqrt{\frac{\tau}{t}} - \frac{1}{\beta}\sqrt{\frac{t}{\tau}}\right). \quad (8.8)$$

Inspecting Eq.(8.8), we see that Q becomes negative for $x_0 < v_\theta t$ and hence the approximation becomes unphysical. In Fig. 8.3 the exact solution Eq.(8.7) for perfect annihilation (solid line) is compared to its adiabatic approximation Eq.(8.8) (open triangles) for two values of $\beta = 8$ and $\beta = 50$. The comparison suggests that the adiabatic approximation works well for a slowly moving trap (large β) and becomes unphysical (negative) for $x_0 < vt$ or $\tau < 2t/\beta$. We note that in our experiments, the boundary of the central

Chapter 8. Validity of an Adiabatic Approximation in a Reaction-Diffusion System

receptor patch moves at an estimated speed of $v_x = 0.003 \mu\text{m}/\text{s}$ in the first 70 s of cell-substrate contact. This boundary speed together with a cluster diffusivity $D \sim 0.01 \mu\text{m}^2/\text{s}$ and $x_0 = 350 \text{ nm}$ (estimated initial distance between clusters) gives $\beta = 20$, suggesting that the adiabatic approximation can be applied to experiments. Finally, In the limit when $\beta \rightarrow \infty$ or equivalently $v \rightarrow 0$, the approximation in Eq.(8.8) becomes Eq.(8.2). Krapivsky

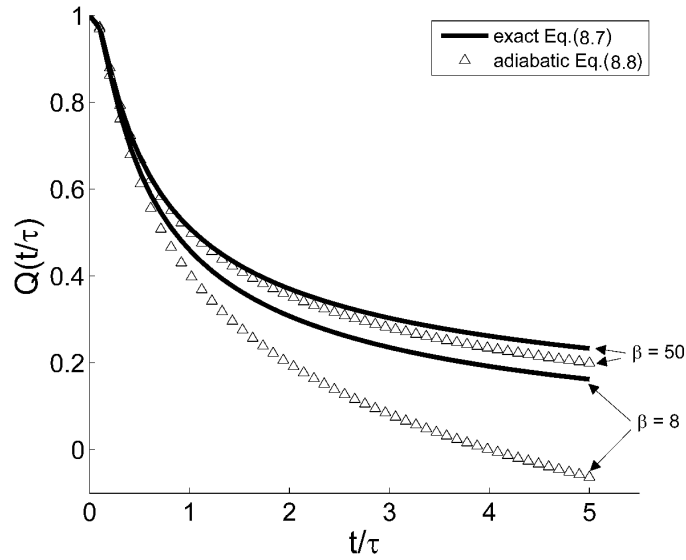


Figure 8.3: The particle moves randomly and the trap is biased towards the particle. When the particle and the trap meet they annihilate instantaneously. Exact solution given in Eq.(8.7) (solid line) compared to adiabatic approximation in Eq.(8.8) (open triangles) for $\beta = 8$ and $\beta = 50$. The approximation given in Eq.(8.8) becomes negative and unphysical when $x_0 < v_t t$.

and Redner [165] analyzed the validity of another adiabatic approximation for the case of a trap receding at a constant speed from a diffusing particle. The trap time dependence was directly inserted into the probability density function $P(x, t)$ of the stationary result. The approximations was obtained by inserting the new $P_{new}(x, t)$ into the diffusion equation and solving for the total survival probability $Q(t)$, which is obtained by integrating $P_{new}(x, t)$ over x .

Next, we consider the same system with finite annihilation for which the exact solution

is given as [164]

$$\begin{aligned}
 Q\left(\frac{t}{\tau}\right) = & 1 - \frac{1}{2} \left(\frac{1}{1 - \xi/\beta} \right) e^{2/\beta} \operatorname{erfc} \left(\frac{1}{2} \sqrt{\frac{\tau}{t}} + \frac{1}{\beta} \sqrt{\frac{t}{\tau}} \right) \\
 & - \frac{1}{2} \left(\frac{1}{1 + \xi/\beta} \right) \operatorname{erfc} \left(\frac{1}{2} \sqrt{\frac{\tau}{t}} - \frac{1}{\beta} \sqrt{\frac{t}{\tau}} \right) \\
 & + \frac{1}{1 - (\xi/\beta)^2} e^{\frac{1}{\beta} + \frac{1}{\xi} + \frac{t}{\tau} \left(\frac{1}{\xi^2} - \frac{1}{\beta^2} \right)} \operatorname{erfc} \left(\frac{1}{2} \sqrt{\frac{\tau}{t}} + \frac{1}{\xi} \sqrt{\frac{t}{\tau}} \right). \quad (8.9)
 \end{aligned}$$

The expression for the total survival probability Q given in Eq.(8.9) starts at 1 and goes to a positive constant $\frac{\xi/\beta}{\xi/\beta - 1}$. This limit is expected since for finite absorption the particle can pass through the trap which is then moving away from the particle and hence might never be absorbed. Hence, to construct an adiabatic approximation, we must include the fact that the trap first moves towards the diffusing particle and if they don't annihilate, the trap moves away from the particle. To approximate this process, x_0 in τ is replaced by $x_0 \pm v_t t$ in the stationary result Eq.(8.4) and the arithmetic average of the two expressions gives an

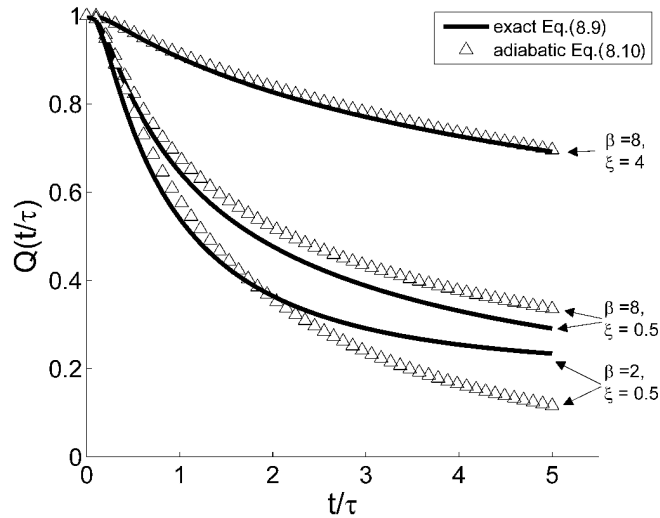


Figure 8.4: The particle moves randomly and the trap is biased towards the particle with finite annihilation. Exact solution given in Eq.(8.9) (solid line) compared to the adiabatic approximation in Eq.(8.10) (open triangles) for $\beta = 8$ with $\xi = 4$ or $\xi = 0.5$ and $\beta = 2$ with $\xi = 0.5$.

approximated survival probability

$$\begin{aligned}
 Q\left(\frac{t}{\tau}\right)_{adia} &= \frac{1}{2}erf\left(\frac{1}{2}\sqrt{\frac{\tau}{t}} - \frac{1}{\beta}\sqrt{\frac{t}{\tau}}\right) + \frac{1}{2}erf\left(\frac{1}{2}\sqrt{\frac{\tau}{t}} + \frac{1}{\beta}\sqrt{\frac{t}{\tau}}\right) \\
 &+ \frac{1}{2}e^{\frac{1}{\xi} + \frac{t}{\tau}\left(\frac{1}{\xi^2} - \frac{2}{\xi\beta}\right)}erfc\left[\frac{1}{2}\sqrt{\frac{\tau}{t}} + \sqrt{\frac{t}{\tau}}\left(\frac{1}{\xi} - \frac{1}{\beta}\right)\right] \\
 &+ \frac{1}{2}e^{\frac{1}{\xi} + \frac{t}{\tau}\left(\frac{1}{\xi^2} + \frac{2}{\xi\beta}\right)}erfc\left[\frac{1}{2}\sqrt{\frac{\tau}{t}} + \sqrt{\frac{t}{\tau}}\left(\frac{1}{\xi} + \frac{1}{\beta}\right)\right]. \tag{8.10}
 \end{aligned}$$

For long time, the approximation given in Eq.(8.10) goes to zero and hence deviates from the exact solution in Eq.(8.9), which approaches a constant except for $\beta \rightarrow \infty$ ($v \rightarrow 0$) or $\xi \rightarrow 0$ ($C \rightarrow \infty$), when it approaches zero as expected. Figure 8.4 compares the adiabatic approximation given in Eq.(8.10) (open triangles) to the exact solution in Eq.(8.9) (solid line) for three different sets of parameters: $\beta = 8$ with $\xi = 4$ or $\xi = 0.5$, and $\beta = 2$ with $\xi = 0.5$. When Fig. 8.3 is compared to Fig. 8.4 for $\beta = 8$ it is apparent that the approximation becomes better at early time when annihilation is not instantaneous.

8.4 Two stationary traps

Thus far, we have considered systems of two moving particles annihilating at a given probability on contact. In the remaining sections, we consider systems of three particles, where one particle is initially placed between two moving boundaries. Both, the particle and boundaries, can undergo probabilistic and/or deterministic motion. For the case of three particles performing probabilistic motion, the exact solution for instantaneous annihilation was worked out by Fisher and Gelfand [166]. In the remaining sections of this chapter, we analyze the validity of an adiabatic approximation for deterministic boundary motion by comparison to exact analytical or numerical solutions. Since exact solutions for three particle systems are only known for perfect absorption, the remaining chapter will focus on instantaneous annihilation.

Chapter 8. Validity of an Adiabatic Approximation in a Reaction-Diffusion System

In order to construct an adiabatic approximation for a system of two moving boundaries and a diffusing particles, the stationary trap result must be obtained. To compute the survival probability of a diffusing particle initially placed at x_0 between two stationary traps we use the general prescription given in chapter 7. In Laplace domain Q , is given in Eq.(7.35) as

$$\tilde{Q}(\epsilon) = \frac{1}{\epsilon} \left[1 - \frac{\sum_r' \tilde{\eta}_r(\epsilon)}{\frac{1}{C_d} + \sum_s' \tilde{\Pi}_{s,r}(\epsilon)} \right] \quad (8.11)$$

where, C is the d-dimensional capture rate, \sum_r' represents the sum over all trap sites, $\tilde{\eta}_r$ is the homogeneous solution at trap site in the absence of the trap, and $\tilde{\Pi}_{s,r}$ it the propagator from trap site r to trap site s in absence of the trap. Due to symmetry in the stationary trap problem, the propagator from trap site $-L$ to L is identical to the propagator from trap site L to $-L$. Hence, for two traps at $x = -L$ and $x = L$, the prescription gives

$$\tilde{Q}(\epsilon) = \frac{1}{\epsilon} \left[1 - \frac{\tilde{\eta}_{-L} + \tilde{\eta}_L}{\frac{1}{C_{ld}} + \tilde{\Pi}_0 + \tilde{\Pi}_{-L-L}} \right], \quad (8.12)$$

where $\tilde{\eta}$ and $\tilde{\Pi}$ are obtained from the one-dimensional free space diffusion propagator

$$P(x, x_0; t) = \frac{1}{\sqrt{4\pi Dt}} e^{-\frac{(x-x_0)^2}{4Dt}}$$

e.g. $\eta_{-L} = P(-L, x_0; t)$, $\Pi_0 = P(0, 0; t)$, $\Pi_{-L-L} = P(-L, -L; t)$, to give

$$\tilde{Q}(\epsilon) = \frac{1}{\epsilon} \left[1 - \frac{e^{-|L+x_0|\sqrt{\frac{\epsilon}{D}}} + e^{-|L-x_0|\sqrt{\frac{\epsilon}{D}}}}{\frac{\sqrt{4D\epsilon}}{C_{ld}} + 1 + e^{-2L\sqrt{\frac{\epsilon}{D}}}} \right]. \quad (8.13)$$

Although, we arrived at this expression independently, we discovered that Eq.(8.13) was derived by Abramson and Wio [167] (note typo in Eq.(6) of [167]). For a finite absorption process, Eq.(8.13) cannot be inverted exactly. However, for perfect absorption $C_{ld} \rightarrow \infty$ and Q becomes for $-L < x_0 < L$

$$\tilde{Q}(\epsilon) = \frac{1}{\epsilon} - \frac{\cosh\left(x_0\sqrt{\frac{\epsilon}{D}}\right)}{\epsilon \cosh\left(L\sqrt{\frac{\epsilon}{D}}\right)}. \quad (8.14)$$

Using a table of Laplace transforms [133], the expression for Q can be inverted to give

$$Q(t) = \frac{\sqrt{D}}{L} \int_0^{\frac{1}{\sqrt{D}}(L+x_0)} \theta_2 \left(\frac{u\sqrt{D}}{2L} \middle| \frac{tD}{L^2} \right) du, \quad (8.15)$$

where $\theta_2(v|x)$ is the theta function defined as

$$\theta_2(v|x) = \frac{1}{\sqrt{\pi x}} \sum_{n=-\infty}^{\infty} (-1)^n e^{-\frac{1}{x}(v+n)^2} \quad (8.16)$$

yielding

$$Q(t) = \sum_{n=-\infty}^{\infty} (-1)^n \left\{ \operatorname{erf} \left[\frac{x_0 + L(2n+1)}{\sqrt{4Dt}} \right] - \operatorname{erf} \left[\frac{nL}{\sqrt{Dt}} \right] \right\}. \quad (8.17)$$

Equation (8.17) is a new expression, which we have not found in the literature. Surely, the stationary two boundary problem can also be solved by a superposition method of images, where one uses an infinite set of images (of the traps) to satisfy the boundary conditions. In our expression (8.17), this superposition of multiple images is reflected by the summation above. Also, the appearance of the theta function above is expected since that function is a solution to the diffusion equation for periodic boundary conditions and an initial Dirac delta function [168, 169]. Therefore it is intriguing that the derivation of the MSD by Kenkre et al. [31] (see Eq.(19) in [31]) is also a theta elliptic function for infinite stationary barriers through which there is a finite particle transmission. It remains to be investigated, how the survival probability Q is connected to the MSD and what the physical meaning of the appearance of the elliptic function is, given that it appears naturally in Ref. [31].

8.5 Two moving boundaries: boundary fixing transformation

The problem of two moving boundaries with an explicitly assigned time dependence can be transformed into a fixed boundary problem for diffusion occurring between two boundaries at $x = S(t)$ and $x = R(t)$ representing the left and right boundary, respectively. Here,

Chapter 8. Validity of an Adiabatic Approximation in a Reaction-Diffusion System

when a diffusing particle reaches one of the boundaries it is absorbed instantaneously. The problem can be described by the standard one-dimensional diffusion equation, which is solved for the probability density $P(x, t)$

$$\frac{\partial P}{\partial t} = D \frac{\partial^2 P}{\partial x^2} \quad (8.18)$$

with $dR/dt = R'$ and $dS/dt = S'$. The boundary conditions are $P[S(t), t] = 0$ and $P[R(t), t] = 0$ with initial conditions $P(x, 0) = \delta(x - x_0)$, $R(0)$, and $S(0)$. To solve Eq.(8.18) for $P(x, t)$, the moving boundary problem is transformed to a fixed boundary problem by introducing a time-dependent scaling factor [119]

$$z = \frac{x - S(t)}{R(t) - S(t)}. \quad (8.19)$$

This transformation fixes the boundaries at $z = 0$ and $z = 1$ for all times. Rewriting $P(x, t)$ as $U[z(x, t), t]$ and introducing a new variable θ , Eq.(8.18) becomes

$$\frac{\partial U}{\partial \theta} = D \frac{\partial^2 U}{\partial z^2} - f(z, \theta) \frac{\partial U}{\partial z}, \quad (8.20)$$

where $d\theta = dt/[R(t) - S(t)]^2$ and $f(z, \theta) = [R(t) - S(t)][R' + z(R' - S')]$. Equation (8.20) is in the form of a convection-diffusion equation, where D is the diffusion coefficient and $f(z, \theta)$ the drift coefficient. To solve the moving two boundary problem with an explicitly assigned time dependence via the stationary trap prescription given in Eq.(8.11), one has to calculate the free space propagator satisfying Eq.(8.20). However, since the drift coefficient is dependent on time, θ , and space z , there is no general solution holding for all drift and diffusion propagators. However, for small times θ_s Risken [150] derived an approximate expression for the free space propagator satisfying the Fokker-Planck equation with time and space dependent drift and diffusion coefficients. Following Risken, the general short time free space propagator for Eq.(8.20) is

$$U(z, z_0, \theta_s) = \frac{1}{\sqrt{4\pi D \theta_s}} \exp \left\{ -\frac{[z - z_0 - f(z_0, \theta_s) \theta_s]^2}{4D \theta_s} \right\}. \quad (8.21)$$

For drift and diffusion coefficients independent of z and θ , Eq.(8.21) is valid for all times. An exact expression for the free space propagator can be obtained for a system of two

Chapter 8. Validity of an Adiabatic Approximation in a Reaction-Diffusion System

boundaries with identical assigned time dependence. For such systems $R' = S'$ and $f(z, \theta)$ is independent of z . In this case, it is straight forward to obtain the exact free space propagator. First, Eq.(8.20) is Fourier transformed to give

$$\frac{\partial \hat{U}(q, \theta)}{\partial \theta} = -[Dq^2 + iqf(\theta)] \hat{U}(q, \theta), \quad (8.22)$$

where the \hat{f} represents the Fourier transform and q is the Fourier transform variable. $R' = S'$ also implies that $R(t) - S(t)$ is a constant and hence $\theta = t/[R(t) - S(t)]^2$. Solving the partial differential equation with the initial condition $\hat{U}(q, \theta = 0) = \exp(-iqz_0)$ we obtain

$$\hat{U}(q, \theta) = e^{-Dq^2\theta - iq[z_0 + \int f(\theta)d\theta]}. \quad (8.23)$$

Inverse Fourier transforming the above expression gives a general free space diffusion propagator for two boundaries undergoing the same motion

$$U(z, z_0; \theta) = \frac{1}{\sqrt{4\pi D\theta}} \exp \left\{ -\frac{[z - z_0 - \int f(\theta)d\theta]^2}{4D\theta} \right\}. \quad (8.24)$$

8.6 Two linearly shifting boundaries

The moving boundary problem of two boundaries initially at $x = -L_0$ and $x = L_0$ and an explicitly assigned boundary time dependence of $R(t) = L_0 + vt$ and $S(t) = -L_0 + vt$ can be solved exactly, since $f(z, \theta) = 2L_0v$ is independent of z . For this system, the free space propagator given in Eq.(8.24) becomes

$$U(z, z_0; t) = \frac{L_0}{\sqrt{\pi Dt}} e^{-\frac{[L_0(z-z_0)-vt/2]^2}{Dt}} \quad (8.25)$$

and the survival probability Q for a diffusing particle initially placed at x_0 is computed by applying the trapping prescription given in Eq.(8.11). Looking at the free space propagator for this problem we see that $U(-L, L; t) \neq U(L, -L; t)$ and hence it is not easy to evaluate $\sum_r' \tilde{\eta}_r(\epsilon)$ and $\sum_s' \tilde{\Pi}_{s,r}(\epsilon)$ by inspection. To obtain the correct superposition of propagators

Chapter 8. Validity of an Adiabatic Approximation in a Reaction-Diffusion System

in Eq.(8.11), we start with a lattice master equation [24, 26, 28] given in Eq.(7.1) and consider the case with two defective sites at site r and s

$$\frac{dP_m}{dt} = F_{mn}P_n - F_{nm}P_m - C_{1d}P_m(\delta_{m,r} + \delta_{m,s}), \quad (8.26)$$

where C_{1d} is the capture rate at trap site s and r . The solution to this problem in Laplace domain is

$$\tilde{P}_m(\epsilon) = \tilde{\eta}_m - C_{1d}\tilde{\Psi}_{m-r}\tilde{P}_r - C_{1d}\tilde{\Psi}_{m-s}\tilde{P}_s. \quad (8.27)$$

In order to find the explicit solution, we must solve the equation for $m = r$ and $m = s$ to find \tilde{P}_r and \tilde{P}_s :

$$\begin{aligned} \tilde{P}_r &= \frac{\tilde{\eta}_r - C_{1d}\tilde{\Psi}_{r-s}\tilde{P}_s}{1 + C_{1d}\tilde{\Psi}_0} \\ \tilde{P}_s &= \frac{\tilde{\eta}_s - C_{1d}\tilde{\Psi}_{s-r}\tilde{P}_r}{1 + C_{1d}\tilde{\Psi}_0} \end{aligned} \quad (8.28)$$

Next we sum over all lattice sites to obtain the survival probability

$$\tilde{Q}(\epsilon) = \frac{1}{\epsilon} \left[1 - C_{1d}(\tilde{P}_r + \tilde{P}_s) \right] \quad (8.29)$$

and substituting in $\tilde{P}_r + \tilde{P}_s$ to obtain

$$\tilde{Q}(\epsilon) = \frac{1}{\epsilon} \left[1 - C_{1d} \frac{\tilde{\eta}_r(1 + C_{1d}\tilde{\Psi}_0 - C_{1d}\tilde{\Psi}_{s-r}) + \tilde{\eta}_s(1 + C_{1d}\tilde{\Psi}_0 - C_{1d}\tilde{\Psi}_{r-s})}{(1 + C_{1d}\tilde{\Psi}_0)^2 - C_{1d}^2\tilde{\Psi}_{s-r}\tilde{\Psi}_{r-s}} \right]. \quad (8.30)$$

We see that this formalism allows analysis for arbitrary capture rate C_{1d} . However, it is not possible to Laplace invert this expression exactly. Because exact solutions are known for perfect absorption only, we focus on instantaneous annihilation where $C_{1d} \rightarrow \infty$ for which

$$\tilde{Q}(\epsilon) = \frac{1}{\epsilon} \left[1 - \frac{\tilde{\eta}_r(\tilde{\Psi}_0 - \tilde{\Psi}_{s-r}) + \tilde{\eta}_s(\tilde{\Psi}_0 - \tilde{\Psi}_{r-s})}{\tilde{\Psi}_0^2 - \tilde{\Psi}_{s-r}\tilde{\Psi}_{r-s}} \right]. \quad (8.31)$$

Chapter 8. Validity of an Adiabatic Approximation in a Reaction-Diffusion System

Here Ψ_0 is the self propagator, Ψ_{s-r} is the propagator from trap site r to s and η_s is the homogeneous solution at the trap site s in the absence of the trap. Needless to say, the above expression in the Laplace domain holds in discrete as well as continuous space [167] as shown in chapter 7. Next we need to compute all propagators in Eq.(8.31). After performing the fixed boundary transformation the boundaries are at $z = 0$ and $z = 1$ representing trap site s and r , respectively. The Laplace transform of Eq.(8.25) after the use of the shifting theorem $\exp[-b^2 t]f(t) \rightarrow \tilde{g}(\epsilon + b^2)$, is known to be [133]

$$\frac{1}{\sqrt{t}} e^{-\frac{(a-bt)^2}{t}} \rightarrow e^{2ab} \sqrt{\frac{\pi}{\epsilon + b^2}} e^{-2a\sqrt{(\epsilon + b^2)}}.$$

This gives the following Laplace transforms for each propagator

$$\begin{aligned} \tilde{\eta}_r(z=1, z_0) &= e^{\frac{\nu L_0(1-z_0)}{D}} e^{-\frac{2L_0(1-z_0)}{\sqrt{D}} \sqrt{\epsilon - \frac{\nu^2}{4D}}}, \\ \tilde{\eta}_s(z=0, z_0) &= e^{-\frac{\nu L_0 z_0}{D}} e^{-\frac{2L_0 z_0}{\sqrt{D}} \sqrt{\epsilon - \frac{\nu^2}{4D}}}, \\ \tilde{\Psi}_{r-s}(z=1, z_0=0) &= e^{\frac{\nu L_0}{D}} e^{-\frac{2L_0}{\sqrt{D}} \sqrt{\epsilon - \frac{\nu^2}{4D}}}, \\ \tilde{\Psi}_{s-r}(z=0, z_0=1) &= e^{-\frac{\nu L_0}{D}} e^{-\frac{2L_0}{\sqrt{D}} \sqrt{\epsilon - \frac{\nu^2}{4D}}}, \\ \tilde{\Psi}_0 &= 1, \end{aligned}$$

with $z_0 = (x_0/L_0 + 1)/2$, *tilde* representing the Laplace transform, and ϵ the Laplace variable. Substituting the above expressions into Eq.(8.31), after some algebra leads to the survival probability being given as

$$\begin{aligned} \tilde{Q}(\epsilon) &= \frac{1}{\epsilon} - \frac{1}{\epsilon} e^{\frac{1}{\nu} \left(1 - \frac{x_0}{L_0}\right)} \frac{\sinh \left[\left(1 + \frac{x_0}{L_0}\right) \sqrt{\tau_b \epsilon + \frac{1}{\nu^2}} \right]}{\sinh \left[2 \sqrt{\tau_b \epsilon + \frac{1}{\nu^2}} \right]} \\ &- \frac{1}{\epsilon} e^{-\frac{1}{\nu} \left(1 + \frac{x_0}{L_0}\right)} \frac{\sinh \left[\left(1 - \frac{x_0}{L_0}\right) \sqrt{\tau_b \epsilon + \frac{1}{\nu^2}} \right]}{\sinh \left[2 \sqrt{\tau_b \epsilon + \frac{1}{\nu^2}} \right]}. \end{aligned} \quad (8.32)$$

Here, $\tau_b = L_0^2/D$ is a new motion time (compare to $\tau = x_0^2/D$) and $\nu = 2D/(\nu L_0)$ is a dimensionless parameter describing the motion of the two walls (compare to $\beta = 2D/(\nu x_0)$).

8.6.1 Survival probability in the time domain for particle starting at midpoint

Our next exercise is to Laplace invert Eq.(8.32) for the case in which the particle starts in the middle of the two boundaries i.e. $x_0 = 0$. For this case, Eq.(8.32) becomes

$$\tilde{Q}(\epsilon) = \frac{1}{\epsilon} \left[1 - \frac{\cosh\left(\frac{1}{v}\right)}{\cosh\left(\sqrt{\tau_b \epsilon + \frac{1}{v^2}}\right)} \right]. \quad (8.33)$$

Equation (8.33) can be inverted exactly by first using the inverse transform [133]

$$\frac{1}{\cosh(a\sqrt{\epsilon})} \rightarrow \frac{1}{a^2} \left[\frac{\partial}{\partial v} \theta_1 \left(\frac{v}{2} \middle| \frac{t}{a^2} \right) \right]$$

together with the shifting and integral theorem to invert $1/\cosh(a\sqrt{\epsilon + b^2})/\epsilon$ (see Appendix B). Note that for moving boundaries one encounters the θ_1 function, whereas for stationary traps the θ_2 function appeared in the Laplace transform. After these operations, the survival probability in time domain is given as

$$\begin{aligned} Q\left(\frac{t}{\tau_b}\right) &= 1 + \frac{1}{2} \cosh\left(\frac{1}{v}\right) \sum_{n=-\infty}^{\infty} (-1)^n e^{-\frac{2n-1}{v}} \\ &\times \left\{ e^{\frac{4n-2}{v}} \operatorname{erfc} \left[\frac{2n-1}{2} \sqrt{\frac{\tau_b}{t}} + \frac{1}{v} \sqrt{\frac{t}{\tau_b}} \right] + \operatorname{erfc} \left[\frac{2n-1}{2} \sqrt{\frac{\tau_b}{t}} - \frac{1}{v} \sqrt{\frac{t}{\tau_b}} \right] \right\}. \end{aligned} \quad (8.34)$$

To our knowledge Eq.(8.34) is a new expression.

8.6.2 Comparison to stationary and single moving boundary

In section 8.4, we solved the problem of a single diffusing particle between two stationary boundaries. For $x_0 = 0$ the survival probability in Eq.(8.17) becomes

$$Q\left(\frac{t}{\tau_b}\right) = \sum_{n=-\infty}^{\infty} (-1)^n \left\{ \operatorname{erf} \left[\frac{2n+1}{2} \sqrt{\frac{\tau_b}{t}} \right] - \operatorname{erf} \left[n \sqrt{\frac{\tau_b}{t}} \right] \right\}. \quad (8.35)$$

Chapter 8. Validity of an Adiabatic Approximation in a Reaction-Diffusion System

The above expression must be equal to the Eq.(8.34) as $v \rightarrow \infty$

$$Q\left(\frac{t}{\tau_b}\right) = 1 + \sum_{n=-\infty}^{\infty} (-1)^n \operatorname{erfc}\left[\frac{2n-1}{2} \sqrt{\frac{\tau_b}{t}}\right]. \quad (8.36)$$

Eqs.(8.35) and (8.36) are equivalent when compared numerically. It is also instructive to compare the solution for two moving boundaries drifting in the same direction to the solution of a single boundary moving either away or towards the particle. The exact solution for a single moving trap with finite absorption is given by Sanchez [164]. In the case of a single boundary moving towards a diffusion particle initially a distance L_0 from the boundary Sanchez's expression reduces to

$$Q\left(\frac{t}{\tau_b}\right) = 1 - \frac{1}{2} \operatorname{erfc}\left[\frac{1}{2} \sqrt{\frac{\tau_b}{t}} \mp \frac{1}{v} \sqrt{\frac{t}{\tau_b}}\right] - \frac{1}{2} e^{\pm \frac{2}{v}} \operatorname{erfc}\left[\frac{1}{2} \sqrt{\frac{\tau_b}{t}} \pm \frac{1}{v} \sqrt{\frac{t}{\tau_b}}\right], \quad (8.37)$$

where the upper signs and the lower signs describe a boundary moving away and towards the diffusing particle, respectively. Comparing Eq.(8.34) to Eq.(8.37) we see that the expression for two moving traps is an infinite sum containing the single trap solution. Similarly, to the stationary solution, the infinite sum in Eq.(8.34) is expected to satisfy the boundary condition for an infinite number of images.

8.6.3 Comparison to numerical solution

In this section, we compare the numerically Laplace inverted analytic solution of the survival probability given in Eq.(8.33) to a numerical solution of the transformed diffusion equation, Eq.(8.20), for various parameters. Ideally, we would compare the analytic expression in the time domain but due to numerical errors, which are inevitably introduced by evaluating Eq.(8.34), we chose to compare its numerical Laplace transform by applying the Gaver-Stehfest method outlined in Appendix C. For $S(t) = -L_0 + vt$ and $R(t) = L_0 + vt$, Eq.(8.20) becomes

$$\frac{\partial U}{\partial t} = \frac{D}{4L_0^2} \frac{\partial^2 U}{\partial z^2} - \frac{v}{2L_0} \frac{\partial U}{\partial z}. \quad (8.38)$$

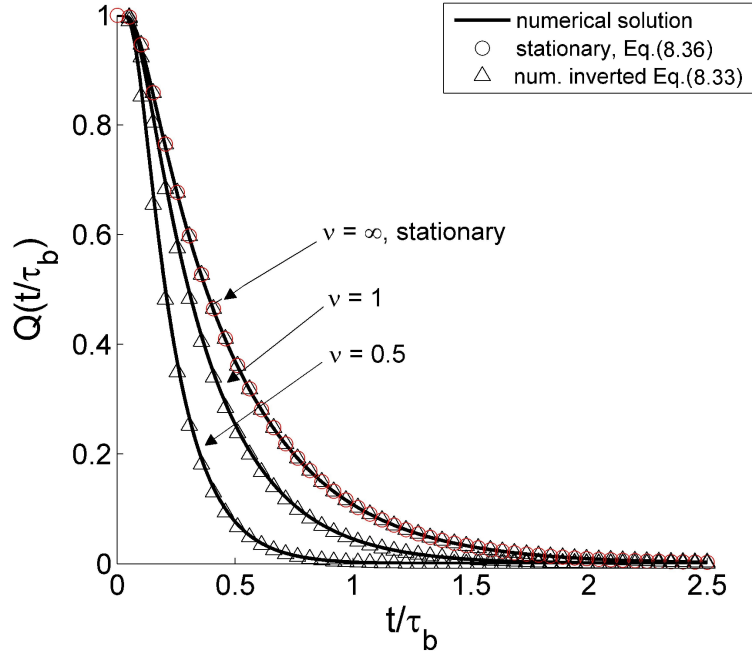


Figure 8.5: Survival probability of a diffusing particle initially placed between two perfectly absorbing moving boundaries. The boundaries move linearly in the same direction. As the speed of the boundary increases (i.e. v decreases), the particle gets trapped faster.

To solve Eq.(8.38) numerically for $U[z(x,t),t]$, one can implement a finite difference algorithm such as the Crank-Nicolson algorithm [170]. After solving for $U[z(x,t),t]$ with the boundary conditions $U(z = 0,t) = 0$, $U(z = 1,t) = 0$ and initial condition $U(z_0,0) = \delta(z - z_0)$ the survival probability $Q(t)$ is obtained by integrating $U[z(x,t),t]$ over z from 0 to 1. Here, we implemented the Crank-Nicolson algorithm as outlined in Appendix E in MATLAB. Figure 8.5 compares the numerical solution (solid line) to the numerically inverted expression given in Eq.(8.33) (open triangles) for $v = 1$, $v = 0.5$, and $v = \infty$. The analytic solution is in excellent agreement with the numerical solution validating the presented methodology. For $v = \infty$, the stationary boundary case, Fig. 8.5 also depicts the analytic solution given in Eq.(8.36) (open circles, red). As the speed of the boundaries increases (i.e. v decreases), the survival probability decays faster than the stationary trap result. This is expected since one of the moving boundaries will eventually

catch up to the diffusing particle.

8.6.4 Adiabatic Approximation

In sections 8.2 and 8.3, we analyzed the validity of an adiabatic approximation for two particle systems by inserting the implicit boundary time dependence into the stationary result. For three particle systems, one can construct an adiabatic approximation in a similar fashion. For two boundaries moving in the same direction the assigned time dependence for the left boundary is $S(t) = -L_0 + vt$ and for the right boundary $R(t) = L_0 + vt$. Hence, for the left boundary L in the stationary solution goes to $L \rightarrow L_0 - vt$ and for the right boundary, $L \rightarrow L_0 + vt$. To satisfy both conditions, an adiabatic solution by an arithmetic average of two expressions is constructed: one by replacing $L \rightarrow L_0 - vt$ and the other by in replacing $L \rightarrow L_0 + vt$ in Eq.(8.35)

$$Q_{adia} \left(\frac{t}{\tau_b} \right) = \sum_{n=-\infty}^{\infty} \frac{(-1)^n}{2} \left\{ \operatorname{erf} \left[(2n+1) \sqrt{\frac{\tau_b}{4t}} + \frac{1}{v} \sqrt{\frac{t}{\tau_b}} \right] - \operatorname{erf} \left[n \sqrt{\frac{\tau_b}{t}} + \frac{2}{v} \sqrt{\frac{t}{\tau_b}} \right] \right\} \\ + \sum_{n=-\infty}^{\infty} \frac{(-1)^n}{2} \left\{ \operatorname{erf} \left[(2n+1) \sqrt{\frac{\tau_b}{4t}} - \frac{1}{v} \sqrt{\frac{t}{\tau_b}} \right] - \operatorname{erf} \left[n \sqrt{\frac{\tau_b}{t}} - \frac{2}{v} \sqrt{\frac{t}{\tau_b}} \right] \right\} \quad (8.39)$$

Figure 8.6 compares the adiabatic approximation Eq.(8.39) (open circles) to the numerical Laplace inverted exact solution given in Eq.(8.33) (solid line) for $v = \infty$ (black) and $v = 0.5$ (red). The adiabatic approximation is only valid for short time. For intermediate time the survival probability obtained from the approximation increases before it decays to zero (see red open circles in Fig. 8.6). This is due to the arithmetic average of the two expressions and indicates that the approximation becomes unphysical since the total survival probability must decrease monotonically to zero for all time.

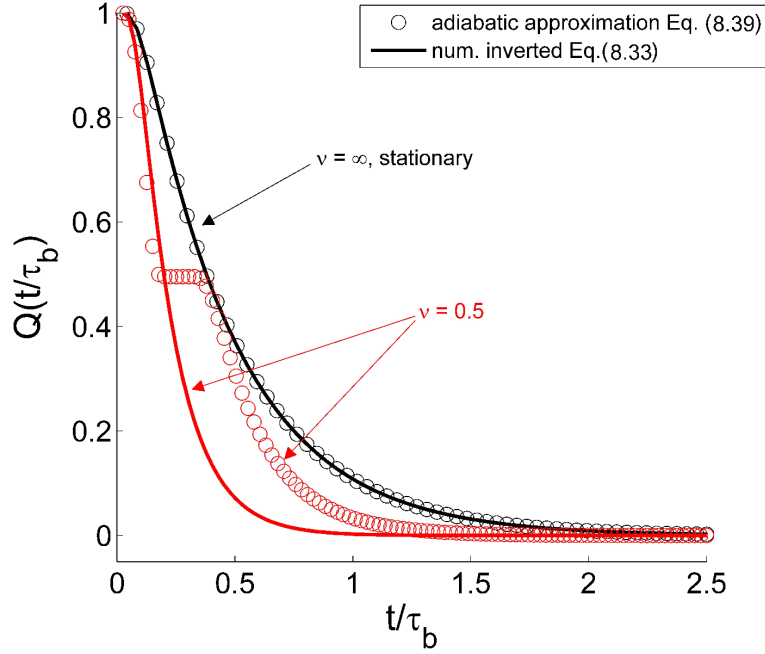


Figure 8.6: Survival probability of a diffusing particle initially placed between two perfectly absorbing boundaries moving in the same direction. An adiabatic approximation Eq.(8.39) (open circles) only holds for short time. Solid line represents the exact solution obtained from numerically Laplace inverting Eq.(8.33) for $v = \infty$ (black) and $v = 0.5$ (red).

8.7 Two linearly receding boundaries

For two perfectly absorbing receding boundaries with assigned time dependence $R(t) = -L_0 - vt$ and $S(t) = L_0 + vt$ an approximation for the survival probability $Q(t)$ is given by Krapivsky and Redner [143]. An exact solution for the probability density $P(x, x_0; t)$ in d -dimensions is given by Bray and Smith [171]. Bray and Smith followed Krapivsky and Redner [143], constructing their solution from the fixed boundary problem. They use the probability density expression for the stationary problem and replace $L \rightarrow L(t)$ and $t/L^2 \rightarrow \int dt'/L(t')^2$, multiply this new expression by an unknown function dependent on space and time and solve for the unknown function by substituting the expression back into the diffusion equation. Since Bray and Smith [171] only report $Q(t \rightarrow \infty)$, the survival probability $Q(t)$ was computed by integrating the d -dimensional

Chapter 8. Validity of an Adiabatic Approximation in a Reaction-Diffusion System

probability density distribution $P(x, x_0, t)$ given in Eq.(23) from Ref. [171] over the entire space

$$Q(t) = \sqrt{\frac{L_0 + vt}{L_0}} e^{\frac{vx_0^2}{4DL_0}} \sum_{n=-\infty}^{\infty} \cos \left[\frac{(2n-1)\pi x_0}{2L_0} \right] e^{-\frac{(2n-1)^2 \pi^2 Dt}{4L_0(L_0+vt)}} \times \int_0^1 \cos \left[\frac{(2n-1)\pi x}{2} \right] e^{-\frac{vx^2(L_0+vt)}{4D}} dx. \quad (8.40)$$

For simplicity, the diffusing particle starts at the midpoint of the linearly expanding boundaries, $x_0 = 0$. Using the stationary result given in Eq.(8.35) an adiabatic approximation to the exact solution can be obtained by replacing $L \rightarrow L_0 + vt$ in the fixed boundary result

$$Q_{adia} \left(\frac{t}{\tau_b} \right) = \sum_{n=-\infty}^{\infty} (-1)^n \operatorname{erf} \left[(2n+1) \left(\frac{1}{2} \sqrt{\frac{\tau_b}{t}} + \frac{1}{v} \sqrt{\frac{t}{\tau_b}} \right) \right] - \sum_{n=-\infty}^{\infty} (-1)^n \operatorname{erf} \left[n \left(\sqrt{\frac{\tau_b}{t}} + \frac{2}{v} \sqrt{\frac{t}{\tau_b}} \right) \right], \quad (8.41)$$

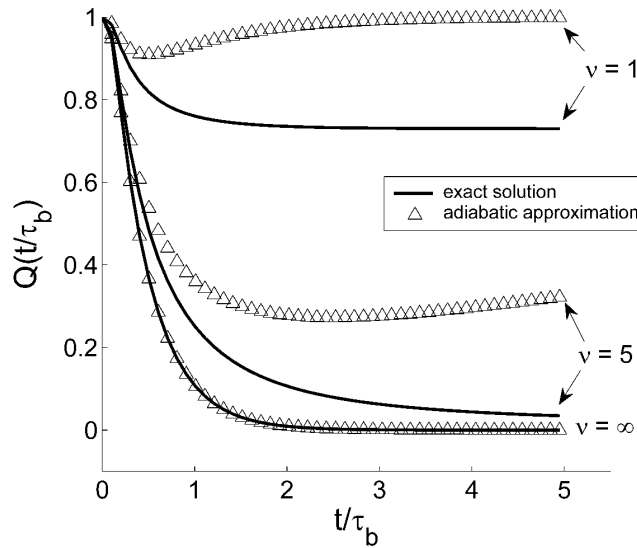


Figure 8.7: Diffusing particle initially placed at the midpoint of two linearly receding traps. Exact solution Eq.(8.42) (line) compared to adiabatic approximation Eq.(8.41) (open triangles) for $v = 1$, $v = 5$, and $v = \infty$.

which is compared to the exact solution for $x_0 = 0$

$$Q\left(\frac{t}{\tau_b}\right) = \sqrt{1 + \frac{2t}{v\tau_b}} \sum_{n=-\infty}^{\infty} e^{-\frac{(2n-1)^2\pi^2vt}{4(v\tau_b+2t)}} \int_0^1 \cos\left[\frac{(2n-1)\pi x}{2}\right] e^{-\frac{x^2}{v}\left(\frac{1}{2} + \frac{t}{v\tau_b}\right)} dx. \quad (8.42)$$

Figure 8.7 compares the adiabatic approximation in Eq.(8.41) (open triangles) to the exact solution Eq.(8.42) (solid line) for $v = 1$, $v = 5$, and $v = \infty$, indicating that the approximation only holds for slowly receding boundaries and short times. For long times the approximation for the survival probability Q always reaches, one which is unphysical since Q is expected to decrease monotonically reaching zero or a constant.

8.8 Two oscillating boundaries

In this section, we discuss the connection of linearly moving boundaries to oscillating boundaries. For a system of two perfectly absorbing oscillating boundaries, one can study two cases. In the first case, the two boundaries oscillate in-phase and in the second, they oscillate out-of-phase. We will study these two cases separately.

8.8.1 In-phase oscillation

When the two boundaries oscillate in-phase one may assign the time dependence as $S(t) = L_0 + A\sin(wt)$ and $R(t) = -L_0 + A\sin(wt)$, where w is the oscillation frequency and A is the amplitude of the oscillation. Here the two boundaries have identical time dependence leading to $S'(t) = R'(t)$ and the free space propagator is obtained from Eq.(8.24)

$$U(z, z_0; t) = \frac{L_0}{\sqrt{\pi Dt}} e^{-\frac{[L_0(z-z_0) - A\sin(wt)/2]^2}{Dt}}. \quad (8.43)$$

To solve the problem of a diffusion particle between two in-phase oscillating perfectly absorbing boundaries, the Laplace transform of Eq.(8.43) is inserted into Eq.(8.31), which is

Chapter 8. Validity of an Adiabatic Approximation in a Reaction-Diffusion System

evaluated at trap sites $s = 0$ and $r = 1$. Since Eq.(8.43) cannot be inverted exactly, the numerical Laplace transform of the free space propagator must be computed. It is worth noting that the numerical inverse Laplace transform algorithm i.e. the Gaver-Stehfest method used in this thesis cannot be applied to oscillatory functions as discussed in the Appendix C. Since it is not the objective to implement a more accurate numerical Laplace inverse transform algorithm, we will not show that this solution is exact, when compared to a numerical solution. The numerical solution is computed after substituting the assigned boundary time dependences into Eq.(8.20) and apply the Crank-Nicolson algorithm as outlined in Appendix E

$$\frac{\partial U}{\partial t} = \frac{D}{4L_0^2} \frac{\partial^2 U}{\partial z^2} - \frac{Aw \cos(wt)}{2L_0} \frac{\partial U}{\partial z}. \quad (8.44)$$

with boundary conditions $U(z = 0, t) = 0$, $U(z = 1, t) = 0$ and initial condition $U(z_0, 0) = \delta(z - z_0)$. The survival probability is obtained by integrating the numerical solution of $U(z, t)$ from $z = 0$ to $z = 1$. Looking at Eq.(8.43), we see that in the limit of small oscillation frequency $\sin(wt) \rightarrow wt$ the expression is equivalent to the propagator given in Eq.(8.25) with boundary speed $v \rightarrow Aw$. Therefore, as expected, for small oscillation frequencies the solution for two moving boundaries in the same direction is an approximation to the in-phase oscillating boundary problem. Figure 8.8 compares the numerical solution of Eq.(8.44) (solid line) to the numerical inverse Laplace transform of Eq.(8.33) (open triangles) for $w\tau_b = 10$ (red) and $w\tau_b = 3$ (black) with $A/L_0 = 0.8$ for a particle initially at $x_0 = 0$. For comparison Fig. 8.8 also depicts the stationary solution (open circles). The survival probability for in-phase boundary oscillation decays faster than the stationary result but slower as Q for moving boundaries. The moving boundary solution is a good approximation for $t/\tau_b < \pi/(4w\tau_b)$, which corresponds to an 8th of the oscillation period. For the red family of curves, one 8th of the period is $t/\tau_b = 0.5$. As expected, for larger t/τ_b the moving boundary solution starts to deviate from the exact solution.

Following our previous methodology, another approximation is obtained by construct-

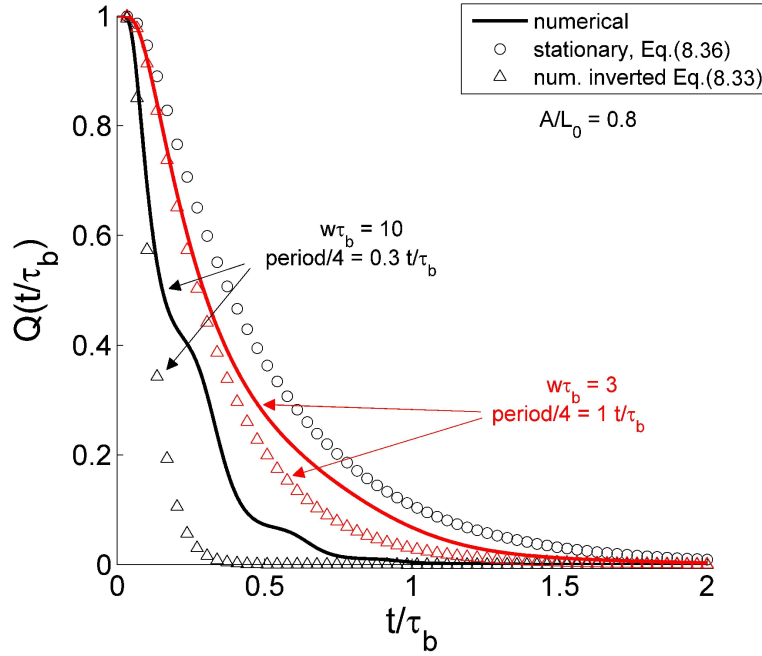


Figure 8.8: Survival probability of a diffusing particle initially placed midway between two oscillating boundaries (solid line). The boundaries oscillate in-phase. The exact solution (solid line) is compared to the solution of two boundaries moving in the same direction (open triangles). The moving boundary approximation is valid in the limit of small oscillation frequency.

ing an arithmetic average of the stationary result given in Eq.(8.35) by replacing L_0 with $L_0 \pm A \sin(wt)$. However, when this approximation is compared to the numerical solution it undergoes significant oscillations which makes the solution unphysical. Since the linearly moving boundary approximation for the chosen parameter used in Fig. 8.8 performed better than our adiabatic approximation, the adiabatic approximation is not depicted in Fig. 8.8. This observation also applies to the next section 8.8.2, where out-of-phase boundary oscillations are studied.

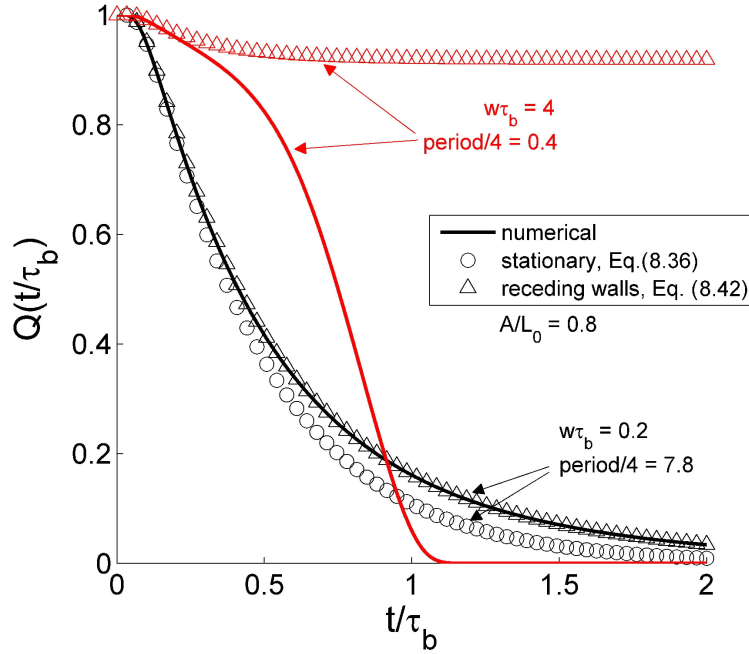


Figure 8.9: Survival probability of a diffusing particle initially placed midway between two oscillating boundaries (solid line). The boundaries oscillate out-of-phase. The exact solution (solid line) is compared to the solution of two receding boundaries (open triangles). The moving boundary approximation is only valid for t/τ_b less than an 8th of the oscillation period. For larger values of t/τ_b the approximation deviates significantly from the exact solution.

8.8.2 Out-of-phase oscillation

The second oscillating boundary case is out-of-phase oscillation. Here the boundary time dependence is assigned as $S(t) = L_0 + A \sin(\omega t)$ and $R(t) = -L_0 - A \sin(\omega t)$ and Eq.(8.20) becomes

$$\frac{\partial U}{\partial t} = \frac{D}{4(L_0 + A \sin(\omega t))^2} \frac{\partial^2 U}{\partial z^2} - \frac{A \omega \cos(\omega t)(2z - 1)}{2L_0 + 2A \sin(\omega t)} \frac{\partial U}{\partial z}. \quad (8.45)$$

Since for out-of-phase oscillations $R' \neq S'$, the free space propagator for Eq.(8.20) cannot be obtained easily, we are not able to apply our trapping prescription to solve for $Q(t)$. However, for small oscillation frequencies $\sin(\omega t) \rightarrow \omega t$, $\cos(\omega t) \rightarrow 1$, the problem of two out-of-phase oscillating boundaries can be approximated by the solution for an expanding

cage in which the two receding boundaries have speed $v = Aw$. Figure 8.9 compares the exact numerical solution of Eq.(8.45) (solid line) to the analytic approximation obtained from the receding boundary problem given in Eq.(8.42) (open triangles) for $w\tau_b = 4$ (red) and $w\tau_b = 0.2$ (black) with $A/L_0 = 0.8$ for $x_0 = 0$. The receding boundary solution holds up to $t/\tau_b = \pi/(4w\tau_b)$, an 8^{th} of the oscillation period. In comparison to the in-phase oscillation problem, the approximation for out-of-phase oscillation starts to deviate significantly for $w\tau_b > 2$, whereas the in-phase oscillation approximation is still a reasonable good approximation for this parameter range.

8.9 Concluding remarks

In this chapter, we analyzed an adiabatic approximation for the particle survival probability in moving trap/boundary problems. In the systems under investigation, the traps/boundaries move with an explicitly assigned time dependence in a deterministic or probabilistic fashion. The approximation is constructed by inserting the trap/boundary time dependence into the stationary solution of the particle survival probability. We know how to solve the latter exactly for sink terms represented by a sum of Delta functions [24, 28, 132]. The construction of an adiabatic approximation is an idea previously used by Krapivsky and Redner [165] followed by Bray and Smith [171]. In these previous approaches the trap/boundary time dependence was directly inserted into the probability density function $P(x, t)$ of the stationary result. The approximation was obtained by inserting the new $P_{new}(x, t)$ into the diffusion equation and solving for the total survival probability $Q(t)$. Our approach is different, since we directly inserted the trap/boundary time dependence into the stationary expression for $Q(t)$. We focused on two- and three-particle systems with a single or two moving traps/boundaries, respectively, and collected known solutions for moving traps/boundaries as well as derived new expressions given in equations (8.32) and (8.34).

Chapter 8. Validity of an Adiabatic Approximation in a Reaction-Diffusion System

In section 8.2 we analyzed the simplest case of a diffusing particle and a trap. The exact solution is easily obtained by transforming the problem into the reference frame of the particle and replacing the particle's diffusion constant in the stationary result with the sum of the trap's and particle's diffusion constants. In such two particle systems, the adiabatic approximation holds well for finite and perfect absorption if the particle and the trap diffuse with a similar diffusion constant. However, when the trap diffuses faster the approximation starts to deviate significantly from the exact solution. For a less simple system of a biased trap moving towards a diffusing particle (section 8.3), the adiabatic approximation only holds for short time and depends on the trapping rate and trap speed. In the long time limit, the approximation yields negative results for perfect absorption and goes to zero for imperfect absorptions. Both results are unphysical since for perfect absorption the survival probability must reach zero and for imperfect absorption a constant. This result indicates the significant limitations of the adiabatic approximation.

Before we analyzed the validity of our adiabatic approximation for two moving boundaries we derived an exact solution for two stationary traps by applying the trapping prescription presented in chapter 7. The final expression for finite absorption in Laplace domain was reported by Abramson and Wio [167] and after inverting this expression for perfect absorption, a new expression given in Eq.(8.17) containing a theta elliptic function was obtained. The appearance of the theta elliptic function is noteworthy since a theta function also appears in the derivation of the mean square displacement by Kenkre et al. [31] (see Eq.(19) in [31]). It remains to be investigated how the survival probability Q is connected to the MSD.

The first problem of two moving boundaries we studied, is a system of two boundaries moving at the same speed in the same direction. Since no exact solution is known for this problem, we outlined a boundary fixing method in section 8.5 through which we were able to derive an exact solution, section 8.6. In sections 8.6.4 and 8.7, we analyzed the validity of our adiabatic approximation for two linearly moving boundary problems. As

Chapter 8. Validity of an Adiabatic Approximation in a Reaction-Diffusion System

expected, the adiabatic approximation is only valid for short time and becomes unphysical for intermediate time when the survival probability obtained from the approximation starts to increase. In the last section 8.8, oscillating boundaries were discussed. Here our adiabatic approximation was only valid for very small oscillations frequencies due to the appearance of significant oscillations in the functional form of the survival probability. However a more accurate approximation, especially for in-phase boundary oscillations, can be obtained by approximating these systems with two linearly moving boundaries.

In conclusion, the detailed analysis presented in this chapter shows that an adiabatic approximation constructed from the stationary result is in general only valid for small times. However, the approximation also performed well for systems where the trap moves slowly especially for deterministic trap motion. The latter result is very useful for the construction of our coalescence theory, predicting that our theory performs well for a slowly moving central patch boundary, which is observed in experiment.

Chapter 9

A Mathematical Model for Receptor Cluster Coalescence

9.1 Introduction

In the present chapter, we develop a coalescence theory and apply it directly to our experimental studies of receptor cluster coalescence. This analysis represents the final step in this dissertation, a result of the interplay between experiment and theory. Modeling the kinetics of receptor cluster coalescence in mast cells is important for understanding the mast cells role in cell-cell communication. It is important to note that the present chapter *does not* bring the investigation of mast cell surface receptor dynamics and distribution to a close; rather, it reiterates the importance of an intense dialog between experimental and theoretical studies to understand more fully the nature of mast cell activation.

The previous two chapters have established a springboard for our coalescence theory. In chapter 7, we collected tools to solve stationary trapping problems. In chapter 8, we investigated the validity of an adiabatic approximation for moving boundary problems by assigning the boundary time dependence explicitly into the stationary trap expression. In

Chapter 9. A Mathematical Model for Receptor Cluster Coalescence

the present chapter, we apply these analyses and develop a receptor cluster coalescence model. As outlined in section 6.3 in essential detail, our coalescence theory is based on a simplified feedback approach. The simplification is that we consider a distribution of non-interacting point particles and a stationary trap at the origin. The trap at the origin grows due to particle absorption and represents the large central receptor patch, which grows due to receptor cluster coalescence in our experiments. Other self-consistent methods for the study of three-dimensional diffusion-controlled particle growth may be found in Refs. [121, 118]. Our own development incorporates a time dependent melding process.

The present chapter is organized as follows. In section 9.2, we present our self-consistent coalescence prescription whose implementation necessitates an approximation. Section 9.3 outlines the approximation. It is based on the insertion of the time dependent trap radius in the stationary trap solution. The approximation yields an algebraic equation, which can be approached analytically by applying an iterative method. In sections 9.5 and 9.6, our coalescence theory for point particles is directly compared to Monte Carlo simulations, showing that the approximation describes the growth of a simulated trap radii well, even for finite-sized particles (see section 9.5.5). After thus developing an analytic approximation for particle coalescence in two-dimensions, we apply our theory to actual experiments in section 9.7.2. Comparison of experiment and theory shows that the observed feature of an initial delay and a subsequent larger rate in cluster coalescence are not compatible with the simplified assumption of a constant capture rate. We address this compatibility problem by generalizing our coalescence theory for a time-dependent melding process. The methodology we use, employs a memory formalism for the capture process itself. Initial discussions of this generalization are presented in section 9.8, which show that the observed delay can be explained by the memory concept. At least quantitatively, we have thus solved the compatibility problem.

9.2 Coalescence feedback approach

In this section, we introduce our coalescence theory on the basis of a self-consistent approach. We first study the problem in one-dimension. The simplest model describes a single stationary trap at the origin and an initial distribution of non-interacting point particles. These particles move and eventually meet the trap, where they get absorbed with a finite probability. Our coalescence theory is based on the following argument. If we know the rate $h(t)$ at which particles disappear, i.e. get absorbed by the trap,

$$\frac{dQ(R,t)}{dt} = h(R,t), \quad (9.1)$$

we also know the rate at which the trap increases

$$\frac{dR(t)}{dt} = -A h(R,t). \quad (9.2)$$

Here A is a constant determined by $R(0)$ and $R(\infty)$. The idea is to start with an initial trap radius $R(0)$ and particle distribution. Then, dQ/dt is computed for the first time step and used in Eq.(9.2) to compute the increase in the trap radius. This result is then fed back into Eq.(9.1) to compute dQ/dt for the next time step. Hence, the presented argument produces a self-consistent theory, in a form ready to compare to experiments and simulations. Since in experiments, as well as simulations, the initial and final trap radius are known, A can be calculated by integrating Eqs.(9.1) and (9.2) and setting $t = \infty$ obtaining

$$A = \frac{R(\infty) - R(0)}{Q(0) - Q(\infty)}.$$

It is worth noting that the initial particle survival probability $Q(0)$ is always one where as its limiting value $Q(\infty)$ approaches zero for only in certain problems. After combining Eqs.(9.1) and (9.2), and inserting the expression for A , we obtain the following exact expression in one-dimension

$$R(t) = R(0) + \left[\frac{R(\infty) - R(0)}{1 - Q(\infty)} \right] [1 - Q(t)]. \quad (9.3)$$

A similar expression in d -dimensions is written as

$$R(t)^d = R(0)^d + \left[\frac{R(\infty)^d - R(0)^d}{1 - Q(\infty)} \right] [1 - Q(t)]. \quad (9.4)$$

In the following section, our goal is to solve Eq.(9.4) exactly. If we cannot do it exactly, we are looking for an analytic approximation.

9.3 Development of an analytic approximation

In our proposed calculation with the feedback idea, there are two equations relating $R(t)$ and $Q(t)$. One of them is Eq.(9.3). The other is an expression that expresses the result of the defect technique calculations in an explicit dependence of Q . For example, as computed in section 7.5, for a perfectly absorbing stationary trap at the origin in one-dimension with the point particles all placed at a distance x_0 from the origin, the survival probability is an error function depending on t , and x_0 . In the discussion of a growing trap, it is appropriate to replace x_0 with $x_0 - R(t)$ to include the time dependence of the effective distance to the trap in the problem.

To validate the proposed calculation, we invent a *model of a model* that we can solve exactly. In this problem, Q and R are related as follows. Instead of the involved actual interrelationship of $Q(t)$ and $R(t)$, we assume

$$\frac{dQ(t)}{dt} + R(t)Q(t) = 0. \quad (9.5)$$

Our goal is to find the solution for the radius evolution obtained by an exact analysis that solves Eq.(9.3) together with Eq.(9.5) and compare it to the approximate analysis we have suggested above.

In the exact analysis, instantaneous particle absorption at the trap boundary is considered, rewriting Eq.(9.3) as

$$\frac{R(\infty) - R(t)}{R(\infty) - R(0)} = \frac{Q(t)}{Q(0)}. \quad (9.6)$$

Chapter 9. A Mathematical Model for Receptor Cluster Coalescence

Using Eq.(9.6) in Eq.(9.5) allows the elimination of Q , yielding an ordinary differential equation for the radius

$$\frac{dR(t)}{dt} = R(\infty)R(t) - R^2(t). \quad (9.7)$$

The solution to this differential equation can be written down exactly

$$R(t) = \frac{R(\infty)}{1 + \left(\frac{R(\infty)}{R(0)} - 1\right) e^{-R(\infty)t}}, \quad (9.8)$$

and after rearranging terms, the expression becomes

$$\frac{R(\infty) - R(t)}{R(\infty) - R(0)} = \frac{R(t)}{R(0)} e^{-R(\infty)t}. \quad (9.9)$$

On the other hand, in the approximate analysis we have suggested above, the radius R in Eq.(9.5) is held constant, giving the following survival probability

$$Q(t) = Q(0)e^{-R(t)t}. \quad (9.10)$$

This expression is now substituted into Eq.(9.6), yielding an algebraic equation

$$\frac{R(\infty) - R(t)}{R(\infty) - R(0)} = e^{-R(t)t}. \quad (9.11)$$

This approximate solution involves the product of t and the instantaneous value $R(t)$ in the exponent and is given as a Newton-like nonlinear algebraic equation that may be solved numerically. Both, the exact and approximate solution for the radius evolution of the invented model decay exponentially. Figure 9.1 compares the exact solution given in Eq.(9.9) (black line) to the approximate solution given in Eq.(9.11) (grey line). For short and long times the approximation holds well. However, for intermediate times, the approximation deviates significantly from the exact solution.

The relation of the approximation given in Eq.(9.11) to the exact analysis presented by Eq.(9.9) becomes clear immediately after casting the exact solution in a similar form to the approximate one

$$\frac{R(\infty) - R(t)}{R(\infty) - R(0)} = \exp\left(-\int_0^t R(s)ds\right). \quad (9.12)$$

Chapter 9. A Mathematical Model for Receptor Cluster Coalescence

A direct t -differentiation shows the equivalence of Eq.(9.12) to Eq.(9.9) since the former satisfies Eq.(9.5). Thus the exact solution for the invented model can be obtained by replacing $tR(t)$ in the approximate exponential of Eq.(9.11) by the integral of $R(s)$ from $s = 0$ to $s = t$. Equation (9.11) differs from Eq.(9.12) in that the former multiplies $R(t)$ and t , whereas the latter integrates $R(t)$ with respect to t .

We now notice that Eq.(9.11) has the form

$$R(t) = f(R(t), R(\infty), R(0)), \quad (9.13)$$

which suggests that we develop an iterative approximation to evaluate $R(t)$. We may either take $R(t) = R(0)$ or $R(t) = R(\infty)$ as our starting point for the iteration. In the first case we obtain as the first order

$$R_{1^{st} \text{ from } R(0)}(t) = R(\infty) - [R(\infty) - R(0)] \exp[-R(0)t]. \quad (9.14)$$

The second order approximation replaces $R(t)$ with $R_{1^{st} \text{ from } R(0)}(t)$

$$R_{2^{nd} \text{ from } R(0)}(t) = R(\infty) - [R(\infty) - R(0)] \exp \left[- \left(R(\infty) - [R(\infty) - R(0)] e^{-R(0)t} \right) t \right], \quad (9.15)$$

and the third order approximation replaces $R(t)$ with $R_{2^{nd} \text{ from } R(0)}(t)$ on the right-hand side of Eq.(9.11). This scheme can be repeated to obtain higher order approximations. Figure 9.1A compares the first few analytic approximations iterated from $R(0)$ (circles) to the numerically solved algebraic approximation given in Eq.(9.11) (grey line) as well as the exact solution to the invented model, Eq.(9.9) (black line). Similarly, the second scheme, iterating away from $R(t) = R(\infty)$, yields to the following first order approximation

$$R_{1^{st} \text{ from } R(\infty)}(t) = R(\infty) - [R(\infty) - R(0)] \exp[-R(\infty)t]. \quad (9.16)$$

Higher order approximations can be obtained in the same way as outlined above. Figure 9.1B compares the first few analytic approximations (circles) iterated from $R(\infty)$ to

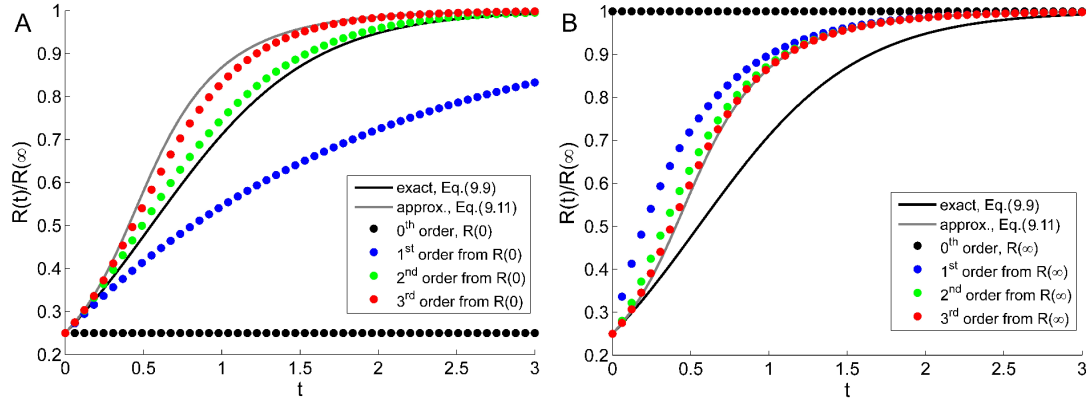


Figure 9.1: Iterative approximation scheme (circles) of the algebraic approximation of Eq.(9.9) (black line) given in Eq.(9.11) (grey line), iterating away from (A) $R(0)$ and (B) $R(\infty)$.

the algebraic approximation given in Eq.(9.11) (grey line) as well as the exact solution to the invented model, Eq.(9.9) (black line). According to Fig. 9.1, iterating away from $R(\infty)$ approaches Eq.(9.11) faster than iterating from $R(0)$, suggesting that the former should be used as approximation scheme. Hence, in the remainder of the present chapter, we iterate away from $R(\infty)$ and drop "from $R(\infty)$ " from the subscript. We emphasize that the iterative procedure we use is indeed an *approximation* and that it incidentally results in faster coalescence kinetics.

9.3.1 Approximation applied to perfect absorption in one-dimension

For the special case of our invented problem (model of a model), we were able to solve Eq.(9.3) exactly. This does not apply to our real coalescence problem. However, if the instantaneous radius is treated as a constant in the expression for the survival probability, we have shown that an approximate algebraic equation can be obtained. This algebraic equation can be solved exactly through numerical methods or approximated through an iterative method. In the current section, the performance of an iterative method for a perfectly absorbing stationary trap in one-dimension is investigated. To apply the feedback

Chapter 9. A Mathematical Model for Receptor Cluster Coalescence

idea, x_0 in the exact expression of the survival probability given in Eq.7.41 must be replaced by $x_0 - R(t)$

$$Q(t) = \text{erf} \left(\frac{x_0 - R(t)}{\sqrt{4Dt}} \right).$$

This substitution reflects that the distance between the diffusing particle and the trap periphery is changing over time. To obtain an approximate solution in form of an algebraic equation, $Q(t)$ is substituted into Eq.(9.6) yielding

$$R(t) = R(\infty) - [R(\infty) - R(0)] \text{erf} \left(\frac{x_0 - R(t)}{\sqrt{4Dt}} \right). \quad (9.17)$$

The above expression can be solved exactly for $R(t)$ by numerical methods or approximated by an iterative method. Following the iteration technique away from $R(\infty)$, the first order approximation is written as

$$R(t)_{1st} = R(\infty) - [R(\infty) - R(0)] \text{erf} \left(\frac{x_0 - R(\infty)}{\sqrt{4Dt}} \right). \quad (9.18)$$

and the second order approximation yields

$$R(t)_{2nd} = R(\infty) - [R(\infty) - R(0)] \text{erf} \left(\frac{x_0 - \left(R(\infty) - [R(\infty) - R(0)] \text{erf} \left(\frac{x_0 - R(\infty)}{\sqrt{4Dt}} \right) \right)}{\sqrt{4Dt}} \right). \quad (9.19)$$

Figure 9.2 compares the first two iterations (circles) to the numerical solution of Eq.(9.17) (solid line). The results suggest that the second order approximation is a very good approximation to the algebraic equation, which was developed by assuming a constant (instantaneous) radius in the expression of the survival probability. Surprisingly, the iterative approximation scheme seems to work better for the real problem involving error functions than for the invented problem, in which $Q(t)$ decayed exponentially.

9.4 Feedback idea in Laplace domain

Results from the feedback validity study suggest that our proposed methodology could be applied readily to problems for which the exact solution of the stationary trapping problem is known. However, in higher dimensions, specifically for our two-dimensional receptor cluster coalescence problem, exact expressions can be obtained only in Laplace domain, see section 7.6. Even though, a numerical inversion scheme to obtain the exact functional form in time domain can be applied, it would be useful to have a coalescence theory applicable in Laplace domain. In the present section, the feedback idea and iteration scheme is applied directly in Laplace domain. Such an analytic expressions can be compared readily to Laplace transformed experimental data. For example, a functional description of experimental data in the time domain allows us to compute its corresponding Laplace transform, which can be compared directly to the approximate theoretical solution in Laplace domain. To our knowledge this approach of addressing data with a time-dependent theory was used for the first time in extensive examination of sensitized luminescence observations in molecular crystals by Kenkre and collaborators [23, 29]. Our search has uncovered

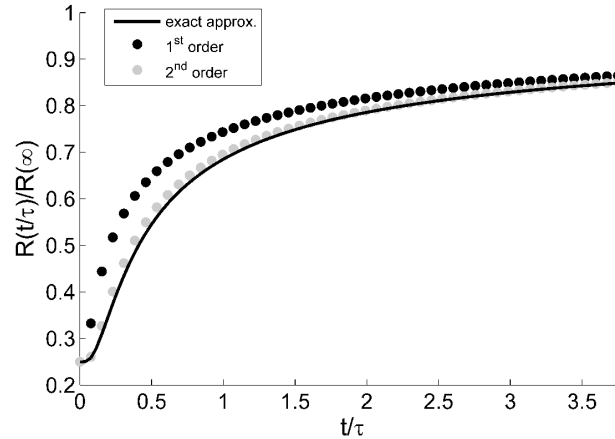


Figure 9.2: Approximation of the increase in trap radius R due to particle absorption, where particles undergo random motion. Numerical solution of Eq.(9.17) (solid line) compared to its first order (black circles) and second order (grey circles) approximation. Here $\tau = [x_0 - R(0)]^2/D$ and $R(\infty)/R(0) = 4$.

only one other later instance [172].

The Laplace transform of Eq.(9.4), treating the radius as a constant in the expression for the survival probability Q , is written as

$$L\{R(t)^d\} = \frac{R(0)^d}{\epsilon} + \left[\frac{R(\infty)^d - R(0)^d}{1 - Q(\infty)} \right] \left[\frac{1}{\epsilon} - \tilde{Q}(\epsilon) \right]. \quad (9.20)$$

Here $L\{f(t)\}$ represents the Laplace transform of $f(t)$ and the subscript d stands for d -dimensions. To apply this expression, one would first Laplace transform $R(t)^d$, e.g. that obtained from experiments, and then compare the functional form to the right-hand side of the expression, where $R(t)$ is replaced with $\epsilon\tilde{R}(\epsilon)$ in $\tilde{Q}(\epsilon)$.

9.4.1 Perfect absorption in one-dimension

For perfect absorption in one-dimension, Eq.(9.20) becomes

$$\tilde{R}(\epsilon) = \frac{R(0)}{\epsilon} + [R(\infty) - R(0)] \left[\frac{1}{\epsilon} - \tilde{Q}(\epsilon) \right]. \quad (9.21)$$

In Laplace domain the expression for $\tilde{Q}(\epsilon)$, holding $R(t)$ constant, is given as

$$\tilde{Q}(\epsilon) = \frac{1}{\epsilon} \left\{ 1 - e^{[x_0 - R(t)]\sqrt{\frac{\epsilon}{D}}} \right\}. \quad (9.22)$$

Substituting Eq.(9.22) into Eq.(9.21) and replacing $R(t)$ with $\epsilon\tilde{R}(\epsilon)$ in $\tilde{Q}(\epsilon)$, we obtain the following algebraic equation

$$\tilde{R}(\epsilon) = \frac{R(0)}{\epsilon} + \frac{[R(\infty) - R(0)]}{\epsilon} e^{-[x_0 - \epsilon\tilde{R}(\epsilon)]\sqrt{\frac{\epsilon}{D}}}. \quad (9.23)$$

Figure 9.3 compares the numerical solution of Eq.(9.17) (black line) to the numerical Laplace inverted solution of Eq.(9.23) (grey line), indicating that the two expressions are very close, deviating only slightly at intermediate times. Therefore, a coalescence theory in Laplace domain, which was obtained through an approximation scheme, might be useful to compare experiments in two- and three-dimensions to theoretical predictions.

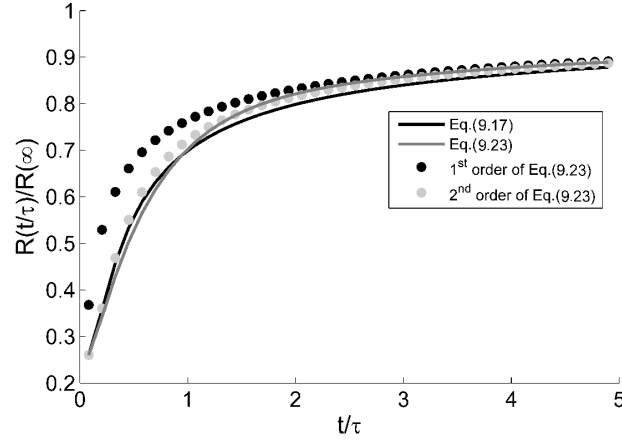


Figure 9.3: Feedback idea applied in Laplace domain. Approximation of the increase in trap radius R due to particle absorption, where particles undergo random motion. Numerical solution of Eq.(9.17) (black line) compared to numerically Laplace inverted Eq.(9.23) (grey line), which is approximated by its first order (black circles) and second order (grey circles). Here $\tau = [x_0 - R(0)]^2/D$ and $R(\infty)/R(0) = 4$.

Following our procedure in time domain, we can also obtain an approximate analytic solution to Eq.(9.23) by an iterative method. The first and second order approximation to Eq.(9.23) iterated away from $R(\infty)$ are

$$\tilde{R}(\epsilon)_{1st} = \frac{R(0)}{\epsilon} + \frac{[R(\infty) - R(0)]}{\epsilon} e^{-[x_0 - R(\infty)]\sqrt{\frac{\epsilon}{D}}}. \quad (9.24)$$

and

$$\begin{aligned} \tilde{R}(\epsilon)_{2nd} &= \frac{R(0)}{\epsilon} + \frac{[R(\infty) - R(0)]}{\epsilon} \\ &\times \exp \left\{ - \left[x_0 - \epsilon \left(\frac{R(0)}{\epsilon} + \frac{[R(\infty) - R(0)]}{\epsilon} e^{-[x_0 - R(\infty)]\sqrt{\frac{\epsilon}{D}}} \right) \right] \sqrt{\frac{\epsilon}{D}} \right\}, \end{aligned} \quad (9.25)$$

respectively. Figure 9.3 indicates that the first two orders (circles) of the numerically Laplace inverted iterations are sufficient to obtain a useful analytic approximation to the Laplace inverted solution of Eq.(9.23) (grey line).

9.4.2 Model of a model in Laplace Domain

Finally, to validate our iterative feedback approach in Laplace domain, we re-investigate our invented model. For constant radius, the survival probability in time domain is given in Eq.(9.10). It is trivial to Laplace transform this expression to obtain $\tilde{Q}(\epsilon) = 1/[\epsilon + R(t)]$ and substitute the expression into Eq.(9.21). After replacing $R(t)$ with $\epsilon\tilde{R}(\epsilon)$, we obtain the following equation

$$\tilde{R}(\epsilon) = \frac{R(\infty)}{\epsilon} - \frac{R(\infty) - R(0)}{\epsilon + \epsilon\tilde{R}(\epsilon)}. \quad (9.26)$$

which can be solved exactly for $\tilde{R}(\epsilon)$

$$\tilde{R}(\epsilon) = \frac{R(\infty)}{2\epsilon} - \frac{1}{2} \pm \frac{\sqrt{R(\infty)^2 - 2\epsilon[R(\infty) - 2R(0)] + \epsilon^2}}{2\epsilon}.$$

This expression gives two solutions for $\tilde{R}(\epsilon)$. After evaluating the long time limit of $R(t)$, which must be $R(\infty)$,

$$\lim_{\epsilon \rightarrow 0} [\epsilon\tilde{R}(\epsilon)] = \frac{R(\infty)}{2} \pm \frac{R(\infty)}{2},$$

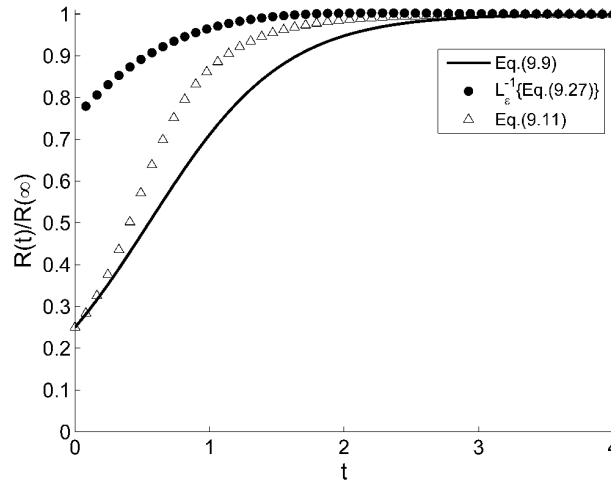


Figure 9.4: Feedback idea applied to the invented model. The exact solution given in Eq.(9.9) (solid line) is compared to two expressions obtained from the feedback method: one, applied in time domain (Eq.(9.11), open triangle) and the other, applied in Laplace domain (numerically inverted Eq.(9.27), open circles).

it is clear that the solution for $\tilde{R}(\epsilon)$ with the negative sign in front of the square root is unphysical. Therefore, the approximate expression for $R(t)$ in Laplace domain for our invented model is

$$\tilde{R}(\epsilon) = \frac{R(\infty)}{2\epsilon} - \frac{1}{2} + \frac{\sqrt{R(\infty)^2 - 2\epsilon[R(\infty) - 2R(0)] + \epsilon^2}}{2\epsilon}. \quad (9.27)$$

This expression cannot be Laplace inverted exactly. Figure 9.4 compares the exact solution of our invented model given in Eq.(9.9) (solid line) to the numerically Laplace inverted Eq.(9.27) (open circles) as well as the numerical solution of Eq.(9.11) (open triangles), which is the solution for the feedback approach applied in time domain. It is apparent from the comparison that our feedback approach in Laplace domain significantly deviates from the exact solution. Moreover, this analysis of our invented model suggests that the feedback approach applied in time domain performs better than the method applied in Laplace domain. We have arrived at a similar conclusion in section 9.4.1, where the feedback method was applied to the simplest one-dimensional trapping problem.

9.5 Coalescence theory compared to Monte Carlo

Calculations in one-dimension

Thus far the validity study of our coalescence theory suggests that the outlined approach works quite well. However, the iterative approximation scheme must be compared to an exact solution to decide whether this approach is useful. Since we do not know the exact solution for the increase in trap radius in our coalescence problem, we performed Monte Carlo calculations. In the present section, lattice random walk simulations of coalescence problems in one-dimension are compared directly to our iterative approximation scheme outlined above. In simulations, a single stationary trap of known initial radius grows due to the absorption of $N = 1000$ non-interacting point particles initially placed at a distance x_0/x_0 away from the trap. Each particle has the same diameter of $a/(100x_0)$, where a is the

lattice constant. Each simulation consisted of 120000 time steps. Final simulation curves were obtained from an average of 10 individual Monte Carlo simulations. This averaging procedure produces an ensemble average, which can be directly compared to our analytic expressions. It is worth noting that an average over 10 runs seemed to be sufficient, since the result did not appear to change significantly, when 100 runs were averaged. Analytic expressions and simulations were employed in MATLAB and the lattice random walk was implemented following Refs. [138] and [164].

9.5.1 Perfect absorption and random particle transport

Simulations were carried out on a one-dimensional lattice. $N = 1000$ noninteracting point particles initially placed at x_0 , hop to their left or right lattice site with a probability of $F\Delta t = 1/2$. Here Δt is the time between steps, and $n\Delta t$ is the time at which the n th step occurs. The diffusion coefficient D in continuum is connected to the discrete simulation as follows (see section 7.4)

$$D = \lim_{\Delta x \rightarrow 0, F \rightarrow \infty} (\Delta x)^2 F = \lim_{\Delta x \rightarrow 0} \frac{(\Delta x)^2}{\Delta t} \frac{1}{2}.$$

In all Monte Carlo simulations, the ration $\frac{(\Delta x)^2}{\Delta t}$ was fixed to $1 \text{ length}^2/\text{time}$, which resulted in a diffusivity of magnitude 0.5. To make meaningful comparisons between analytic expressions and simulation results, the following unitless parameters were defined: $\tau = x_0^2/D$ describing a motion time and $\mathcal{R}(t/\tau) = R(t/\tau)/x_0$ representing the normalized trap radius.

Using these two parameters, Eq.(9.17) becomes

$$\mathcal{R}\left(\frac{t}{\tau}\right) = \mathcal{R}(\infty) - [\mathcal{R}(\infty) - \mathcal{R}(0)] \operatorname{erf}\left(\frac{1}{2}\sqrt{\frac{\tau}{t}}\left[1 - \mathcal{R}\left(\frac{t}{\tau}\right)\right]\right). \quad (9.28)$$

This expression can be solved numerically for $\mathcal{R}\left(\frac{t}{\tau}\right)$. Moreover, following our iterative

procedure, the first two order approximations of Eq.(9.28) are

$$\mathcal{R}_{1st}\left(\frac{t}{\tau}\right) = \mathcal{R}(\infty) - [\mathcal{R}(\infty) - \mathcal{R}(0)] \operatorname{erf}\left(\frac{1}{2}\sqrt{\frac{\tau}{t}}[1 - \mathcal{R}(\infty)]\right) \quad (9.29)$$

and

$$\begin{aligned} \mathcal{R}_{2nd}\left(\frac{t}{\tau}\right) = & \mathcal{R}(\infty) - [\mathcal{R}(\infty) - \mathcal{R}(0)] \\ & \times \operatorname{erf}\left\{\frac{1}{2}\sqrt{\frac{\tau}{t}}\left[1 - \left(\mathcal{R}(\infty) - [\mathcal{R}(\infty) - \mathcal{R}(0)] \operatorname{erf}\left(\frac{1}{2}\sqrt{\frac{\tau}{t}}[1 - \mathcal{R}(\infty)]\right)\right]\right\}, \end{aligned} \quad (9.30)$$

respectively.

Figure 9.5 compares the time dependence of the growing trap radius of Monte Carlo simulations (red line) to our coalescence model in one-dimensions (black line and open circles)

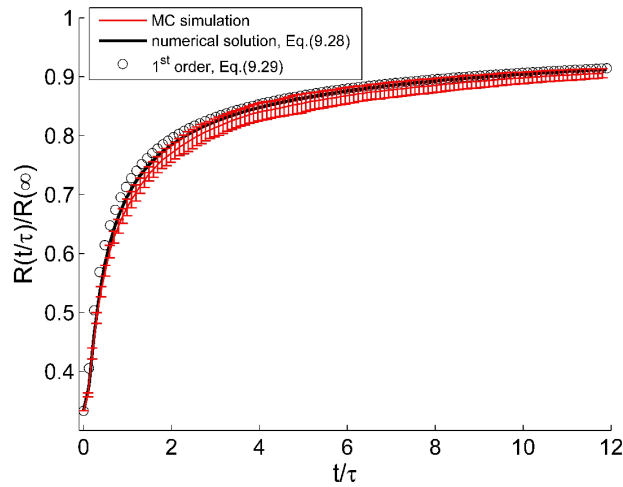


Figure 9.5: Functional form of trap radius $\mathcal{R}(t/\tau)/\mathcal{R}(\infty) = R(t/\tau)/R(\infty)$ obtained from Monte Carlo simulations (red line) and coalescence theory (black line and open circles) due to instantaneous particle absorption at trap boundary-particle contact. Point particles were non-interacting and performed a random walk. The numerical solution to the algebraic Eq.(9.28) (black line) and its analytic first order approximation, Eq.(9.29) (open circles) are in very good agreement with simulations. Error bars represent the standard deviation obtained from 10 individual simulations.

circles). From the figure, it is apparent that the numerical solution to Eq.(9.28) (black line) as well as the first order approximation given in Eq.(9.29) (open circles) fit the simulation (black line) very well. This excellent agreement might be surprising. However, from our previous validity study of an adiabatic approximation for moving boundary problems, in which the time dependence of the moving boundary is explicitly inserted into the static solution (see chapter 8), we know that for slowly moving boundaries, our coalescence theory is expected to work well.

9.5.2 Perfect absorption and biased particle transport

Next, the approximate coalescence theory is compared to simulations for biased diffusion. In these simulations, a probability describing particle bias towards the trap was added to the algorithm. To compute this probability, the problem is analyzed on a discrete lattice. If a random walk is biased to the left, then the hopping rates around a lattice site m can be illustrated as in Fig. 9.6. From Fig. 9.6, we see that the leftward shift is $(F + f) - (F - f) = 2f$ and hence the velocity towards the trap is $2f$ per Δt . In continuum the velocity is then given as

$$v = \lim_{\Delta x \rightarrow 0, f \rightarrow \infty} 2f \Delta x, \quad (9.31)$$

where f remains to be determined. Using Fig.1, the probability to jump to the left is given as $q = (F + f)\Delta t$. Since $F\Delta t = 1/2$, $f = (q - 1/2)/\Delta t$ and

$$v = \lim_{\Delta x \rightarrow 0, \Delta t \rightarrow 0} (2q - 1) \frac{\Delta x}{\Delta t}, \quad (9.32)$$

where q is the jump probability to the left, which is a simulation input parameter. A similar expression is given in Ref. [164] for a jump probability to the right with bias to the right. When $q = 1/2$ and $v = 0$, the unbiased case (see above) is recovered. As expected, when $q = 1/4$ and v is negative for a walker moving away from the trap, the jump probability to the right $1 - q$ is greater than $1/2$. From the above equation q is easily obtained, if

Chapter 9. A Mathematical Model for Receptor Cluster Coalescence

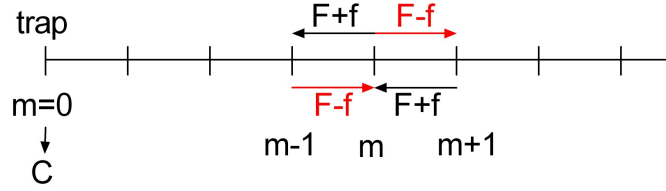


Figure 9.6: Illustration of different hopping rates for a biased random walk on a lattice (biased to the left). F and f are both positive numbers representing the magnitude of the hopping rate in the direction of the corresponding arrow. Here, the trap is located to the left.

v is known. After defining the following unitless parameter $v = \frac{2D}{vx_0}$, describing the drift process, the jump probability to the left is given as

$$q = \frac{1}{2} \left(\frac{\Delta x}{vx_0} + 1 \right), \quad (9.33)$$

where $\frac{(\Delta x)^2}{\Delta t} = 1$ and $D = 1/2$ from section 9.5.1.

To construct our coalescence theory for biased diffusion, the exact expression for Q given in Eq.(8.37) is used

$$Q\left(\frac{t}{\tau}\right) = 1 - \frac{1}{2} e^{-\frac{2}{v}} \operatorname{erfc} \left(\frac{1}{2} \sqrt{\frac{\tau}{t}} - \frac{1}{v} \sqrt{\frac{t}{\tau}} \right) - \frac{1}{2} \operatorname{erfc} \left(\frac{1}{2} \sqrt{\frac{\tau}{t}} + \frac{1}{v} \sqrt{\frac{t}{\tau}} \right).$$

Replacing x_0 with $x_0 - R(t)$ and using the unitless trap radius $\mathcal{R}(\frac{t}{\tau})$, the above expression becomes

$$\begin{aligned} Q\left(\frac{t}{\tau}\right) = & 1 - \frac{1}{2} e^{-\frac{2}{v}[1-\mathcal{R}(\frac{t}{\tau})]} \operatorname{erfc} \left(\frac{1}{2} \sqrt{\frac{\tau}{t}} [1 - \mathcal{R}(\frac{t}{\tau})] - \frac{1}{v} \sqrt{\frac{t}{\tau}} \right) \\ & - \frac{1}{2} \operatorname{erfc} \left(\frac{1}{2} \sqrt{\frac{\tau}{t}} [1 - \mathcal{R}(\frac{t}{\tau})] + \frac{1}{v} \sqrt{\frac{t}{\tau}} \right), \end{aligned} \quad (9.34)$$

which goes to $Q(\infty) = 1 - e^{-\frac{2}{v}[1-\mathcal{R}(\infty)]}$ for large time. Substituting the above expression with $Q(\infty)$ and $Q(0) = 1$ into Eq.(9.3), the trap radius as a function of time can be approx-

imated by the following algebraic equation

$$\begin{aligned} \dot{R}\left(\frac{t}{\tau}\right) = \dot{R}(0) + & \left[\frac{\dot{R}(\infty) - \dot{R}(0)}{2e^{-\frac{2[1-\dot{R}(\infty)]}{v}}} \right] e^{-\frac{2[1-\dot{R}(\frac{t}{\tau})]}{v}} \operatorname{erfc}\left(\frac{1}{2}\sqrt{\frac{\tau}{t}}\left[1 - \dot{R}\left(\frac{t}{\tau}\right)\right] - \frac{1}{v}\sqrt{\frac{t}{\tau}}\right) \\ & + \left[\frac{\dot{R}(\infty) - \dot{R}(0)}{2e^{-\frac{2[1-\dot{R}(\infty)]}{v}}} \right] \operatorname{erfc}\left(\frac{1}{2}\sqrt{\frac{\tau}{t}}\left[1 - \dot{R}\left(\frac{t}{\tau}\right)\right] + \frac{1}{v}\sqrt{\frac{t}{\tau}}\right). \end{aligned} \quad (9.35)$$

Equation (9.35) can be solved numerically and a first order adiabatic approximation is

$$\begin{aligned} \dot{R}_{1st}\left(\frac{t}{\tau}\right) = \dot{R}(0) + & \left[\frac{\dot{R}(\infty) - \dot{R}(0)}{2e^{-\frac{2[1-\dot{R}(\infty)]}{v}}} \right] e^{-\frac{2[1-\dot{R}(\infty)]}{v}} \operatorname{erfc}\left(\frac{1}{2}\sqrt{\frac{\tau}{t}}\left[1 - \dot{R}(\infty)\right] - \frac{1}{v}\sqrt{\frac{t}{\tau}}\right) \\ & + \left[\frac{\dot{R}(\infty) - \dot{R}(0)}{2e^{-\frac{2[1-\dot{R}(\infty)]}{v}}} \right] \operatorname{erfc}\left(\frac{1}{2}\sqrt{\frac{\tau}{t}}\left[1 - \dot{R}(\infty)\right] + \frac{1}{v}\sqrt{\frac{t}{\tau}}\right). \end{aligned} \quad (9.36)$$

Figure 9.7 compares the time dependence of the growing trap radius obtained from Monte Carlo simulations (red line) to our coalescence model (black line and open circles)

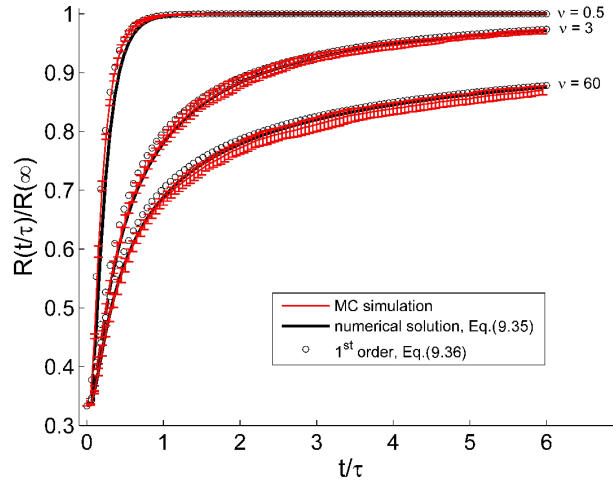


Figure 9.7: Functional form of trap radius $\dot{R}(t/\tau)/\dot{R}(\infty) = R(t/\tau)/R(\infty)$ obtained from Monte Carlo simulations (red line) and coalescence theory (black line and open circles) due to instantaneous particle absorption at trap-particle contact. Point particles were non-interacting and performed a biased random walk towards the trap. The numerical solution to the algebraic Eq.(9.35) (black line) and its analytic first order approximation, Eq.(9.36) (open circles) are in good agreement with simulations. Here, $v = 0.5, 2, 60$, representing a jump probability of $q = 0.52, 0.505, 0.5002$, respectively. Error bars represent the standard deviation obtained from 10 individual simulations.

for biased particle transport in one-dimensions. The depicted curves represent $v = 0.5, 2$, and 60 , corresponding to jump probabilities of $q = 0.52, 0.505$, and 0.5002 , respectively. Since the bias of the particle towards the trap is small, i.e. the jump probability is close to 0.5 , the approximation is expected to perform well as predicted by our validity study for moving boundaries. Indeed, the numerical solution to Eq.(9.35) (black line) as well as the first order approximation given in Eq.(9.36) (open circles) fit the simulation (black line) very well.

9.5.3 Imperfect absorption and random particle transport

In this section, our coalescence theory is validated for imperfect trapping. Here, the trapping probability is obtained by equating the product of absorption time $\Delta t_{abs} = \frac{1}{C}$ and the probability of absorption P_{abs} to the product of hopping time $\Delta t_h = \frac{1}{2F}$ and the probability of reflection $1 - P_{abs}$

$$\frac{1}{2F} (1 - P_{abs}) = \frac{1}{C} P_{abs}, \quad (9.37)$$

which yields

$$P_{abs} = \frac{C}{2F + C} = \frac{C\Delta x}{2D + C\Delta x}. \quad (9.38)$$

The above expression for the absorption probability is also given in Ref. [138]. Here, $\lim_{\Delta x \rightarrow 0} (F\Delta x^2) = D$ is the diffusion coefficient and $\lim_{\Delta x \rightarrow 0} (\Delta x C) = C$ is the continuum capture rate. When $C \rightarrow 0$, then $P_{abs} = 0$, which corresponds to no absorption. When $C \rightarrow \infty$ then $P_{abs} = 1$ reduces to the expected probability for perfect trapping case. Simulations were performed on a lattice and particles jumped to their neighboring sites according to a rate $F = 0.5/\Delta t$. When a particle reached a trapping site at time t_1 , it had the probability P_{abs} to be absorbed at time $t_2 = t_1 + \Delta t$, resulting in a larger trap at t_2 . In case the particles is not absorbed, it gets reflected back to the site to the right of the trap at time t_2 .

For an imperfect absorber at the origin and point particles initially placed at x_0 , the exact expression for the total survival probability is given in Eq.(7.40)

$$Q\left(\frac{t}{\tau}\right) = \text{erf}\left(\frac{1}{2}\sqrt{\frac{\tau}{t}}\right) + e^{\frac{1}{\xi} + \frac{1}{\xi^2}\frac{t}{\tau}} \text{erfc}\left(\frac{1}{2}\sqrt{\frac{\tau}{t}} + \frac{1}{\xi}\sqrt{\frac{t}{\tau}}\right),$$

where $\tau = x_0^2/D$ is the motion parameter and $\xi = 2D/(Cx_0)$ describes the trapping process. To approximate the increase of trap radius due to particle absorption, x_0 is replaced with $x_0 - R(t)$ and the unitless trap radius $\dot{R}(t/\tau)$ is used, giving

$$Q\left(\frac{t}{\tau}\right) = \text{erf}\left[\frac{1}{2}\sqrt{\frac{\tau}{t}}\left(1 - \dot{R}\left(\frac{t}{\tau}\right)\right)\right] + e^{\frac{1}{\xi}\left(1 - \dot{R}\left(\frac{t}{\tau}\right)\right) + \frac{1}{\xi^2}\frac{t}{\tau}} \text{erfc}\left[\frac{1}{2}\sqrt{\frac{\tau}{t}}\left(1 - \dot{R}\left(\frac{t}{\tau}\right)\right) + \frac{1}{\xi}\sqrt{\frac{t}{\tau}}\right]. \quad (9.39)$$

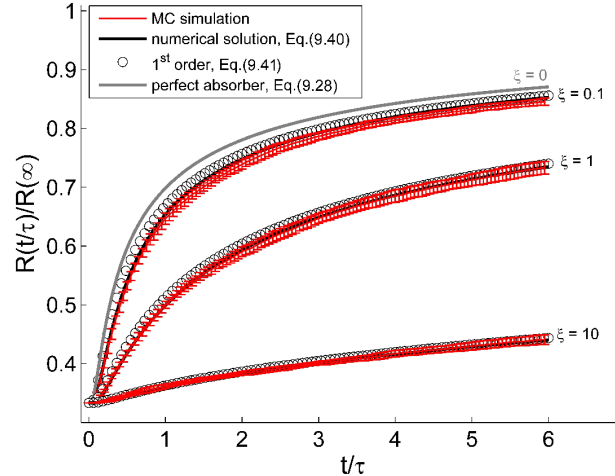


Figure 9.8: Functional form of trap radius $\dot{R}(t/\tau)/\dot{R}(\infty) = R(t/\tau)/R(\infty)$ obtained from Monte Carlo simulations (red line) and coalescence theory (black line and open circles) due to finite particle absorption at trap-particle contact. Point particles were non-interacting and performed a random random walk towards the trap. Here, $\xi = 0, 0.1, 1$, and 10 represents an absorption probability of $P_{abs} = 1, 0.31, 0.043$, and 0.0045 , respectively. The numerical solution to the algebraic Eq.(9.40) (black line) and its analytic first order approximation, Eq.(9.41) (open circles) are in very good agreement with simulations. The solid grey curve represents the numerical solution to Eq.(9.28), describing perfect absorption. Error bars represent the standard deviation obtained from 10 individual simulations.

Chapter 9. A Mathematical Model for Receptor Cluster Coalescence

Substituting this expression into Eq.(9.3) yields to an algebraic equation for increase in trap radius due to imperfect absorption and random particle transport in one-dimension

$$\begin{aligned} \mathcal{R}\left(\frac{t}{\tau}\right) = & \mathcal{R}(\infty) - [\mathcal{R}(\infty) - \mathcal{R}(0)] \operatorname{erf} \left[\frac{1}{2} \sqrt{\frac{\tau}{t}} \left(1 - \mathcal{R}\left(\frac{t}{\tau}\right) \right) \right] \\ & - [\mathcal{R}(\infty) - \mathcal{R}(0)] e^{\frac{1}{\xi}(1-\mathcal{R}(\frac{t}{\tau})) + \frac{1}{\xi^2} \frac{t}{\tau}} \operatorname{erfc} \left[\frac{1}{2} \sqrt{\frac{\tau}{t}} \left(1 - \mathcal{R}\left(\frac{t}{\tau}\right) \right) + \frac{1}{\xi} \sqrt{\frac{t}{\tau}} \right]. \end{aligned} \quad (9.40)$$

This expression can be solved numerically as well as approximated by the following first order expression

$$\begin{aligned} \mathcal{R}_{1st}\left(\frac{t}{\tau}\right) = & \mathcal{R}(\infty) - [\mathcal{R}(\infty) - \mathcal{R}(0)] \operatorname{erf} \left[\frac{1}{2} \sqrt{\frac{\tau}{t}} (1 - \mathcal{R}(\infty)) \right] \\ & - [\mathcal{R}(\infty) - \mathcal{R}(0)] e^{\frac{1}{\xi}(1-\mathcal{R}(\infty)) + \frac{1}{\xi^2} \frac{t}{\tau}} \operatorname{erfc} \left[\frac{1}{2} \sqrt{\frac{\tau}{t}} (1 - \mathcal{R}(\infty)) + \frac{1}{\xi} \sqrt{\frac{t}{\tau}} \right]. \end{aligned} \quad (9.41)$$

Figure 9.8 compares the time dependence of the growing trap radius obtained from Monte Carlo simulations (red line) to our coalescence model (black line and open circles). The curves depict $\xi = 0, 0.1, 1$, and 10 , corresponding to absorption probabilities of $P_{abs} = 1, 0.31, 0.043$, and 0.0045 , respectively. The numerical solution to Eq.(9.35) (black line) as well as the first order approximation given in Eq.(9.41) (open circles) fit the simulation (black line) very well.

9.5.4 Imperfect absorption and biased particle transport

To simulated imperfect absorption and biased diffusion, the expression for the jump probability to the left (towards the trap) given in Eq.(9.33) is used. Here, the particles drift towards the trap and the hopping rate to the right changes from F to $F - f$ as depicted in Fig. 9.6, resulting in a new hopping time $\Delta t_h = \frac{1-q}{F-f}$ to the right. According to section 9.5.2, $f = (q - 1/2)/\Delta t$ and $F = 0.5/\Delta t$, and following section 9.5.3, the hopping time away from the trap Δt_h multiplied by the probability of reflection $1 - P_{abs}$ must equal the

Chapter 9. A Mathematical Model for Receptor Cluster Coalescence

absorption time $\Delta t_{abs} = 1/C$ multiplied by the probability of absorption

$$\frac{1-q}{F-f}(1-P_{abs}) = \frac{1}{C}P_{abs}. \quad (9.42)$$

From this expression it is straight forward to compute the absorption probability at trap-particle contact

$$P_{abs} = \frac{1}{\left(\frac{F-f}{(1-q)C}\right) + 1}, \quad (9.43)$$

where C is defined via the continuum capture rate $\lim_{\Delta x \rightarrow 0} (\Delta x C) = C$. To verify this expression, we look at a few limiting cases. For perfect absorption, $C \rightarrow \infty$ and P_{abs} becomes 1 as expected. Similarly, if particles get never absorbed on trap contact, $C \rightarrow 0$ and $P_{abs} = 0$. Finally, when there is no motion bias towards the trap, i.e. $f = 0$ and $q = 1/2$, the absorption probability reduces to $P_{abs} = \frac{C}{2F+C}$, which was derived previously in section 9.5.3, see Eq.(9.38).

To construct our coalescence theory, we used the expression of $Q(t)$ given by Sanchez [164], which we have re-derived independently by applying the stationary trap prescription

$$\begin{aligned} Q\left(\frac{t}{\tau}\right) = & 1 - \frac{1}{2} \left(\frac{1}{1 - \xi/v} \right) \text{erfc} \left(\frac{1}{2} \sqrt{\frac{\tau}{t}} + \frac{1}{v} \sqrt{\frac{t}{\tau}} \right) \\ & - \frac{1}{2} \left(\frac{1}{1 + \xi/v} \right) e^{\frac{-2}{v}} \text{erfc} \left(\frac{1}{2} \sqrt{\frac{\tau}{t}} - \frac{1}{v} \sqrt{\frac{t}{\tau}} \right) \\ & + \left(\frac{1}{1 - (\xi/v)^2} \right) e^{\frac{-1}{v} + \frac{1}{\xi} + \frac{t}{\tau} \left(\frac{1}{\xi^2} - \frac{1}{v^2} \right)} \text{erfc} \left(\frac{1}{2} \sqrt{\frac{\tau}{t}} + \frac{1}{\xi} \sqrt{\frac{t}{\tau}} \right). \end{aligned} \quad (9.44)$$

Replacing $x_0 \rightarrow x_0 - R(t)$ and defining our unitless trap radius $\mathcal{R}(\frac{t}{\tau}) = R(\frac{t}{\tau})/x_0$, the survival

probability becomes

$$\begin{aligned}
 Q\left(\frac{t}{\tau}\right) = & 1 - \frac{1}{2} \left(\frac{1}{1 - \xi/v} \right) \operatorname{erfc} \left(\frac{1}{2} \sqrt{\frac{\tau}{t}} \left[1 - \mathcal{R}\left(\frac{t}{\tau}\right) \right] + \frac{1}{v} \sqrt{\frac{t}{\tau}} \right) \\
 & - \frac{1}{2} \left(\frac{1}{1 + \xi/v} \right) e^{\frac{-2}{v} [1 - \mathcal{R}(\frac{t}{\tau})]} \operatorname{erfc} \left(\frac{1}{2} \sqrt{\frac{\tau}{t}} \left[1 - \mathcal{R}\left(\frac{t}{\tau}\right) \right] - \frac{1}{v} \sqrt{\frac{t}{\tau}} \right) \\
 & + \left(\frac{e^{\left(\frac{-1}{v} + \frac{1}{\xi}\right) [1 - \mathcal{R}(\frac{t}{\tau})] + \frac{t}{\tau} \left(\frac{1}{\xi^2} - \frac{1}{v^2}\right)}}{1 - (\xi/v)^2} \right) \operatorname{erfc} \left(\frac{1}{2} \sqrt{\frac{\tau}{t}} \left[1 - \mathcal{R}\left(\frac{t}{\tau}\right) \right] + \frac{1}{\xi} \sqrt{\frac{t}{\tau}} \right),
 \end{aligned} \tag{9.45}$$

which goes to

$$Q(\infty) = 1 - \left(\frac{1}{1 + \xi/v} \right) e^{\frac{-2}{v} [1 - \mathcal{R}(\infty)]}.$$

Substituting this expression with Eq.(9.45) into Eq.(9.3), the following algebraic equation, approximating the growth of the trap due to imperfect absorption and biased particle diffusion, is obtained

$$\begin{aligned}
 \mathcal{R}\left(\frac{t}{\tau}\right) = & \mathcal{R}(0) + \left[\frac{\mathcal{R}(\infty) - \mathcal{R}(0)}{\left(\frac{1}{1 + \xi/v} \right) e^{\frac{-2}{v} [1 - \mathcal{R}(\infty)]}} \right] \\
 & \times \left\{ \begin{aligned} & \frac{1}{2} \left(\frac{1}{1 - \xi/v} \right) \operatorname{erfc} \left(\frac{1}{2} \sqrt{\frac{\tau}{t}} \left[1 - \mathcal{R}\left(\frac{t}{\tau}\right) \right] + \frac{1}{v} \sqrt{\frac{t}{\tau}} \right) \\ & + \frac{1}{2} \left(\frac{1}{1 + \xi/v} \right) e^{\frac{-2}{v} [1 - \mathcal{R}(\frac{t}{\tau})]} \operatorname{erfc} \left(\frac{1}{2} \sqrt{\frac{\tau}{t}} \left[1 - \mathcal{R}\left(\frac{t}{\tau}\right) \right] - \frac{1}{v} \sqrt{\frac{t}{\tau}} \right) \\ & - \left(\frac{1}{1 - (\xi/v)^2} \right) e^{\left(\frac{-1}{v} + \frac{1}{\xi}\right) [1 - \mathcal{R}(\frac{t}{\tau})] + \frac{t}{\tau} \left(\frac{1}{\xi^2} - \frac{1}{v^2}\right)} \\ & \times \operatorname{erfc} \left(\frac{1}{2} \sqrt{\frac{\tau}{t}} \left[1 - \mathcal{R}\left(\frac{t}{\tau}\right) \right] + \frac{1}{\xi} \sqrt{\frac{t}{\tau}} \right) \end{aligned} \right\}.
 \end{aligned} \tag{9.46}$$

Equation (9.46) can be solved numerically for $\mathcal{R}\left(\frac{t}{\tau}\right)$ and its first order analytic approximation is

$$\begin{aligned}
 \mathcal{R}_{1st}\left(\frac{t}{\tau}\right) = & \mathcal{R}(0) + \left[\frac{\mathcal{R}(\infty) - \mathcal{R}(0)}{\left(\frac{1}{1 + \xi/v} \right) e^{\frac{-2}{v} [1 - \mathcal{R}(\infty)]}} \right] \\
 & \times \left\{ \begin{aligned} & \frac{1}{2} \left(\frac{1}{1 - \xi/v} \right) \operatorname{erfc} \left(\frac{1}{2} \sqrt{\frac{\tau}{t}} \left[1 - \mathcal{R}(\infty) \right] + \frac{1}{v} \sqrt{\frac{t}{\tau}} \right) \\ & + \frac{1}{2} \left(\frac{1}{1 + \xi/v} \right) e^{\frac{-2}{v} [1 - \mathcal{R}(\infty)]} \operatorname{erfc} \left(\frac{1}{2} \sqrt{\frac{\tau}{t}} \left[1 - \mathcal{R}(\infty) \right] - \frac{1}{v} \sqrt{\frac{t}{\tau}} \right) \\ & - \left(\frac{1}{1 - (\xi/v)^2} \right) e^{\left(\frac{-1}{v} + \frac{1}{\xi}\right) [1 - \mathcal{R}(\infty)] + \frac{t}{\tau} \left(\frac{1}{\xi^2} - \frac{1}{v^2}\right)} \\ & \times \operatorname{erfc} \left(\frac{1}{2} \sqrt{\frac{\tau}{t}} \left[1 - \mathcal{R}(\infty) \right] + \frac{1}{\xi} \sqrt{\frac{t}{\tau}} \right) \end{aligned} \right\}.
 \end{aligned} \tag{9.47}$$

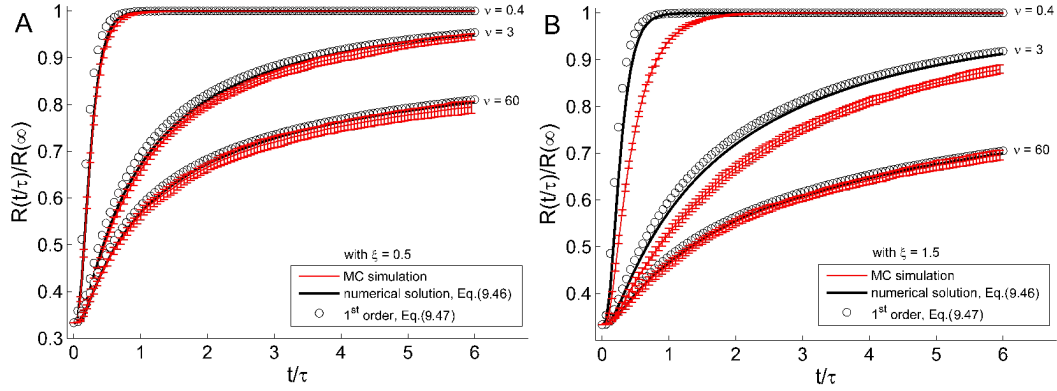


Figure 9.9: Functional form of trap radius $\hat{R}(t/\tau)/\hat{R}(\infty) = R(t/\tau)/R(\infty)$ obtained from Monte Carlo simulations (red line) and coalescence theory (black line and open circles) due to finite particle absorption at trap-particle contact. Point particles were non-interacting and performed a biased diffusion towards the trap. Here, $\nu = 0.4, 3$, and 60 with $\xi = 0.5$ in (A) and $\xi = 1.5$ in (B). The numerical solution to the algebraic Eq.(9.46) (black line) and its analytic first order approximation, Eq.(9.47) (open circles) approximated the simulation better for small ξ (high absorption probability) and large ν (small bias towards trap) as expected. Error bars represent the standard deviation obtained from 10 individual simulations.

Figure 9.9 compares the time dependence of the growing trap radius obtained from Monte Carlo simulations (red line) to our coalescence model (black line and open circles) for biased particle transport and imperfect absorption in one-dimension. The figure depicts curves for $\nu = 0.4, 3$, and 60 with $\xi = 0.5$ in (A) and $\xi = 1.5$ in (B). The numerical solution to Eq.(9.46) (black line) as well as the first order approximation given in Eq.(9.47) (open circles) fit the simulation (black line) very well for large ν (small motion bias towards trap) and small ξ (high absorption probability). For small ν and large ξ , our coalescence theory is expected to deviate significantly from the exact solution, as predicted from our previous validity study of an adiabatic approximation for moving boundary problems.

9.5.5 Validation of theory for finite sized particles

Thus far, we have compared our coalescence theory to simulations of non-interacting point particles, i.e. the size of each particle was chosen to be about 100 times smaller than the lattice constant. In this section, our theory is compared to simulations of finite-sized particles, which perform biased diffusion towards an imperfect trap. Here, the particle size is taken to be 5 times the lattice constant and 6 non-interacting particles are initially placed 100 lattice sites away from the origin, where a finite-sized trap is located. Each simulation performs 40000 hops. Figure 9.10 compares the result obtained from 10 simulations to the first order approximation given in Eq.(9.47) (open triangles) and the fifth order approximation (open circles). According to the presented data, even for finite-sized particles, our approximate theory seems to predict the functional form of the trap radius well since large error bars obtained from the Monte Carlo simulations makes an interpretation difficult.

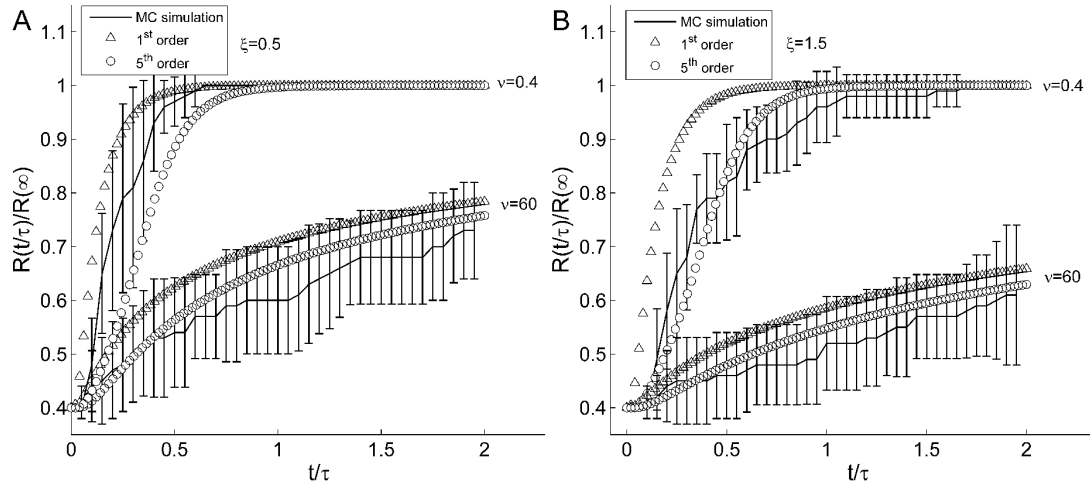


Figure 9.10: Functional form of trap radius $R(t/\tau)/R(\infty) = R(t/\tau)/R(\infty)$ obtained from Monte Carlo simulations (line) compared to a first and fifth order approximation depicted as open triangles and circles, respectively. Here particle had a finite size and performed biased hops towards the trap. At particle-trap contact the particles were absorbed at a finite rate, with $v = 0.4$ and 60 with $\xi = 0.5$ in (A) and $\xi = 1.5$ in (B). Error bars represent the standard deviation obtained from 10 individual simulations.

9.6 Coalescence theory compared to Monte Carlo Calculations in two-dimensions

In section 9.5, our one-dimensional approximate coalescence theory was directly compared to exact solutions obtained from Monte Carlo simulations. For random particle transport, finite reaction, and weakly biased particle motion towards the growing trap, our developed theory approximated simulated particle growth well. This agreement was expected from our validity study of an adiabatic approximation for moving boundary problems. In the present section, we perform a validity study for two-dimensional problems. According to an earlier validity study in Laplace domain, see section 9.4.1, we expect our two-dimensional approximation to deviate more from the exact solution than the one-dimensional approximation applied directly in time domain.

In the present section, Monte Carlo simulations were performed in the continuum, rather than on a two-dimensional lattice. In two-dimensions, a continuous diffusion simulation is less computationally expensive than its discrete lattice counterpart. It is worth noting that in the limit of long times, these two approaches are equivalent when the step size or hop length is small and the result is averaged over many individual trajectories. For investigations presented in the present chapter, these requirements are fulfilled, since we are interested in an ensemble average over many particles. We have directly compared these two approaches for a trap growth due to perfect absorption and random particle transport in one-dimensions. For parameters of interest, these two approaches were in excellent agreement (data not shown). Therefore, in the present section, a random-step-length algorithm as outlined in section 4.4 was implemented. In Monte Carlo calculations, a stationary trap of radius $R(0)$ was placed at the origin and an initial radial symmetric homogeneous distribution of 10000 non-interacting diffusing point particles were placed at r_0 in sections 9.6.1 and 9.7.1. On trap-particle contact, a particle was either absorbed instantaneously in section 9.6.1 or at a finite rate in section 9.7.1. After successful trap-particle melding,

the trap radius grew from $R(t)$ to $\sqrt{R(t)^2 + R_0^2}$, where $R_0/r_0 = 1 \times 10^{-3}$ is the radius of a single point particle. This assumes an isotropic melding of particles with the central disk. The hop length Δ_{xy} of a particle in the x and y directions was set to $\Delta_{xy}/r_0 = 1.7 \times 10^{-2}$. Each Monte Carlo simulation was iterated over 100000 time steps.

9.6.1 Perfect absorption and localized initial condition

To validate the coalescence theory we have developed in two dimensions, we investigate the problem of a stationary perfectly absorbing trap of radius $R(0)$ at the origin and an initial radial distribution of non-interacting point particles at r_0 . An approximate expression for the increase in trap radius due to particle absorption is given in Eq.(9.4), which becomes in two-dimensions

$$R(t)^2 = R(0)^2 + \left[\frac{R(\infty)^2 - R(0)^2}{1 - Q(\infty)} \right] [1 - Q(t)]. \quad (9.48)$$

As mentioned earlier, in two-dimensions, an exact expression for the survival probability Q is only available in Laplace domain, see Eq.(7.82)

$$\tilde{Q}(\epsilon) = \frac{1}{\epsilon} \left\{ 1 - \frac{K_0 \left[r_0 \sqrt{\frac{\epsilon}{D}} \right]}{K_0 \left[R(0) \sqrt{\frac{\epsilon}{D}} \right]} \right\}.$$

Treating the trap radius in this expression as a constant and substituting the Laplace transform of \tilde{Q} into Eq.(9.48) gives our approximate unitless expression for the time dependence of the trap radius

$$\dot{R}(t/\tau)^2 = \dot{R}(0)^2 + [\dot{R}(\infty)^2 - \dot{R}(0)^2] L_\epsilon^{-1} \left\{ \frac{K_0 \left[[1 - \epsilon \tilde{R}(\epsilon)] \sqrt{\epsilon \tau} \right]}{\epsilon K_0 \left[\dot{R}(0) \sqrt{\epsilon \tau} \right]} \right\}. \quad (9.49)$$

Here, r_0 was replaced with $r_0 - \epsilon \tilde{R}(\epsilon)$, $\tau = r_0^2/D$, $\dot{R}(t/\tau) = R(t/\tau)/r_0$, and for a circular perfect absorbing trap $Q(\infty) = 0$. A first order approximation of Eq.(9.49), following the iterative procedure outlined in section 9.4.1, can be written as

$$\dot{R}_{1st}(t/\tau)^2 = \dot{R}(0)^2 + [\dot{R}(\infty)^2 - \dot{R}(0)^2] L_\epsilon^{-1} \left\{ \frac{K_0 \left[[1 - \dot{R}(\infty)] \sqrt{\epsilon \tau} \right]}{\epsilon K_0 \left[\dot{R}(0) \sqrt{\epsilon \tau} \right]} \right\}. \quad (9.50)$$

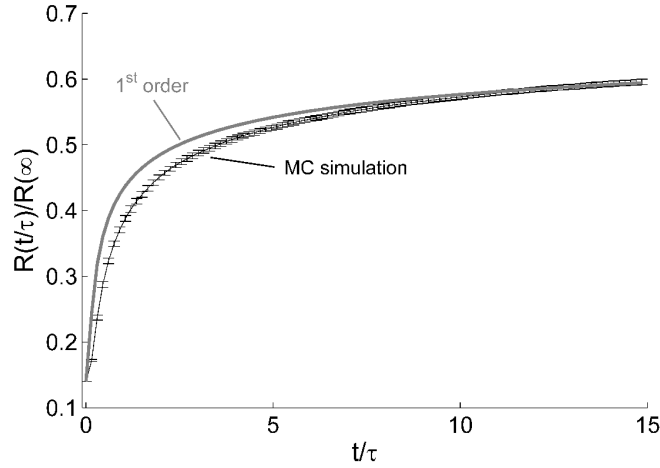


Figure 9.11: Radial symmetric functional form of trap radius $R(t/\tau)/R(\infty) = R(t/\tau)/R(\infty)$ obtained from Monte Carlo simulations (black line) compared to a first order approximation of our coalescence theory (grey line), given in Eq.(9.50). Diffusing point particles merged instantaneously with the trap on contact. Error bars represent the standard deviation obtained from 10 individual simulations.

In this expression, the Laplace transform of the Bessel functions must be evaluated numerically, e.g. by applying a numerical inversion algorithm as outlined in appendix C.

Figure 9.11 compares the first order approximation given in Eq.(9.50) (grey line) to the result obtained from Monte Carlo simulations (solid line), which was obtained from an average over 10 individual simulations. The approximate analytical expression deviates from Monte Carlo results at early times $t/\tau < 10$. This deviation was expected, since the feedback idea applied in Laplace domain deviates more from the exact solution as the feedback idea applied in time domain, see section 9.4.1. Nevertheless, our two-dimensional approximate coalescence theory describes the exact solution well. It is important to note that the functional form of the Monte Carlo simulation is dependent on the number of initial point particles. The time at which the black line crosses the grey line in Fig. 9.11 depends on the number of initial particles. If the number is less than 10000, the crossing will occur at later time. If the number is more than 10000, the crossing occurs at earlier

Chapter 9. A Mathematical Model for Receptor Cluster Coalescence

time. However, at long times both curves will meet again and approach the value 1 in the limit.

Comparison in Laplace domain

As mentioned above, Eq.(9.49) can also be evaluated in Laplace domain

$$L_{\varepsilon} \{ \dot{R}(t/\tau)^2 \} = \frac{\dot{R}(0)^2}{\varepsilon} + [\dot{R}(\infty)^2 - \dot{R}(0)^2] \left\{ \frac{K_0 [1 - \varepsilon \tilde{R}(\varepsilon)] \sqrt{\varepsilon \tau}}{\varepsilon K_0 [\dot{R}(0) \sqrt{\varepsilon \tau}]} \right\}, \quad (9.51)$$

and compared directly to the Laplace transformed functional form of $R(t)^2$ obtained from simulations. Looking at Eq.(9.51), we see that the left-hand side becomes

$$L_{\varepsilon} \{ \dot{R}(t/\tau)^2 \} = \frac{1}{2\pi i} \int_{c-i\infty}^{c+i\infty} \tilde{R}(u) \tilde{R}(\varepsilon - u) du,$$

where c is a line parallel to the imaginary axis and to the right of all singularities of the integrand. Substituting this expression into Eq.(9.51) leads to a complex algebraic-like equation in Laplace domain, which is not too useful. Therefore, we will use expression in the form of a first order approximations, e.g. Eq.(9.50), to compare experimental results to our coalescence theory.

9.6.2 Perfect absorption and random initial condition

Thus far, we have focused on localized initial conditions. In this section, the performance of our coalescence theory is validated for an initial random distribution of point particles. This initial distribution is significant, since receptor clusters were observed to follow such a distribution in experiments. In our experiments, we observed that the number of clusters found at a radial distance r from the center of the cell-substrate contact area is proportional to r . This functional dependence as depicted in Fig. 3.6 indicates that the clusters are randomly distributed within the contact area. Since the radius of the contact area r'_0 can be

estimated from experiments, the new survival probability can be written as a superposition (see section 7.5.2) by integrating Q over the normalized initial point-particle distribution

$$\tilde{Q}(\epsilon) = \frac{2}{r_0^2 - R(0)^2} \int_{R(0)}^{r_0} \tilde{Q}(\epsilon; r) r dr. \quad (9.52)$$

Note that the lower limit of the integration is $R(0)$. After integrating $\tilde{Q}(\epsilon)$ over the initial particle distribution, replacing $r_0 \rightarrow r_0 - R(\infty)$ and substituting this expression into Eq.(9.50), the approximate time dependence of the radius squared for a random initial distribution of particles can be written as

$$\dot{R}_{1st}(t/\tau)^2 = \dot{R}(0)^2 + [\dot{R}(\infty)^2 - \dot{R}(0)^2] L_\epsilon^{-1} \left\{ \frac{\frac{2}{[1 - \dot{R}(\infty)]^2 - \dot{R}(0)^2} \int_{\dot{R}(0)}^{1 - \dot{R}(\infty)} \dot{r} K_0 [\dot{r} \sqrt{\epsilon \tau}] d\dot{r}}{\epsilon K_0 [\dot{R}(0) \sqrt{\epsilon \tau}]} \right\}. \quad (9.53)$$

Here, $\dot{r} = r/r'_0$ and the dimensionless parameters are defined as $\tau = (r'_0)^2/D$, $\xi_{2d} = DR(0)/[C_{2d} r'_0]$, and $\dot{R}(t) = R(t)/r'_0$. Moreover, the integral in Eq.(9.53) can be

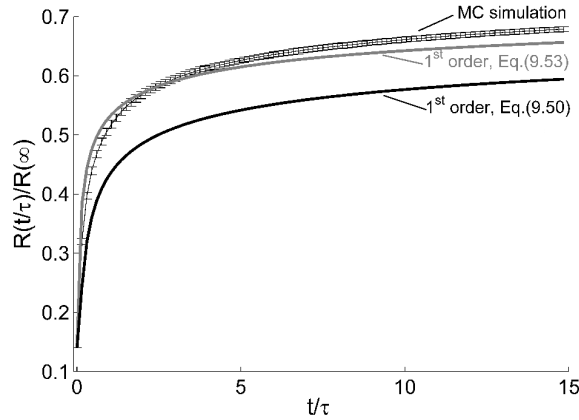


Figure 9.12: Functional form of trap radius $\dot{R}(t/\tau)/\dot{R}(\infty) = R(t/\tau)/R(\infty)$ for an initial random distribution obtained from Monte Carlo simulations (black line with error bars) compared to a first order approximation of our coalescence theory (grey line), given in Eq.(9.53). Diffusing point particles merged instantaneously with the trap on contact. Error bars represent the standard deviation obtained from 10 individual simulations. For comparison the first order approximation for a radial localized initial condition given in Eq.(9.50) is shown as black solid line.

Chapter 9. A Mathematical Model for Receptor Cluster Coalescence

evaluated exactly

$$\int_{R(0)}^{1-R(\infty)} r K_0 [r \sqrt{\epsilon \tau}] dr = \frac{R(0) K_1 [R(0) \sqrt{\epsilon \tau}]}{\sqrt{\epsilon \tau}} - \frac{[1 - R(\infty)] K_1 [(1 - R(\infty)) \sqrt{\epsilon \tau}]}{\sqrt{\epsilon \tau}}. \quad (9.54)$$

Figure 9.12 compares the first order approximation given in Eq.(9.53) (grey line) to the result obtained from Monte Carlo simulations (black line with error bars), which was obtained from an average over 10 individual simulations. The approximate analytical expression for an initial random distribution follows the exact solution well. As expected, the radius increases faster for a random initial distribution of point particles compared to a localized initial condition (black line).

Finite-sized particles

In section 9.5.5, results obtained from a one-dimensional Monte Carlo simulation for finite-sized non-interacting particles were compared to our theory, indicating that our analytic approximation describes the simulated data quite well. In the present section, a similar validity study is performed in two-dimensions for instantaneous melding. Here, the particle radius is taken to be twice the hopping length Δ_{xy} and 5 particles are randomly distributed within a circle of radius 58 times Δ_{xy} centered at the origin, where a finite sized trap is located. Each simulation was iterated 100000 times and the result was averaged over 20 runs. Figure 9.13 compares the Monte Carlo result (black error bars) to the first order approximation given in Eq.(9.53) (grey line). According to the depicted data, our approximate theory predicts faster coalescence kinetics as obtained from simulations. This result is expected, since Eq.(9.53) is a first order approximation iterated away from $R(\infty)$.

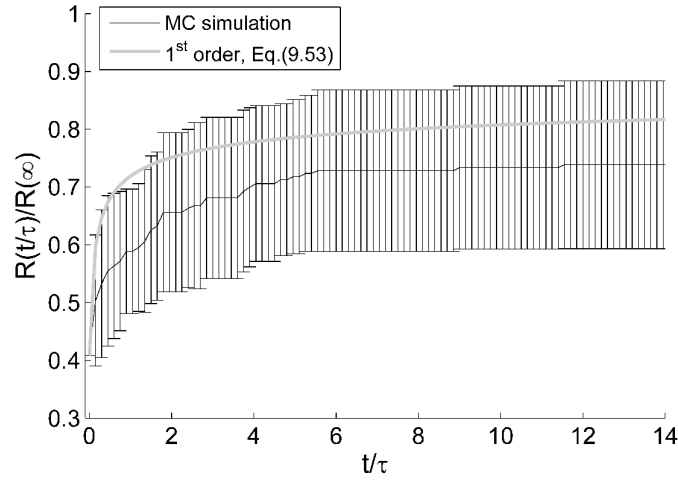


Figure 9.13: Functional form of trap radius $\bar{R}(t/\tau)/\bar{R}(\infty) = R(t/\tau)/R(\infty)$ obtained from two-dimensional Monte Carlo simulations (black error bars) compared to the first order approximation given in Eq.(9.53) (grey line). Here particles had a finite size and performed random motion. At particle-trap contact the particles were absorbed instantaneously. Error bars represent the standard deviation obtained from 20 individual simulations.

9.7 Comparison of theory to experiments

In our experiments, we observed receptor clusters coalescence, which resulted in the formation of a large central receptor patch. Since in our experimental system, the central receptor patch boundary was impermeable, and only grows after a successful receptor-patch melding event, expressions for Q in higher dimensions derived from the trapping prescription is not useful, since these expressions describe permeable membranes. Therefore, expressions for impermeable membranes and finite reaction rate must be used. Fortunately, such expressions are available readily from our previous investigations of the equivalence between the stationary trapping theory and the theory of conduction in heat and solids, see section 7.9.1.

9.7.1 Radiative trap boundary

An expression for the total survival probability, satisfying radiative boundary conditions, can be obtained from Eq.(7.136)

$$\frac{\tilde{c}(r, \epsilon)}{c_0} = \frac{1}{\epsilon} \left\{ 1 - \frac{hK_0 \left[r \sqrt{\frac{\epsilon}{D}} \right]}{\sqrt{\frac{\epsilon}{D}} K_1 \left[R(0) \sqrt{\frac{\epsilon}{D}} \right] + hK_0 \left[R(0) \sqrt{\frac{\epsilon}{D}} \right]} \right\}.$$

This expression in Laplace domain, describes the radial symmetric concentration profile $c(t)$ for radiative boundary conditions at radius $R(0)$ and an initial continuous distribution c_0 . To obtain an equivalent expression for Q , the reaction rate h is replaced by $C_{2d}/[2\pi DR(0)]$, see section 7.8.3, yielding

$$\tilde{Q}(\epsilon) = \frac{1}{\epsilon} \left\{ 1 - \frac{K_0 \left[r_0 \sqrt{\frac{\epsilon}{D}} \right]}{\frac{2\pi DR(0)}{C_{2d}} \sqrt{\frac{\epsilon}{D}} K_1 \left[\sqrt{\frac{R(0)^2 \epsilon}{D}} \right] + K_0 \left[\sqrt{\frac{R(0)^2 \epsilon}{D}} \right]} \right\}. \quad (9.55)$$

Here, r was replaced with r_0 , since this expression holds for a radially symmetric distribution of initial point particles at r_0 . It is worth noting that Eq.(9.55) reduces to Eq.(9.4) in the perfect absorption limit, i.e. $C_{2d} \rightarrow \infty$, as expected. To obtain the first order approximation for the time dependence of the trap radius, we follow our previous methodology to obtain

$$\begin{aligned} \mathcal{R}_{1st}(t/\tau)^2 &= \mathcal{R}(0)^2 + [\mathcal{R}(\infty)^2 - \mathcal{R}(0)^2] \\ &\times L_\epsilon^{-1} \left\{ \frac{K_0 \left[[1 - \mathcal{R}(\infty)] \sqrt{\epsilon \tau} \right]}{\xi_{2d} \epsilon^{3/2} \sqrt{\tau} K_1 \left[\mathcal{R}(0) \sqrt{\epsilon \tau} \right] + \epsilon K_0 \left[\mathcal{R}(0) \sqrt{\epsilon \tau} \right]} \right\}. \end{aligned} \quad (9.56)$$

Here, dimensionless parameters are defined as $\tau = r_0^2/D$ and $\xi_{2d} = 2\pi DR(0)/[C_{2d} r_0]$.

To obtain an expression for radiative boundary conditions and an initial random distribution of particles, r_0 in Eq.(9.55) is integrated over the initial distribution. After substituting this expression into Eq.(9.56), a first order approximation of the time dependence of

the radius squared for a random initial distribution of particles and a radiative trap boundary is written as

$$\begin{aligned} \dot{R}_{1st}(t/\tau)^2 &= \dot{R}(0)^2 + \\ &2 \times L_\epsilon^{-1} \left\{ \frac{\dot{R}(0)K_1[\dot{R}(0)\sqrt{\epsilon\tau}] - [1 - \dot{R}(\infty)]K_1[(1 - \dot{R}(\infty))\sqrt{\epsilon\tau}]}{\xi_{2d}\epsilon^2\tau K_1[\dot{R}(0)\sqrt{\epsilon\tau}] + \epsilon^{3/2}\sqrt{\tau}K_0[\dot{R}(0)\sqrt{\epsilon\tau}]} \right\}. \end{aligned} \quad (9.57)$$

Here, the dimensionless parameters are defined as $\tau = (r'_0)^2/D$, $\xi_{2d} = 2\pi DR(0)/[C_{2d} r'_0]$, and $\dot{R}(t) = R(t)/r'_0$.

9.7.2 Experimental growth of central patch

Our experimental analysis of individual receptor trajectories showed that receptor cluster have both a diffusive and directed motion component. However, further analysis indicated that the biased motion component of receptor cluster transport had no preferred radial direction (see section 3.4.1). Therefore, the approximate analytic expression for random particle transport given in Eq.(9.57) can be directly applied to experimental data.

Experimental data was obtained from TIRF images of fluorescently labeled IgE-FcεRI complexes in contact with a fluid ligand presenting bilayer with 25 mol% DNP-Cap PE. To each image in the time series a thresholding algorithm outlined in section 2.10 was applied to extract the radius of the largest receptor patch at each time point. After computing the largest receptor patch radius in individual images, the corresponding average at each time point from four individual cell data sets was computed. It is important to note that individual data sets are of different length. Therefore, the standard error of the mean was used as an estimate for the expected error at each time point. To compare the observed time-dependent central patch radius directly to our theoretical model, the radius of the largest receptor cluster was normalized by the maximum radius of the cell-substrate contact area

$r'_0 = 7.3 \mu m$. This radius was obtained from the largest estimated cell-substrate contact zone of each time series. The average diffusion coefficient obtained from over 100 individual receptor cluster trajectories in 4 cell data sets was $9.1 \times 10^{-3} \mu m^2/s$, which allows us to normalize our time series by the motion parameter $\tau = (r'_0)^2/D = 5.9 \times 10^3 s$. The initial radius of the central receptor patch was $R(0) = 700 nm$, estimated from the average of the first 10 data points. The largest possible central patch radius was $R(\infty) = 3 \mu m$. This parameter was estimated from the maximum total area covered by receptors and patches in each time series and averaging the result. In graphical comparison of experiment and theory below (see Figs. 9.14 and 9.15), the growing trap radius was normalized by the time τ_c in which the initial average distance between two clusters is covered diffusively. This distance is estimated to be 350 nm giving $\tau_c = 14 s$.

Figure 9.14 compares the experimental data (black error bars) to the two-dimensional coalescence theory for randomly distributed particles given in Eq.(9.57). Here, particles were absorbed at a finite rate on trap contact, for $\xi = 0$ (instantaneous melding), $\xi = 0.1$,

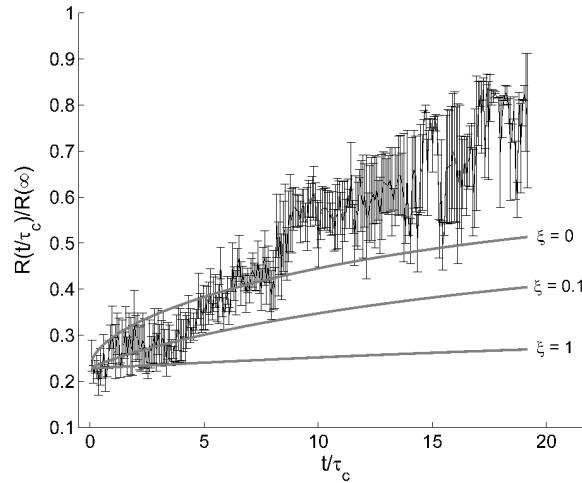


Figure 9.14: Experimental data (error bars) compared to two-dimensional coalescence theory for finite melding probability given in Eq.(9.57) for $\xi = 0$ (instantaneous melding), $\xi = 0.1$, and $\xi = 1$ (solid grey lines). The experimental data represents the normalized radius of the biggest receptor patch at each time point averaged over four data sets. The error bars represent the standard error of the mean.

and $\xi = 1$ (solid grey lines). From this direct comparison of theory and experiment, we conclude the following. First, at early time $t/\tau_c < 5$, experimentally observed receptor cluster coalescence in mast cells, when presented to a fluid ligand-bearing membrane, seems to be delayed. This observation suggests that our coalescence theory for a constant capture rate, does not explain our experimental data at early time. Second, for longer times $t/\tau_c > 10$, it is apparent that cluster coalescence is more rapid than theory predicts. This observation might be expected, since our coalescence theory models non-interacting particles, which could effectively decrease the collision frequency. However, other explanations are equally tenable and are further discussed in section 9.9.

9.8 Incorporation of a time-dependent capture rate

Figure 9.14 suggests that the measured radius of the largest receptor patch over time is of sigmoidal form. This functional form together with qualitative observations that only at late time points ($>1\text{min}$) every contact of two clusters leads to melding, supports the contention that receptor cluster coalescence is delayed. Theoretically, we have shown that if cluster coalescence were not delayed, the absorber radii would increase faster at short time (see black line for $\xi = 0$ in Fig. 9.14). The observed delay in coalescence might be due to actin reorganization [13] and changes in cell membrane morphology (see section 3.6) that are known to occur on mast cell stimulation. Therefore, our coalescence theory must be generalized to address this observation for times $t/\tau_c < 5$. This necessitates the introduction of a new feature in our theory, as we outline below: a time-dependent capture rate.

9.8.1 Time-dependent capture rate in form of a memory function

It appears at least qualitatively, that the solution to the delay problem described above may lie in constructing a coalescence theory in which capture is time-dependent in that the process happens with a threshold in time. In order to develop such a theory we return to section 7.2. The natural modification, the replacement of the discrete constant capture rate C by a time-dependent $C(t)$, is not easy (or to our knowledge even possible) to implement theoretically. This fact, combined with the prior existence [22] of a formalism developed for capture via a "memory function" leads us to rewrite the capture term in the standard Master equation in the form

$$\frac{dP_m(t)}{dt} = \text{motion terms} - \int_0^t C_M(t-s) \delta_{m,r} P_m(s) ds, \quad (9.58)$$

where C_M is the capture memory in discrete space. In the Markovian limit C_M has a short relaxation time compared to $P_{m=r}$ and $C(t)$ is obtained simply by integrating $C_M(t)$. This treatment of the capture rate as a memory allows us to proceed with our analysis in Laplace domain, with no change except the replacement of the constant C by the Laplace transform $\widetilde{C}_M(\epsilon)$ of the capture memory: thus in continuous space the prescription becomes,

$$\widetilde{Q}(\epsilon) = \frac{1}{\epsilon} \left(1 - \frac{\widetilde{\eta}_r(\epsilon)}{\frac{1}{\widetilde{C}_M(\epsilon)} + \widetilde{\Psi}_0(\epsilon)} \right). \quad (9.59)$$

For $C_M(t) = C\delta(t)$, i.e. the memory decays infinitely rapidly and $\widetilde{C}_M(\epsilon) = C$, reducing Eq.(9.59) to the trapping prescription for constant capture given in Eq.(7.35). Therefore, Eq.(9.59) is a generalization [22] of the trapping prescription for a time-dependent capture rate in form of a memory function, obtained by simply replacing C in Eq.(7.35) with $\widetilde{C}_M(\epsilon)$. This observation can be directly applied to our coalescence theory, which generalizes the model for a time-dependent capture rate. For example, to apply our generalized coalescence theory to our experiments, the capture rate C_{2d} in the capture parameter ξ of

Eq.(9.57) is replaced by $\widetilde{C}_M(\epsilon)$ to give

$$\begin{aligned} \dot{R}_{1st}(t/\tau)^2 &= \dot{R}(0)^2 + \\ &2 \times L_\epsilon^{-1} \left\{ \frac{\dot{R}(0)K_1[\dot{R}(0)\sqrt{\epsilon\tau}] - [1 - \dot{R}(\infty)]K_1[(1 - \dot{R}(\infty))\sqrt{\epsilon\tau}]}{\frac{2\pi D\dot{R}(0)}{\widetilde{C}_M(\epsilon)}\epsilon^2\tau K_1[\dot{R}(0)\sqrt{\epsilon\tau}] + \epsilon^{3/2}\sqrt{\tau}K_0[\dot{R}(0)\sqrt{\epsilon\tau}]} \right\}. \end{aligned} \quad (9.60)$$

9.8.2 Possible functional form of the capture memory

As mentioned above, our experimental observations suggest that at early times of cell-substrate contact ($< 1\text{min}$), receptor clusters do not coalesce on contact. Only at late times is the merging process more frequent. Accordingly, an appropriate time-dependent capture rate must be increasing over time. We introduce one candidate for the memory $C_M(t)$, which has this characteristic. This candidate is a exponential capture memory decaying in time

$$C_M(t) = ae^{-bt}, \quad (9.61)$$

where a and b are arbitrary constants of units $length^2/time$ and $1/time$, respectively. This expression can be Laplace transformed readily

$$\widetilde{C}_M(\epsilon) = \frac{a}{\epsilon + b}, \quad (9.62)$$

and inserted into Eq.(9.60). Note that this expression has no constant offset, since experimental observations suggest that receptor cluster coalescence does not occur at early times. To validate $\widetilde{C}_M(\epsilon)$ given in Eq.(9.62), the Laplace transformed expression

$$\begin{aligned} \dot{R}_{1st}(t/\tau)^2 &= \dot{R}(0)^2 + 2a \\ &\times L_\epsilon^{-1} \left\{ \frac{\dot{R}(0)K_1[\dot{R}(0)\sqrt{\epsilon\tau}] - [1 - \dot{R}(\infty)]K_1[(1 - \dot{R}(\infty))\sqrt{\epsilon\tau}]}{2\pi D\dot{R}(0)(\epsilon + b)\epsilon^2\tau K_1[\dot{R}(0)\sqrt{\epsilon\tau}] + \epsilon^{3/2}\sqrt{\tau}K_0[\dot{R}(0)\sqrt{\epsilon\tau}]} \right\} \end{aligned} \quad (9.63)$$

is fit up to $t/\tau_c = 10$ to the experimental data. The fit was performed by minimizing chi-squared

$$\chi^2 = \sum_{i=1}^N \left(\frac{f(x_i) - \mu_i}{\sigma_i} \right)^2, \quad (9.64)$$

which typically is used as a metric to determine the goodness of a fit [173]. Here $N = 118$ is the number of data points in the time series, μ_i is the observed mean of the data with a standard deviation σ_i (we used the standard error of the mean instead), and $f(x_i)$ is the predicted mean obtained from the Laplace inverse of Eq.(9.63).

Figure 9.15A compares the best fit of Eq.(9.63) (red) to experimental data (black error bars). At early times $t/\tau_c < 10$, a capture memory of exponential form fits the data very well, showing that the delay can be explained by a memory for the capture rate. For $t/\tau_c > 10$, the theoretical predicted trap radius approaches the result obtained for constant capture rate and perfect absorption (grey).

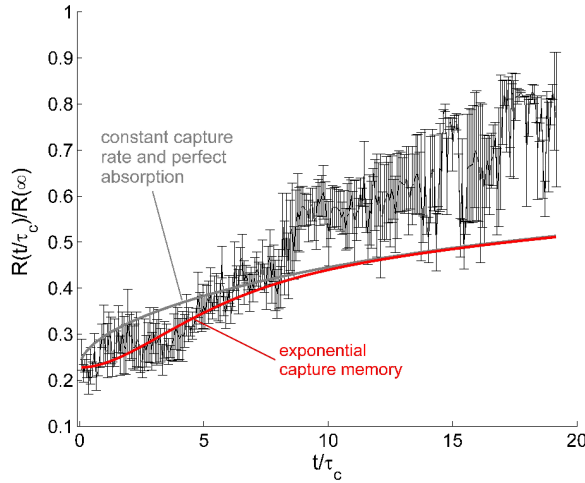


Figure 9.15: Weighted fit of Laplace inverted Eq.(9.63) (red) with $a = 3.8 \text{ length}^2/\text{time}$ and $b = 7.1 \times 10^{-12} / \text{time}$ to experimental data up to $t/\tau_c = 10$ (black error bars). The experimental data represents the normalized radius of the biggest receptor patch at each time point averaged over four data sets. The error bars represent the standard error of the mean. Grey curve represents our theory for an infinite melting probability $\xi = 0$ given in Eq.(9.57).

9.9 Concluding Remarks

The main goal of this chapter was to gain insight into the unknown kinetics of receptor cluster coalescence in mast cells. This investigation was based on developing a new coalescence theory [174], which was directly applied to our experimental observations. Our theoretical model is based on a self-consistent feedback approach, which was introduced in form of a prescription in section 9.2. Due to the complexity of the problem, the prescription cannot be evaluated exactly. However, we were able to develop an analytic approximation, whose validity we examined with the help of a highly simplified invented model for which exact solutions could be obtained. This approximation was based on our previous analysis of moving boundary problems in chapter 8, where the time dependence of the boundary was explicitly inserted into the stationary trapping solution. The approximate iteration scheme was validated by direct comparisons to results obtained from Monte Carlo simulations in one- and two-dimensions as outlined in sections 9.5 and 9.6, respectively. These validity studies showed that our analytic approximation performed very well when the trap boundary grew at a rate similar to diffusion-limited particle transport for instantaneous and finite particle-trap reactions. Moreover, direct comparison to simulations in section 9.5.5 validated our model for finite-sized particle coalescence. As expected from our studies of moving boundary problems, our coalescence theory did not perform well for strongly biased particle transport towards the trap, see section 9.5.4. However, this observation did not affect the applicability of the coalescence theory to actual experiments, since our experimental studies have shown that the directed motion component for receptor cluster transport has no preferred direction (see section 3.4.1).

Encouraged by the success of our coalescence theory in a Monte Carlo simulation validity study, the model was compared to experimental observations [175] in section 9.7.2. The comparison revealed that a coalescence model describing random particle transport with a *constant* melding probability cannot fully explain the observed kinetics of receptor cluster coalescence. At early times, $t/\tau_c < 5$, the model does not describe the experimen-

Chapter 9. A Mathematical Model for Receptor Cluster Coalescence

tally observed delay in cluster coalescence. Qualitative experimental evidence suggest that the observed delay is connected to a time-dependent coalescence probability; at early times of cell-substrate contact, cluster-cluster contact does not lead to melding, whereas at later times almost every contact of two clusters leads to coalescence. This time-dependent change in reaction rate might be due to a biological or kinetic response mechanism, which is coupled to the observed delay in cluster coalescence, leading to a non-local coalescence process in time. This argument motivated that we employ a generalization [22] of our coalescence theory with a trapping process characterized by a memory kernel. In section 9.8, we developed such a model. Comparison of this model to experiment clearly shows that the biological coalescence delay can be explained by a time-dependent capture rate. The origin of this delay remains to be investigated through further theoretical and experimental investigations. For example, an experiment in the near future will investigate the effect of cytoskeletal polymerization and depolymerization on cluster coalescence by applying an actindepolymerizing drug such as latrunculin A [176]. The investigation is motivated by our previous studies [13], which suggested that at late times of cell-substrate contact the actin cytoskeleton depolymerizes at the central region of the contact area. This change in the actin cytoskeleton might be a origin for the observed coalescence delay.

Direct comparisons of our theory to experiments have shown also that at longer times, $t/\tau_c > 10$, biological coalescence is significantly faster than predicted by the simple form of the theory we have presented. We believe that the origin of this enhancement to be due to the following events. First, our theory considers non-interacting point particles, which can react only with the central trap. It is highly likely that particle size dependence and size increase due to aggregation and/or motion leads to the enhancement. The latter contribution might be mitigated by an opposing effect of size-dependent particle diffusivity, in which larger particles diffuse slower [76, 77]. However, our experimental data suggest that cluster hop length does not depend significantly on cluster size for receptor clusters ranging from 0.4 to 1 μm in diameter (see Fig. 3.11), suggesting that size-dependent cluster motion might not be a essential parameter. Another tenable explanation for the observed

Chapter 9. A Mathematical Model for Receptor Cluster Coalescence

coalescence enhancement, is the existence of an effective, potentially short range, attractive potential between clusters. Theoretically, this effect may be modeled by an effective increase in trap size, and an experimental signature may be a change in hop length before melding events. This list of possible events suggests that our present neglect of changing particle size could cause the slow coalescence kinetics. Therefore, to improve our coalescence model, a clear future direction of the research presented here, is studying effects of an effective increase in capture rate or particle diffusivity at later times, possibly including another mechanism, which is not treated in the model described in the dissertation. Our studies have already shown that the radially uncorrelated biased particle motion that we have observed suggests an enhancement of the cluster diffusivity by a factor of 2. The increase in particle size during the process of aggregation, and the consequent decrease in the interparticle distance needed to be traversed before melding might well make the enhancement even larger. If we take the resultant such enhancement to be by a factor of 5, we get a much improved fit of our generalized theory with exponential memory which we

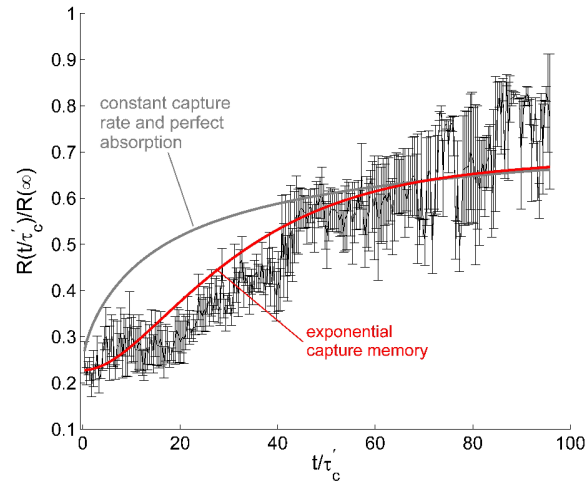


Figure 9.16: 5 fold enhancement in diffusivity with corresponding diffusion time $\tau'_c = 3$ s. Weighted fit of Laplace inverted Eq.(9.63) (red) with $a = 6.1 \text{ length}^2/\text{time}$ and $b = 2.2 \times 10^{-11} \text{ /time}$ to experimental data (black error bars). The error bars represent the standard error of the mean. Grey curve represents our theory for an infinite melding probability $\xi = 0$ given in Eq.(9.57).

Chapter 9. A Mathematical Model for Receptor Cluster Coalescence

show in Fig. 9.16.

In conclusion, our new coalescence model based on a feedback idea advanced our understanding of previously unknown receptor cluster coalescence in mast cells. Direct comparisons to experiment clearly outlines further theory-guided experiments. They also induced us to generalize our theory in the manner shown. Further work is on the way along these lines. We believe that a successful continuation of these investigations strongly depends upon a meaningful collaboration between experimental and theoretical investigations.

Chapter 10

Conclusions

The unifying thread throughout the 10 chapters of this dissertation has been the study of dynamics and distribution of immunoglobulin E receptors in mast cells, when triggered by membrane-bound monovalent ligands. This study has been an exceptional example for the possibility of an intense dialog between experimental (chapters 2–5) and theoretical (chapters 6–9) physics to learn more about the system under investigation. As result of this intense dialog, new insight into mast cell function has been gained, further experiments have been proposed, and generalizations of the theory have been put forward, naturally continuing the dialog between experiment and theory in the field of mast cell signaling. In the remainder of this concluding chapter, the main results are summarized briefly.

The motivation for this research project was found in immune signaling by mast cells. Typically, a mast cell is stimulated by multivalent ligand, which crosslinks two or more IgE-loaded Fc ϵ RI receptors [2]. Therefore, it was interesting to learn that also monovalent ligand incorporated into a two-dimensional substrate such as a lipid bilayer can trigger mast cells [5]. Since monovalent ligand cannot crosslink individual IgE-receptor complexes, another physical mechanism must result in receptor aggregation. Initial studies focused on investigating this mechanism. During these investigations, specifically on

Chapter 10. Conclusions

fluid membranes, it was observed that after initial receptor aggregation or receptor cluster formation, receptor clusters moved and eventually coalesced to form a large receptor patch [13]. To understand the underlying kinetics of the patch formation, a dialog between experimental and theoretical physics was necessary. From a biological point of view, investigating this model system is also important to advance the understanding of the mast cell's role in cell-cell and cell-parasite communication. (Mast cells in contact with a fluid ligand-bearing membrane can mimic such systems.)

To investigate the mechanism of initial receptor cluster formation, TIRF microscopy was implemented together with a single-cell micromanipulation technique. With these experimental techniques, it was shown for the first time that the mechanism of receptor cluster formation is diffusion mediated receptor trapping at cell-substrate contact points. These clusters were initially randomly distributed. On fluid ligand-bearing membranes, clusters moved and eventually coalesced to form a large receptor patch. This central patch formed predominantly in the center of the contact zone. The underlying mode of cluster transport on fluid membrane substrates, before cluster-cluster coalescence, was determined by calculating the MSD from cluster trajectories obtained by implementing a single-particle tracking algorithm. This analysis showed that clusters performed directed diffusion without statistically significant centripetal bias. Single-particle tracking was applied also in chapter 4 to investigate IgE-receptor mobility within cluster and patches. Results suggested that individual IgE-receptor complexes remain mobile within clusters and patches, providing further evidence that receptor immobilization is not a prerequisite for signaling. In the last chapter of presented experimental investigations, chapter 5, it was shown that at late times (> 2 min) the large central receptor patch is surrounded by a receptor cluster depletion zone.

The second part of this dissertation developed a new theory of coalescence to model the kinetics of receptor cluster coalescence in mast cells. The simple model, outlined in chapter 6, is formulated as a stationary trapping problem with a trap whose boundary changes

Chapter 10. Conclusions

dynamically due to isotropic cluster melding with a centrally located circular patch at a finite rate. In this simplified model, clusters were represented by non-interacting point particles. The purpose of the proposed calculation was to calculate the time evolution of the central patch or trap radius in three steps. The first step was outlined in chapter 7 and focused on solving stationary trapping problems by applying the standard defect technique. Following this technique, a general prescription for the total particle survival probability for any particle motion and dimension can be obtained. This prescription was applied to many different stationary trapping problems in continuum, obtaining some new expressions, which were collected in a repository. In the second part of the proposed calculation, presented in chapter 8, the difficult problem of moving boundaries was investigated. Due to the complexity of the cluster coalescence problem, the time-dependence of the growing central patch due to particle melding cannot be solved exactly. Therefore, an adiabatic approximation, in which the time-dependence of the moving boundary is explicitly inserted into the stationary trapping problem, was constructed. This approximation was validated by comparison to exact solutions available in one-dimension. A detailed validity study showed that the approximation performs well for a slowly moving boundary, which was observed also in experiments. Chapter 9 outlined the last step in the construction of the coalescence theory, in which the time-dependent central patch radius was related to the total cluster survival probability in a self-consistent way. Detailed comparison of theoretical results to Monte Carlo simulations in one- and two-dimensions showed that the proposed calculation works well for unbiased cluster transport. Such a model can describe also the experimentally observed directed cluster diffusion without centripetal bias. Therefore, the simple theory, describing cluster-patch coalescence at a finite rate, was applied directly to experiments. This comparison showed that the simple theory cannot describe the observed delay in biological cluster coalescence. A generalization of the simple theory for a time-dependent coalescence rate quantitatively explained the delay. The existence of such a delay is supported by experimental observations and may have its origin in the known rearrangement of the cell cytoskeleton upon mast cell stimulation by fluid ligand-bearing

Chapter 10. Conclusions

membranes.

From this work, it has become clear that neither experimental nor theoretical methods alone can accomplish the goal of advancing fundamental understanding of cell function. Of course, this observation also applies to other subjects that naturally cross traditional boundaries between disciplines. In the future, the author wants to continue research at the border between physics and biology, move on the middle ground between experiment and theory, and actively promote cross-disciplinary collaborations to expand her scientific portfolio into new directions.

Chapter 11

Appendices

Appendix A

Image Correlation Spectroscopy of Randomly Distributed Disks

Image correlation spectroscopy (ICS), applied to fluorescence microscopy images, has been widely used to quantify the number densities, aggregation states, and dynamics of macromolecules in cells and on cell membranes [21, 32, 33, 34, 35, 36, 37, 14]. In this dissertation ICS has been used to quantify the size of Fc ϵ RI receptor cluster on RBL cells due to different ligand-presenting surfaces, see chapter 3 section 3.2. When the membrane proteins are randomly distributed, ICS may be used to estimate protein densities, provided the proteins behave as point-like objects. At high protein area fraction, however, even randomly placed proteins cannot obey Poisson statistics, because of excluded area. The difficulty can arise if the protein effective area is quite large, or if proteins form large complexes or aggregate into clusters. In these cases, there is a need to determine the correct form of the intensity correlation function for hard disks in two dimensions, including the excluded area effects. Even though the ICS community has been aware of this effect [34, 35] thus far high particle concentrations have been thought to be unphysical [35] (even though interparticle interactions and area effects have been extensively studied in the context of fluorescence correlation spectroscopy (FCS) [177, 178]). However in our inves-

Appendix A. Image Correlation Spectroscopy of Randomly Distributed Disks

tigations (outlined in chapter 3) of the distribution of IgE receptor microclusters on RBL cells, the clusters were found to occupy a large area fraction, necessitating the derivation of the intensity c.f. for homogeneously distributed hard disks, presented in section 5.3. It is worth noting that very recently Kurniawan and Rajagopalan [179] extended spatiotemporal ICS to finite-sized particle systems, using a template analysis method. While template analysis gives a correct particle diffusion coefficient, it does not give mathematical relationships to compute particle number and size for finite-sized particle systems.

In this part of the appendix, we present an approximate but highly accurate algorithm for the computation of an image c.f. for disk-like fluorescent objects. To develop this algorithm, we use the hard disk c.f. for a uniform intensity profile derived in section 5.3 and show that this algorithm can be readily modified to compute exact intensity c.f. for any probe geometry, interaction potential, and fluorophore distribution.

Parts of this chapter have been published previously in Ref. [39].

A.1 Conventional image correlation spectroscopy

Conventional image correlation spectroscopy was introduced by St-Pierre and Peterson [21] using the two dimensional intensity autocorrelation function [32], see Eq.(3.1)

$$g_N(\epsilon, \kappa) = \frac{\langle i(x, y) i(x + \epsilon, y + \kappa) \rangle}{\langle i(x, y) \rangle^2} - 1,$$

where the angular brackets denote spatial averaging over all pixels in the image $i(x, y)$, and ϵ and κ are spatial lag variables. With Poisson-distributed point particles, the intensity variance is proportional to the average number of particles in the diffraction-limited observation volume, after removal of the photon shot noise and the camera read noise. Since shot noise and read noise are spatially uncorrelated, they may be excluded by taking the extrapolated limit of the correlation function at zero spatial lag, rather than using the

Appendix A. Image Correlation Spectroscopy of Randomly Distributed Disks

value of g_N measured there. For such an ideal system Eq.(3.1) gives the average number of particles $\langle N \rangle$ in the observation volume [32]

$$\lim_{\epsilon, \kappa \rightarrow 0} \lim_{Poisson} g_N(\epsilon, \kappa) = \lim_{Poisson} \frac{\langle i(x, y)^2 \rangle - \langle i(x, y) \rangle^2}{\langle i(x, y) \rangle^2} = \frac{1}{\langle N \rangle}, \quad (\text{A.1})$$

where $\langle i(x, y)^2 \rangle - \langle i(x, y) \rangle^2$ is the variance. Away from the origin, the shape of the correlation function is determined by the point spread function of the optics. Throughout this appendix, this method will be referred to as *conventional* ICS.

Real particles have a finite size, and this will modify both the shape of the correlation function and its extrapolated intercept at zero lag. In only moderately dense systems the particle distribution deviates significantly from Poissonian, and the relation between the estimated variance and the mean will not be as simple as given in Eq.(A.1). Figure A.1 depicts the relation between the occupied area fraction η and the variance for a Poisson distribution and a distribution of homogenous hard disks, following Mohn and Stavem [180]. The variance for randomly distributed hard disks significantly deviates from a Poisson distribution for area fractions of 5% or more.

Thus, in dense systems conventional ICS analysis leads to a substantial overestimate of the mean number of particles in a diffraction-limited observation volume. However in our investigations outlined in chapter 3 of the distribution of IgE receptor microclusters on RBL cells, the clusters were found to occupy an area fraction of $\eta \sim 0.30$ necessitating the derivation of the intensity correlation function (c.f.) for homogeneously distributed hard disks, presented here. Here the area fraction is given as $\eta = \rho \pi R_c^2$ with $\rho = 1.145$ clusters per μm^2 for a POPC fluid bilayer with 25 mol% DNP-Cap PE (see section 3.3.2) and an average cluster radius of $R_c = 0.3 \mu m$ (see section 3.2.2 taking into account that the FWHM gives an estimate for the typical diameter of a receptor cluster).

Appendix A. Image Correlation Spectroscopy of Randomly Distributed Disks

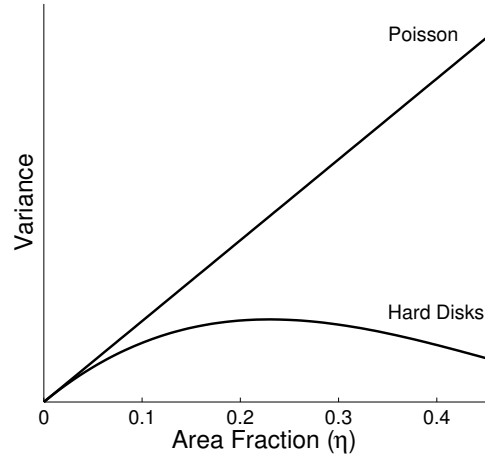


Figure A.1: Relationship between variance and occupied area fraction η for a Poisson distribution and a distribution of homogeneous hard disks, following the free area model by Mohn and Stavem [180] with a division side width of $b = 320$ arb. unit and disk radius $r = 2$ arb. unit. For high densities of disks the actual variance is less than what is predicted from the free area model [180]. Taken from Ref. [39].

A.2 Hard disk image correlation spectroscopy

In this section, we derive the c.f. of an image of randomly distributed disks with uniform intensity obtained from a light microscope image in the presence of diffraction. A fluorescence microscope image is mathematically obtained by the convolution of the point spread function (PSF) with the source distribution, which is the hard disk correlation function derived in section 5.3. In this case, the c.f. cannot be readily normalized as described in Eq.(5.11), owing to the potential overlap of the images of the individual disks. We have therefore chosen to leave the normalization C of the image autocorrelation as a free (fitting) parameter; the disk size and number density are separate parameters, which will modify the autocorrelation via the direct c.f., Eq.(5.5).

We approximate the PSF with a Gaussian function [181]. In polar coordinates

$$PSF(r) = e^{-\frac{r^2}{2\sigma^2}}, \quad (\text{A.2})$$

Appendix A. Image Correlation Spectroscopy of Randomly Distributed Disks

neglecting normalization. Using the Fourier transform correlation and convolution theorems, it is straightforward to show that the autocorrelation of a convolution of two functions (real or complex) is the convolution of the autocorrelations of each function separately. Thus

$$g_{PSF}(r) = C' g_c(r) \star [PSF(r) \otimes PSF(r)], \quad (\text{A.3})$$

where \star represents convolution, \otimes correlation, and $g_c(r)$ is given in Eq.(5.2). The autocorrelation of the Gaussian PSF given in Eq.(A.2) is

$$PSF(r) \otimes PSF(r) = e^{-\frac{r^2}{4\sigma^2}} \quad (\text{A.4})$$

and the convolution in polar coordinates in Eq.(A.3) can be written as

$$g_{PSF}(r) = C' \int_0^\infty \int_0^{2\pi} g_c(r'') \exp\left[-\frac{[r^2 + (r'')^2 - 2rr''\cos(\theta - \theta')]}{4\sigma^2}\right] d\theta' r'' dr''. \quad (\text{A.5})$$

In Eq.(A.5), θ can be set to zero due to rotational symmetry and the integral over θ can be evaluated, giving the hard disk ICS equation

$$g_{PSF}(r) = C' \int_0^\infty g_c(r'') e^{-\frac{[r^2 + (r'')^2]}{4\sigma^2}} I_0\left(\frac{rr''}{2\sigma^2}\right) r'' dr'', \quad (\text{A.6})$$

where $I_0()$ is the zeroth order modified Bessel function. C is a scaling constant, which can be estimated by fitting Eq.(A.6) to the rotationally averaged intensity c.f. of the microscope image after deleting the $g_{PSF}(0)$ datum (which includes uncorrelated camera shot and read noise). In general, to determine the number and radius of disk particles, the fit is made using three parameters C , R_c , and N . The width of the Gaussian, σ , can be estimated from images of fluorescent beads that are much smaller than the microscope resolution limit, by fitting the radially averaged intensity c.f. of the bead image to Eq.(A.4).

A.3 Simulations of typical microscope images

Simulations were used to verify the developed algorithm and compare it to the conventional ICS analysis under different conditions. Test images of randomly distributed non-overlapping disks with a top-hat intensity profile were created in MATLAB using the DIP-image toolbox. Each disk, independent of its radius, and point-like particle had a constant integrated intensity of 10000 ADU. All microscope image simulations had an image size of 640×640 pixels. The images were convolved with the Gaussian function given in Eq.(A.2) with $\sigma = 6$ pixel before adding Poisson noise (built in DIPimage function). The magnitudes of the parameters were chosen to simulate an image with a pixel size of ~ 20 nm and a typical Gaussian PSF width of $\sigma \sim 130$ nm. The intensity c.f. of each microscope test image was calculated by Fourier transform methods and rotationally averaged.

A.4 Accuracy of conventional image correlation spectroscopy

The purpose of this section is to explore the magnitude of error caused by the application of conventional ICS analysis to finite-sized particle systems, and to compare the conventional methodology to our more accurate algorithm for computing the intensity correlation function for distributions of disk-like particles. Such disk-like systems could include small receptor clusters, or protein complexes in which each subunit is fluorescently labelled. We also show how to modify the formulae to describe large proteins with a single label in the following section. The conventional ICS analysis assumes point-like particles and approximates the intensity c.f. by a Gaussian function reflecting the point spread function of the

Appendix A. Image Correlation Spectroscopy of Randomly Distributed Disks

microscope optics. Following this ICS methodology [32] the rotationally averaged c.f. is

$$g_{ICS}(r) = g_{ICS}(0)e^{-\frac{r^2}{4\sigma_{ICS}^2}}, \quad (\text{A.7})$$

where $g_{ICS}(0)$ and σ_{ICS} are fitting parameters and the average number of particles N_{ICS} in the diffraction limited observation volume can be estimated by evaluating

$$N_{ICS} = \frac{\text{imagearea}}{g_{ICS}(0)\pi 4\sigma_{ICS}^2}. \quad (\text{A.8})$$

In Eqs. (A.7) and (A.8) the subscript refers to parameters estimated by the conventional method. In order to compare conventional ICS analysis to the developed hard disk ICS, microscope test images were simulated for randomly distributed disks of different radii R_c and area fractions η as outlined in section A.3. To estimate the average number of particles as well as their size, resulting rotationally averaged intensity c.f.s were fit to conventional ICS given in Eq.(A.7) and hard disk ICS given in Eq.(A.6). All fits were implemented in MATLAB; the zero spatial lag $g_N(0)$ datum, which includes uncorrelated shot noise, was discarded.

A.4.1 Sensitivity to detect disk size

Figure A.2A compares the ratio of the Gaussian width obtained from conventional ICS, σ_{ICS} , to the actual width σ for different particle radii R_c and three area fractions; $\eta = 0.01$ (open circles), $\eta = 0.10$ (filled squares), and $\eta = 0.40$ (open triangles). In conventional ICS, data that yield a Gaussian width σ_{ICS} within 30% of the true value are typically accepted as a good fit to Eq.(A.7) [32, 33]. This 30% criterion is represented by the shaded area in Fig. A.2A. According to Fig. A.2A, for area fractions of less than 1% ($\eta = 0.01$), conventional ICS successfully detects disks with a radius larger than 1.5σ , or 200 nm when imaged with a typical high numerical aperture objective. In other words, disks of this size give intensity c.f.s that are clearly distinguishable from point particles, by the 30% criterion. However, for higher densities with area fractions larger than 40%

Appendix A. Image Correlation Spectroscopy of Randomly Distributed Disks

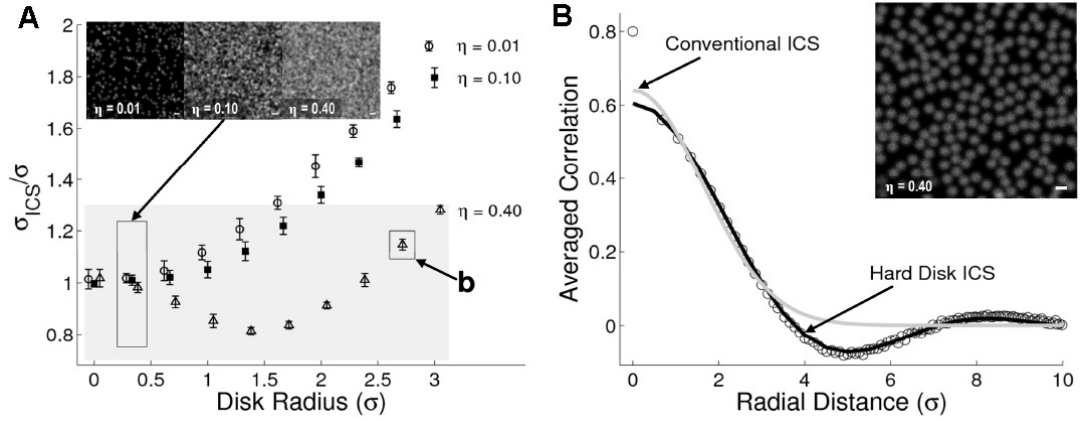


Figure A.2: In (A) ratio of σ_{ICS} obtained from conventional image correlation spectroscopy analysis, Eq.(A.7) fitted within a 4σ radius, to true σ for different disk radii R_c and three area fractions η . Error bars represent the standard deviation of ten simulations and the shaded area represents σ_{ICS} within 30%. Small insets depict typical simulated microscope images for disks of 0.66σ in diameter for $\eta = 0.01$ ($N = 326$), $\eta = 0.10$ ($N = 3259$) and $\eta = 0.40$ ($N = 13038$). Data points are offset for visualization purpose. In (B) rotationally averaged c.f. of image in inset for 204 disks of radius $R_c = 2.67\sigma$ and $\eta = 0.40$. Hard disk ICS, Eq.(A.6) fitted within a 14σ radius with fixed σ (black line) and conventional ICS (grey line). Taken from Ref. [39]. Bar represents 6σ .

($\eta = 0.40$) this criterion cannot distinguish between point-like particles and disk-like particles of radius up to 3.0σ or 400 nm. The deterioration in distinguishability is not surprising, as at these concentrations the images of individual particles begin to overlap significantly, owing to diffraction. In contrast, hard disk ICS can estimate any disk radius independent of area fraction. Figure A.2B shows a typical radially averaged intensity c.f. of a simulated microscope image (inset in Fig. A.2B) with disks of 2.67σ in radius covering 40% of the image area (open circles). The new algorithm fits the c.f. well (black line) giving a disk radius of $R_c = 2.74\sigma$, which is within 3% of the true value. For comparison, Fig. A.2B also depicts the fit to conventional ICS (grey line) which gives $\sigma_{ICS} = 1.1\sigma$. Even though σ_{ICS} satisfies the 30% criterion, the Gaussian approximation completely misses the oscillatory decay of the rotational averaged c.f., emphasizing the need to determine the correct form of the c.f. by the algorithm presented here.

A.4.2 Sensitivity to estimate disk number

As discussed in the introduction it is well known that conventional ICS overestimates the average number of disks for moderate area fractions. Figure A.3A depicts the ratio of the number N_{FIT} obtained from conventional ICS (filled circles) and hard disk ICS (open diamonds) to the simulated number N for different area fractions η with constant disk radius $R_c = 0.33\sigma$. Even at a small disk size (~ 40 nm) conventional ICS significantly overestimates the real number of disks for area fractions of 5% or more. For area fractions of 40% or more N_{ICS} can be larger by more than an order of magnitude. In contrast hard disk ICS accurately estimates the average number for all area fractions as shown in Fig. A.3A (open diamonds) verifying the accuracy of the developed algorithm. For disk radii significantly smaller than the laser beam radius, both conventional ICS and hard disk ICS fit the spatial correlation function very well. Figure A.3B depicts typical fits to the intensity

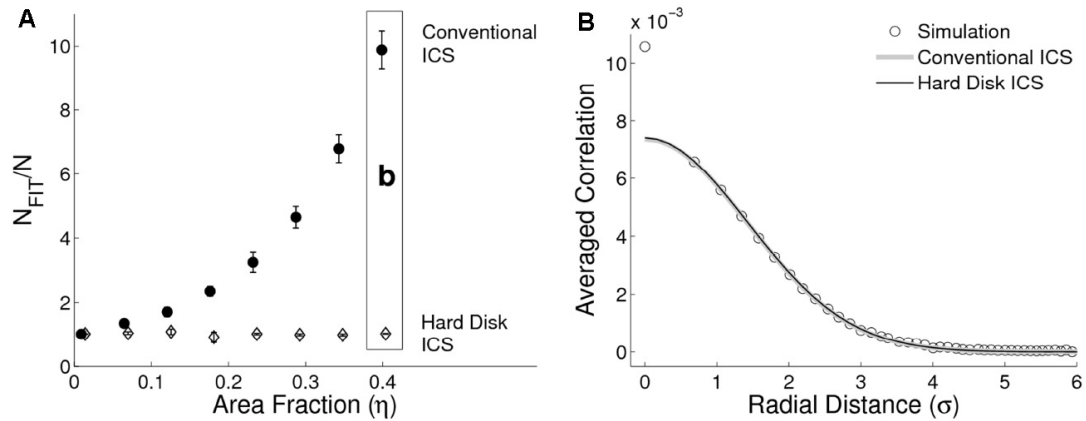


Figure A.3: In (A) ratio of the number N_{FIT} obtained from conventional image correlation spectroscopy (filled circles, Eq.(A.7)) and hard disk ICS (open diamonds, Eq.(A.6)) to the simulated number N for different area fractions η with constant disk radius $R_c = 0.33\sigma$. Error bars represent the standard deviation of ten simulations for conventional ICS and three simulations for hard disk ICS. Data points are offset for visualization purpose. (B) Autocorrelation function of a simulated image with disk size $R_c = 0.33\sigma$ and $\eta = 0.40$ ($N = 13038$) compared to conventional ICS (grey line) and hard disk ICS (black line). Taken from Ref. [39].

Appendix A. Image Correlation Spectroscopy of Randomly Distributed Disks

c.f. of a simulated microscope image with disks of radius $R_c = 0.33\sigma$ covering an area fraction of 40%. Both conventional ICS (grey line) and hard disk ICS (black line) fit the intensity c.f. (open circles) very well. However the estimated number from conventional ICS overestimates the true value by an order of magnitude (Fig. A.3A) whereas hard disk ICS gives an estimate within 20%.

A.5 Image correlation spectroscopy of large fluorescent proteins

A.5.1 Single fluorophore at center

The algorithm in Eq.(5.2) with the approximate hard disk pair c.f. $\gamma(r)$ can be applied to other isotropic systems, such as large proteins labeled with single fluorophore at the center. For a disk with a point-like label at its center, the autocorrelation equals the normalized two dimensional delta function $g_{auto}(r) = \delta(r)/r$. Thus, the intensity c.f. convolved with the (autocorrelated) microscope PSF for a protein of radius R_c labeled with a single fluorophore at the center is

$$g_{PSF}(r) = C' \left\{ e^{-\frac{r^2}{4\sigma^2}} + \rho \int_0^\infty e^{-\frac{(r-r')^2}{4\sigma^2}} [\gamma(r') - 1] 2r' dr' \right\}, \quad (\text{A.9})$$

with $\gamma(r)$ computed as above, using area fraction $\eta = \rho\pi R_c^2$. Equation (A.9) can be used to estimate the radius as well as the number of proteins in the observation volume. Figure A.4 shows a fit of Eq.(A.9) (solid line) to the intensity c.f. of a simulated image (open circles) of proteins 1.3σ in diameter covering an area fraction of 30%. The new algorithm estimates the true number of 2200 as well as protein size within 5%. In contrast conventional ICS (fit not shown) overestimates the true value by a factor of five.

Appendix A. Image Correlation Spectroscopy of Randomly Distributed Disks

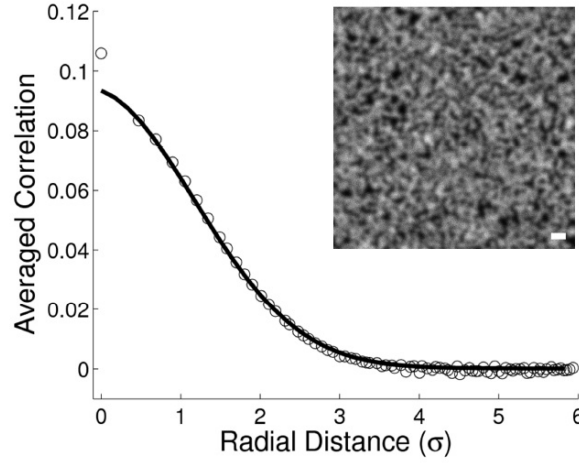


Figure A.4: Rotationally averaged intensity correlation function of a simulated microscope image (inset with $\sigma = 6$ pixel) of 2200 proteins 1.3σ in diameter labeled with a single fluorophore at the center (open circles) compared to the theoretical intensity correlation function given by Eq.(A.9) (solid line) for $w = 600$ pixel and $\eta = 0.30$. Taken from Ref. [39]. Bar represents 6σ .

A.5.2 Fluorophores forming a radially symmetric ring

Another geometry for which the hard disk pair correlation function can be applied is a random distribution of hard rings. Such a geometry might be appropriate to describe, for example, certain multisubunit channels or receptors in which each subunit is labeled. From geometry, one can derive the normalized autocorrelation for a ring $g_{auto,ring}$ of inner radius R_1 and outer radius R_2 as follows.

First, the autocorrelation function can be derived from geometrical considerations and

Appendix A. Image Correlation Spectroscopy of Randomly Distributed Disks

for $2R_1 \leq (R_2 - R_1)$ the c.f. can be written as

$$g_{auto,ring}(r; R_1, R_2) = \frac{1}{(R_2^2 - R_1^2)} \begin{cases} R_2^2 - R_1^2, r = 0 \\ R_2^2 g_{auto}(r; R_2) - R_1^2 g_{auto}(r; R_1) - 2R_1^2 [1 - g_{auto}(r; R_1)], 0 < r < 2R_1 \\ R_2^2 g_{auto}(r; R_2) - 2R_1^2, 2R_1 \leq r \leq (R_2 - R_1) \\ R_2^2 g_{auto}(r; R_2) - 2R_1^2 g_{cross}(r), (R_2 - R_1) < r < (R_2 + R_1) \\ R_2^2 g_{auto}(r; R_2), (R_2 + R_1) \leq r < 2R_2 \\ 0, otherwise \end{cases} \quad (A.10)$$

and for $(R_2 - R_1) \leq 2R_2$ one obtains

$$g_{auto,ring}(r; R_1, R_2) = \frac{1}{(R_2^2 - R_1^2)} \begin{cases} R_2^2 - R_1^2, r = 0 \\ R_2^2 g_{auto}(r; R_2) - R_1^2 g_{auto}(r; R_1) - 2R_1^2 [1 - g_{auto}(r; R_1)], \\ 0 < r \leq (R_2 - R_1) \\ R_2^2 g_{auto}(r; R_2) - R_1^2 g_{auto}(r; R_1) - 2R_1^2 [g_{cross}(r) - g_{auto}(r; R_1)], \\ (R_2 - R_1) < r < 2R_1 \\ R_2^2 g_{auto}(r; R_2) - 2R_1^2 g_{cross}(r), 2R_1 \leq r < (R_2 + R_1) \\ R_2^2 g_{auto}(r; R_2), (R_2 + R_1) \leq r < 2R_2 \\ 0, otherwise \end{cases} \quad (A.11)$$

In Eqns. (A.10) or (A.11) g_{auto} is given in Eq.(5.3) and from geometry the normalized intensity crosscorrelation function g_{cross} of two disks of radius R_1 and R_2 ($R_1 \neq R_2$) is

$$g_{cross}(r) = \begin{cases} 1, 0 \leq r \leq (R_2 - R_1) \\ \frac{\theta R_2^2}{\pi R_1^2} + \frac{\phi}{\pi} - z(r; R_1, R_2), (R_2 - R_1) < r < (R_2 + R_1) \\ 0, otherwise \end{cases} \quad (A.12)$$

Appendix A. Image Correlation Spectroscopy of Randomly Distributed Disks

with

$$z(r; R_1, R_2) = \begin{cases} \frac{hr}{\pi R_1^2}, \phi < 90 \\ \frac{R_2^2}{\pi R_1^2} \cos(\theta) \sin(\theta), \phi = 90 \\ \frac{R_2^2}{\pi R_1^2} \cos(\theta) \sin(\theta) - \frac{h\sqrt{R_1^2 - h^2}}{\pi R_1^2}, \text{otherwise} \end{cases} \quad (\text{A.13})$$

where $h = R_2 \sin(\theta) = R_1 \sin(\phi)$, $\theta = \cos^{-1} \left(\frac{R_2^2 + r^2 - R_1^2}{2R_2 r} \right)$, and $\phi = \cos^{-1} \left(\frac{R_1^2 + r^2 - R_2^2}{2R_1 r} \right)$. Equations (A.10) or (A.11) can be substituted into Eq.(5.2) instead of the normalized intensity c.f. of a disk, Eq.(5.3), to obtain the rotationally averaged c.f. of randomly distributed hard rings with a uniform intensity profile, $g_{ring}(r)$, where the area fraction is defined as $\eta = \rho\pi R_2^2$ in Eq.(5.5). To estimate the number of rings in a given observation volume one has to compute the appropriate scaling constant. Following Eq.(3.1) the scaling constant is given as

$$C_{ring} = \left[\frac{x^2}{N\pi(R_2^2 - R_1^2)} - 1 \right] \frac{1}{g_{ring}(0; R_1, R_2)} \quad (\text{A.14})$$

and the un-normalized rotationally averaged intensity c.f. for hard rings can be computed by evaluating

$$g_{N,ring}(r) = \left[\frac{x^2}{N\pi(R_2^2 - R_1^2)} - 1 \right] \frac{g_{ring}(r; R_1, R_2)}{g_{ring}(0; R_1, R_2)}. \quad (\text{A.15})$$

Equation (A.15) was verified by simulating a test image (inset in Fig. A.5A) of rings with inner radius $R_1 = 5$ pixel and outer radius $R_2 = 10$ pixel, $w = 600$ pixel, $\eta = 0.30$. These parameters were used to compute the theoretical intensity c.f. for hard rings. Figure A.5A shows that the theoretical c.f. (solid line) fits the simulated data (open circles) quite well verifying that the presented algorithm can also be applied to distributions of hard rings as expected. Following the presented algorithm one can obtain an expression for hard ring ICS by convolving Eq.(A.10) or Eq.(A.11) with the autocorrelation of the Gaussian PSF:

$$g_{PSF}(r) = C' \int_0^\infty g_{ring}(r'') e^{-\frac{[r^2 + (r'')^2]}{4\sigma^2}} I_0 \left(\frac{rr''}{2\sigma^2} \right) r'' dr''. \quad (\text{A.16})$$

Appendix A. Image Correlation Spectroscopy of Randomly Distributed Disks

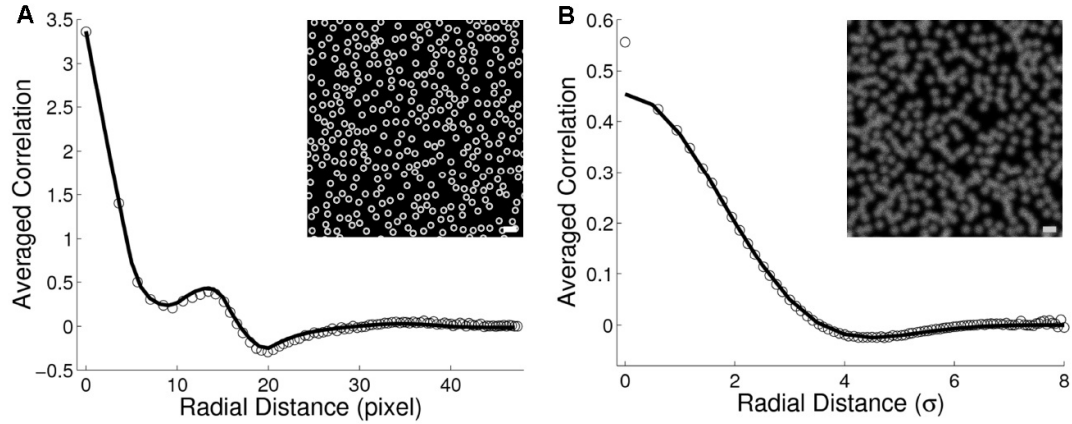


Figure A.5: (A) Rotationally averaged spatial correlation function of a simulated distribution (inset) of 350 homogeneous hard rings (open circles) compared to the theoretical intensity correlation function given by Eq.(A.15) (solid line) for $R_1 = 5$ pixel, $R_2 = 10$ pixel, $w = 600$ pixel, and $\eta = 0.30$. Bar represents 36 pixel. (B) Best fit of Eq.(A.15) (solid line) to the intensity c.f. (open circles) of a simulated microscope image (inset). Simulation parameters are the same as in (A) with $\sigma = 6$ pixel. Taken from Ref. [39]. Bar represents 6σ .

C' is a scaling constant which can be estimated by fitting Eq.(A.16) to the rotationally averaged intensity c.f. of a microscope image after deleting the $g_{PSF}(0)$ datum. Figure A.5B shows the best fit (solid line) to the intensity c.f. (open circles) of a simulated microscope image (inset). Hard ring ICS fits the intensity c.f. of the blurred image very well even though one cannot distinguish between disks or rings by eye. Hard ring ICS estimates the true number of rings within 5%. The estimate of the inner radius R_1 is 0.78σ and of the outer radius R_2 is 1.66σ . Both values are within 10%.

A.5.3 Single fluorophore placed off-center

In this section, we outline a procedure suitable for large proteins, each with a single, off-center label at the same distance from the protein center. In this case, the different roles for g_{auto} in Eq.(5.2) must be explicitly considered. The term outside the integral is the pure autocorrelation, which is a delta function for a point label, $g_{auto}(r) = \delta(r)/r$.

Appendix A. Image Correlation Spectroscopy of Randomly Distributed Disks

The term inside the integral is an effective crosscorrelation, which is to be averaged over all orientations. The orientationally averaged crosscorrelation of two off-center labels is the same as the crosscorrelation of two infinitesimally thin annular rings, which can be calculated exactly, giving a simple form.

The c.f. for two infinitely narrow rings each of radius R is obtained by writing each ring as a delta function and calculating the overlap integral. With one ring centered at the origin and the other at r , the correlation is

$$g_{auto,\delta-ring}(r) = \int_0^\infty \int_0^{2\pi} \frac{1}{4\pi^2(r')^2} \delta(r' - R) \delta(r' - [r^2 + R^2 + 2rR \cos \theta']^{1/2}) r' dr' d\theta', \quad (\text{A.17})$$

where the prefactors are normalizations for the delta functions, and the law of cosines was used. (θ' is the angle between the point of interest in the plane and the line between ring centers.) The integral over r' is carried out by applying the first delta; to compute the integral over θ' , the second delta is treated as a function of θ' . Then

$$\delta(f(\theta')) = \sum_{\theta'_0} \frac{\delta(\theta - \theta'_0)}{|f'(\theta'_0)|}, \quad (\text{A.18})$$

where the summation is taken over the zeroes of f , where $\theta = \theta'_0$. When the rings overlap, there will be two zeroes of f , corresponding to the two points of overlap and Eq.(A.18) becomes

$$g_{auto,\delta-ring}(r) = \begin{cases} \frac{1}{2\pi^2 R} \frac{1}{r \sin \theta'_0}, & 0 < r < 2R \\ 0, & \text{otherwise} \end{cases} \quad (\text{A.19})$$

From geometry, $\sin(\theta'_0) = [1 - r^2/(4R^2)]^{1/2}$, completing the derivation.

We note, however, that the accuracy of the model depends on having a sufficiently large population that all relative angular orientations of the proteins occur with approximately equal frequency; no such requirement exists for rotationally symmetric rings or disks. Therefore, extracting parameters such as the protein diameter and label location for singly-labelled proteins from ICS is likely to be experimentally demanding.

A.5.4 General formalism

Following the steps outlined here, one can derive the analytical intensity c.f. for any probe geometry, interaction potential, and fluorophore distribution from Eq.(5.1). For example, for any given interaction potential $V(r)$ the Ornstein-Zernike equation, Eq.(5.4), is solved by applying the following closure relation which relates $h(r)$ and $c(r)$ to the pair correlation function [103, 182]

$$\gamma(r) = e^{-\frac{V(r)}{k_B T}} e^{h(r)-c(r)+b(r)}, \quad (\text{A.20})$$

where k_B is the Boltzmanns constant, T the temperature, and $b(r)$ the bridge function (which is typically neglected). To obtain the intensity c.f. of hard disks, $b(r)$ is set to zero and the Percus-Yevick approximation (which expands the second exponential to linear order) and a hard-core potential were applied. For a review on different closure relations and potential models the reader is referred to Li et al. [103] and references therein.

Throughout this work, we have assumed that all particles are identical and that the distribution of fluorescent sources within a particle is known. In the case of identical particles, that distribution may sometimes be determined from external knowledge: for example, a large protein may be engineered with a single, genetically encoded fluorophore at a position known from crystal structure. In the case of an annular protein complex, it may be known that every subunit is labeled. (In the case of protein complexes or clusters, we note that the random absence of labels from some subunits will not affect the form of the image autocorrelation, merely its amplitude.) If the label distribution is unknown, it may be possible to determine it from control experiments on dilute proteins, using deconvolution algorithms as outlined in Refs. [183] and [184] and references therein.

Lastly, it is important to recognize that, although (random) variations in labeling do not affect the validity of the results, variations in the underlying structural elements would. To allow for such variation, one must use a modified pair correlation function that appropriately weights the different species.

A.6 Concluding Remarks

The analytical intensity correlation function for hard disks was first derived in section 5.3, using geometric considerations and the pair correlation function, as determined via the Ornstein-Zernike equation. Though not simply expressible, the correlation function, convolved with the microscope PSF autocorrelation, is readily implementable in computer-based fitting algorithms. It extends the conventional ICS analysis, which assumes point-like particles, to disk-like particles of uniform fluorescence intensity. We call this analysis *hard disk ICS*. The hard disk pair correlation function is readily applied to describe ICS of large proteins, with labels on center, and hard rings. We have simulated microscope images and compared the new semianalytical algorithm to the conventional method under different conditions. The results show that for large area fractions conventional ICS fails to detect disks significantly smaller than the laser beam radius. Moreover, conventional ICS significantly overestimates the average number of disks for area fractions of 5% or more which is equivalent to a density of 10 large proteins (i.e. 80 nm in diameter) per μm^2 . In contrast hard disk ICS accurately estimates the number and size of disks in an image for any area fraction and should therefore be applied to distributions of disk-like objects and high particle densities in which excluded area effects occur.

Appendix B

Common Laplace transforms in reaction-diffusion systems

In this appendix, we list common Laplace transforms, which are used to solve reaction-diffusion systems, in table B.1. Most of these transforms are directly taken from Ref. [133]. Moreover, some of the Laplace transforms used in this dissertation were obtained by applying the well known shifting theorem

$\exp[-b^2t]f(t) \rightarrow \tilde{g}(\epsilon + b^2)$ and

$$\frac{1}{\epsilon} \tilde{g}(\epsilon) \rightarrow \int_0^t f(u) du.$$

Here, and in the dissertation, \tilde{g} denotes the Laplace transform and ϵ the Laplace variable.

Table B.1: Common Laplace transforms to solve reaction-diffusion systems.

$f(t)$	$\tilde{g}(\epsilon)$
$I_m(2Ft) \exp(-2Ft)$	$(2F)^m / [(\epsilon^2 + 2F)^2 - (2F)^2]^{-1/2}$ $\times \frac{(2F)^m}{\left[\epsilon + 2F + \sqrt{(\epsilon^2 + 2F)^2 - (2F)^2} \right]^m}$
Continued on next page	

Appendix B. Common Laplace transforms in reaction-diffusion systems

Table B.1 – continued from previous page

$f(t)$	$\tilde{g}(\epsilon)$
$I_0(at) + I_1(at)$	$\frac{1}{a} \left[\frac{\sqrt{\epsilon+a}}{\sqrt{\epsilon-a}} - 1 \right]$
$p[I_0(pt) + I_1(pt)] + \delta(t)$	$\frac{\sqrt{\epsilon+p}}{\sqrt{\epsilon-p}}$
$I_a(pt)$	$\frac{p^a}{\sqrt{\epsilon^2-p^2} [\epsilon + \sqrt{\epsilon^2-p^2}]^a}$
$e^{-Ct} + p \int_0^t e^{-C\sqrt{t^2-w^2}} I_1(w) dw$	$\frac{1}{C + \sqrt{\epsilon^2-p^2}}$
$\frac{a}{t} I_a(pt)$	$\left[\frac{\epsilon - \sqrt{\epsilon^2-p^2}}{p} \right]^a$
$1/\sqrt{t}$	$\sqrt{\pi/\epsilon}$
$1/\sqrt{t} e^{-a/t}$	$\sqrt{\pi/\epsilon} e^{-2\sqrt{a\epsilon}}$
$erf\left(\frac{\sqrt{b}}{2\sqrt{t}}\right)$	$\frac{1}{\epsilon} \left[1 - e^{-\sqrt{b\epsilon}} \right]$
$erf\left(\frac{a}{\sqrt{t}}\right) - e^{2ab+b^2t} erfc\left(\frac{a}{\sqrt{t}} + b\sqrt{t}\right)$	$\frac{e^{-2a\sqrt{\epsilon}}}{\epsilon(1+\sqrt{\epsilon/b})}$
$1 + (2a^2t - 1) e^{a^2t} erfc(a\sqrt{t}) - \frac{2a}{\sqrt{\pi}} \sqrt{t}$	$\frac{a^2}{\epsilon(\sqrt{\epsilon}+a)^2}$
$\frac{(1-e^{-t})^\nu}{(1-ce^{-t})^\mu}$	$B(\epsilon, \nu+1) {}_2F_1(\mu, \epsilon; \epsilon + \nu + 1; c)$
$\sqrt{\frac{\gamma}{2\pi D}} \frac{1}{\sqrt{\exp(2\gamma t)-1}}$	$\frac{\sqrt{\gamma}}{\epsilon\sqrt{2D}} \frac{\Gamma\left(\frac{\epsilon}{2\gamma}+1\right)}{\Gamma\left(\frac{\epsilon}{2\gamma}+\frac{1}{2}\right)}$
$(e^t - 1)^{\nu-1} e^{-\frac{a}{\exp(t)-1}}$	$a^{\frac{\nu-1}{2}} e^{\frac{a}{2}} \Gamma(\epsilon - \nu + 1) W_{\frac{\nu-1}{2}-\epsilon, \frac{\nu}{2}}(a)$
$\sqrt{\frac{\gamma}{2\pi D}} \frac{\exp(\gamma t)}{\sqrt{\exp(2\gamma t)-1}} \exp\left[-\frac{\gamma x_0^2/(2D)}{\exp(2\gamma t)-1}\right]$	$\sqrt{\frac{1}{8\pi\gamma D}} \left(\frac{x_0^2\gamma}{2D}\right)^{-1/4} e^{\frac{x_0^2\gamma}{4D}} \Gamma\left(\frac{\epsilon}{2\gamma}\right)$
$\left(e^{a\mu/2} - e^{t\mu}\right) e^{\left[\frac{-a/2}{\exp(t)-1}\right]} W_{\mu, \nu}\left(\frac{a}{\exp(t)-1}\right)$	$\times W_{\frac{1}{4}-\frac{\epsilon}{2\gamma}, \frac{1}{4}}\left(\frac{x_0^2\gamma}{2D}\right)$ $\frac{\Gamma(\epsilon+1/2+\nu)\Gamma(\epsilon+1/2-\nu)}{\Gamma(\epsilon'+1-\mu)} W(-\epsilon, \nu, a)$
$erf\left(\frac{\sqrt{A}}{\exp(2\gamma t)-1}\right)$	$\frac{1}{\epsilon} - A^{-1/4} \exp(A/2) / [2\gamma\sqrt{\pi}]$ $\times \frac{\Gamma(\epsilon'+1/4)\Gamma\left(1-\frac{\epsilon}{2\gamma}\right)}{\Gamma\left(1.5-\frac{\epsilon}{2\gamma}\right)} W_{\frac{\epsilon}{2\gamma}-\frac{1}{4}, \frac{1}{4}}(A)$
$1 - \exp[-t/a]$	$1/(a\epsilon^2 + \epsilon)$
$\exp(-t/a)/a$	$1/(a\epsilon + 1)$

Continued on next page

Appendix B. Common Laplace transforms in reaction-diffusion systems

Table B.1 – continued from previous page

$f(t)$	$\tilde{g}(\epsilon)$
$\frac{1}{4\pi Dt} e^{-\epsilon_0/(2t)} I_0[\epsilon_0/(2t)]$	$\frac{1}{2\pi D} K_0\left(\sqrt{\frac{\epsilon}{\epsilon_0}}\right) I_0\left(\sqrt{\frac{\epsilon}{\epsilon_0}}\right)$
$\frac{1}{4\pi Dt} e^{-(\epsilon_0+\gamma_0)/(4t)} I_0[\epsilon_0\gamma_0/(2Dt)]$	$\frac{1}{2\pi D} K_0\left(\sqrt{\frac{\epsilon}{\gamma_0}}\right) I_0\left(\sqrt{\frac{\epsilon}{\epsilon_0}}\right)$
$erfc\left(\frac{a}{\sqrt{t}}\right) - e^{2ab+b^2t} erfc\left(\frac{a}{\sqrt{t}} + b\sqrt{t}\right)$	$b \exp(-2a\sqrt{\epsilon}) / [\epsilon(b + \sqrt{\epsilon})]$
$\exp(-a/t) \sinh(a/t)$	$1/(2\epsilon) - \sqrt{2a/\epsilon} K_1(\sqrt{8a\epsilon})$
$\exp(-a/t) \sinh(b/t), a > b$	$\sqrt{(a-b)/\epsilon} K_1[2\sqrt{(a-b)\epsilon}]$
$1/t^{3/2} \exp(-b/t) I_0(b/t)$	$-\sqrt{(a+b)/\epsilon} K_1[2\sqrt{(a+b)\epsilon}]$
$1/t^{3/2} \exp(-a/t)$	$\int_{\epsilon}^{\infty} du \sqrt{\frac{\pi}{u}} \left[I_0(\sqrt{8bu}) - L_0(\sqrt{8bu}) \right]$
$\delta(t-a)$	$\sqrt{\pi/a} \exp(-2\sqrt{a\epsilon})$
t^{ν}	$e^{-a\epsilon}$
$e^{-a/t}$	$\frac{\Gamma(\nu+1)}{\epsilon^{\nu+1}}$
$1/\sqrt{t} \exp(-a/t)$	$2\sqrt{\frac{a}{\epsilon}} K_1[2\sqrt{a\epsilon}]$
$-\frac{a}{2t^{3/2}\sqrt{\pi}} \sum_{n=-\infty}^{n=\infty} (-1)^n (2n-1) \exp\left[-\frac{a^2}{2t} (2n-1)^2\right]$	$\sqrt{\pi/\epsilon} \exp(-2\sqrt{a\epsilon})$
$-\frac{1}{2} \sum_{n=-\infty}^{n=\infty} (-1)^n e^{-ab(2n-1)}$	$1 / [\cosh(a\sqrt{\epsilon})]$
$\times \left[e^{2ab(2n-1)} erfc\left(\frac{a(2n-1)}{2\sqrt{t}} + b\sqrt{t}\right) + erfc\left(\frac{a(2n-1)}{2\sqrt{t}} - b\sqrt{t}\right) \right]$	$1 / \left[\epsilon \cosh\left(a\sqrt{\epsilon + b^2}\right) \right]$
$1 - \sum_{n=-\infty}^{n=\infty} (-1)^n \left\{ erf\left[\frac{a(2n+1)+\nu}{2\sqrt{t}}\right] - erf\left[\frac{a\nu}{\sqrt{t}}\right] \right\}$	$\cosh(\nu\sqrt{\epsilon}) / [\epsilon \cosh(a\sqrt{\epsilon})]$

Here $E_{\gamma} = 0.5772\dots$ is the Euler's constant and further function definitions can be found in table B.2.

Appendix B. Common Laplace transforms in reaction-diffusion systems

Table B.2: Function definitions for table B.1.

Formula	Function name
$I_{\nu}(x) = \sum_{n=0}^{\infty} (x/2)^{\nu+2n} / [n! \Gamma(\nu + n + 1)]$	Modified Bessel function
$2/\sqrt{\pi} \int_0^x \exp(-u^2) du$	Error function
$2/\sqrt{\pi} \int_x^{\infty} \exp(-u^2) du$	Complementary error function
$\Gamma(x)$	Gamma function
$B(a, b) = \Gamma(a)\Gamma(b)/\Gamma(a + b)$	Beta function
${}_2F_1(a, b; c, 1) = \Gamma(c)\Gamma(c - a - b) / [\Gamma(c - a)\Gamma(c - b)]$	Gauss's hypergeometric function
$U(a, b, z) = z^{-a} {}_2F_0(a, 1 + a - b; ; -z^{-1})$	Confluent hypergeometric function
$W_{a,b}(z) = \exp(-z/2) z^{b+1/2} U(-a + b + 1/2, 2b + 1, z)$	Whittaker W-function
$L_{\nu}(z) = \exp[-(\nu + 1)\pi i/2] \sum_{n=0}^{\infty} \frac{(-1)^n}{\Gamma(n+3/2)\Gamma(\nu+n+3/2)} \times \left[\frac{z}{2} \exp(\pi i/2) \right]^{\nu+2n+1}$	Struve function

Appendix C

Numerical Laplace transform

C.1 Introduction

In this part of the appendix, we discuss numerical Laplace transform algorithms.

The main idea behind the Laplace transformation is that we can solve an equation (or system of equations) containing differential and integral terms by transforming the equation in time (t) domain into Laplace (ϵ) domain. For example, Laplace transforms are used to turn an initial value problem into an algebraic problem which is easier to solve. After the problem is solved in Laplace domain one finds the inverse transform of the solution and hence solved the initial value problem. The Laplace transform of $f(t)$ is

$$\tilde{f}(\epsilon) = \int_0^{\infty} e^{-\epsilon t} f(t) dt, \quad (\text{C.1})$$

where ϵ is a complex variable known as the Laplace variable. The inverse integral is defined as the Bromwich contour integral ($\epsilon \rightarrow \gamma + i\infty$)

$$f(t) = \frac{1}{2\pi i} \int_{\gamma - i\infty}^{\gamma + i\infty} e^{\epsilon t} \tilde{f}(\epsilon) d\epsilon, \quad (\text{C.2})$$

Appendix C. Numerical Laplace transform

where γ is chosen so the all singular points of $\tilde{f}(\epsilon)$ lie to the left of the line $\Re(\epsilon) = \gamma$ in the complex ϵ -plane. In simple cases, the inverse transform can be found via analytical methods or with the help of tables. One can also compute the Laplace transform by evaluation of the complex integral of inverse transformation. Unfortunately, it is not always easy to find the inverts. One possible reason is that the inverse is not a named function or can not be represented by a *simple* formula. Moreover, if the Laplace transform is computable or measurable on the real and positive axis only the problem is ill-posed. Two time domain functions which differ at a single point in time for example will have the same transform. This case is very complicated simply because of absence of the exact inversion formula. In these cases a numerical method must be used. There are several numerical algorithms in literature and each individual method has its own applications and is suitable for a particular type of function [185]. The numerical inversion of $f(t)$ depends on the sensitivity of the inversion procedure. Algorithmic and finite precision errors (i.e. increasing round off error for large numbers) can lead to exponential divergence of numerical solutions i.e. Eq.(C.2) includes a potentially increasing large exponent $e^{\epsilon t}$. In the this section we will briefly introduce the Fourier Series expansion and the Gaver-Stehfest method as well as show for which functions the Gaver-Stehfest can be applied.

C.2 Fourier Series Expansion

This method is based on the Bromwich contour inversion integral, which can be expressed as the integral of a real valued function of a real variable by choosing a specific contour. One first converts the inversion integral into the Fourier transform and then approximates the transform by a Fourier series (use trapezoidal rule) with a specific discretization error. As outlined in Ref. [186] the method utilizes the standard Bromwich contour $\epsilon \rightarrow \gamma + i\omega$

Appendix C. Numerical Laplace transform

(choose a specific contour) to rewrite the Laplace transform integral given in Eq.(C.2) as

$$f(t) = \frac{e^{\gamma t}}{2\pi} \int_{-\infty}^{\infty} e^{i\omega t} \tilde{f}(\gamma + i\omega) d\omega, \quad (\text{C.3})$$

which is in the form of a Fourier transform. We can even go further and rewrite $e^{i\omega t}$ in Eq.(C.3) to obtain

$$f(t) = \frac{e^{\gamma t}}{2\pi} \int_{-\infty}^{\infty} [\cos(\omega t) + i \sin(\omega t)] \tilde{f}(\gamma + i\omega) d\omega. \quad (\text{C.4})$$

This equation can then be rewritten in real and imaginary parts

$$f(t) = \frac{e^{\gamma t}}{2\pi} \int_{-\infty}^{\infty} [\mathcal{R}e\{\tilde{f}(\gamma + i\omega)\} \cos(\omega t) - \mathcal{I}m\{\tilde{f}(\gamma + i\omega)\} \sin(\omega t)] d\omega. \quad (\text{C.5})$$

With the assumption that $f(t)$ is non-negative, $f(-t) = 0$ for $t > 0$, and $\mathcal{R}e(\tilde{f})$ is even and $\mathcal{I}m(\tilde{f})$ is odd we are only interested in the real part and we may write

$$f(t) = \frac{2e^{\gamma t}}{\pi} \int_0^{\infty} \mathcal{R}e\{\tilde{f}(\gamma + i\omega)\} \cos(\omega t) d\omega. \quad (\text{C.6})$$

Equation (C.6) can now be approximated by the trapezoidal rule

$$\int_a^b f(x) dx \approx \frac{b-a}{n} \left(\frac{f(a) + f(b)}{2} \right) + \sum_{k=1}^{n-1} f\left(a + k \frac{b-a}{n}\right)$$

with a step size $h = (b-a)/n$:

$$f(t) \approx \frac{he^{\gamma t}}{\pi} \mathcal{R}e\{\tilde{f}(\gamma + i\omega)\} + \frac{2he^{\gamma t}}{\pi} \sum_{k=1}^{\infty} \mathcal{R}e\{\tilde{f}(\gamma + ikh)\} \cos(kht), \quad (\text{C.7})$$

and can be further simplified if $h = \pi/(2t)$ and $\gamma = A/(2t)$ and written as a nearly alternating series

$$f(t) \approx \frac{e^{A/2}}{2t} \mathcal{R}e\left\{\tilde{f}\left(\frac{A}{2t}\right)\right\} + \frac{e^{A/2}}{t} \sum_{k=1}^{\infty} (-1)^k \mathcal{R}e\left\{\tilde{f}\left(\frac{A + 2k\pi i}{2t}\right)\right\}. \quad (\text{C.8})$$

Equation (C.8) can now be computed numerically by summing over a finite number of k . A and k are parameters which must be optimized for increasing accuracy. This method turns out to be very accurate. The disadvantage of this method is that it is difficult to implement and requires a large computation time [187] (i.e. sum over many terms).

C.3 Gaver-Stehfest Method

Another method requires sampling of the Laplace space function $\tilde{f}(\epsilon)$ only on the real line and is discussed in detail in Refs. [188, 189]. Similarly to the Fourier Method, Eq.(C.2) has to be transformed by defining a new complex variable $z = \epsilon t$ rewriting Eq.(C.2) as:

$$f(t) = \frac{1}{2\pi it} \int_{C'} \tilde{f}\left(\frac{z}{t}\right) e^z dz, \quad (\text{C.9})$$

where C' is the same contour as in Eq.(C.2). Next $\exp(z)$ is approximated by a rational function

$$e^z \approx \sum_{k=0}^n \frac{\omega_k}{\alpha_k - z},$$

where ω_k and α_k are complex numbers and called weights and nodes respectively. Using this approximation and applying the Cauchy integral formula one obtains

$$f(t) \approx \frac{1}{t} \sum_{k=0}^n \omega_k \tilde{f}\left(\frac{\alpha_k}{t}\right). \quad (\text{C.10})$$

Equation (C.10) approximates the inverse Laplace transform by a linear combination of transform values. The nodes and weights are complex numbers typically depend upon n . Since the weights are initially left unspecified it is typically called a framework rather than algorithm. Hence, Eq.(C.10) is referred to as *Unified Framework for Numerical Laplace Inversion* [188] since many different algorithms can be put into this framework including the Fourier method for which the nodes are complex values, Eq.(C.8) [188].

The Gaver-Stehfest method considers the case in which $f(t)$ is real-valued and the weights and nodes are real which leads to very accurate result for functions of type $\exp(-\alpha t)$. Stehfest's algorithm is based on a probabilistic derivation [189] and approximates the time domain solution using the following equation [185, 189]

$$f(t) \approx \frac{\ln(2)}{t} \sum_{k=1}^{2M} \omega_k \tilde{f}\left(\frac{k \ln(2)}{t}\right), \quad (\text{C.11})$$

Appendix C. Numerical Laplace transform

with the weights

$$\omega_k = (-1)^{M+k} \sum_{j=\lfloor (k+1)/2 \rfloor}^{\min(k,M)} \frac{j^{M+1}}{M!} \binom{M}{j} \binom{2j}{j} \binom{j}{k-j} \quad (\text{C.12})$$

where $\lfloor x \rfloor$ being the greatest integer or less than or equal to x . Equation (C.11) with weights computed from the above equation is implemented in MATLAB using double precision, which restricts M to be less than 7. Hence, the Gaver-Stehfest method only evaluates the function at real and positive values of the Laplace variable ϵ and sums a total of fourteen ($2M$) terms. This method is easy to implement and very accurate for functions of type $\exp(-\alpha t)$ as shown in Fig. C.1A. Since the functional form of the particle survival probability Q is of this type, e.g. Q goes as $\text{erf}(1/\sqrt{t})$ in Fig. C.1B, we chose the Gaver-Stehfest inversion algorithm for numerical Laplace inversions implemented in this dissertation. For functions with oscillatory behavior in time domain, the Gaver-Stehfest algorithm fails and only for short time one obtains a good approximation, Fig. C.1C. The implemented MATLAB code of the Gaver-Stehfest algorithm is given in section C.3.1.

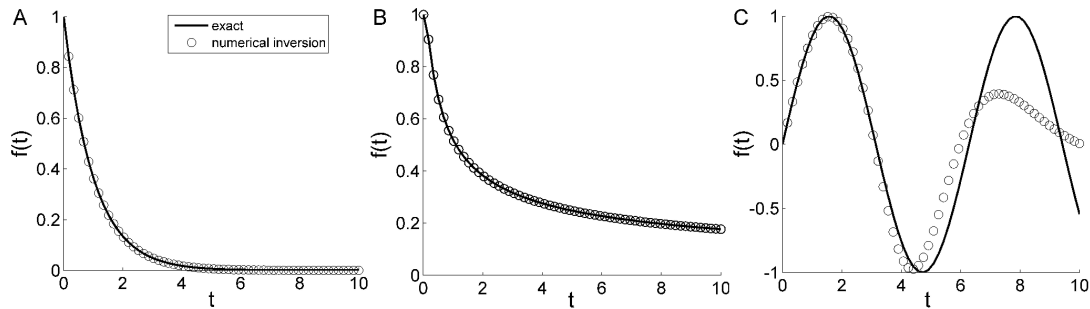


Figure C.1: Numerical Laplace inversion (open circles) compared to exact analytic solution (solid line) for (A) $f(t) = \exp(-\alpha t)$, $\tilde{f}(\epsilon) = 1/(\epsilon + 1)$, (B) $f(t) = \text{erf}(1/\sqrt{4t})$, $\tilde{f}(\epsilon) = [1 - \exp(-\sqrt{\epsilon})]/\epsilon$, and (C) $f(t) = \sin(t)$, $\tilde{f}(\epsilon) = 1/(\epsilon^2 + 1)$.

Appendix C. Numerical Laplace transform

C.3.1 MATLAB code

```
% Approximate numerical Laplace inversion based on the Gaver-Stehfest algorithm [188]
% implementing Eqs.(C.11) and (C.12).
%%%%%% Begin of MATLAB code
close all
clear all
time = linspace(0.01,10,100);
%%%%%% input function for numerical inversion, where s=ε
% lapfunc = @(s) 1./(s+1);
% lapfunc = @(s) (1-exp(-sqrt(s)))./s;
lapfunc = @(s) 1./(s.^2+1);
%%%%%% input analytical function in time domain, only for comparison (if known)
% func = @(t) exp(-t);
% func = @(t) erf(1./sqrt(4*t));
func = @(t) sin(t);
%%%%%% Compute weights and nodes
M = 7;
k = linspace(1,2*M,2*M);
for i = 1:2*M
Xi(i) = xi(i,M); %Eq.(C.12)
end
for n=1:length(time) %Eq (C.11)
invlap(n) = log(2)/time(n)*sum(Xi.*lapfunc(k*log(2)/time(n)));
end
%%%%%% plot
plot(time,invlap,'ko','LineWidth',1)
hold on
```

Appendix C. Numerical Laplace transform

```
plot(time,func(time),'r','LineWidth',2)
```

```
hold off
```

```
xlabel('t','FontSize',20)
```

```
ylabel('f(t)','FontSize',20)
```

```
legend('numerical','analytical')
```

```
%%%%%% sub-function to compute weights, Eq.(C.12
```

```
function [su] = xi(k,M)
```

```
j = floor((k+1)/2);
```

```
uplim = min([k,M]);
```

```
j = linspace(j,uplim,uplim-j+1);
```

```
n = 1;
```

```
for m=min(j):max(j)
```

```
arg(n) = log(j(n)^(M+1)/factorial(M)) + log(nchoosek(M,j(n)))
```

```
+ log(nchoosek(2*j(n),j(n))) + log(nchoosek(j(n),k-j(n))); n = n+1;
```

```
end
```

```
su = (-1)^(M+k)*sum(exp(arg));
```

Appendix D

Validation of general prescription for any initial distribution

In this part of the appendix we validate the general prescription for dQ/dt in one-dimensions obtained in chapter 7 section 7.5.3. This prescription allows us to calculate the particle survival probability for any initial distribution of non-interacting particles which diffuse in the presence of a single stationary trap at the origin. In the remainder of this appendix, we evaluate the following prescription

$$\frac{dQ(t)}{dt} = -\frac{C}{4\sqrt{\pi}} (Dt)^{-3/2} \int_0^{\infty} x e^{-\frac{x^2}{4Dt}} h(x) dx, \quad (\text{D.1})$$

given

$$h(x) = \int_0^x \rho(x-x_0) e^{-px_0} dx_0, \quad (\text{D.2})$$

where $\rho(x_0)$ is the initial distribution, which is taken to be a localized initial condition.

D.1 Initial point particle

In this section, the above general prescription is used to compute $Q(t)$ for an initial localized distribution, $\rho(x_0) = \delta(x_0 - x_1)$. We start with the expression

$$h(t) = \int_0^x \rho(x - x') e^{-px'} dx' \quad (\text{D.3})$$

and substitute $y = x - x'$ to write

$$h(x) = e^{-px} \int_0^x \rho(y) e^{py} dy. \quad (\text{D.4})$$

Now if we set $\rho(y) = \delta(y - x_1)$ and compute $h(x)$ we obtain for $x_1 = x_0$

$$h(x) = e^{-px} e^{px_0} \Theta(x - x_0), \quad (\text{D.5})$$

where Θ is the Heaviside step function. Substituting Eq.(D.5) into Eq.(D.1), we are left to evaluate

$$\frac{dQ(t)}{dt} = -\frac{C}{4\sqrt{\pi}} (Dt)^{-3/2} \exp(px_0) \int_{x_0}^{\infty} x e^{-\frac{x^2}{4Dt}} e^{-px} dx. \quad (\text{D.6})$$

D.1.1 Details of calculation

Since the evaluation of Eq.(D.6) was rather tedious, the goal in this subsection is to outline the main steps in the calculation.

To evaluate Eq.(D.6), the integral property $\int_{x_0}^{\infty} = \int_0^{\infty} - \int_0^{x_0}$ was used. From Ref. [135] we know that

$$\int_0^{\infty} x e^{-\mu x^2 - 2vx} dx = \frac{1}{2\mu} - \frac{v}{2\mu} \sqrt{\frac{\pi}{\mu}} e^{\frac{v^2}{\mu}} \left[1 - \operatorname{erf}\left(\frac{v}{\sqrt{\mu}}\right) \right],$$

Appendix D. Validation of general prescription for any initial distribution

setting $\mu = 1/(4Dt)$ and $v = p/2$, we obtain the result to one of the two integrals

$$\int_0^{\infty} x e^{-\frac{x^2}{4Dt} - px} dx = 2Dt - 2p\sqrt{\pi}(Dt)^{3/2} e^{p^2 Dt} \left[1 - \operatorname{erf}\left(p\sqrt{Dt}\right) \right]. \quad (\text{D.7})$$

The second integral was obtained by integration by parts

$$\int_a^b u \frac{dv}{dx} dx = uv \Big|_a^b - \int_a^b \frac{du}{dx} v dx,$$

where $u = x$ and $dv/(dx) = \exp(-x^2/(4Dt) - px)$. $v(x)$ is obtained from Ref. [135], where

$$\int e^{-\frac{x^2}{4\beta} - \gamma x} dx = \sqrt{\pi\beta} e^{\beta\gamma^2} \operatorname{erf}\left(\gamma\sqrt{\beta} + \frac{u}{2\sqrt{\beta}}\right)$$

and after setting $\beta = Dt$ and $\gamma = p$,

$$\begin{aligned} \int_0^{x_0} e^{-\frac{x^2}{4Dt} - px} x dx &= x_0 \sqrt{\pi}(Dt)^{1/2} e^{p^2 Dt} \operatorname{erf}\left(\frac{x_0}{2\sqrt{Dt}} + p\sqrt{Dt}\right) \\ &\quad - \sqrt{\pi}(Dt)^{1/2} e^{p^2 Dt} \int_0^{x_0} \operatorname{erf}\left(\frac{x_0}{2\sqrt{Dt}} + p\sqrt{Dt}\right) dx. \end{aligned} \quad (\text{D.8})$$

Since $\int \operatorname{erf}(z) dz = z \operatorname{erf}(z) + \frac{1}{\sqrt{\pi}} \exp(-z^2)$, the above expression becomes

$$\begin{aligned} \int_0^{x_0} \operatorname{erf}\left(\frac{x_0}{2\sqrt{Dt}} + p\sqrt{Dt}\right) dx &= \\ &\quad \sqrt{4Dt} \left[\left(\frac{x_0}{2\sqrt{Dt}} + p\sqrt{Dt}\right) \operatorname{erf}\left(\frac{x_0}{2\sqrt{Dt}} + p\sqrt{Dt}\right) \right] \\ &\quad - 2(Dt)^{1/2} \left[\frac{-1}{\sqrt{\pi}} e^{-\frac{x_0^2}{4Dt} - p^2 Dt - x_0 p} + p\sqrt{Dt} \operatorname{erf}\left(p\sqrt{Dt}\right) + \frac{1}{\sqrt{\pi}} e^{-p^2 Dt} \right]. \end{aligned} \quad (\text{D.9})$$

Now, if Eq.(D.9) is substituted into Eq.(D.8) and subtracted from Eq.(D.7), many terms cancel and we were able to evaluate

$$\int_{x_0}^{\infty} x e^{-\frac{x^2}{4Dt} - px} dx = \int_0^{\infty} x e^{-\frac{x^2}{4Dt} - px} dx - \int_0^{x_0} x e^{-\frac{x^2}{4Dt} - px} dx,$$

Appendix D. Validation of general prescription for any initial distribution

as

$$\int_{x_0}^{\infty} x e^{-\frac{x^2}{4Dt} - px} dx = 2Dt e^{-\frac{x_0^2}{4Dt} - px_0} - 2p\sqrt{\pi}(Dt)^{3/2} e^{p^2 Dt} \operatorname{erfc}\left(\frac{x_0}{2\sqrt{Dt}} + p\sqrt{Dt}\right). \quad (\text{D.10})$$

Next, substituting the above expressions into Eq.(D.6) gives

$$\frac{dQ}{dt} = \frac{1}{\xi^2 \tau} e^{\frac{1}{\xi} + \frac{1}{\xi^2} \frac{t}{\tau}} \operatorname{erfc}\left(\frac{\sqrt{\tau}}{2\sqrt{t}} + \frac{1}{\xi} \sqrt{\frac{t}{\tau}}\right) - \frac{1}{\sqrt{\pi} \xi \sqrt{\tau t}} e^{-\frac{\tau}{4t}}, \quad (\text{D.11})$$

where $\tau = x_0^2/D$ is a motion time and $\xi = 2D/(Cx_0)$ describes the capture process.

D.2 Comparison to the rate of disappearance

After obtaining an expression for the rate of disappearance by applying a general prescription, we are left to validate the result. We have previously calculated the survival probability for imperfect absorption given in Eq.(7.40)

$$Q(t) = \operatorname{erf}\left(\frac{1}{2}\sqrt{\frac{\tau}{t}}\right) + e^{\frac{1}{\xi} + \frac{1}{\xi^2} \left(\frac{t}{\tau}\right)} \operatorname{erfc}\left(\frac{1}{2}\sqrt{\frac{\tau}{t}} + \frac{1}{\xi} \sqrt{\frac{t}{\tau}}\right)$$

from which we can directly obtain $dQ/(dt)$. Since $\frac{d}{dz} \operatorname{erf}(z) = 2/\sqrt{\pi} \exp(-z^2)$, we can write

$$\frac{d}{dt} \operatorname{erf}\left(\frac{\sqrt{\tau}}{2\sqrt{t}}\right) = \frac{\sqrt{\tau}}{2\sqrt{\pi} t^{3/2}} e^{-\frac{\tau}{4t}},$$

as well as

$$\frac{d}{dt} \operatorname{erf}\left(\frac{\sqrt{\tau}}{2\sqrt{t}} + \frac{1}{\xi} \sqrt{\frac{t}{\tau}}\right) = \frac{2}{\sqrt{\pi}} e^{-\left(\frac{1}{\xi} + \frac{1}{\xi^2} \frac{t}{\tau} + \frac{\tau}{4t}\right)} \left(\frac{1}{2\xi\sqrt{\tau t}} - \frac{\sqrt{\tau}}{4t^{3/2}}\right).$$

Next using $d/(dz) \operatorname{erfc}(z) = -d/(dz) \operatorname{erf}(z)$ we obtain

$$\frac{d}{dt} \operatorname{erfc}\left(\frac{\sqrt{\tau}}{2\sqrt{t}} + \frac{1}{\xi} \sqrt{\frac{t}{\tau}}\right) = \frac{2}{\sqrt{\pi}} e^{-\left(\frac{1}{\xi} + \frac{1}{\xi^2} \frac{t}{\tau} + \frac{\tau}{4t}\right)} \left(\frac{\sqrt{\tau}}{4t^{3/2}} - \frac{1}{2\xi\sqrt{\tau t}}\right).$$

Appendix D. Validation of general prescription for any initial distribution

and after substituting all the above terms, the rate of change of the particle survival probability is given as

$$\frac{dQ}{dt} = \frac{1}{\xi^2 \tau} e^{\frac{1}{\xi} + \frac{1}{\xi^2} \frac{t}{\tau}} \operatorname{erfc} \left(\frac{\sqrt{\tau}}{2\sqrt{t}} + \frac{1}{\xi} \sqrt{\frac{t}{\tau}} \right) - \frac{1}{\sqrt{\pi \xi} \sqrt{\tau t}} e^{-\frac{\tau}{4t}}, \quad (\text{D.12})$$

which is the same expression as Eq.(D.11) obtained through our prescription. This concludes the validation.

Appendix E

The Crank-Nicolson method

As outlined in chapter 8, specifically section 8.5, the problem of two moving boundaries described by a diffusion equation can be solved by applying a boundary fixing transformation. For two boundaries with explicitly assigned time dependence at $x = S(t)$ and $x = R(t)$, Eq.(8.20) can be written as

$$\frac{\partial U}{\partial t} = \frac{D}{[R(t) - S(t)]^2} \frac{\partial^2 U}{\partial z^2} + \frac{\partial z}{\partial t} \frac{\partial U}{\partial z}, \quad (\text{E.1})$$

where

$$z = \frac{x - S(t)}{R(t) - S(t)}. \quad (\text{E.2})$$

is a time dependent scaling factor [119]. This transformation fixes the boundaries at $z = 0$ and $z = 1$ for all times with boundary conditions $U(z = 0, t) = 0$, $U(z = 1, t) = 0$ and initial condition $U(z_0, 0) = \delta(z - z_0)$ where $0 < z_0 < 1$. We solved for $U[z(x, t), t]$ by implementing the Crank-Nicolson algorithm [170] in MATLAB. The survival probability $Q(t)$ is obtained by integrating $U[z(x, t), t]$ over z from 0 to 1.

The Crank-Nicolson algorithm is based on a central difference scheme in space, and the trapezoidal rule in time, giving second-order convergence in time

$$\frac{\partial u}{\partial t} = F\left(u, x, t, \frac{\partial u}{\partial x}, \frac{\partial^2 u}{\partial x^2}\right) \quad (\text{E.3})$$

Appendix E. The Crank-Nicolson method

letting $u = u(i\Delta x, k\Delta t)$. This method is an implicit method: to get the *next* value of u in time, a system of algebraic equations must be solved. Hence, advancing in time involves the solution of a system of nonlinear algebraic equations. For linear diffusion, the algebraic problem is tridiagonal and may be efficiently solved with the tridiagonal matrix algorithm, which gives a fast direct solution. Following Crank-Nicolson we can write each differential term in Eq.(E.1) as

$$\begin{aligned}\frac{\partial U}{\partial t} &= \frac{u_i^{k+1} - u_i^k}{\Delta t}, \\ \frac{\partial U}{\partial z} &= \frac{u_{i+1}^{k+1} - u_{i-1}^{k+1}}{4\Delta z} + \frac{u_{i+1}^k - u_{i-1}^k}{4\Delta z}, \\ \frac{\partial^2 U}{\partial z^2} &= \frac{u_{i+1}^{k+1} - 2u_i^{k+1} + u_{i-1}^{k+1}}{2\Delta z^2} + \frac{u_{i+1}^k - 2u_i^k + u_{i-1}^k}{2\Delta z^2},\end{aligned}\tag{E.4}$$

with time and space dependent constants

$$\begin{aligned}a(z, t) &= \frac{\partial z}{\partial t}, \\ b(z, t) &= \frac{D}{[R(t) - S(t)]^2}.\end{aligned}\tag{E.5}$$

The constants have to be discretized for each term step i.e. for $k\Delta t$ terms, $a(z, t) \rightarrow a(z_i, t_k)$ and for $(k+1)\Delta t$ terms, $a(z, t) \rightarrow a(z_i, t_{k+1})$. Substituting the above expressions into Eq.(E.1) one obtains

$$\begin{aligned}\frac{u_i^{k+1} - u_i^k}{\Delta t} &= b(z_i, t_{k+1}) \frac{u_{i+1}^{k+1} - 2u_i^{k+1} + u_{i-1}^{k+1}}{2\Delta z^2} + b(z_i, t_k) \frac{u_{i+1}^k - 2u_i^k + u_{i-1}^k}{2\Delta z^2} \\ &+ a(z_i, t_{k+1}) \frac{u_{i+1}^{k+1} - u_{i-1}^{k+1}}{4\Delta z} + a(z_i, t_k) \frac{u_{i+1}^k - u_{i-1}^k}{4\Delta z}.\end{aligned}\tag{E.6}$$

Appendix E. The Crank-Nicolson method

After defining the following parameters

$$\begin{aligned}
 \alpha_1 &= \frac{a(z_i, t_{k+1})\Delta t}{4\Delta z}, \\
 \alpha_2 &= \frac{a(z_i, t_k)\Delta t}{4\Delta z}, \\
 \beta_1 &= \frac{b(z_i, t_{k+1})\Delta t}{2\Delta z^2}, \\
 \beta_2 &= \frac{b(z_i, t_k)\Delta t}{2\Delta z^2},
 \end{aligned} \tag{E.7}$$

and collecting all k terms on the left-hand side and all $k + 1$ terms on the right-hand side of Eq.(E.6) one obtains

$$\begin{aligned}
 u_i^{k+1} (1 + 2\beta_1) - u_{i+1}^{k+1} (\beta_1 + \alpha_1) - u_{i-1}^{k+1} (\beta_1 - \alpha_1) &= u_i^k (1 - 2\beta_2) + u_{i+1}^k (\beta_2 + \alpha_2) \\
 &+ u_{i-1}^k (\beta_2 - \alpha_2).
 \end{aligned} \tag{E.8}$$

To implement the Crank-Nicolson algorithm numerically a matrix A describing the left-hand side and a matrix B representing the right-hand side of Eq.(E.8) are defined resulting in

$$A(i, k + 1)T^{k+1} = B(i, k)T^k. \tag{E.9}$$

Once the boundary conditions are added to these matrices, Eq.(E.8) can be solved numerically for the unknown quantity T^{k+1}

$$T^{k+1} = A(i, k + 1)^{-1} B(i, k) T^k. \tag{E.10}$$

Since inverting a matrix is computationally expensive, the Gauss elimination method was used and the algorithm was implemented in MATLAB. To test the accuracy of the Crank-Nicolson algorithm, the numerical algorithm was compared to the linearly receding boundary problem with a diffusing particle starting at $x_0 = 0$ for which the exact solution is known, Eq(8.42). For this specific problem the time dependent boundary motion is given

Appendix E. The Crank-Nicolson method

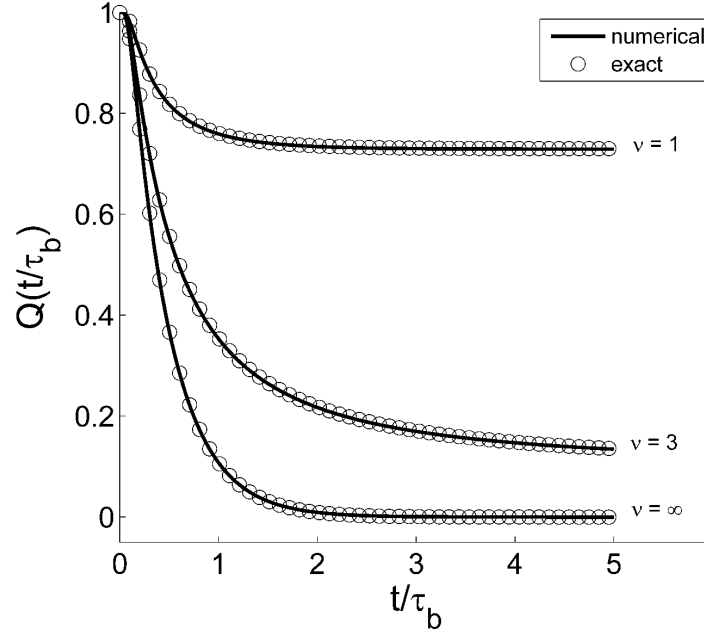


Figure E.1: Comparison of numerical solution obtained by applying the Crank-Nicolson method (solid line) to exact solution of two linearly receding boundaries given in Eq.(8.42) (open circles). The numerical solution is in excellent agreement with the exact result validating the implemented algorithm.

as $S(t) = -L_0 - vt$ and $R(t) = L_0 + vt$ for the left and right boundary, respectively. Inserting the boundary time dependence into the scaling factor defined in Eq.(E.2) gives

$$z = \frac{x + L_0 + vt}{2L_0 + 2vt} \quad (\text{E.11})$$

yielding in Eq.(E.5) to

$$\begin{aligned} a(z, t) &= \frac{(2vz - v)}{2(L_0 + vt)}, \\ b(z, t) &= \frac{D}{4(L_0 + vt)^2}. \end{aligned} \quad (\text{E.12})$$

The outlined Crank-Nicolson method was implemented in MATLAB and compared to the exact solution, Eq(8.42), for various parameters. As shown in Fig. (E.1) the numerical

Appendix E. The Crank-Nicolson method

solution (solid line) is in excellent agreement with the functional form of the exact solution given in Eq.(8.42) (open circles) validating the implemented algorithm.

References

- [1] I.J. Uings and S.N. Farrow. Cell receptors and cell signalling. *J. Clin. Pathol.: Mol. Pathol.*, 53:295–299, 2000.
- [2] K. Murphy, P. Travers, and Walter P. *Janeway's Immunobiology*. Garland Science, Taylor and Francis Group, LLC, 2008.
- [3] H. Metzger. Transmembrane signaling: the joy of aggregation. *J. Immunol.*, 149:1477–1487, 1992.
- [4] T.J. Galli, M. Tsai, and A.M. Piliponsky. The development of allergic inflammation. *Nature*, 454:445–454, 2008.
- [5] R.M. Weis, K. Balakrishnan, B.A. Smith, and H.M. McConnell. Stimulation of fluorescence in a small contact region between rat basophil leukemia cells and planar lipid membrane targets by coherent evanescent radiation. *J. Biol. Chem.*, 257:6440–6445, 1982.
- [6] L.A. Tempelman and D.A. Hammer. Receptor-mediated binding of IgE-sensitized rat basophilic leukemia cells to antigen-coated substrates under hydrodynamic flow. *Biophys. J.*, 66:1231–1243, 1994.
- [7] A.L. DeMond, K.D. Mossman, T. Starr, M.L. Dustin, and J.T. Groves. T cell receptor microcluster transport through molecular mazes reveals mechanism of translocation. *Biophys. J.*, 94:3286–3292, 2008.
- [8] P. Tolar, H.W. Sohn, and S.K. Pierce. Viewing the antigen-induced initiation of B-cell activation in living cells. *Immunol. Rev.*, 221:64–76, 2008.
- [9] H.W. Sohn, P. Tolar, and S.K. Pierce. Membrane heterogeneities in the formation of B cell receptor-Lyn kinase microclusters and the immune synapse. *J. Cell Biol.*, 182:367–379, 2008.

References

- [10] Y. Kaizuka, A.D. Douglass, R. Varma, M.L. Dustin, and R.D. Vale. Mechanisms for segregating T cell receptor and adhesion molecules during immunological synapse formation in jurkat T cells. *PNAS*, 104:20296–20301, 2007.
- [11] A. Grakoui, S.K. Bromley, C. Sumen, M.M. Davis, A.S. Shaw, P.M. Allen, and M.L. Dustin. The immunological synapse: a molecular machine controlling T cell activation. *Science*, 285:221–227, 1999.
- [12] C.R. Monks, B.A. Freiberg, H. Kupfer, N. Sciaky, and A. Kupfer. Three-dimensional segregation of supramolecular activation clusters in T cells. *Nature*, 395:82–86, 1998.
- [13] A. Carroll-Portillo, K. Spendier, J. Pfeiffer, G. Griffiths, H. Li, K.A. Lidke, J.M. Oliver, D.S. Lidke, J.L. Thomas, B.S. Wilson, and J.A. Timlin. Formation of a mast cell synapse: FcεRI membrane dynamics upon binding mobile or immobilized ligands on surfaces. *J. Immunol.*, 184:1328–1338, 2010.
- [14] K. Spendier, A. Carroll-Portillo, K.A. Lidke, B.S. Wilson, J.A. Timlin, and J.L. Thomas. Distribution and dynamics of rat basophilic leukemia immunoglobulin E receptors (FcεRI) on planar ligand-presenting surfaces. *Biophys. J.*, 99:388–397, 2010.
- [15] A. Carroll-Portillo, Z. Surviladze, A. Cambi, D.S. Lidke, and B.S. Wilson. Mast cell synapses and exosomes: membrane contacts for information exchange. *Frontiers in Immunol.*, 3(46):1–9, 2012.
- [16] A.Y. Hershko and J. Rivera. Mast cell and T cell communication; amplification and control of adaptive immunity. *Immunol. Lett.*, 128:98–104, 2010.
- [17] N. Gaudenzio, N. Espagnolle, L.T. Mars, R. Liblau, S. Valitutti, and E. Espinosa. Cell-cell cooperation at the T helper cell/mast cell immunological synapse. *Blood*, 114:4979–4988, 2009.
- [18] D. Axelrod. Cell-substrate contacts illuminated by total internal reflection fluorescence. *J. Cell Biol.*, 89:141, 1981.
- [19] M.J. Saxton and K. Jacobson. Single-particle tracking: applications to membrane dynamics. *Annu. Rev. Biophys. Biomol. Struct.*, 26:373–399, 1997.
- [20] R. Waugh and E.A. Evans. Thermoelasticity of red blood cell membrane. *Biophys. J.*, 26:115–132, 1979.
- [21] P.R. St-Pierre and N.O. Petersen. Average density and size of microclusters of epidermal growth factor receptors an A432 cells. *Biochem.*, 31:2459–2463, 1992.

References

- [22] V.M. Kenkre. private communication (unpublished notes).
- [23] V.M. Kenkre and P. Reineker. *Exciton Dynamics in Molecular Crystals and Aggregates*. Springer, Berlin, 1982, and references therein.
- [24] V.M. Kenkre. Theory of excitation annihilation in molecular crystals. *Phys. Rev. B*, 22:2089–2098, 1980.
- [25] V.M. Kenkre and Y.M. Wong. Theory of exciton migration experiments with imperfectly absorbing end detectors. *Phys. Rev. B*, 22:5716–5722, 1980.
- [26] V.M. Kenkre and Y.M. Wong. Effect of transport coherence on trapping: quantum-yield calculations for excitons in molecular crystals. *Phys. Rev. B*, 23:3748–3755, 1981.
- [27] V.M. Kenkre. A theoretical approach to exciton trapping in systems with arbitrary trap concentration. *Chem. Phys. Lett.*, 93:260–263, 1982.
- [28] V.M. Kenkre and P.E. Parris. Exciton trapping and sensitized luminescence: A generalized theory for all trap concentrations. *Phys. Rev. B*, 27:3221–3234, 1983.
- [29] V.M. Kenkre, P.E. Parris, and D. Schmid. Investigation of the appropriateness of sensitized luminescence to determine exciton motion parameters in pure molecular crystals. *Phys. Rev. B*, 32:4946–4955, 1985.
- [30] D. Tholen and X.-G. Zhu. The mechanistic basis of internal conductance: a theoretical analysis of mesophyll cell photosynthesis and CO₂ diffusion. *Plant Physiology*, 156:90–105, 2011.
- [31] V.M. Kenkre, L. Giuggioli, and Z. Kalay. Molecular motion in cell membranes: Analytic study of fence-hindered random walks. *Phys. Rev. E*, 77:051907, 2008.
- [32] N.O. Petersen, P.L. Hddelius, P.W. Wiseman, O. Olle Seger, and K.-E. Magnusson. Quantitation of membrane receptor distributions by image correlation spectroscopy: concept and application. *Biophys. J.*, 65:1135–1146, 1993.
- [33] N.O. Petersen, C. Brown, A. Kaminski, R. Rocheleau, M. Srivastava, and P.W. Wiseman. Analysis of membrane protein cluster densities and sizes in situ by image correlation spectroscopy. *Faraday Discuss.*, 111:289–305, 1998.
- [34] S. Costantino, J.W.D. Comeau, D.L. Kohlin, and P.W. Wiseman. Accuracy and dynamic range of spatial image correlation and cross-correlation spectroscopy. *Biophys. J.*, 89:1251–1260, 2005.

References

- [35] D.L. Kohlin, S. Costantino, and P.W. Wiseman. Sampling effects, noise, and photobleaching in temporal image correlation spectroscopy. *Biophys. J.*, 90:628–639, 2006.
- [36] D.L. Kohlin and P.W. Wiseman. Advances in image correlation spectroscopy: measuring number densities, aggregation states, and dynamics of fluorescently labeled macromolecules in cells. *Cell Biochem. Biophys.*, 49:141–164, 2007.
- [37] E. Keating, A. Nohe, and N.O. Petersen. Studies of distribution, location and dynamic properties of EGFR on the cell surface measured by image correlation spectroscopy. *Eur. Biophys. J.*, 37:469–481, 2008.
- [38] K. Spendier, D.S. Lidke, K.A. Lidke, and J.L. Thomas. Single-particle tracking of immunoglobulin E receptors (Fc ϵ RI) in micron-sized clusters and receptor patches. *FEBS Lett.*, 586:416–421, 2012.
- [39] K. Spendier and J.L. Thomas. Image correlation spectroscopy of randomly distributed disks. *J. Biol. Phys.*, 37:477–492, 2011.
- [40] J.L. Thomas, T.T. Feder, and W.W. Webb. Effects of protein concentration on IgE receptor mobility in rat basophilic leukemia cell plasma membranes. *Biophys. J.*, 61(5):1402–1412, 1992.
- [41] J.L. Thomas, D. Holowka, B. Baird, and W.W. Webb. Large-scale co-aggregation of fluorescent lipid probes with cell surface proteins. *J. Cell Biol.*, 125:795–802, 1994.
- [42] R.G. Posner, K. Subramanian, B. Goldstain, J. Thomas, T. Feder, D. Holowka, and B.A. Baird. Simultaneous cross-linking by two nontriggering bivalent ligands causes synergistic signaling of IgE Fc ϵ RI complexes. *J. Immunol.*, 155:3601–3609, 1995.
- [43] F.-T. Liu, J.W. Bohn, E.L. Ferry, H. Yamamoto, C.A. Molinaro, L.A. Sherman, and Katz David H. Klinman, N.R. Monoclonal dinitrophenyl-specific murine IgE antibody: preparation isolation and characterization. *J. Immunol.*, 124:2728–2736, 1980.
- [44] J. Seagrave, J.R. Pfeiffer, C. Wofsy, and J.M. Oliver. Relationship of IgE receptor topography to secretion in RBL-2H3 mast cells. *J. Cell Physiol.*, 148:139–151, 1991.
- [45] J.H. Werner, G.A. Montano, A.L. Garcia, N.A. Zurek, E.A. Akhadow, G.P. Lopez, and A.P. Shreve. Formation and dynamics of supported phospholipid membranes on a periodic nanotextured substrate. *Langmuir*, 25:2986–2993, 2009.

References

- [46] D.J. Griffiths. *Introduction to Electrodynamics*. Prentice-Hall, 1999.
- [47] C.L.L. Hendriks, L.J. van Vliet, B. Rieger, G.M.P. van Kempen, and M. van Ginkel. DIPIImage: a scientific image processing toolbox for MATLAB. *Quantitative Imaging Group, Faculty of Applied Sciences, Delft, The Netherlands*, 1999.
- [48] Andor Technology PLC. Digital camera fundamentals. Technical report, 2000.
- [49] M.A. Silverman, J. Shoag, J. Wu, and G.A. Koretzky. Disruption of SLP-76 interaction with gads inhibits dynamic clustering of SLP-76 and Fc ϵ RI signaling in mast cells. *Mol. Cell. Biol.*, 26:1826–1838, 2006.
- [50] E. Evans and D. Needham. Physical properties of surfactant bilayer membranes: thermal transitions, elasticity, rigidity, cohesion, and colloidal interactions. *J. Phys. Chem.*, 91:4219–4228, 1987.
- [51] A. Tözeren, K.P. Sung, L.A. Sung, M.L. Dustin, P.-Y. Chan, T.A. Springer, and S. Chien. Micromanipulation of adhesion of a jurkat cell to a planar bilayer membrane containing lymphocyte function-associated antigen 3 molecules. *J. Cell Biol.*, 116:997–1006, 1992.
- [52] S.E. Chesla, P. Selvaraj, and C. Zhu. Measuring two-dimensional receptor-ligand binding kinetics by micropipette. *Biophys. J.*, 75:1553–1572, 1998.
- [53] M.A. McCloskey and M. Poo. Contact-induced redistribution of specific membrane components: local accumulation and development of adhesion. *J. Cell Biol.*, 102:2185–2196, 1986.
- [54] S.M. Patrick, S. Kim, N.S. Braunstein, C.M. Maldarelli, J.L. Thomas, and E.F. Leonard. Controlled cell deformation produces defined areas of contact between cells and ligand-coated surfaces. *Ann. Biomed. Eng.*, 29:1–8, 2001.
- [55] M.I. Snijder-Van As, B. Rieger, B. Joosten, V. Subramaniam, C.G. Figdor, and J.S. Kanger. A hybrid total internal reflection fluorescence and optical tweezers microscope to study cell adhesion and membrane protein dynamics of single living cells. *J. Microsc.*, 233:84–92, 2009.
- [56] D. Sage, F.R. Neumann, F. Hediger, S.M. Gasser, and M. Unser. Automatic tracking of individual fluorescence particles: application to the study of chromosome dynamics. *IEEE Trans. on Image Processing*, 14:1372–1383, 2005.
- [57] N.L. Andrews, K.A. Lidke, J.R. Pfeiffer, A.R. Burns, B.S. Wilson, and J.M. Oliver. Actin restricts Fc ϵ RI diffusion and facilitates antigen-induced receptor immobilization. *Nat. Cell Biol.*, 10:955–963, 2008.

References

- [58] M.J. Saxton. Single-particle tracking: The distribution of diffusion coefficients. *Biophys. J.*, 72:1744–1753, 1997.
- [59] T. Savin and P.S. Doyle. Static and dynamic errors in particle tracking microrheology. *Biophys. J.*, 88:623, 2005.
- [60] T. Ridler and S. Calvard. Picture thresholding using an iterative selection method. *IEEE Trans. Syst. Man Cybern.*, 8:630–632, 1978.
- [61] W. Niblack. *An Introduction to Digital Image Processing*. Prentics Hall, 1986.
- [62] A.J. Smith, J.R. Pfeiffer, J. Zhang, M.A. Martinez, G.M. Griffiths, and B.S. Wilson. Microtubule-dependent transport of secretory vesicles in RBL-2H3 cells. *Traffic*, 4:302–312, 2003.
- [63] L. Chang, T. Kious, M. Yorgancioglu, D. Keller, and J. Pfeiffer. Cytoskeleton of living, unstained cells imaged by scanning force microscopy. *Biophys. J.*, 64:1282–1286, 1993.
- [64] Z. Ma, K.A. Sharp, P.A. Janmey, and T.H. Finkel. Surface-anchored monomeric agonist pMHCs alone trigger TCR with high sensitivity. *PLoS Biol.*, 328:342, 2008.
- [65] Z. Ma, P.A. Janmey, and T.H. Finkel. The receptor deformation model of TCR triggering. *FASEB J.*, 22:1002–1008, 2008.
- [66] M.A. Digman, R. Dalal, A.F. Horwitz, and E. Gratton. Mapping the number of molecules and brightness in the laser scanning microscope. *Biophys. J.*, 94:2320–2332, 2008.
- [67] M.M. Hamawy, C. Oliver, and R.P. Siraganian. Inhibition of IgE binding to RBL-2H3 cells by a monoclonal antibody (BD6) to a surface protein other than the high affinity IgE receptor. *J. Immunol.*, 148:524–531, 1992.
- [68] J.M. Oliver, J. Seagrave, R.F. Stump, J.R. Pfeiffer, and G.G. Deanin. Signal transduction and cellular response in RBL-2H3 mast cells. *Prog. Allergy*, 42:185–245, 1988.
- [69] P.W. Wiseman and N.O. Petersen. Image correlation spectroscopy. II. optimization for ultrasensitive detection of preexisting platelet-derived growth factor- β receptor oligomers on intact cells. *Biophys. J.*, 76:963–977, 1999.
- [70] J.R. Unruh and E. Gratton. Analysis of molecular concentration and brightness from fluorescence fluctuation data with an electron multiplied CCD camera. *Biophys. J.*, 95:5385–5398, 2008.

References

- [71] K.A. Lidke, B. Rieger, D.S. Lidke, and T.M. Jovin. The role of photon statistics in fluorescence anisotropy imaging. *IEEE Trans. on Image Processing*, 14:1237–1245, 2005.
- [72] A.R. Larson, J.A. Gosse, D.A. Holowka, B.A. Baird, and W.W. Webb. Temporally resolved interactions between antigen-stimulated IgE receptors and Lyn kinase on living cells. *J. Cell Biol.*, 171:527–536, 2005.
- [73] A.K. Menon, D. Holowka, W.W. Webb, and B. Baird. Cross-linking of receptor-bound IgE to aggregates larger than dimers leads to rapid immobilization. *J. Cell Biol.*, 102:541–550, 1986.
- [74] S. Torquato, G. Lu, and J. Rubinstein. Nearest-neighbour distribution function for systems of interacting particles. *J. Phys. A: Math. Gen.*, 23:L103–L107, 1990.
- [75] T. Yokosuka, K. Sakata-Sogawa, W. Kobayashi, M. Hiroshima, A. Hashimoto-Tane, M. Tokunaga, M.L. Dustin, and T. Saito. Newly generated T cell receptor microclusters initiate and sustain T cell activation by recruitment of Zap70 and SLP-76. *Nat. Immunol.*, 6:1253–1262, 2005.
- [76] P.G. Saffman and M. Delbrück. Brownian motion in biological membranes. *Proc. Nat. Acad. Sci. USA*, 72:3111–3113, 1975.
- [77] E.P. Petrov and P. Schwille. Translational diffusion in lipid membranes beyond the Saffman-Delbrück approximation. *Biophys. J.*, 94:L41–L43, 2008.
- [78] X. Liu, Z.-y. Tang, Z. Zeng, X. Chen, W.-j. Yao, Z.-y. Yan, Y. Shi, H.-x. Shan, D.-g. Sun, D.-q. He, and Z.-y. Wen. The measurement of shear modulus and membrane surface viscosity of RBC membrane with ektacytometry: A new technique. *Math. Biosci.*, 209:190–204, 2007.
- [79] J. Gorelik, A.I. Shevchuk, G.I. Frolenkov, I.A. Diakonov, M.J. Lab, C.J. Kros, G.P. Richardson, I. Vodyanoy, C.R.W. Edwards, D. Klenerman, and Y.E. Korchev. Dynamic assembly of surface structures in living cells. *PNAS*, 100:5819–5822, 2003.
- [80] J. Aaron, A. Carroll-Portillo, J. Pfeiffer, and J.A. Timlin. Imaging adaptive immune response in single cells using TIRF microscopy. *Microsc. Microanal.*, 15:858–859, 2009.
- [81] J.R. Pfeiffer, J. Seagrave, B.H. Davis, G.G. Deanin, and J.M. Oliver. Membrane and cytoskeletal changes associated with IgE-mediated serotonin release from rat basophilic leukemia cells. *J. Cell Biol.*, 101:2145–2155, 1985.

References

- [82] N.L. Andrews, J. Pfeiffer, M.A. Martinez, D.M. Haaland, R.W. Davis, T. Kawakami, J.M. Oliver, B.S. Wilson, and D.S. Lidke. Small, mobile Fc ϵ RI aggregates are signaling competent. *Immunity*, 31:469–479, 2009.
- [83] D Axelrod, D.E. Koppel, J. Schlessinger, E. Elson, and W.W. Webb. Mobility measurement by analysis of fluorescence photobleaching recovery kinetics. *Biophys. J.*, 16:1055–1069, 1976.
- [84] D. Madge, E. Elson, and W.W. Webb. Thermodynamic fluctuations in a reacting system - measurement by fluorescence correlation spectroscopy. *Phys. Rev. Lett.*, 29:705–708, 1972.
- [85] H. Qian, M.P. Sheetz, and E.L. Elson. Single particle tracking: Analysis of diffusion and flow in two-dimensional systems. *Biophys. J.*, 60:910–921, 1991.
- [86] X. Michalet. Mean square displacement analysis of single-particle trajectories with localization error: Brownian motion in an isotropic medium. *Phys. Rev. E*, 82:041914, 2010.
- [87] B. Rieger, H.R.C. Dietrich, L.R. Van den Doel, and L.J. Van Vliet. Diffusion of microspheres in sealed and open microarrays. *Microsc. Res. Tech.*, 65:218–225, 2004.
- [88] M.J. Saxton. Single-particle tracking: Effect of corrals. *Biophys. J.*, 69:389–398, 1995.
- [89] T. Bickel. A note on confined diffusion. *Physica A*, 377:24–32, 2007.
- [90] A. Kusumi, Y. Sako, and M. Yamamoto. Confined lateral diffusion of membrane receptors as studied by single particle tracking (nanovid microscopy). Effects of calcium-induced differentiation in cultured epithelial cells. *Biophys. J.*, 65:2021–2040, 1993.
- [91] W.F. Wade, J.H. Freed, and M. Edidin. Translational diffusion of class II major histocompatibility complex molecules is constrained by their cytoplasmic domains. *J. Cell Biol.*, 109:3325–3331, 1989.
- [92] D.S. Lidke, N.L. Andrews, J.R. Pfeiffer, H.D.T. Jones, M.B. Sinclair, D.M. Haaland, A.R. Burns, B.S. Wilson, J.M. Oliver, and K.A. Lidke. Exploring membrane protein dynamics by multicolor single quantum dot imaging using wide field, TIRF, and hyperspectral microscopy. *Proc. of SPIE*, 6448:64480Y, 2007.
- [93] I.M. Chakravarti, R.G. Laha, and J. Roy. *Handbook of Methods of Applied Statistics, Volume I*. John Wiley, 1967.

References

- [94] E. Evans. Probing the relation between force-lifetime-and chemistry in single molecular bonds. *Annu. Rev. Biophys. Biomol. Struct.*, 30:105128, 2001.
- [95] K. Xu, B. Goldstein, D. Holowka, and B. Baird. Kinetics of multivalent antigen DNP-BSA binding to IgE-Fc ϵ RI in relationship to the stimulated tyrosine phosphorylation of Fc ϵ RI. *J. Immunol.*, 160:3225–3235, 1998.
- [96] T. Baumgart, B. Cararo, C. Zhu, and S.L. Das. Thermodynamics and mechanics of membrane curvature generation and sensing by proteins and lipids. *Annu. Rev. Phys. Chem.*, 62:483–506, 2011.
- [97] M.J. Cavallaro, L. Botto, E.P. Lewandowski, M. Wang, and K.J. Stebe. Curvature-driven capillary migration and assembly of rod-like particles. *PNAS*, 108:20923–20928, 2011.
- [98] T. Kruglov. Correlation function of the excluded volume. *J. Appl. Cryst.*, 38:716–720, 2005.
- [99] X. Li, C.-Y. Shew, Y. Liu, R. Pynn, E. Liu, K.W. Herwig, G.S. Smith, J.L. Robertson, and W.-R. Chen. Prospect for characterizing interacting soft colloidal structures using spin-echo small angle neutron scattering. *J. Chem. Phys.*, 134, 2011.
- [100] F.H. Stillinger. Pair distribution in the classical rigid disk and sphere system. *J. Comp. Phys.*, 7:367–384, 1971.
- [101] X. Guo and U. Riebel. Theoretical direct correlation function for two-dimensional fluids of monodisperse hard spheres. *J. Chem. Phys.*, 125:144504, 2006.
- [102] M. Adda-Bedia, E. Katzav, and D. Vella. Solution of the percus-yevick equation for hard disks. *J. Chem. Phys.*, 128:184508, 2008.
- [103] X. Li, C.-Y. Shew, Y. Liu, R. Pynn, E. Liu, K.W. Herwig, G.S. Smith, J.L. Robertson, and W.-R. Chen. Theoretical studies on the structure of interacting colloidal suspensions by spin-echo small angle neutron scattering. *J. Chem. Phys.*, 132:174509, 2010.
- [104] S.Y. Qi, J.T. Groves, and A.K. Chakraborty. Synaptic pattern formation during cellular recognition. *PNAS*, 98:6548–6553, 2001.
- [105] T.R. Weikl and R. Lipowsky. Pattern formation during T-cell adhesion. *Biophys. J.*, 87:3665, 2004.
- [106] M. Figge and M. Meyer-Hermann. Modeling receptor-ligand binding kinetics in immunological synapse formation. *Eur. Phys. J. D*, 51:153–160, 2009.

References

- [107] P.K. Tsourkas, N. Baumgarth, S.I. Simon, and S. Raychaudhuri. Mechanisms of B-cell synapse formation predicted by Monte Carlo simulation. *Biophys. J.*, 92:4196–4208, 2007.
- [108] P.K. Tsourkas, M.L. Longo, and S. Raychaudhuri. Monte Carlo study of single molecule diffusion can elucidate the mechanism of B cell synapse formation. *Biophys. J.*, 95:1118–1125, 2008.
- [109] P.K. Tsourkas, and S. Raychaudhuri. Modeling of B cell synapse formation by Monte Carlo simulation shows that directed transport of receptor molecules is a potential formation mechanism. *Cell. Molec. Bioeng.*, 3:256–268, 2010.
- [110] E. Ruckenstein and B. Pulvermacher. Kinetics of crystallite sintering during heat treatment of supported metal catalysts. *AIChE J.*, 19:356, 1973.
- [111] E. Ruckenstein and B. Pulvermacher. Growth kinetics and the size distributions of supported metal crystallites. *J. Catalysis*, 29:224–245, 1973.
- [112] D. Kashchiev. Kinetics of thin film coalescence due to crystallite surface migration. *Surface Science*, 55:477–493, 1976.
- [113] B. Lewis and J.C. Anderson. *Nucleation and growth of thin films*. Academic Press, 1978.
- [114] D. Kashchiev. *Nucleation: Basic Theory and Applications*. Butterworth-Heinemann, 2000.
- [115] M.v. Smoluchowski. Über brownische Molekularbewegung unter Einwirkung äußere Kräfte und deren Zusammenhang mit der verallgemeinerten Diffusionsgleichung. *Ann. Physik*, 48:1103–1112, 1915.
- [116] S. Chandrasekhar. Stochastic problems in physics and astronomy. *Rev. Mod. Phys.*, 15:1–89, 1943.
- [117] J. Crank. *Free and moving boundary problems*. Clarendon press, 1987.
- [118] L.Ts. Adzhemyan, A.N. Vasil’ev, A.P. Grinin, and A.K. Kazansky. Self-similar solution to the problem of vapor diffusion toward the droplet nucleated and growing in a vapor–gas medium. *Colloid J.*, 68:381–383, 2006.
- [119] S.I. Barry and J. Caunce. Exact and numerical solutions to a Stefan problem with two moving boundaries. *Appl. Math. Mod.*, 32:83–98, 2008.
- [120] H.L. Frisch and F.C. Collins. Diffusional processes in the growth of aerosol particles. II. *J. Chem. Phys.*, 21:2158–2165, 1953.

References

- [121] F.C. Goodrich. On diffusion-controlled particle growth: the moving boundary problem. *J. Phys. Chem.*, 70:3660–3665, 1966.
- [122] T. SA. Witten, Jr and L.M. Sander. Diffusion-limited aggregation, a kinetic critical phenomenon. *Phys. Rev. Lett.*, 47:1400–1403, 1981.
- [123] P. Jensen, A.-L. Barabasi, H. Larralde, S. Havlin, and H.E. Stanley. Deposition, diffusion, and aggregation of atoms on surfaces: A model for nanostructure growth. *Phys. Rev. B*, 50:15316–15329, 1994.
- [124] C.R. Doering and D. ben-Avraham. Interparticle distribution functions and rate equations for diffusion-limited reactions. *Phys. Rev. A*, 38:3035–3042, 1988.
- [125] D. ben-Avraham. Complete exact solution of diffusion-limited coalescence, $A + A \rightarrow A$. *Phys. Rev. Lett.*, 81:4756–4759, 1998.
- [126] J.M. Sancho, A.H. Romero, A.M. Lacasta, and K. Lindenberg. Langevin dynamics of $A + A$ reactions in one dimension. *J. Phys.: Condens. Matter*, 19:065108, 2007.
- [127] V. Privman, C.R. Doering, and H.L. Frisch. Crossover from rate-equation to diffusion-controlled kinetics in two-particle coagulation. *Phys. Rev. E*, 48:846, 1993.
- [128] D. Zhong and D. ben Avraham. Diffusion-limited coalescence with finite reaction rates in one dimension. *J. Phys. A: Math. Gen.*, 28:33–44, 1995.
- [129] M. Hoyuelos and H.O. Martin. Rate equation of the $A + A \rightarrow A$ reaction with probability of reaction and diffusion. *Phys. Rev. E*, 48:3309–3313, 1993.
- [130] F. Leyvraz. Scaling theory and exactly solved models in the kinetics of irreversible aggregation. *Phys. Reports*, 383:95, 2003.
- [131] E. W. Montroll and B. West. Scattering of waves by irregularities in periodic discrete lattice spaces. I. Reduction of problem to quadratures on a discrete model of the Schroedinger equation. *J. Stat. Phys.*, 13:17–42, 1975, and references therein.
- [132] A. Szabo, G. Lamm, and G.H. Weiss. Localized partial traps in diffusion processes and random walks. *J. Stat. Phys.*, 34:225–238, 1984.
- [133] G.E. Roberts and H. Kaufman. *Table of Laplace Transforms*. W. B. Saunders Company, 1966.
- [134] G.B. Arfken and J.W. Weber. *Mathematical methods for physicists*. Elsevier Academic Press, 2005.

References

- [135] I.S. Gradshteyn, I.M. Ryzhik, and A. Jeffrey. *Table of integrals, series, and products*. Academic Press, 1994.
- [136] J.L. Spouge. Exact solution for a diffusion-reaction process in one dimension. *Phys. Rev. Lett.*, 60:871–874, 1988.
- [137] V.M. Kenkre and H.-L. Wu. Interplay of quantum phases and nonlinearity in the nonadiabatic dimer. *Phys. Lett. A*, 135:120–124, 1989.
- [138] M.A. Rodriguez, G. Abramson, H.S. Wio, and A. Bru. Diffusion-controlled biomolecular reactions: Long- and intermediate-time regimes with imperfect trapping within a galanin approach. *Phys. Rev. E*, 48:829–836, 1993.
- [139] A.D. Sanchez, M.A. Rodriguez, and H.S. Wio. Results in trapping reactions for mobile particles and a single trap. *Phys. Rev. E*, 57:6390–6397, 1998.
- [140] A.D. Sanchez. Trapping reactions for mobile particles and a trap in the laboratory frame. *Phys. Rev. E*, 59:5021–5025, 1999.
- [141] H.S. Carslaw and J.C. Jaeger. *Conduction of heats in solids*. Oxford University Press, 1959.
- [142] S. Redner and D. ben-Avraham. Nearest-neighbor distances of diffusing particles from a single trap. *J. Phys. A: Math. Gen.*, 23:L1169–L1173, 1990.
- [143] S. Redner. *A guide to first-passage processes*. Cambridge University Press, 2001.
- [144] R.A. Blythe and A.J. Bray. Survival probability of a diffusing particle in the presence of poisson-distributed mobile traps. *Phys. Rev. E*, 67:041101, 2003.
- [145] E. Ben-Naim, S. Redner, and G.H. Weiss. Partial absorption and virtual traps. *J. Stat. Phys.*, 71:75–88, 1993.
- [146] D.C. Torney and M. McConnell. Diffusion-limited reactions in one dimension. *J. Phys. Chem.*, 87:1941–1951, 1983.
- [147] W. Ebeling, F. Schweitzer, and B. Tilch. Active brownian particles with energy depots modeling animal mobility. *Biosystems*, 49(1):17–29, 1999.
- [148] L. Giuggioli, G. Abramson, V. M. Kenkre, C. Parmenter, and T. Yates. Theory of home range estimation from displacement measurements of animal populations. *J. Theoretical Biology*, 240:126–135, 2006.
- [149] see L.E. Reichl. *A Modern Course in Statistical Physics*. WILEY-VCH Verlag, 2009.

References

- [150] H. Risken. *The Fokker-Planck equation: Methods of solution and applications*. Springer-Verlag, 1989.
- [151] M. Abramowitz and I.A. Stegun. *Handbook of Mathematical Functions*. Dover Publications, 1970.
- [152] B. Bagchi, G.R. Fleming, and D.W. Oxtoby. Theory of electronic relaxation in solution in the absence of an activation barrier. *J. Chem. Phys.*, 78:7375–7385, 1983.
- [153] H. Taitelbaum. Nearest-neighbor distances at an imperfect trap in two dimensions. *Phys. Rev. A*, 43:6592–6596, 1991.
- [154] R.H. Ritchie and A.Y. Sakakura. Asymptotic expansions of solutions of the heat conduction equation in internally bounded cylindrical geometry. *J. Appl. Phys.*, 27:1453, 1956.
- [155] S.H. Park, H. Peng, S. Parus, H. Taitelbaum, and R. Kopelman. Spatially and temporally resolved studies of convectionless photobleaching kinetics: line trap. *J. Phys. Chem. A*, 106:7586–7592, 2002.
- [156] R.G. Herrmann. Biogenesis and evolution of photosynthetic (thylakoid) membranes. *Biosci. Rep.*, 19:355, 1999.
- [157] S.A. Rice. *Comprehensive Chemical Kinetics: Diffusion-limited Reactions (Vol. 25)*. Elsevier Science Publishers, 1985.
- [158] G. Doetsch. *Guide to the applications of the Laplace and Z-transforms*. London, New York, Van Nostrand-Reinhold, 1971.
- [159] E.B. Krissinel and N. Agmon. Spherical symmetric diffusion problem. *J. Comp. Chem.*, 17:1085, 1995.
- [160] F.C. Collins and G.E. Kimball. Diffusion-controlled reaction rates. *J. Colloid. Sci.*, 4:425–437, 1949.
- [161] H. Taitelbaum, R. Kopelman, G.H. Weiss, and S. Havlin. Statistical properties of nearest-neighbor distances at an imperfect trap. *Phys. Rev. A*, 41:3116–3120, 1990.
- [162] K. Spendier and V.M. Kenkre. Some useful results in reaction-diffusion theory. *in preparation*.
- [163] G. Wilemski and M. Fixman. General theory of diffusion-controlled reactions. *J. Chem. Phys.*, 58:4009–4019, 1973.

References

- [164] A.D. Sanchez. Trapping with biased diffusion species. *Physica A*, 284:1–12, 2000.
- [165] P.L. Krapivsky and S. Redner. Life and death in an expanding cage and at the edge of a receding cliff. *Am. J. Phys.*, 64:546–552, 1996.
- [166] M.E. Fisher and M.P. Gelfand. The reunion of three dissimilar vicious walkers. *J. Stat. Phys.*, 53:175–189, 1988.
- [167] G. Abramson and H.S. Wio. Time behavior for diffusion in the presence of static imperfect traps. *Chaos, Solitons and Fractals*, 6:1–5, 1995.
- [168] R. Bellmann. *Brief Introduction of theta functions*. Holt, Rinehart and Winston, 1961.
- [169] K.B. Wolf. *Integral transforms in Science and Engineering*. Plenum Press, 1979.
- [170] W.Y. Yang, W. Cao, T. Chung, and Morris. *Applied numerical methods using MATLAB*. John Wiley and Sons, 2005.
- [171] A.J. Bray and R. Smith. Survival of a diffusing particle in an expanding cage. *J. Phys. A: Math. Theor.*, 40:10965–10972, 2007.
- [172] J. Membrez, P.P. Infelta, and A. and Renken. Use of the Laplace transform technique for simple kinetic parameters evaluation. Application to the adsorption of a protein on porous beads. *Chem. Eng. Sci.*, 51:4489, 1996.
- [173] J.R. Taylor. *An Introduction to Error Analysis*. University Science Books, 1982.
- [174] V.M. Kenkre and K.Spendier. A mathematical model of particle coalescence. *in preparation*.
- [175] K. Spendier, J.L. Thomas, J.A. Timlin, and V. M. Kenkre. A mechanism of receptor cluster coalescence in mast cells. *in preparation*.
- [176] M. Coue, S.L. Brenner, I. Spector, and E.D. Korn. Inhibition of actin polymerization by latrunculin A. *FEBS Lett.*, 213:316–318, 1987.
- [177] J.R. Abney, B.A. Scalettar, and C.R. Hackenbrock. On the measurement of particle number and mobility in non-ideal solutions by fluorescence correlation spectroscopy. *Biophys. J.*, 58:261–265, 1990.
- [178] B. Wu, Y. Chen, and J.D. Muller. Fluorescence correlation spectroscopy of finite-sized particles. *Biophys. J.*, 94:2800–2808, 2008.
- [179] N.A. Kurniawan and R. Rajagopalan. Probe-independent image correlation spectroscopy. *Langmuir*, 27:2775–2782, 2011.

References

- [180] E. Mohn and P. Stavem. On the distribution of randomly placed discs. *Biometrics*, 30:137–156, 1974.
- [181] B. Zhang, J. Zerubia, and J.-C. Olivo-Marin. Gaussian approximations of fluorescence microscope point-spread function models. *Appl. Opt.*, 46:1819–1829, 2007.
- [182] P. Attard, D.R. Berard, C.P. Ursenbach, and G.N. Patey. Interaction free energy between planar walls in dense fluids: an Ornstein-Zernike approach with results for hard-sphere, Lennard-Jones, and dipolar systems. *Phys. Rev. A*, 44:8224–8234, 1991.
- [183] T.J. Holmes and Y.-H. Liu. Richardson-Lucy/maximum likelihood image restoration algorithm for fluorescence microscopy: further testing. *Appl. Opt.*, 28:4930–4938, 1989.
- [184] T.J. Holmes. Blind deconvolution of quantum-limited incoherent imagery: maximum-likelihood approach. *J. Opt. Soc. Am. A*, 9:1052–1061, 1992.
- [185] H. Hassanzadeh and M. Pooladi-Darvish. Comparison of different numerical Laplace inversion methods for engineering applications. *Appl. Math. Comp.*, 189:1966–1981, 2007.
- [186] J. Abate. Numerical inversion of Laplace transforms of probability distributions. *ORSA J. Comp.*, 7:36–43, 1995.
- [187] K.S. Crump. Numerical inversion of Laplace transforms using a Fourier series approximation. *J. Ass. Comp. Mach.*, 23:89–96, 1976.
- [188] J. Abate and W. Whitt. Unified framework for numerically inverting Laplace transforms. *INFORMS J. Comp.*, 18:408–421, 2006.
- [189] D.P. Graver Jr. Observing stochastic processes and approximate transform inversion. *Operations Research*, 14:444–459, 1966.